Battery energy storage systems

Power electronics interface and grid integration

Stecca, M.

DOI
10.4233/uuid:e2413727-192f-415d-8a4d-248f729b80ff

Publication date
2022

Document Version
Final published version

Citation (APA)
Stecca, M. (2022). *Battery energy storage systems: Power electronics interface and grid integration*. [Dissertation (TU Delft), Delft University of Technology]. https://doi.org/10.4233/uuid:e2413727-192f-415d-8a4d-248f729b80ff

BATTERY ENERGY STORAGE SYSTEMS

POWER ELECTRONICS INTERFACE AND GRID INTEGRATION

BATTERY ENERGY STORAGE SYSTEMS

POWER ELECTRONICS INTERFACE AND GRID INTEGRATION

Dissertation

for the purpose of obtaining the degree of doctor
at Delft University of Technology
by the authority of the Rector Magnificus prof.dr.ir. T.H.J.J. van der Hagen
chair of the Board for Doctorates
to be defended publicly on
Friday 24th of February 2023 at 10 o'clock

by

Marco STECCA

Master of Science in Electrical Engineering, Politecnico di Milano, Italy
born in Abano Terme, Italy.

This dissertation has been approved by the promotors.

Composition of the doctoral committee:

Rector Magnificus,	chairperson
Prof. dr. ir. P. Bauer	Delft University of Technology, promotor
Prof. dr. P. Palensky	Delft University of Technology, promotor
Dr. L.M. Ramirez Elizondo	Delft University of Technology, co-promotor

Independent members:

Prof. dr. R. Teodorescu	Aalborg University
Prof. dr. D. Lascu	Universitatea Politehnica Timișoara
Prof. dr. ir. Z. Lukszo	Delft University of Technology
Prof. dr. ir. A.H.M. Smets	Delft University of Technology

Rijksdienst voor Ondernemend
Nederland

The research leading to these results was performed within the project 'Integration of Battery Energy Storage Systems in Distribution Grids (FLEXBat)' - funded by the Dutch financial source 'Urban Energy' from RVO (Rijksdienst voor Ondernemend Nederland), Project TEUE117013.

Printed by Ridderprint | www.ridderprint.nl

Cover design by Davide Martignon

ISBN 978-94-6366-656-5

An electronic version of this dissertation is available at
http://repository.tudelft.nl/.

To mom and dad.

Contents

SUMMARY

One of the fundamentals of a sustainable society is the production of electricity from renewable sources. Many countries and institutions are investing heavily for reaching this objective. However, the non-controllable nature of most renewable sources brings new challenges to the existing electrical networks. Energy storage systems can help the electrical network to increase its renewable energy hosting capacity, and, among them, battery-based storage systems are particularly suitable for supporting the grid due to their fast response and flexible operation. Nonetheless, the wide adoption of Battery Energy Storage Systems (BESSs) is nowadays limited by the high initial investments and the not always clear business case. Therefore, this thesis investigates how to reduce the investments and operating costs by optimizing the power electronics interface, and how to enhance the system revenues by combining multiple functionalities and enabling new ones, to make the deployment of BESS more financially viable.

POWER ELECTRONICS CONVERTER

BESSs are connected to the electrical grids through a power electronics converter. This device converts the energy of the battery, which operates in direct current (DC), into alternating current (AC), which is how the electrical grid operates. The conversion process from DC to AC, and vice versa, generates losses, due to the energy flow through the power electronics converter. The energy losses are a cost for the storage system's owner, therefore, researchers in academia and industry continuously strive to enhance the conversion efficiency of power electronics converters, while maintaining low manufacturing costs, and extending the system lifetime.

In this thesis, a methodology to evaluate the lifetime of the main BESS components, namely the electrochemical storage, the semiconductors, and the electrolytic capacitors, based on degradation models available in the literature, is proposed. This methodology is then applied for a BESS providing primary frequency regulation, considering the case of Germany, the United Kingdom, and the Netherlands. The lifetime information is used for optimizing the service provision to obtain the maximum net present value. Overall, it is found that the provision of primary frequency regulation utilizing a BESS can be profitable in all the three countries analyzed, with the present remuneration tariffs and BESS capital costs, and that the highest revenues can be found in the Netherlands.

Furthermore, in the context of enhancing the storage system conversion efficiency, the possibility of utilizing hybrid Si/SiC switches as semiconductors for the BESS converter is studied. Hybrid switches, which are a more efficient alternative to the traditional Si IGBTs, are modeled and experimentally characterized to benchmark the hybrid switch performances and costs versus traditional single technology switches, when implemented in a BESS performing primary frequency regulation. The analysis shows that hybrid switches are particularly competitive versus the full Si IGBTs solutions when the BESS operates at low partial loads, which is often the case in grid-connected applications.

POWER REDISTRIBUTOR FUNCTIONALITY

BESSs are typically deployed for supporting grid users and network operators, or for participating in energy and ancillary services. All these applications require the BESS to exchange symmetric power with the grid. However, there are grid services, such as the power redistributor functionality, which require asymmetric power exchange, meaning that the three phases process different power between them. The power redistributor service is generally performed by separate compensators, placed by the system operators, to reduce the phase unbalance, which is detrimental to the grid operation. In this context, the BESS's power electronics converter has the potential to enable the storage system to provide the power redistributor functionality.

Therefore, in this thesis, it is investigated how to enable the power redistributor functionality and its impacts on the design and operation of a grid-connected BESS. It is shown that the asymmetric operation can be enabled in an already deployed BESS without significant hardware expansions. However, the additional current harmonics flowing in the battery due to the unbalance operation can lead to additional degradation. All in all, the power redistributor functionality can be implemented as an add-on functionality in a grid-connected BESS, creating an additional source of revenue.

DISPATCH OF A GRID-CONNECTED BESS

The last point discussed in this thesis is related to the dispatching of a grid-connected BESS. More specifically, it is evaluated how a BESS can participate in energy and ancillary services markets while providing services to a third party, in this case, a photovoltaic-assisted electric vehicle fast-charging station. An optimization problem is formulated using mixed-integer linear programming to combine battery storage system operation in the day-ahead and frequency regulation market, and the remunerated services offered to the charging station. The study shows that such battery storage system implementation is economically and technically advantageous for the players involved; the battery storage system can stack additional revenues on top of the market revenues, the charging station benefits from the reduced grid connection costs, and the system operator would indirectly benefit from the shaved power profile of the charging station.

SAMENVATTING

Eén van de grondbeginselen van een duurzame samenleving is de productie van elektriciteit uit duurzame bronnen. Veel landen en instellingen investeren fors om dit doel te bereiken. Het onbeheersbare karakter van de meeste duurzame bronnen brengt echter nieuwe uitdagingen met zich mee voor de bestaande elektrische netwerken. Energieopslagsystemen kunnen het elektriciteitsnet helpen haar capaciteit voor het hosten van duurzame energie te vergroten, en onder meer zijn op batterijen gebaseerde opslagsystemen bijzonder geschikt om het net te ondersteunen vanwege hun snelle reactie en flexibele werking. Desalniettemin wordt de brede acceptatie van Battery Energy Storage Systems (BESS's) tegenwoordig beperkt door de hoge initiële investeringen en de niet altijd duidelijke business case. Daarom onderzoekt dit proefschrift hoe de investeringen en bedrijfskosten kunnen worden verlaagd door de vermogenselektronica-interface te optimaliseren, en hoe de systeeminkomsten kunnen worden verhoogd door meerdere functionaliteiten te combineren en nieuwe mogelijk te maken, om de inzet van BESS financieel haalbaarder te maken.

VERMOGENSELEKTRONICA-OMVORMER

BESS's zijn verbonden met het elektriciteitsnet via een vermogenselektronica-omvormer. Dit apparaat zet de energie van de batterij, die werkt met gelijkstroom (DC), om naar wisselstroom (AC), dat is hoe het elektriciteitsnet werkt. Het omzettingsproces van DC naar AC en vice versa resulteert in verliezen vanwege de energiestroom door de vermogenselektronica-omvormer. De energieverliezen zijn een kostenpost voor de eigenaar van het opslagsysteem. Daarom streven onderzoekers in de academische wereld en de industrie er voortdurend naar om het rendement van vermogenselektronica-omvormers te verbeteren, terwijl de productiekosten laag blijven en de levensduur van het systeem wordt verlengd.

In dit proefschrift wordt een methodologie voorgesteld om de levensduur van de belangrijkste BESS-componenten, namelijk de elektrochemische opslag, de halfgeleiders en de elektrolytische condensatoren, te evalueren, gebaseerd op degradatiemodellen die beschikbaar zijn in de literatuur. Deze methodologie wordt vervolgens toegepast voor een BESS die primaire frequentieregeling biedt, rekening houdend met gevallen van Duitsland, het Verenigd Koninkrijk en Nederland. De informatie over de levensduur wordt gebruikt om de dienstverlening te optimaliseren om de maximale netto contante waarde te verkrijgen. Al met al blijkt dat het aanbieden van primaire frequentieregeling voor een BESS in alle drie de geanalyseerde landen winstgevend kan zijn, met de huidige vergoedingstarieven en BESS kosten, en dat de hoogste opbrengsten in Nederland te vinden zijn.

Verder wordt, in de context van het verbeteren van het rendement van het opslagsysteem, de mogelijkheid bestudeerd om hybride Si/SiC-schakelaars te gebruiken als halfgeleiders voor de BESS-omvormer. Hybride schakelaars, die een efficiënter alternatief zijn voor de traditionele Si IGBT's, zijn gemodelleerd en experimenteel gekarakteriseerd om de prestaties en kosten van hybride schakelaars te vergelijken met traditionele schakelaars met één technologie, wanneer geïmplementeerd in een BESS die primaire frequentieregeling

uitvoert. Uit de analyse blijkt dat hybride schakelaars bijzonder vergelijkbaar zijn ten opzichte van de volledige Si IGBT's oplossingen wanneer de BESS werkt bij lage deellasten, wat vaak het geval is in netgekoppelde toepassingen.

STROOMHERVERDELINGSFUNCTIONALITEIT

BESS's worden doorgaans ingezet ter ondersteuning van netgebruikers en netbeheerders, of voor deelname aan energie- en ondersteunende diensten. Al deze toepassingen vereisen dat de BESS symmetrische stroom met het net uitwisselt. Er zijn echter netdiensten, zoals de stroomherverdelingsfunctionaliteit, die asymmetrische stroomuitwisseling vereisen, wat betekent dat de drie fasen verschillende stromen tussen hen verwerken. De stroomherverdelingsservice wordt over het algemeen uitgevoerd door afzonderlijke compensatoren, geplaatst door de netbeheerders, om de fase-onbalans te verminderen, die nadelig is voor de werking van het net. In deze context heeft de vermogenselektronica-omzetter van de BESS de potentie om het opslagsysteem in staat te stellen de stroomherverdelingsfunctionaliteit te leveren.

Daarom wordt in dit proefschrift onderzocht hoe de stroomherverdelingsfunctionaliteit kan worden ingeschakeld en de effecten ervan op het ontwerp en de werking van een op het elektriciteitsnet aangesloten BESS. Er wordt aangetoond dat de asymmetrische werking kan worden ingeschakeld in een reeds geïmplementeerde BESS zonder noemenswaardige hardware-uitbreidingen. De extra harmonischen in de stroom die de batterij invloeien als gevolg van de onbalans, kunnen echter tot extra degradatie leiden. Al met al kan de stroomherverdelingsfunctionaliteit worden geïmplementeerd als een add-on-functionaliteit in een op het net aangesloten BESS, waardoor een extra bron van inkomsten ontstaat.

AFGIFTE VAN VERMOGEN DOOR EEN NETGEKOPPELDE BESS

Het laatste punt dat in dit proefschrift wordt besproken, heeft betrekking op het afgeven van vermogen door een netgekoppelde BESS. Meer specifiek wordt geëvalueerd hoe een BESS kan deelnemen aan de markten voor energie en ondersteunende diensten en tegelijkertijd diensten kan leveren aan een derde partij, in dit geval een snellaadstation voor elektrische voertuigen met fotovoltaïsche ondersteuning. Er wordt een optimalisatieprobleem geformuleerd met behulp van lineaire programmering met gemengde gehele getallen om de werking van batterijopslagsystemen in de day-ahead- en frequentiereguleringsmarkt te combineren met de betaalde diensten die aan het laadstation worden aangeboden. De studie toont aan dat de implementatie van een dergelijk batterijopslagsysteem economisch en technisch voordelig is voor de betrokken spelers; het batterijopslagsysteem kan extra inkomsten bovenop de marktinkomsten stapelen, het laadstation profiteert van de lagere netaansluitingskosten en de systeembeheerder zou indirect profiteren van het veminderde vermogensprofiel van het laadstation.

List of Figures

List of Tables

1

INTRODUCTION

1.1. MOTIVATION

The existing electrical networks have been designed according to the old paradigm that foresees mainly large generation plants, connected at the transmission grids, providing most of the required energy. Distribution grids, instead, have been planned to host consumption points and not distributed generation. However, the increase in solar and wind-based production, together with the introduction of new types of loads, such as electric vehicles and heat pumps, has brought substantial changes. Renewable energy-based generators often have small sizes and are connected to the distribution grid through power electronics devices. Moreover, new loads are larger and have the potential to offer more flexibility than traditional loads. For these reasons, distribution system operators now face new technical challenges, primarily due to the seasonal and environmental dependency of renewable sources, such as wind and solar-based generators. For example, the introduction of generators into the distributor grids leads to a bidirectional power flow, therefore the well-consolidated practices for controlling the power flow, voltage level, and power quality are becoming insufficient.

It is then necessary to develop new technically and economically efficient strategies to manage the system and to ensure its safe operation. Battery Energy Storage Systems (BESSs) have great potential for solving the previously mentioned technical challenges, thus deferring extra network investments. As a consequence, BESSs recently found new space in the electrical grids due to their ability to provide multiple services to the grid operators. Through BESSs, the operators can manage active and reactive power flow, for example, to control the substations' voltage, reduce the loading of the conductors, minimize the system losses, and flatten the power profile of renewable sources. Despite the strong technical suitability, BESSs do not yet find wide deployment, mainly due to their high initial costs and not always clear business case. In this context, this thesis aims are tackling this issue, by researching how to facilitate the deployment of BESSs in distribution grids.

Currently, BESSs are typically deployed either to support other grid uses, by shaving the peaks of power consumption or production or to participate in regulated energy and ancillary services markets [214]. Participation in market activities has the advantage of offering a

clear remuneration scheme. Nonetheless, sole participation in the day-ahead energy market has been studied to be not profitable enough in the central European market [270]. It has to be noted, that when this research started, daily price spreads of 300-400 €/MWh in the day ahead market repeating day after day, due to the current geopolitical situation, were almost unimaginable. Additionally, ancillary services markets, such as the frequency regulation markets, are accepting BESSs as service providers. The inertia of the electrical system and its regulating power is decreasing, due to a large amount of Power Electronics (PE) interfaced distributed plants that are being deployed [177, 63]. Therefore, system operators are then in need of finding new balancing resources, and BESSs are particularly suitable for various frequency balancing services [72, 144, 145]. Although lithium-ion BESSs show good technical suitability for primary frequency regulation [227, 224], the high initial investment required to deploy such systems represents a barrier for system operators and private investors [21, 130]. Therefore, to better analyze the financial feasibility of the BESSs, its lifetime becomes a key factor that should be optimized to obtain the maximum revenues.

Grid-connected BESSs have three main components, the battery, which stores the energy, the power electronics converter, which interface the battery with the grid, and the transformer which is used to step up the output voltage of the power electronics converter to the AC grid level [172, 34, 226]. Lithium-based batteries have been the preferred choice by the industry, due to their higher power and energy density, efficiency, and lower daily self-discharge, than other technologies such as, lead acid, sodium-sulfur, and redox-flow batteries [261, 193]. The power electronics converter used to interface the battery to the grid can be assembled with different circuit topology. Among the preferred choices of industry, due to its simplicity and robustness, there is the two-level converter, which consists of three half-bridge legs, one for each phase, a DC-link, and an AC filter for limiting the current and voltage harmonics at the point of connection with the grid [244, 172]. Other elements, such as EMI filters, circuit breakers, contactors, and measurement devices are also vital for the operation of the converter. The two-level converter is also widely used for other industrial applications, such as motor drives and renewable energy [191, 207, 264], however, its application in grid-connected BESSs requires to take into account the peculiarities of batteries. For example, the cells' terminal voltage can vary up to 40% between the fully charged and fully discharged status [238], but also the limitations and requirements in terms of safety, harmonic content, and P-Q capabilities set by the technical standards and national grid codes need to be considered [101, 100].

All these factors ultimately influence the selection of the power electronics converter components and control method. In this context, Silicon (Si) IGBTs are currently the dominant power semiconductor technology for industrialized high power grid-connected Voltage Source Converters (VSCs), due to their robustness, relatively low cost, and good conduction performance at high currents [171]. Nonetheless, Si IGBTs have unsatisfactory performance at low current conditions, e.g., partial load efficiency, and, especially in high voltage class devices [183], which are often the case in BESSs. In this context, Silicon Carbide (SiC) MOSFETs have gained popularity due to their excellent switching performance, the easy paralleling feature that can enable a higher power handling, and, above all, the higher temperature capability of the SiC material, which can simplify the thermal management of the system [264, 88, 277]. The major drawback of the SiC MOSFET is the higher manufacturing cost and unproven reliability when compared to the traditional Si IGBT [161]. The significantly higher cost of the SiC MOSFET and the unsatisfactory performances of the Si IGBT

call for a compromised solution, e.g., a hybrid Si/SiC switch, which is obtained by paralleling Si IGBTs and SiC MOSFETs and have the potential of improving the performances of Si IGBTs while remaining cost competitive. Hybrid switches have been already investigated in literature, however, in this thesis, a variation of the hybrid switch concept proposed in literature is analyzed and characterized. Furthermore, the implementation of hybrid switches in BESSs is studied. Ultimately, the improvements given by a more performing and at the same time cost competitive converter would allow for a reduction of the BESS's operating costs, thus enhancing its profitability.

In the context of enhancing the profitability of BESSs, other than reducing operating costs, one could think about boosting revenues, for example, by enabling new functionalities, therefore creating new revenue streams, or performing multiple services with the same unit. As previously mentioned, BESSs are typically deployed for supporting other grid users, the grid operator, or participating in regulated markets. All these services require the BESS to exchange symmetrical active or reactive power with the grid. Nonetheless, a grid-connected BESS is also capable to exchange asymmetric power with the grid through its power electronics converter [71, 126]. By providing asymmetric power, the BESS can act as a power redistributor, meaning that it can balance the power flow within the three phases and ensure better utilization of the grid assets, which leads to an efficient and reliable grid operation [61, 139, 138]. This capability could allow BESSs to provide additional functionalities to grid operators which could enhance the BESS's profitability. The implementation and the impact of this functionality in a BESS and on its components is investigated in this thesis since it has not been studied in literature.

The provision of multiple services by a single BESS has been reported to be an efficient way to enhance its profitability [38, 275, 160]. In this context, the dual participation of a BESS in remunerated energy and ancillary services markets has been proven to be profitable in several European countries [117]. Previous literature has investigated the technical performance and schedule definition problem of participating in two different markets with a single unit [170, 38, 275, 160, 218]. Furthermore, several studies have presented the benefits of deploying BESS in the premises of an electric vehicle charging station, or a renewable energy source power plant [106, 86, 127]. Nonetheless, the stacking of market activities with the service provision to grid users has not been widely investigated due to technical and regulatory issues, and this is the motivation for the study presented in this thesis.

1.2. THESIS OBJECTIVE AND RESEARCH QUESTIONS

The main objective of this thesis is as follows.

"To research methods and components to improve the design of the power electronics interface and to support potential market services of grid-connected battery storage systems, so that a more profitable integration of battery storage systems into distribution grids is achieved."

The main research is then divided into several research questions with individual objectives. The research questions correspond to the thesis' chapters, and are as follows:

Q1 *To what extent can the lifetime of a BESS providing primary frequency regulation be optimized to yield the maximum economic profits?*

The inertia of the electrical system and its regulating power is decreasing, due to a large amount of Power Electronics (PE) interfaced distributed plants that are being deployed

[177, 63]. To provide additional regulating power, BESSs are being widely employed for Primary Frequency Regulation (PFR), also due to its regulated remuneration scheme. Although Lithium-ion BESSs show good technical suitability for PFR [227, 224], the high initial investment required to deploy such systems represents a barrier for system operators and private investors [21, 130]. Consequently, BESS's lifetime becomes a key factor for defining its business case. Chapter 3 presents a mission profile-based lifetime analysis of BESSs performing PFR as ancillary grid service, considering the degradation of the three main components subjected to wear, the IGBT modules, the electrolytic capacitors, and the electrochemical storage. This analysis is conducted based on analytical models of the electro-thermal performances of the converter. Three case studies, particular to Germany, the United Kingdom (UK), and the Netherlands, with their differences in technical implementation and remuneration, are considered, and the PFR parameters are optimized to extend the BESS lifetime and yield the maximum profits.

Q2 *How much can the efficiency and costs of a BESS converter be improved by hybrid switches?*

Silicon (Si) IGBTs are currently the dominant power semiconductor technology for industrialized high-power grid-connected Voltage Source Converters (VSCs), which are also used in battery systems. Nonetheless, Si IGBTs have unsatisfactory performance at low current conditions, e.g., partial load efficiency, and, especially high voltage class devices exhibit high switching losses [183]. On the other hand, Silicon Carbide (SiC) MOSFETs, which have superior performances, have gained popularity [264, 88, 277]. The major drawback of the SiC MOSFET is the higher cost and unproven reliability when compared to the traditional Si IGBT [161]. The significantly higher cost of the SiC MOSFET calls for a compromised solution, e.g., a hybrid Si/SiC switch (HyS), which is obtained by paralleling Si IGBTs and SiC MOSFETs. In Chapter 4 an alternative HyS concept with minimum SiC MOSFET conduction (mcHyS) is investigated. The mcHyS concept is analytically modeled, experimentally characterized, and a chip area model is used to benchmark the mcHyS modulation concepts against single technology switches and typical HyS modulation when implemented in a BESS' VSC when performing primary frequency regulation.

Q3 *How can unbalanced compensation be enabled in a BESS without significant hardware expansion?*

Low Voltage (LV) distribution grids are characterized by the connection of single-phase loads, which can lead to unbalanced power consumption between the three phases during the real-time operation [138, 195], and this phenomenon can negatively affect the distribution grid. A power redistributor can be used to balance the phase powers and ensure an efficient and reliable grid operation [54]. BESSs can leverage their power electronics converter to provide the power redistribution functionality, which contrary to the typical BESS applications, it involves the exchange of asymmetrical power. Nonetheless, the integration of such functionality in a BESS requires particular attention in the design of the BESS converter. Chapter 5 thoroughly investigates the design and application of a BESS' converter for power unbalance redistribution in distribution grids when this functionality is provided as an add-on service to grid-connected BESS already deployed in the grid. Analytical modeling and design guidelines for the DC-link of a three-leg four-wire two-level VSC operating under unbalanced loads are detailed.

Q4 *How can a BESS participate in energy and ancillary services markets and provide services to a third party in a profitable way?*

Battery Energy Storage Systems (BESSs) can relieve the distribution networks of peak demand, line congestion, and power quality issues, which are caused by RES generator and electric vehicles (EVs) Fast Charging Stations (FCS) [255]. Furthermore, BESSs can buy and sell energy for profits and participate in ancillary services markets. However, the sole participation in energy products underestimates revenues and the batteries' capabilities. In this context, the dual participation of BESS in remunerated energy and ancillary services markets has been proven to be profitable in several European countries [117]. Additionally, several studies have presented the benefits of deploying BESS in the premises of a FCS, or a RES plant [106, 86, 127]. Nonetheless, the stacking of these two service categories has not been widely investigated due to technical and regulatory issues. Chapter 6 evaluates the potential business case of battery storage systems integrating market applications and services to a photovoltaic (PV) assisted electric vehicle fast-charging station (FCS). The evaluation is performed through an optimization routing based on mixed integer linear programming, which takes into account actual power profiles of PV and FCS stations and the historical prices of energy and frequency prices in the Netherlands.

1.3. CONTRIBUTIONS

The main contributions of this thesis to the field of power electronics for BESSs and their integration in distribution grids are summarized below:

- The review of several aspects of the integration of battery energy storage system in distribution grids, from the battery technologies and the main DC-AC converter topologies for BESS, to the review of worldwide BESS installations (**Chapter 2**);
- The methodology for the lifetime evaluation of a grid-connected BESS and the insights derived from the economic analysis of a BESS providing primary frequency regulation (**Chapter 3**);
- The analytical modeling, chip area optimization, and experimental characterization of two hybrid switch concepts, and the insights on their application in a BESS providing primary frequency regulation (**Chapter 4**);
- The modeling and design of the DC-link of a three-legs four-wires voltage source converter of a BESS providing the power redistributor functionality (**Chapter 5**);
- The dispatch algorithm for a BESS participating in energy and ancillary services markets, and providing services to a third party; and the insights derived from the analysis of the BESS integrated into a PV assisted fast charging station case (**Chapter 6**);

1.4. THESIS OUTLINE

The outline of the remainder of this thesis and the relations between the chapters are schematically shown in Figure 1.1. Chapter 2 reviews the current practice for the integration BESSs in distribution grids, investigating the possible battery chemistry, converter topologies, existing installations, and the methods used in previous studies for placing, sizing, and con-

trolling BESSs in distribution grids. Chapter 3 provides a lifetime analysis of BESS's components, which is later used for the optimization of the BESS revenues deriving from the provision of primary frequency regulation. Chapter 4 analytically models and experimentally verifies a hybrid switch concept, furthermore, it explores the application of such a hybrid switch in BESS converters. Chapter 5 studies the implementation of the power redistributor functionalities in BESS, by focusing on the impact of this functionality on the BESS's DC-link. Chapter 6 evaluates the economic profitability of a BESS providing services to a fast charging station while participating in energy and ancillary services markets. To conclude, Appendix A provides the modeling methods used in this thesis, especially in Chapter 3 and Chapter 5, for the power electronics converter and its components, and Appendix B details the experimental setups used for the experimental verification of the analysis presented in the other chapters.

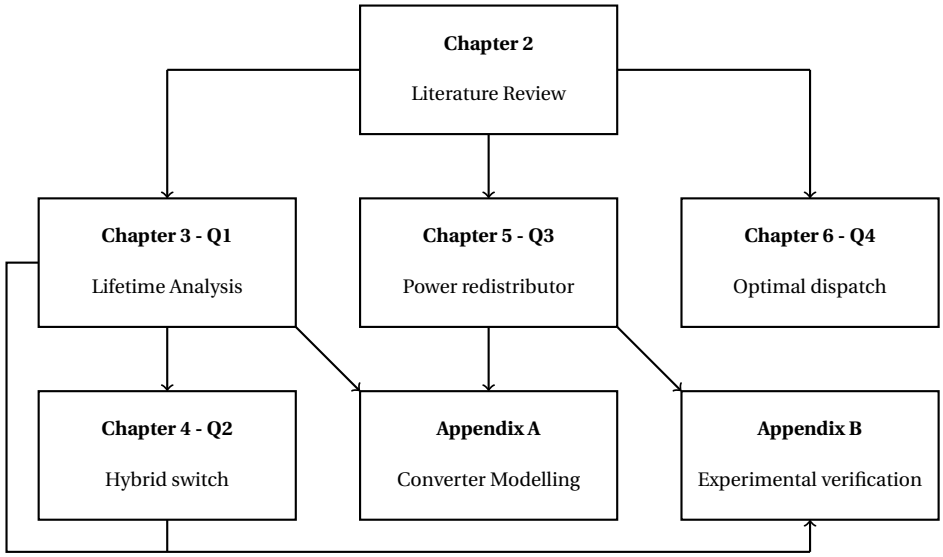

Figure 1.1: Block structure of the thesis and relations between chapters.

2

BATTERY ENERGY STORAGE SYSTEM IN DISTRIBUTION GRIDS: AN OVERVIEW

This chapter reviews different aspects of the BESS's integration in distribution grids. At first, the physical layer will be considered, focusing on the main battery technologies commercially available and on the power electronics converter. Secondly, the different functionalities that a grid-connected BESS can provide will be investigated, and then its sizing, location and control in distribution network will be discussed. In addition, an overview of actual BESSs installations is given. All in all, this chapter aims at providing a comprehensive view of BESSs integration in distribution grids, highlighting the main focus, challenges, and research gaps for each one of these aspects.

This chapter is based on:

- M. Stecca, L.R. Elizondo, T.B. Soeiro, P. Bauer, P. Palensky, "A Comprehensive Review of the Integration of Battery Energy Storage Systems Into Distribution Networks", IEEE Open Journal of the Industrial Electronics Society, 2020, vol.1, pp. 46-65.

2.1. INTRODUCTION

The increase in solar and wind energy production, together with the introduction of new types of loads, such as electric vehicles and heat pumps, have brought heavy changes in distribution networks [43, 249]. For these reasons, Distribution System Operators (DSOs) now face new technical challenges, especially due to the seasonal and environmental dependency of solar and wind power and the unpredictable loading of Electric Vehicles (EVs) charging stations [55, 167, 29]. Energy Storage Systems (ESSs) might be a valid alternative to network reinforcements. However, their benefits and economic viability are not completely clear [53]. In addition, adverse policies might hamper the deployment of such systems [31, 147, 271]. Although many energy storage technologies have been developed, the focus of this work is on battery-based energy storage systems. Due to their flexibility and expected decreasing costs [279, 230], BESSs have attracted the attention of the scientific community, resulting in a considerable number of studies. Technical aspects such as BESS components, functionality, planning, control, and installations are generally studied and reviewed independently from each other.

This chapter, instead, aims to provide a comprehensive view of BESSs integration in AC distribution grids. At first, in Section 2.2, the main electrochemical storage technologies and the possible research gaps related to the design of grid-connected power electronics converters for battery energy storage are investigated. Secondly, in Section 2.3, the main BESS electrical services will be discussed, providing insights on the possible applications and the deriving revenues. Moreover, in Sections 2.4 and 2.5, it will be shown how the studies related to energy storage planning and control differ in terms of BESS ownership, modeling, and application for which the storage is deployed. Finally, in Section 2.6, energy storage installations and pilot projects will be considered, to analyze how and to what extent BESSs have been deployed and which are the key players in the commercialization of storage systems. Section 2.7 presents the conclusion of this review.

2.2. BATTERY ENERGY STORAGE SYSTEMS COMPONENTS

In this Section, the physical components of battery energy storage systems are investigated. Figure 2.1 shows a circuit schematic of a grid-connected BESS. The main components are the battery bank, the DC-AC converter, the DC and AC filters, the protection circuits, and the step-up transformer. The parts by interest considered in this Section are the battery bank and the power electronics converter.

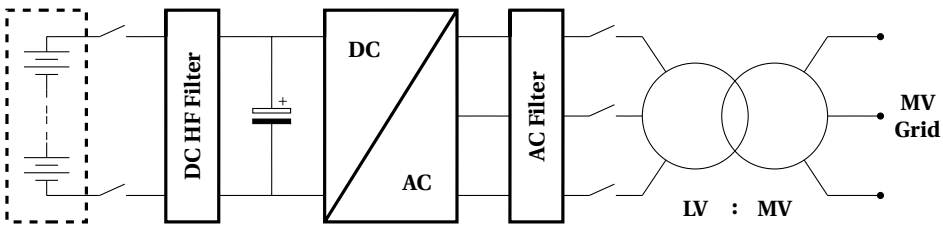

Figure 2.1: Basic schematic of a grid-connected battery energy storage system.

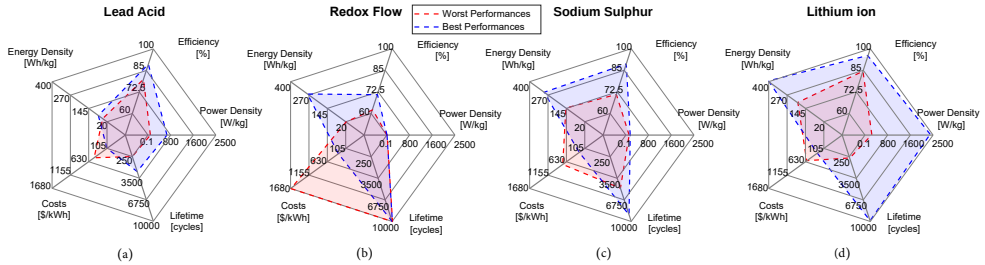

Figure 2.2: Performances of different electrochemical battery technologies: (a) lead acid (b) redox flow (c) sodium sulfur (d) lithium ion - author's elaboration from [261, 193].

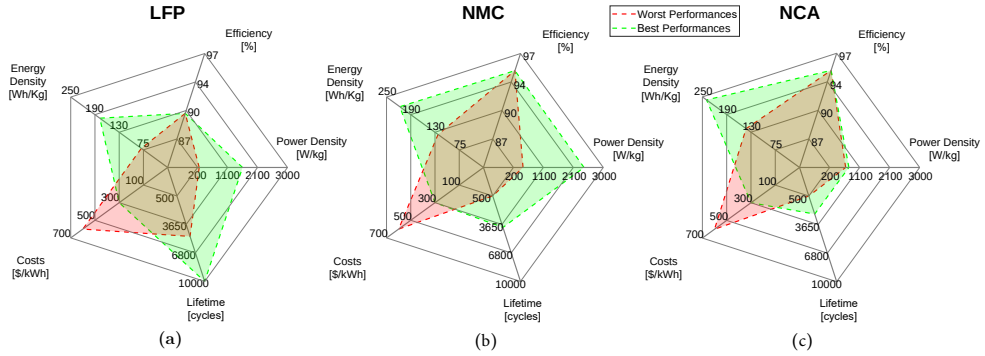

Figure 2.3: Performances of different lithium-ion battery technologies: (a) Lithium iron phosphate (b) Lithium nickel manganese cobalt (c) Lithium nickel aluminium cobalt - author's elaboration from [35, 193].

2.2.1. ELECTROCHEMICAL BATTERY TECHNOLOGIES

The main electrochemical technologies that have been used in grid applications are lithium-ion, sodium-sulfur, lead-acid, and redox flow batteries. Grid-connected electrochemical storage is characterized in terms of energy density, efficiency, lifetime, and costs, as illustrated in Figure 2.2 and Figure 2.3 and discussed in the following paragraphs.

Lead-Acid batteries were the first rechargeable battery technology invented in 1889 by the French physicist Gaston Planté. Nowadays lead-acid batteries are considered a mature technology, which is characterized by a low cell cost (50-600 $/kWh) and good efficiency (80-90 %) [135, 36, 261]. Their main drawback is the low cycling life (up to 2500 cycles), compared to other technologies, [261, 193] and low energy density (20-30 Wh/kg). Besides, lead-acid batteries' lifetime is negatively affected by a high depth of discharge [96, 85].

Redox Flow (RF) batteries were first developed by NASA in 1974 [237]. They consist of two separate tanks, where the two chemical reactants are contained, and two electrodes separated by a membrane, where the two components are combined and the reaction of oxidation-reduction (redox) occurs. The energy capacity of flow batteries is defined by the amount of reactants stored in the tanks, whereas the power is defined by the electrodes and membrane system. Power and energy ratings are then separated, and this adds flexibility to the design and operation. Redox flow batteries have a low energy density (15-30 Wh/kg) and efficiency up to 75% [124]. Nevertheless, flow batteries are not subject to limitations in terms of reactants' life cycle and by the depth of discharge [180]. Besides the technical

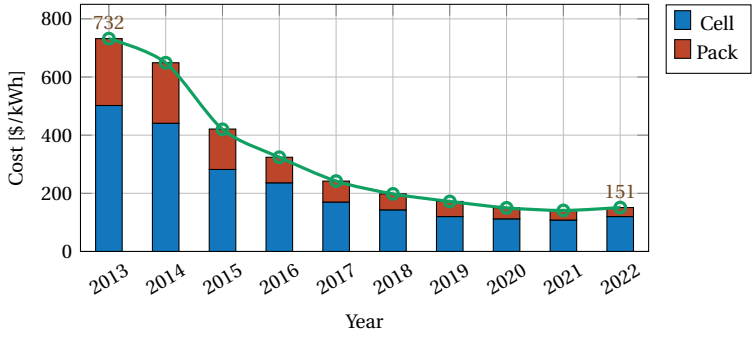

Figure 2.4: Costs of lithium-ion battery cells and packs over the years 2013 to 2022 - author's elaboration from [20].

peculiarities, redox flow batteries have been recognized as a potential candidate for grid-scale storage also due to their economic performance [2]. Several chemical compositions for the reactants have been studied and proposed. However, Vanadium based and Zn-Br are the most prominent technologies, serving large-scale and long-duration applications [66].

Sodium-sulfur (NaS) batteries were developed by NGK Insulators Ltd in collaboration with TEPCO. NaS batteries are characterized by high operating temperature (around 300° C), reasonable efficiency (>80%), high energy density (in the range of 150-240 Wh / kg) and long cycling life (up to 4500 cycles) [132, 115]. This technology has been already adopted as grid-connected energy storage to mitigate the impact of renewable energy based generators [269, 236, 115].

Lithium-ion batteries were first commercialized by Sony in 1991. The electrochemical properties of Li-ion batteries are defined by the chemical composition of the cathode, typically a lithium metal oxide, and of the anode, typically graphite [35]. This technology shows high efficiency, which can reach over 90%, although some commercial products offer a rated round trip efficiency of over 95% [24], high energy density (90-190 Wh/kg) [60], and a long lifetime, that can reach up to 10000 cycles depending on the Li-ion chemistry, as shown in Figure 2.3 [35, 193]. The lifetime is nonetheless affected by the cell temperature, which is a critical factor in the degradation process [7]. Li-ion batteries have been widely used in electronic devices, and in recent years, it has become the main technology for EVs. Despite being still relatively expensive, this technology is well suited for grid-connected applications [279]. Today, many Li-ion technologies exist, e.g., Lithium cobalt oxide-based ($LiCoO_2$), Lithium manganese oxide-based ($LiMn_2O_4$), Lithium nickel oxide-based ($LiNiO_2$), Lithium nickel cobalt aluminium oxide-based ($Li\,NiCoAlO_2$), Lithium nickel manganese oxide-based cobalt ($LiNiMnCoO_2$), Lithium titanate oxide-based ($Li_{24}Ti_5O_{12}$), and Lithium iron phosphate-based ($LiFePO_4$) [213]. Figure 2.3 presents the performances of three technologies selected due to their relevance for stationary energy storage applications [35, 193]. In such application, in fact, lower costs and cycling lifetime are preferred, while extremely high energy and power density are not primary requirements. In this context, lithium iron phosphate (LFP) cathodes currently offer lower cost, excellent cycling lifetime, and feature high cell safety. Lithium nickel manganese cobalt (NMC) and lithium nickel aluminium cobalt (NCA) cathodes can reach excellent round trip efficiency and higher energy density than LFP cathodes, which made NMC and NCA batteries the primary choice for lithium-based stationary storage and EVs batteries [278, 240]. Nonetheless, the social

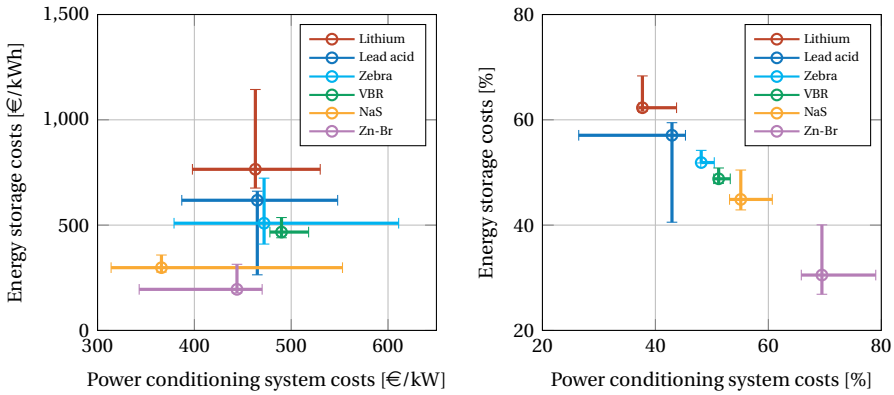

(a) (b)

Figure 2.5: Energy storage systems (a) absolute and (b) relative costs for different electrochemical technologies, (b) refers to battery energy storage systems designed for 1 - C application, so that the ratio of the BESS' rated kWh/kW is equal to 1, e.g. a 1MW/1MWh system - author's elaboration from [269].

responsibilities involving the supply chain of cobalt are favouring a shift towards LFP cells.

Figure 2.4 shows the cost of Lithium-ion battery cells and packs over the past years [19]. What stands out is the substantial cost reduction, roughly -80% in 9 years, from 734 $/kWh in 2013 to 151 $/kWh in 2022, despite the slight increase in the last year. Furthermore, in light of the current mandate of the European commission targeting a highly circular battery industry, additional value could be extracted by the recycling and reusing of battery materials [45]. Consequently, with the potential of lower total cost of ownership (TCO) with respect to recent years, energy storage systems could further establish themselves in the electricity sector.

Figure 2.2 and 2.3 illustrate the main performance indicators of the electrochemical battery technologies previously discussed. Lithium-ion batteries outperform the other technologies, offering higher power and energy density, efficiency, and low daily self-discharge. Consequently, they have been the preferred choice by the industry, as it will be discussed in Section 2.6.

2.2.2. POWER ELECTRONICS DC-AC CONVERTER

The connection of battery storage systems to the AC distribution grid is made through power electronics based converters. In lithium-ion and lead-acid batteries based storage systems, the Power Conditioning System (PCS) accounts for a minor part of the total costs, as Figure 2.5 shows, however the decreasing trend of battery cells costs, illustrated in Figure 2.4, will lead to a higher share of costs for the PCS, as also foreseen in [193]. In this perspective, it is advisable to design the power electronics converter to ensure high efficiency and reliability, i.e., to limit the total cost of ownership [269].

Batteries have some peculiarities that need to be considered for the inverter design. The cells' terminal voltage variations between fully charged and fully discharged status can be up to 40% [238]. Moreover, to ensure a highly efficient DC-AC conversion, the AC voltage should be kept as high as possible, to reduce the current stress in the semiconductors, which

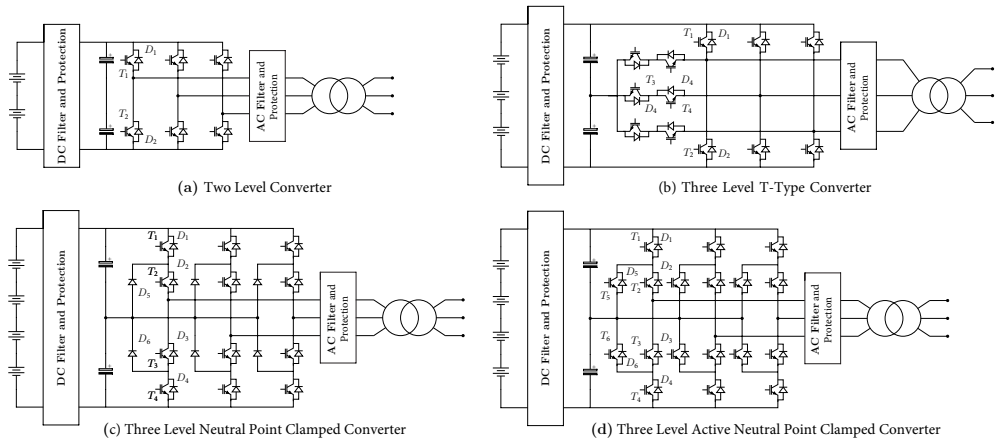

Figure 2.6: Transformer based two-level and three-level DC-AC converter topologies: (a) two-level (b) three-level T-Type (c) three-level Neutral Point Clamped (d) three-level Active Neutral Point Clamped.

is the dominant source of loss within the power electronics converter.

While the maximization of the efficiency will push for increasing the rated AC and DC voltages, the international norms fix the boundary between low and Medium Voltage (MV) at 1.5 kV [98], with additional safety requirements for appliances working at MV. Besides, the series connection of a high number of battery cells can lead to lower system reliability [134]. Furthermore, the limitations and requirements in terms of safety, harmonic content, and P-Q capabilities set by the technical standards and national grid codes need to be considered [101, 100].

Power electronics converters can be firstly classified depending on the presence or not of a step-up transformer. Moreover, when transformers are not adopted, the step-up in voltage, necessary for the connection at MV, can be achieved through the series connections of semiconductors or sub-modules. Also, the DC voltage can be controlled through an auxiliary DC-DC converter placed in between the battery and the grid connected DC-AC converter. However, the extra conversion step adds complexity, costs and it can lead to additional power losses. This choice needs to be justified by technical or operational challenges. Two-level Voltage Source Converters (VSCs), shown in Figure 2.6 (a), are the preferred choice by the industry for interfacing stationary energy storage with the MV grid [244, 172]. However several other topologies, such as three-level T-type, Neutral Point Clamped (NPC) converter, and Active Neutral Point Clamped (ANPC) converter, shown in Figure 2.6 (b)-(c)-(d) respectively, have been developed [75, 250].

Figure 2.7 shows the semiconductors module efficiency for 100 kW two and three-level VSCs connected to a 400 V line-to-line AC grid with different switching frequencies f_s. The

Table 2.1: Specifications considered for the efficiency and loss distribution comparisons between circuit topologies.

Parameter	P_n	$U_{DC,n}$	$U_{ac,ll}$	$\cos\varphi$	f_s
Value	100 kW	900 V	400 V	1	3-16 kHz

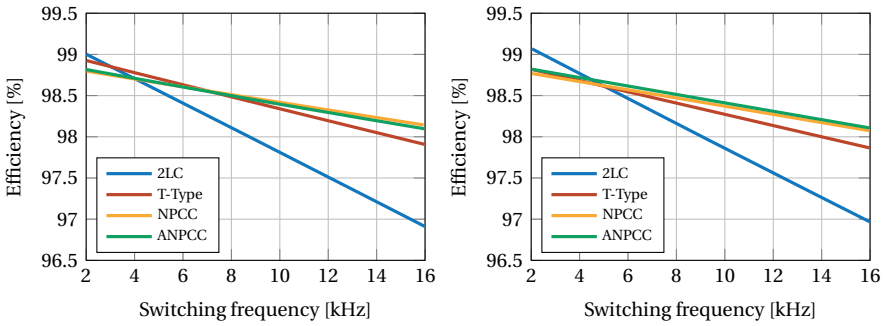

Figure 2.7: Efficiency at rated power of PWM Modulated two-level and three-level VSC topologies when (a) discharging and (b) charging the battery for different switching frequency following the converter specifications given in Table 2.1.

converter specifications are given in Table 2.1. For the analysis, appropriately rated IGBT-Diode modules from [205] are chosen. Three-level topologies outperform two-level converters at higher switching frequencies, moreover, in particular NPC topologies, show a better distribution of losses between the components, as displayed in Figure 2.8. Further advantages from higher switching frequencies derive from the lower volume of the AC output harmonic filter, thus increasing the converter power density and the shifting away from the human audible noise frequencies. In reality, large grid-connected BESS are confined in containers and mostly installed away from people, which allows the power electronics to operate at low switching frequencies, e.g., 4 kHz, well within the human audible noise range. This leads to low switching loss across the semiconductors, displayed in red in Figure 2.8. Additionally, two-level VSC displays outstanding conduction losses, as depicted in Figure 2.8, which justify its wide utilization at those low levels of f_s.

The cost comparison for energy storage MV converters presented in [250] indicates that Cascaded H Bridge (CHB), shown in Figure 2.9, is a cheaper solution with respect to classic topologies, two and three-level converters, and the Modular Multilevel Converters (MMCs), depicted in Figure 2.10. Multilevel topologies, such as the CHB and MMC, have been proved well performing circuit topologies for grid connected energy storage applications; providing a lower overall harmonic content, high power density, and high efficiency at high switching frequency [250, 172, 113, 91, 14].

The reliability of energy storage systems, considering power electronics and battery cells, is studied in [134]. The authors performed a comparative study between two BESS configurations, a fully rated 2L converter, and four partially rated 2L converters. The two configurations are tested under different operating conditions, number of cycles that the battery cells are performing, battery power, and series-parallel cell configurations. The study highlighted how low power applications could ensure higher reliability. Moreover, it was found that there is an inverse proportional relationship between reliability, power level, and the number of cycles. This study can be a reference for further reliability analysis and comparisons between different topologies and battery's cell configurations.

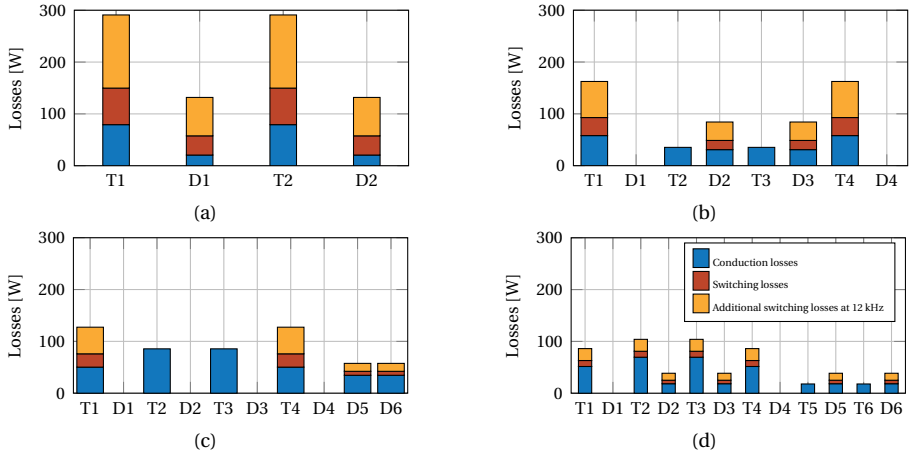

Figure 2.8: Losses distribution in two-level (a) and three-level (b)-(c)-(d) topologies during inverter operation, with switching frequency f_S=4 kHz (blue+red) and f_S=12 kHz (blue+red+yellow), considering the specifications in Table 2.1 and the components nomenclature of Figure 2.6.

2.2.3. DISCUSSION

From the literature considered, it is found that despite the two-level VSC is the most used topology for grid-connected BESS converters, alternative topologies can guarantee better performances in terms of efficiency, cost, power density, and system reliability. Particularly overwhelming advantages can be achieved when wide band-gap (WBG) semiconductors such as SiC-Mosfets are used as replacement for Si-IGBTs. However, particular attention needs to be paid on the initial cost of the PCS because similarly rated SiC Mosfet are relatively more expensive than their counter-part Si-IGBTs. Alternatively, hybrid switches, assembled paralleling Si-IGBT and SiC-MOSFET can also be considered. Furthermore, the influence of the operating conditions and then of the battery functionality on converters efficiency and reliability has been proved. Nonetheless, few researches show how BESS cost of ownership is influenced by adopting a more performing converter, in this context and from the insights gained from Figure 2.7 and 2.8, further work can be focused on showing how different converter topologies impact on BESSs technical and economic performances. It is also essential to perform this analysis for different grid functionalities, such as the ones discussed in Section 2.3, showing how the different operation requirements affect the DC-AC converter performances and design.

2.3. APPLICATIONS OF GRID CONNECTED BATTERY ENERGY STORAGE SYSTEMS

Grid-connected energy storage systems might be used to provide several services to grid operators, Distributed Generators (DGs) plant owners, energy retailers, and consumers [90, 135]. Figure 2.11 lists some possible grid applications and classify them as power or energy intensive, meaning that their provision requires high energy reserve or high power capability, and according to the time scale of their deployment, from milliseconds to hours. Before analyzing how storage has been applied for the provision of these services, it can be useful

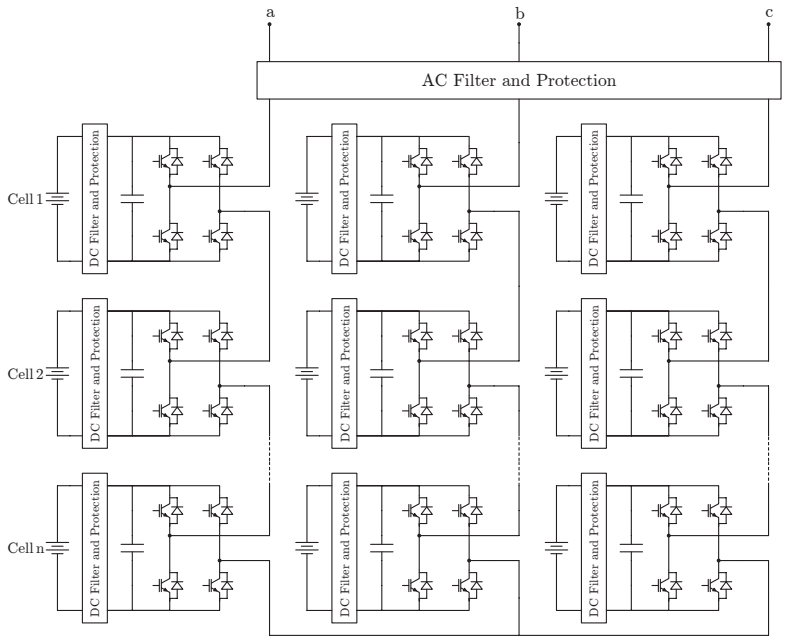

Figure 2.9: Three Phase DC-AC Cascaded H-Bridge converter.

to have an overview of the services themselves.

2.3.1. POWER QUALITY

Power quality indexes are used to measure the distortion of the voltage and current waveform with respect to an idealized pure sinusoidal one. Distortions can have a transient characteristic, for example, in the turning on or off of loads or generators, or be constant at steady state, for instance, due to the operation of non-linear loads or power electronic interfaced generation [17]. Energy storage has been investigated for this application, and it has been proved an effective solution [131, 187].

The rise of intermittent power sources has as well brought forward the issue of power swing in the network. The solar irradiation and wind speed fluctuations can lead to a sudden high variation of Distributed Generation plants and this can negatively affect the network. In this context, energy storage can be added to the DG plant and used to buffer the short term power variation [122, 276, 169]. When deployed for this scope BESS represent an additional cost component to the RES plant, decreasing the system revenue. In this context, economic incentives to the plant owners for the power fluctuation mitigation might be a way to offset the revenue losses [169].

In addition to the voltage waveform measurements and to the output power fluctuations, also the continuity of service is monitored. System Average Interruption Frequency Index (SAIFI) and System Average Interruption Duration Index (SAIDI), between the many available indexes, are used to define the DSOs' remuneration bonus. Moreover, national grid codes can foresee fines or payments from DSOs to the users in case of service interruptions [12]. In the context of improving the continuity of service of distribution grids, energy

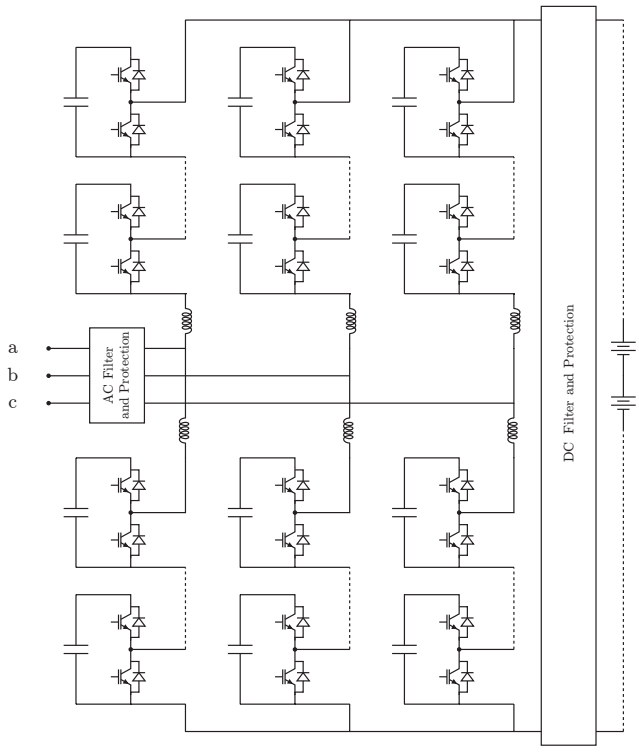

Figure 2.10: Three Phase DC-AC Modular Multilevel Converter. Other MMC circuit topologies are available, for example integrating a distributed BESS in each sub module.

storage systems can be implemented to facilitate the *black start* procedures and to allow the *islanding operation* of the distribution feeder. These two situations are consequent of one or multiple faults that bring a portion of a distribution network to operate disconnected from the main transmission grid. In the case of blackouts, storage systems could be integrated into the grid restoration plans and facilitate the recovery procedure [274]. Besides, high penetration of distributed generation together with storage systems could allow a safe operation also during unintentional islanding [1]. In a hypothetical islanding procedure, BESSs will be required to monitor and mitigate the transient due to the fault, and the sudden load-generation unbalance to have a smooth transition between grid-connected and islanded mode [107].

2.3.2. VOLTAGE CONTROL

Voltage control in distribution grids can be performed through several devices, among them tap changers, capacitor banks, voltage regulators, and static VAR compensators [142, 274]. However, as previously discussed, it might be necessary to add extra flexibility in managing distribution grids, and BESSs can play a crucial role in the future paradigm of voltage management. Since DG injection could make ineffective the regulating devices at the substation, such as transformers tap changers, the possibility of having several units distributed

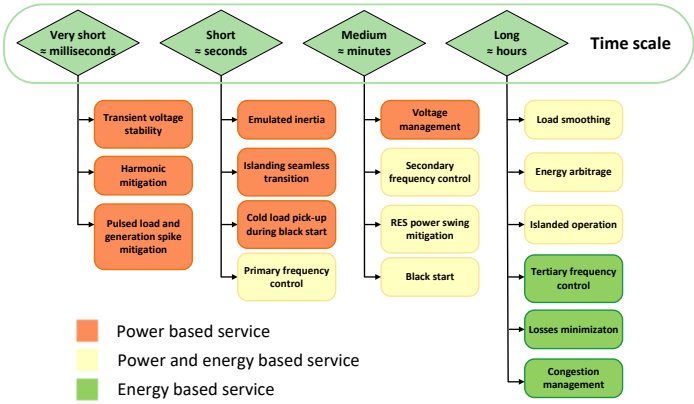

Figure 2.11: Ancillary services which can be provided by a BESS - author's elaboration from [109].

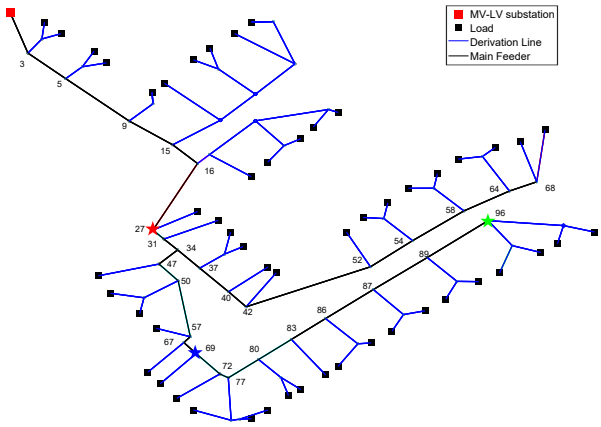

Figure 2.12: IEEE European Test Feeder schematic [99] - highlighted with a star the three nodes considered for locating the energy storage units in the analysis of Figure 2.13.

along the network, able to selectively generate reactive power, could allow an easier voltage control [8]. The implementation of storage units in the voltage control scheme has been proved technically effective [256, 197].

The voltage profiles of one of the two main feeders of the IEEE European test network, displayed in Figure 2.12, are evaluated and plotted in Figure 2.13. Figure 2.13 (a) shows the voltage profile before and after the introduction of PV generators, it is possible to see how the photovoltaic generators can lead to overvoltages at the end of the network. Figure 2.13 (b) display the potential of BESS in reducing the overvoltages. The colored lines represent the voltage profiles with the activation of the BESS system targeting the overvoltage reduction. The different colors indicate the different positions of the energy storage in the network. For each case, the node where the BESS is located is highlighted with a diamond. The number is assigned according to Figure 2.12. The influence of the energy storage location on voltage regulation can also be seen in Figure 2.13, the green case shows a better overvoltage reduction, nonetheless storage systems present a good potential for voltage regulation.

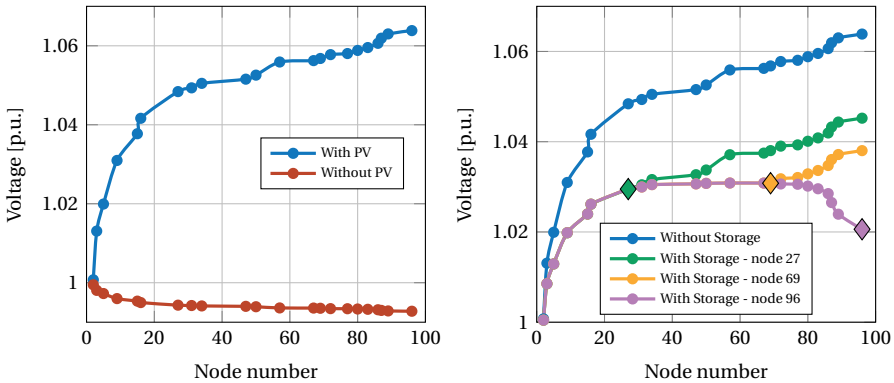

Figure 2.13: Voltage profiles along the network: (a) with and without PV generation and (b) with PV generation and with storage units used to reduce the over voltage, the storage units are located in the node marked with a diamond - the nodes numbers are referred to the numeration of Figure 2.12.

Table 2.2: Primary control parameters in some European Countries - data obtained from [185, 186, 234, 69, 188, 194].

Parameter	**DE**	**FR**	**ES**	**NL**	**BE**	**GB**
Full Availability	≤ 30s	≤ 30s	≤ 30s	≤ 30s	≤ 30s	≤ 30s
Droop	-	3-6 %	≤ 7.5%	10%	-	3-5%
Dead Band	10 mHz	10mHz	-	-	10mHz	15mHz
Full Deployment	± 200 mHz	± 200 mHz	± 200 mHz	± 200 mHz	± 200 mHz	± 200 mHz
Service Procurement	Tenders	Bilateral contracts	Not remunerated	Tenders	Tenders	Tenders

To limit the impact on the grid's voltage of DGs, besides the introduction of voltage regulating devices in the DSOs voltage control strategies, national and international energy regulators have introduced in the grid codes the obligation for DGs connected to the distribution grids of following $Q(V)$ or $\cos\varphi(V)$ droop curves. In the most recent versions of the national technical standards, these requirements have also been extended to energy storage systems, e.g. in the Italian standards CEI 0-16 [32] and CEI 0-21 [108] and in the German standards VDE-AR-N 4110 [46] and VDE-AR-N 4105 [229]. This service has to be provided automatically and in parallel to the main functionality. It helps to mitigate the overvoltage, through the absorption of reactive power, and the undervoltage, through the injection of reactive power, in distribution network feeders.

2.3.3. PEAK SHAVING AND LOAD SMOOTHING

Peak shaving and load smoothing consist of flattening the generation and load profiles so that the maximum power seen by the grid is reduced. In real-time operation, this scheme can allow the solution of network congestion, relieving the overloading of the conductors due to generation and load peak power. Moreover, in a planning horizon, network rein-

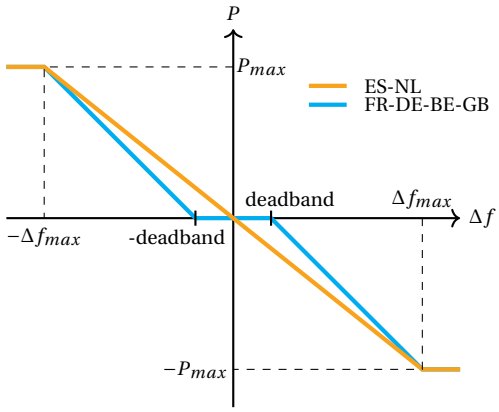

Figure 2.14: Example of P-f curves for primary frequency control - the curves are made according to the data of Table 2.2.

forcements, such as feeder re-conducting or substituting a transformer, might be avoided and deferred in time through the installation of energy storage systems [182, 179]. In this application, energy storage might be a promising solution, since DSOs are required to guarantee the adequacy of the network infrastructure so that the network can accommodate both the nominal power of the load and of the connected generators. In addition to the upgrade deferral, peak shaving and load smoothing may have a beneficial impact on network losses. In this regard, increasing the profile matching between load and local generation, BESS operation can further reduce system losses [73, 166].

2.3.4. FREQUENCY CONTROL

Frequency control is a commercial service typically offered by generators connected to the transmission networks in the ancillary service market. In recent years, also generators and energy storage systems connected at the distribution network have been allowed to provide this service. Generators and BESS adopt a droop control that follows the frequency unbalances and reacts accordingly, changing the power output. An example of the droop control logic is shown in Figure 2.14. In Table 2.2, the main parameters defining the primary frequency control logic for some European countries are shown. The provision of frequency control has been proven a profitable functionality for energy storage systems [173, 146]. Energy storage systems might be limited by their maximum and minimum State of Charge (SoC), to mitigate this problem, several techniques for controlling the SoC have been proposed [224]. Depending on the country, the droop logic is implemented with different parameters, defining or not the deadband and varying the droop value. The remuneration scheme is often through tenders, where the participants bids couples of regulating power and the required price.

2.3.5. ENERGY ARBITRAGE

Energy arbitrage consists of buying and selling energy in the spot energy market. Since the electricity sector in most countries is unbundled, only a commercial user is allowed to perform energy arbitrage. This can be performed by a couple BESS+DG or BESS+load, where

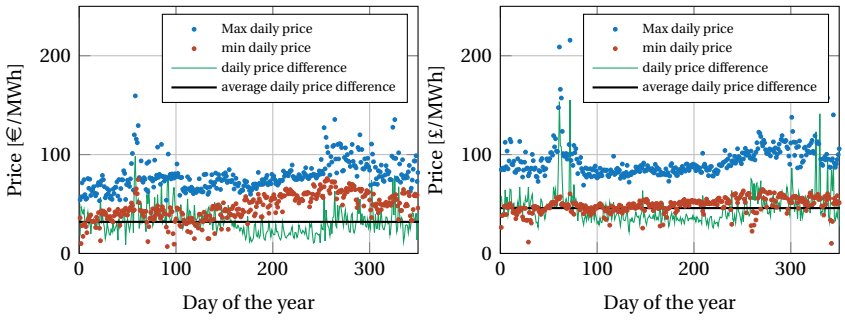

(a) (b)

Figure 2.15: Analysis of Day Ahead Market prices of year 2018 for Italy (a) and the UK (b). Elaboration of the author's from data obtained from [82] - [165].

the storage unit is used to shift the energy production or generation to profit the most from the price variations of the energy market [52]. Business cases could be built out of energy arbitrage, however present central European spot market prices might be not high enough if only energy arbitrage is considered as revenue stream [270]. Considering the Day-Ahead-Market (DAM) price data of the year 2018 for Italy and the UK, the minimum and maximum daily prices are extracted [82, 165]. These are plotted in Figure 2.15, together with the daily maximum price difference and its average over the year. It is possible to see that the daily average price difference is below 50 €/MWh. For a storage system rated 1MWh/1MW, considering € 50 as net revenues per cycle, neglecting power losses revenue taxes and battery capacity fading, and assuming the battery lifetime as 4000 cycles and the battery capital costs as 500 €/kWh, the revenues would be significantly lower than the assumed cost, confirming the findings of [270]. Following the same assumptions, the target price for break-even within 4000 cycles would be 125 €/MWh, a too high price for the present market, while 10000 cycles would be required to reach the break even for 50 €/MWh.

2.3.6. DISCUSSION

Although ESS grid applications have been so far presented individually, several studies in the literature analyze ESS performances when multiple functionalities are selected. Multi-functional BESSs can be subject to contrasting technical requirements and regulatory position, due to the combination of the different services. Moreover, the minimum power for the eligibility on the provision of specific services, for example, frequency regulation, could be too high, especially for units connected at the low voltage network. The synergies and contrasts between the different applications have been explored and the overall revenue increase, with respect to the provision of the single service separately, has been proven [80, 175, 150, 181].

Future research might address how to efficiently combine multiple services, from the technical, economic, and regulatory point of view. Research should be oriented on showing how to successfully exploit at maximum the battery characteristics through designing a coherent scheme for services provision. Also, it is found that through the involvement of several stakeholders, the chances for a positive business case increase.

Table 2.3: Mathematical programming vs heuristic methods.

	Mathematical programming	**Heuristic methods**
Pros	• Mature in power systems • Good computational performances • Strong in finding global optimum	• Avoid complex derivations • Less computationally demanding
Cons	• Convergence difficulties • Explicit mathematical formulation required	• May converge to local optimum • Less accuracy

2.4. BESS SIZING AND LOCATION IN DISTRIBUTION NETWORK

The problem of the optimal sizing and siting of storage systems in the distribution network has been widely studied in the literature [87, 267, 198, 53]. Several variables need to be defined to approach it, the solving technique, the performance metric for the optimum evaluation, the battery technology and modeling, and the test network where to perform the studies. There are two main approaches to this problem: mathematical programming and heuristic methods. The distinctions between the two consist in how to set the optimization problem and in the solving algorithm. Other approaches, such as analytical methods, can perform well in small networks, but they are not suitable or too computational demanding in complex scenarios [267, 87].

Mathematical programming consists in describing the problem with a set of equations, and, according to the characteristics of these, different solving techniques can be applied. Traditionally these are categorized as Linear Programming (LP), Quadratic Programming (QP), and Non-Linear Programming (NLP). Among these, some conventional programs, such as LP, Semi Definite Programming (SDP), or Second Order Cone Programming (SOCP) are finding wide application in solving power system related problems. Many commercially available solvers can solve convex optimization problem, and these have been widely used in power systems applications with good computational performances. Mathematical programming requires an explicit analytical formulation of the objective function and the constraints. Heuristic methods do not require explicit mathematical formulations and, for this reason, they are suitable for multi-objective optimization. The general pattern in applying these algorithms consists of adopting artificial intelligence methods for the size and location of the storage systems and then evaluating the fitness of the candidates through classic optimal power flow algorithms. Heuristic methods found several derivations, however, some of the most common algorithms are Particle Swarm Optimization (PSO) [40] and Genetic Algorithms (GA) [92]. PSO has been adopted to solve some of the classical power system problems, for example, load flow, voltage control, and economic dispatch [243]. Due to the nature of the energy storage sizing and placement problem, PSO and GA are valid candidates as an optimization algorithm. Table 2.3 shows a brief comparison between the two categories of optimization techniques. As previously discussed, when convex programs are adopted, an explicit formulation of the problem is required. In this aspect, heuristic methods are more flexible at the expense of the accuracy of the solution. These algorithms do not ensure reaching the global optimum, and they may get trapped in a local optimum.

An overview of studies regarding the planning of the distribution system, including energy storage, is provided in Table 2.4. These studies are selected due to their relevance for the topic, covering a broad spectrum of approaches to tackle the sizing and siting of storage problem, highlighting the assumptions adopted in the problem settings. Through this

Table 2.4: Energy storage systems sizing and location studies.

Main objective	Secondary Objective	Problem	Analysis	Opt technique	ESS technology	ESS model	Test grid	RES included	Reference
Power quality and reliability	Equipment costs (CAPEX of BESS and switches)	Sizing and siting	Technical and Economical	NSGA and Pareto dominance	Not specified	Not specified	Portuguese radial feeder	No	[247]
DG curtailment minimization	Congestion and voltage management	Sizing	Technical	Multi period AC OPF	Li-ion	85% Fixed efficiency	English MV network	Wind	[5]
Congestion management	Minimize ESS costs	Pre determined siting + discrete sizing	Economical	PSO	Not specified	Not specified	IEEE 24-bus / transmission	PV + Wind	[89]
System costs	System upgrade, losses, arbitrage and interruption	Siting + discrete sizing	Economical	GA and LP + Monte Carlo analysis for the probabilistic approach	LA, NaS, VR	Fixed efficiency	33-bus radial	Wind	[13]
	Active power flow at primary substation	Sizing and siting	Economical	SOCP OPF	Lead acid	Not specified	69-bus 12.66kV	PV	[84]
	Arbitrage, peak shaving, reverse flow	Pre determined siting + sizing	Economical (NPV)	Stochastic optimization	NaS	81% Fixed efficiency	Modified IEEE 13-bus	PV	[141]
	Arbitrage, environmental emissions, transmission access fee and losses	Sizing + siting	Economical (NPV)	GA combined with LP	VRB	75% Fixed efficiency	Iranian LV grid	PV	[111]
	Voltage control, losses and congestion management	Sizing and siting	Economical	SOCP and ADMM	Li ion	Losses quadratic with power	287-bus Swiss network	PV	[163]
	Voltage control	Sizing + siting	Economical	LP and statistic modelling of random parameters	Li-ion	Fixed efficiency	IEEE 13-bus balanced	PV	[3]
System upgrade deferral	Arbitrage, Var power flow and incentives	Discrete sizing + siting	Economical (NPV)	GA and SQP	Redox Flow	72% Fixed efficiency	17-bus MV	PV + Wind	[30]
Voltage improvement	Losses and storage size	First siting then sizing	Technical for siting and Economical for sizing	CSA and SDP	Not specified	Not specified	Italian LV 17-bus, IEEE 34-bus and 200 random grids	PV	[83]
Losses minimization	Investment costs	First siting then sizing	Technical	Siting = losses sensitivity analysis / Sizing = Pattern search (PS) / (OPF = Backward/Forward Seep Method (BFSM) + MIQCQP)	Li-ion	95 % Fixed efficiency	CIGRE 14-bus MV and 17-bus sub transmission grid	No	[121]
Min virtual op costs	Voltage, feeder current, losses, energy cost and load curtailment	Sizing and siting	Technical and Economical	MI SOCP	Not specified	Losses quadratic with power	Modified IEEE 34-bus	PV + Wind	[162]
Minimize energy purchase costs	BESS lifetime	Siting	Economical	MI SOCP	Lead acid	81 % Fixed efficiency	11-bus system	PV + Wind	[28]

NPV = Net Present Value, NSGA = Non-dominated Sorting Genetic Algorithms, OPF = Optimal Power Flow, SOCP = Second Order Cone Program, ADMM = Alternating Direction Method of Multipliers, SQP = Sequential Quadratic Program, SDP = Semi Definite Program, CSA = Clustering and Sensitivity Analysis, MI SOCP = Mixed Integer SOCP

information it might be possible to reveal the limitations of the studies analyzed and the potential improvements with respect to state of the art. Table 2.4 clearly shows that the energy storage planning problem has been widely considered both through mathematical programming, where storage is placed targeting the optimization of virtual operation costs [162], of the energy purchase costs [28], and of system costs, losses and the energy flow at the substation [84], and through artificial intelligence based algorithms. Heuristic methods have been adopted for evaluating the optimal storage capacity, for minimizing losses and voltage violations after finding the best location through loss sensitivity analysis (PSO) [114], for solving the grid expansion plan aiming at lowering the total system costs (PSO) [204] (GA) [116], for minimizing storage capital costs, where BESS are used to mitigate overvoltages (GA) [51] and for avoiding network congestion (PSO) [89]. Hybrid approaches, combining heuristic methods and convex programs, have been used for the minimization of the VAR power flow at the HV/MV substation (GA+SQP) [30], for maximizing revenues from arbitrage, upgrade deferral, improving in system reliability and losses reduction (GA+LP) [13] and for optimizing system costs and revenues from arbitrage, environmental emission reduction, transmission access fee and loss reduction (GA+LP) [111]. The last study couples DIgSILENT PowerFactory and MATLAB, the first for the network models and the second for the optimization algorithms. From the literature, it is found that a few articles base their analysis only on technical parameters. The main trend, in fact, consists of targeting the minimization of system costs on a long term horizon. This can be explained by the need to justify the high initial investment of storage units not only through technical improvements of the grid but also with a feasible business plan. Technical parameters, such as branch current, node voltages and the generators and BESS capability curves, are included in most relevant studies under the form of constraints of the problem. Furthermore, several studies introduce also constraints in the short term power fluctuations. In this respect BESS are adopted to mitigate the power swing of the associated renewable energy based generator to comply to the eventual TSOs or DSOs requests, as detailed in Section 2.3.1 [122, 276, 169]. In addition, it is found that mostly, as simplification, the planning problem is considered in a discrete way [30], in the sense that the sizing of the storage is considered by steps of 10 or 100 kWh, or in sequential approach [121, 162], first, the optimal location is found, and secondly, the battery capacity is evaluated. These strategies might simplify the setting of the problem at the expense of the solution's accuracy. Another interesting approach for the deployment of several storage units consists of dividing the network into different clusters and finding the optimal location of the units within each cluster [83]. Several electrochemical technologies have been considered, for instance, lithium-ion, vanadium redox, NaS, and lead-acid, yet, in most cases, the differences in the modeling are accounted for in terms of capital cost, lifetime and round trip efficiency. Modeling battery efficiency as fixed value is a common practice [13, 5, 141, 111, 3, 30, 121, 28]. More accurate solutions, such as electrical models, are rarely taken into account at the planning phase, although a too simplified model can lead to significant errors in the lifetime and aging estimation [27]. In [68] the energy storage planning and scheduling optimization routine is run both using an accurate BESS description, equivalent electrical circuit, and a simplified one. The study shows that when the simplified model is used the BESS lifetime is negatively influenced by a non-optimal BESS scheduling. However, in the case presented, the computational time significantly increase, remaining nonetheless acceptable.

At the planning stage, the focus of the researches is on deploying ESSs for mitigating the

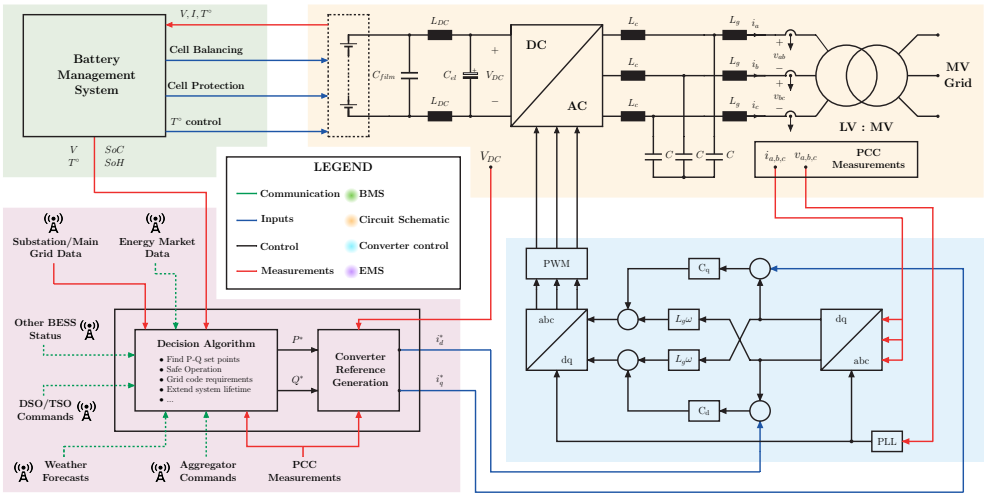

Figure 2.16: BESS' circuit schematic and main components.

impact of RES generation whereas providing a cheap solution for upgrading the network. In this aspect, to improve the accuracy of the analysis, future research should consider more detailed battery models, such as considering variable efficiency or equivalent electrical circuits, since battery modelling is not adequately addressed in most of the planning studies, both in terms of performances and lifetime. These strongly depend on the BESS operating conditions, rarely taken into account at the planning phase [65, 64]. Also, since the electricity sector is undergoing profound changes, properly considering the future evolution of distribution networks, in terms of load and generation increase as well as the introduction of new types of loads, can provide a clear understanding of the role of energy storage.

2.5. BESS MANAGEMENT AND OPERATION

The main components necessary for the functioning of a battery energy storage system are illustrated in Figure 2.16. The Battery Management System (BMS) collects measurements data from the electrochemical storage and it is responsible for balancing the cells' voltage, protecting them from overloading, and for minimizing the temperature gradient to guarantee an even ageing of the cells [119]. The BMS computes the state of charge and the state of health of the battery, feeding this information to the Energy Management System (EMS), i.e., the unit in charge of the storage system operations and protection. The EMS, as shown in Figure 2.16, in addition to the battery parameters received from the BMS, it collects inputs from different sources, e.g., when available, electrical measurements at the Point of Common Coupling (PCC), weather forecasts, energy market data, and commands from DSOs, TSOs and aggregators. Given these data, the decision algorithm embedded in the EMS finds the P-Q set points of the storage systems [25]. These are digitally converted into the reference values for the DC-AC converter and sent to the control board that drives the system. In Figure 2.16, the block with light blue background illustrates a current control scheme based on the dq frame for the storage system [268]. Additionally, the EMS is responsible for scheduling BESS operation and, when multiple BESSs are present, for coor-

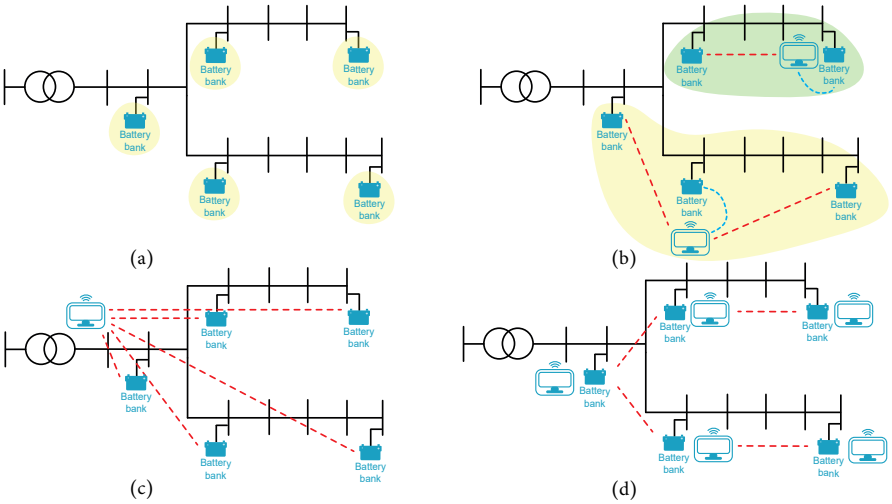

Figure 2.17: Example of BESS management strategies: a) Local control, b) Decentralized control, c) Centralized control d) Distributed control.

dinating the different storage units. Each BESS unit may be equipped by an independent EMS, managing the storage system based on local measurements, as depicted in Figure 2.17 (a), alternatively, there may be a supervisory unit managing a portion of the grid, Figure 2.17 (b), or the full network Figure 2.17 (c), or each unit equipped with a decision making algorithm able to communicate with the neighbouring units Figure 2.17 (d). These management strategies may be classified as Local, Decentralized, Centralized , and Distributed control [8].

The main challenges when designing a control system for battery storage systems consist of the communication infrastructure, developing the decision-making algorithm, and managing the uncertainties in the data and the errors in the forecasts. The communication infrastructure can be costly, especially in geographically vast grids. Moreover, for an effective control strategy, the requirements in terms of reliability, latency, and data rate might be stringent.

In Table 2.5, a summary of selected papers that study the BESSs' optimal control and operation is presented. These are selected so to have an overview of the relation between control method applied and other model parameters, such as controlling agent, efficiency model, and control inputs. What it is possible to notice at first sight from the table is that most studies consider the DSO as controlling agent of the storage units. Mostly, the articles' focus is on mitigating the impact of PVs, and the approach developed is tailored for DSOs [254, 86, 42, 272, 257] or to be applied locally by the single devices [248, 123, 273, 257]. However, regarding the control strategy, there is not a solution that emerges as the most common. Photovoltaic panels are generally considered in the network, and so BESS are often studied for reducing the overvoltages created by the PV generators. The studies presented in Table 2.5 are related to both medium and low voltage distribution grids. Despite sharing similar problems, the two voltage levels have different degrees of monitoring and automation. These peculiarities need to be considered when designing the control sys-

Figure 2.18: Example of a Li-ion based battery energy storage system rated up to 3.1 MW/MWh [4].

tem of storage devices in order to optimally exploit the already available resources and to minimize the extra costs for the integration of new systems.

The most frequently considered ESS technologies are Li-ion [248, 123, 273, 81] or lead-acid [10, 254, 211], besides, electrical models are also widely used [248, 123, 42, 257, 81]. The common adoption of electrical models shows a difference from what is found in the analysis of the planning stage studies of Table 2.4, where simpler solutions are preferred. In [68] the energy storage planning and scheduling optimization routine is run both using an accurate BESS description, through an equivalent electrical circuit, and neglecting the accurate model for the storage system. The study shows that when the accurate model is neglected the BESS lifetime is negatively influenced by a non-optimal BESS scheduling. This article shows the importance of an accurate BESS description in the operation optimization for extending the storage lifetime.

Regarding the data available for the decision algorithm, it is possible to see that in most of the analyzed cases, the control algorithm relies on local electrical measurements. Moreover, some studies consider also weather conditions [272]. Articles [168, 140] consider a fully monitored network for coordinated or centralized control. However, this might be not cost-effective or easy to realize, especially at the LV level, due to the high number of LV networks and their low degree of automation and monitoring devices. In other studies, a limited amount of network measurements are fed to a state estimator [42, 81]. The second solution, although more computationally expensive and complex to design, offers a solution more compatible with the state of the art of distribution grids. Another interesting insight coming from the literature is that when distributed control is applied the different units share their State of Charge to properly share the required regulating power [273].

As previously discussed, the EMS is responsible for the scheduling of the storage systems. Energy market data, RES plant production and grid parameters, such as node voltage and branch current, are only partly predictable. In this context, the scheduling algorithm, based on available data, historical data and forecasts, is in charge of defining the BESS operation for a fixed horizon. However, real time data and more accurate forecasts can be obtained during operation and this might change the optimal storage scheduling. Model Predictive Control is a well established technique used for dealing with uncertainties and forecasts in multi period optimization and it has also been applied for the scheduling of energy storage systems operations [58, 81, 272, 199].

For future research, it is worth to properly take into account robustness against uncertainty and forecasts errors, e.g., through Model Predictive Control. Especially when cen-

Table 2.5: Energy storage systems management and operation studies.

Main service	Extra services	Controller	Control input	ESS control	ESS technology	ESS model	Test grid	RES included	Reference
Voltage control	No	DSO	Local voltage, remaining battery life, SoC and voltage sensitivities	Non coordinated / Coordinated	VRLA	Fixed efficiency	Residential UK grid	PV	[254]
	No	DSO ESS / Local PV	Short term forecast of load and PV and sensitivities	Centralized	Not specified	Not specified	23-bus LV danish	PV	[86]
	Voltage and frequency control	Main control center	Voltage, current, frequency and SoC	Coordinated + main control center	Li-ion	Electrical model	MV Korean	No	[123]
	No	Local	Voltage and SoC	Local	Li-ion	Electrical model	Real German grid	PV	[248]
	No	DSO	State estimator fed by real time measurement	Centralized	General electrochemical + super capacitor	Electrical model	Mod. IEEE 34-bus	PV	[42]
	No	Local / Distributed	Local voltage and SoC of BESSs	Coordinated	Li-ion	Linear efficiency	Realistic 7-bus LV	PV	[273]
	Losses minimization	DSO	Irradiation, T$^{\circ}$ C, substation measures and historic data of load and DG	Receding horizon control	Not specified	Varying efficiency	Italian LV 17-buses	PV	[272]
	No	Local / Distributed	Local voltage and SoC	Distributed + localized	VRB	Electrical model	6-bus LV/ 13-bus LV	PV	[257]
	Active power dispatch	DSO	Power and voltage or state estimation	Model predictive control	Li-ion	Electrical model	IEEE 34-nodes MV and CIGRE benchmark LV grid	PV	[81]
Curtailment minimization	No	DSO	State of load, generator, ESS and OLTC	Fully monitored network	Li-ion	Fixed efficiency	English MV	Wind	[5]
Frequency control	Voltage and frequency control	Main control center	Voltage, current, frequency and SoC	Coordinated + main control center	Li-ion	Electrical model	MV Korean	No	[123]
Power profile flattening	No	DSO / Local	Predictions of load and generation and network topology	Centralized / Decentralized / Distributed	Not specified	Not specified	Small residential network	PV	[262]
Optimal Day Ahead bidding	No	DSO	Historical data, ESS and topology	Centralized	Lead acid	Fixed efficiency	IEEE 15-bus 11kV	PV + Wind	[211]
Power quality	Voltage control	Local	Local Voltage	Local	Lead acid + Ultra capacitor	Not specified	16-bus network LV	PV	[10]
	Local energy balancing	DSO	Fully monitored network	SQP	Not specified	Not specified	13-bus CIGRE	PV + Wind	[168]
Minimize energy costs	No	DSO	Full awareness considered	MI SOCP	Not specified	Fixed efficiency	11-bus and 42-bus	PV + Wind	[140]
Local energy balancing	Power quality	DSO	Fully monitored network	SQP	Not specified	Not specified	13-bus CIGRE	PV + Wind	[168]
Active power dispatch	Voltage control	DSO	Power and voltage or state estimation	Model predictive control	Li-ion	Electrical model	IEEE 34-nodes MV and CIGRE benchmark LV grid	PV	[81]
	Peak shaving	DSO	Reference SoC and day ahead profile	Model predictive control	Not specified	Not specified	12 kV grid	PV	[58]

VRLA = Valve Regulated Lead Acid, MI SOC = Mixed Integer Second order Cone Program, SQP = Sequential Quadratic Programming, OLTC = On Load Tap Changer, SoC = State of Charge, T = Temperature, DG= Distributed Generators,

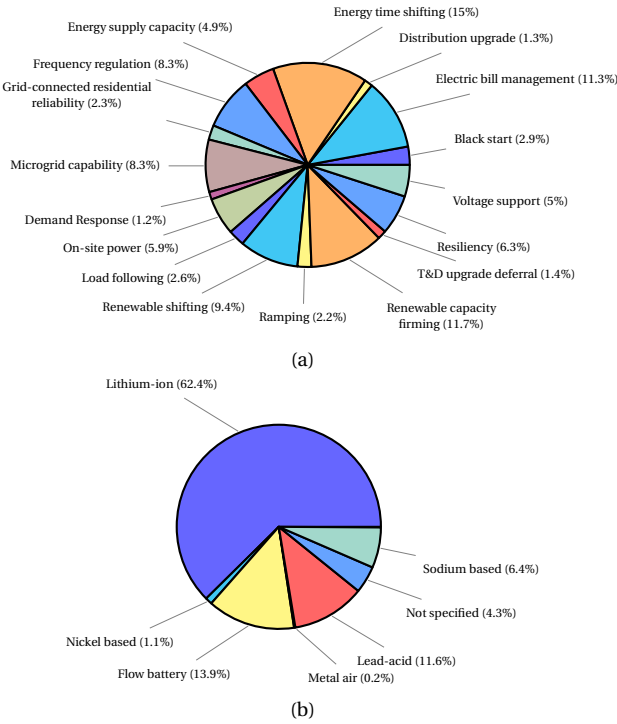

Figure 2.19: Storage application (a) and technologies (b) - author's elaboration from [242].

tralized control strategies are adopted, a state estimation algorithm might be necessary to create an accurate overview of the network. As expected local control offers the poorest performances; however, in particular situations, it may be an appropriate solution. Distributed or coordinated control is the trade-off that allows higher flexibility to distributed storage systems and might be the most efficient solution for future applications. Future research should aim at developing control strategies that fulfil the targeted objective, but at the same time, take into account the reality of distribution networks and of the communication infrastructure.

2.6. ENERGY STORAGE SYSTEMS INSTALLATIONS

Energy storage systems are usually designed and commercialized by an Energy Storage Systems Integrator (ESSI). ESSIs buy or internally manufacture the battery packs, the power conditioning system, the auxiliary system, and the controlling software. These are then assembled inside the containers. They offer modular BESS solutions, in terms of power and energy ratings, ranging from hundreds of kW to few MW. An example of the final ESS product is displayed in Figure 2.18. ESSIs play a crucial role in the proliferation of energy storage systems, striving for an optimized product and seeking for new applications and use cases. Navigant Research, a market research and advisory firm in the field of the energy industry, identifies Fluence, Nidec ASI, Tesla, RES, Powin Energy, Greensmith, LG CNS, NEC Energy Solutions, NextEra Energy Resources, and Doosan GridTech as main players

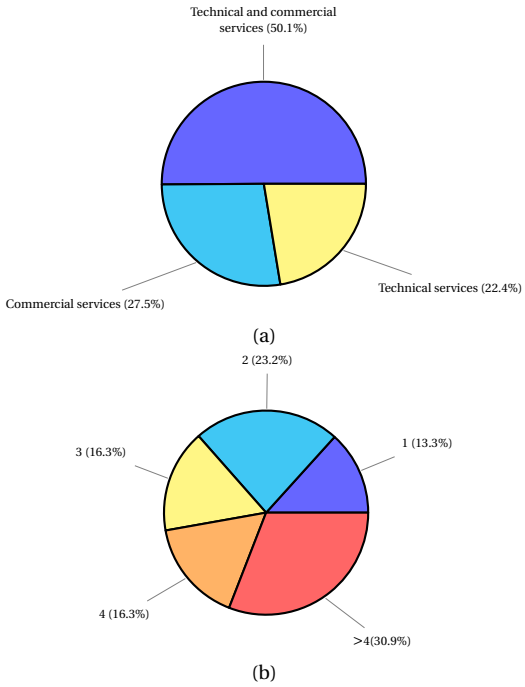

Figure 2.20: Percentage of BESSs installation performing technical and commercial services (a) and number of services that each installation performs (b) - author's elaboration from [242].

in the utility scale ESSI market [158, 76]. Other Energy Storage Systems Integrators are, for instance, ABB, Alfen, General Electric, and Schneider Electric. Concerning the battery cell manufacturing, some of the main players in the market today are, for lithium-ion based technologies: A123Systems, CATL, Electrovaya, Fiamm, Johnson Control, LG, Panasonic, Saft, Samsung, and Toshiba; for Flow Batteries: CellCube, Primus Power, Rongke Power, UniEnery Technologies, and Vionx Energy; and for Sodium Sulfur batteries NGK Insulators.

Regarding BESS installations and pilot projects, the database on energy storage installations maintained by National Technology & Engineering Sciences of Sandia, LLC (NTESS), operator of Sandia National Laboratories for the U.S. Department of Energy / National Nuclear Security Administration [242], contains information, such as power and energy rating, location, applications, owner, storage technology, and status, of installations located worldwide. To adhere to the review's focus, only the active installations, with sufficient information, adopting electrochemical technology and power rating less or equal to 5 MW are considered. At the time of consultation, this resulted in a set of 466 projects. The selected projects are analyzed to extract the services performed by the storage and the electrochemical technology, the two pie charts of Figure 2.19 display this. What stands out from Figure 2.19 (a) is the fact that there is not a single use case that predominates the BESS application. Additionally, six services, electric bill management, energy time shifting, frequency regulation, microgrid capability, renewable generation shifting, and renewable capacity firming, are the most frequent BESS use cases. On the other hand, Figure 2.19 (b) clearly shows how lithium-ion technologies are by far the most common solution. Figure 2.20 shows that BESS

are often deployed as multi-functional and that they are mostly involved in both commercial and technical services, in line with what was discussed in Section 2.3.

Besides general information regarding battery based storage projects, a closer look in a specific project where BESS were tested for frequency control is given. In this context, TenneT B.V., Dutch TSO, conducted a pilot project regarding the provision of Frequency Containment Reserves (FCR) through aggregators of different sources, including energy storage [235]. During the pilot, several aggregated pools have been tested for the provision of FCR in the Dutch market. Between the several aggregator pools also lead-acid and lithium-ion batteries have been tested. The minimum bid size was reduced from 1 MW to 100 kW, and the participants were required to submit their bids each week for the following week. Batteries' performance has shown to be strongly dependent on the battery management system, on the other hand, the energy limitation of the energy storage did not hamper the FCR provision. The main result of the pilot shows that all assets were technically able to provide FCR and that the main difficulties were related to the frequency measurement and the communication infrastructure between the TSO and the aggregators. It is shown that TSO's requirements in terms of minimum power step might be challenging for BESSs. The reduction of the bidding period and the measuring requirements have been identified as main points for easing aggregators' participation in the FCR market.

2.7. CONCLUSION

This chapter has focused on the different aspects of the integration of energy storage systems in distribution networks. It has been shown that the storage system has the potential to strengthen and improve the electrical grid in several aspects. Nevertheless, energy storage systems are struggling to achieve mass deployment. From the review of the literature, some key challenges that demand further investigation, so that both technical and economic performances of battery storage systems can be enhanced, have been highlighted.

At fist, the design of the DC-AC energy storage converter should consider more advanced circuit technologies, wide band gap semiconductor switches, or hybrid Si-IGBT and SiC MOSFET switches. Furthermore, it is found that few studies rightly consider the peculiarity of electrochemical storage and the difference in the operating conditions according to the grid application for the DC-AC converter design. The BESS mission profile can have great impact on the converter performances and lifetime, and so on the total cost of ownership, therefore it should be considered in the design stage. Secondly the provision of multiple grid services from the technical and regulatory point of view should be considered. The high initial investment and the unclear revenue streams are the main barriers for the BESS deployment. In this respect, it is found that the combination of various services can enhance BESS profitability. One application that has shown strong positive business case is primary frequency regulation. However the provision of multiple functionality is still recommended to boost the revenues from BESS operation. This is confirmed by the analysis of Section 2.6, where it is pointed out that the majority of running installations perform multiple services and often target both technical, e.g., voltage regulation, network upgrade deferral, microgrid capabilities, and black start, and market related activities, such as energy arbitrage, frequency regulation, and demand response. Nonetheless, these can lead to contrasting technical and regulatory requirements. Further research is then necessary on how to optimally integrate the provision of multiple services from the same storage unit. At last, accurate and computationally performing battery models are necessary to fully un-

lock the BESS potential. Studies have proved that a too simplified battery model can lead to excessive capacity fading due to non-optimal scheduling. The usage of detailed models comes at the price of computational performances. Further research should then be focused on developing models that precisely describe the battery performance and lifetime, but at the same time do not overly rise the computational time. In this way, these may be applied not only for the short term scheduling but also for network planning.

3

POWER ELECTRONICS GRID INTERFACE

This chapter investigates how to optimize the lifetime of Battery Energy Storage Systems (BESSs) providing Primary Frequency Regulation (PFR) considering IGBT modules, electrolytic capacitors and electrochemical storage degradation. The lifetime information is used to estimate BESS's Net-Present-Value (NPV), evaluating the benefits of deploying PE-based BESS in the European grid. A comparison between different countries, Germany, the Netherlands, and the UK, is performed, considering the PFR implementation and remuneration differences. The analysis shows that the BESS management strategy can extend its lifetime and that the component that exhibits the shortest lifetime is the electrochemical storage. The PE components are subject to low wear due to the low power utilization and, therefore, small thermal swings while performing PFR. In conclusion, the provision of PFR by means of BESS has been found to be profitable in all three countries. However, in the Netherlands, the potential NPV has been estimated to be 47% and 76% higher than in Germany and the UK, respectively.

This chapter is based on:

- M. Stecca, T.B. Soeiro, L.R. Elizondo, P. Bauer, P. Palensky, "Lifetime Estimation of Grid-Connected Battery Storage and Power Electronics Providing Primary Frequency Regulation", IEEE Open Journal of the Industrial Electronics Society, 2021, vol.2, pp. 240-251;

3.1. INTRODUCTION

The inertia of the electrical system and its regulating power is decreasing, due to the large amount of Power Electronics (PE) interfaced distributed plants which are being deployed [177, 63]. System operators are then in need of finding new balancing resources. In this context, Battery Energy Storage Systems (BESSs) are particularly suitable for various frequency balancing services [72, 144, 145]. Among these, BESSs are being widely employed for Primary Frequency Regulation (PFR), also due to its clearly regulated remuneration, as opposed to other potential BESSs applications, i.e. voltage control, congestion management, peak shaving. PFR consists of varying the generator's power output proportionally to the fundamental frequency deviations from the nominal value, i.e., 50 Hz in Europe and China and 60 Hz in America. Although Lithium-ion BESSs show good technical suitability for PFR [227, 224], the high initial investment required to deploy such systems represents a barrier for system operators and private investors [21, 130]. Consequently, BESS's lifetime becomes a key factor for defining its business case. Research in power electronic reliability shows that the main components within the VSCs subject to failure due to wear are the IGBT modules and the DC-link electrolytic capacitors [252, 265, 95, 176]. Additionally, Lithium-ion based batteries have a limited lifetime, strongly influenced by the cycling pattern [27], and which generally spans from 3000 to 10000 cycles, depending on the lithium technology and the cycling conditions [35]. The IGBT modules, the electrolytic capacitors, and the electrochemical storage are then the components that are the most subject to wear in a BESS. Therefore, this study focus on estimating the lifetime of these three elements.

This chapter presents a mission profile based lifetime analysis of BESSs performing PFR as ancillary grid service. This grid service's choice is driven by the well defined technical, economic and regulatory framework of PFR, which allows the definition of a positive BESS's business case. The lifetime is defined by investigating the degradation of IGBT modules, electrolytic capacitors, and electrochemical storage. The components' lifetime models adopted, derived through accelerated lifetime testing, are taken from the manufacturers [15, 260, 49] and from the literature [222, 220]. The methodology is general; it can be used to estimate BESS's component lifetime for any BESS application, and, unlike other mission profile based BESS lifetime estimation methods proposed in literature [130, 224], it considers both electrochemical storage and power electronics wear. Additionally, three case studies, particular to Germany, the United Kingdom (UK), and the Netherlands, with their differences in technical implementation and remuneration, are considered. To conclude, the economic viability of BESSs deployed to perform PFR is evaluated based on the information about components' replacement derived from the lifetime analysis.

3.2. PRIMARY FREQUENCY REGULATION MARKET

Primary frequency regulation is an ancillary service typically offered by generators connected to the transmission networks. This service may assume different names depending on the country, however, in the remainder of the chapter, it will be referred to as PFR. PFR is a process to maintain stability in the power system by reacting to frequency variations. When a frequency change Δf occurs after a fluctuation in the generation or load, the PFR operates to adjust the active power output of the generators and other available controllable units in the system, such as BESSs. The power output is adjusted according to a droop characteristic that follows Δf. An example of such droop control logic is shown

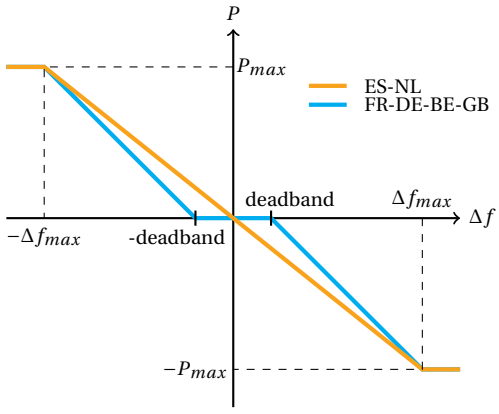

Figure 3.1: Example of a P-f droop control curve for PFR provision.

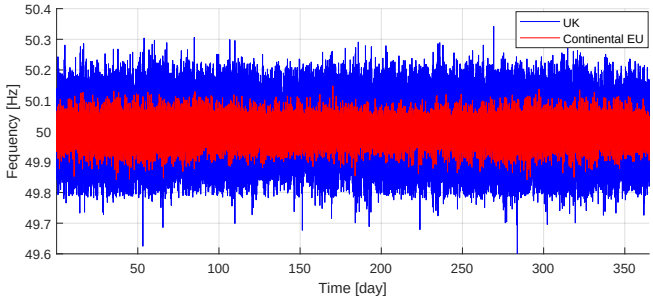

Figure 3.2: Measured frequency trend in UK [157] and continental Europe [159] during 2018.

in Figure 3.1. Both the UK and Germany adopt a deadband, which is a frequency interval around the nominal value in which the system is not required to exchange power with the grid. This deadband has a different amplitude for UK [157] and Germany [189], i.e. ±15mHz and ±10mHz respectively [185]. In the Netherlands, an insensitivity range of ±10mHz is implemented instead [232]. The insensitivity range acts as a moving deadband, requiring the unit to change its power output only if a frequency variation greater than 10 mHz from the current operating point is detected [232]. Despite the differences in the deadband and insensitivity range, in all three countries the maximum regulating power has to be delivered for frequency variations higher than a preset threshold, i.e., 200 mHz in Germany [189] and the Netherlands [232], and 500 mHz in the UK [157]. Additionally, energy limited resources, such as BESSs, are required to be able to keep the maximum power for frequency variations ≥200 mHz for at least 15 or 30 minutes. The minimum required power of generators and BESSs providing such service is generally >1MW. However, owners of multiple sources of low power grid assets, such as stationary batteries, industrial processes, renewable energy generation, and Electric Vehicles (EVs) charging stations, can cluster their power capability together to deliver the minimum required power [144, 157, 232, 189].

To participate in the PFR market, Balance Service Providers (BSPs) submit their bids to the responsible TSO. The bids are composed of the available regulating power and the re-

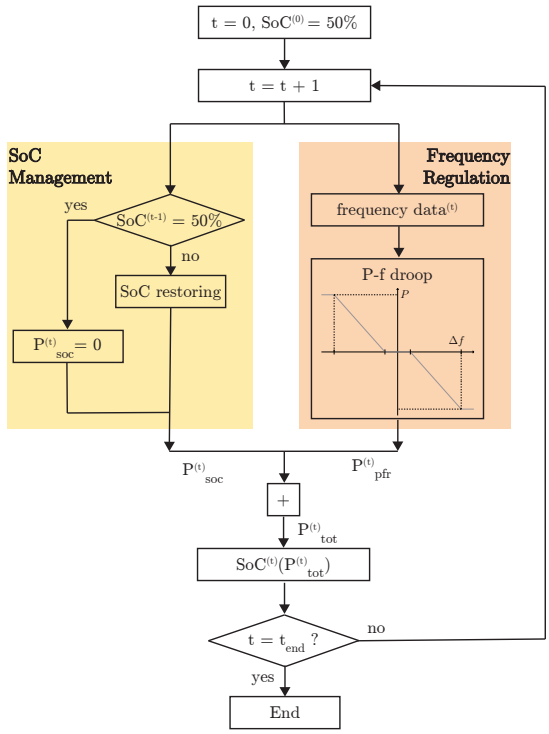

Figure 3.3: Flowchart describing the algorithm for PFR provision, where t indicates the time instant and P^t_{pfr} and P^t_{SoC} are respectively the frequency regulation power and the SoC control power at the instant t.

quired price for activation. Each TSO defines how much regulating power must be available in their control area at each instant; with this information they set up the tenders. After collecting all BSPs's bids, the cheapest feasible bids (that guarantee the required regulating power in the area) are selected.

The frequency trend of continental Europe [189] and the UK [156] during the year 2018 are plotted in Figure 3.2. From this figure, it is possible to see that in the UK, the grid frequency is subject to wider variations than in continental Europe; this is due to the lower inertia of the system. By following the frequency oscillations, energy limited resources, such as BESSs, will inevitably see a deviation of their SoC. Then, to ensure the system's continuous availability in providing PFR, the SoC of the battery has to be controlled. In this context, a fraction of the BESS power can be reserved for managing the SoC and for keeping it close to a reference value. Consequently, the frequency regulation service is provided only with the remaining available power. Alternatively, when the deadband is contemplated in the droop function, the SoC control can be done when the frequency variations are inside the deadband, and so the output power of the system for PFR should be zero. Nonetheless, a recent guidance published by National Grid, the system operator of the UK, recommends that BESSs should withhold a fraction of the power for the SoC management, and not use the deadband for regulating the SoC [154]. For these reasons, in the remainder of the chapter, only the SoC management strategy through the withholding of a fraction of the full system

Table 3.1: BESS' design specifications and components selection.

Design Parameter		Value	Components selected	
Rated VSC power	S_n	150kVA	IGBT modules	Infineon FF300R12KE4
DC link voltage	$V_{dc,n}$	750 - 1000V	Electrolytic Capacitors	Cornell Dubilier Type 500C
AC line-to-line voltage	$V_{ac,ll}$	400 V	Battery technology	$LiFePO_4$
Switching frequency	f_s	12 kHz	Heat Sink	From Infineon inverter stack 6PS0300R12KE3

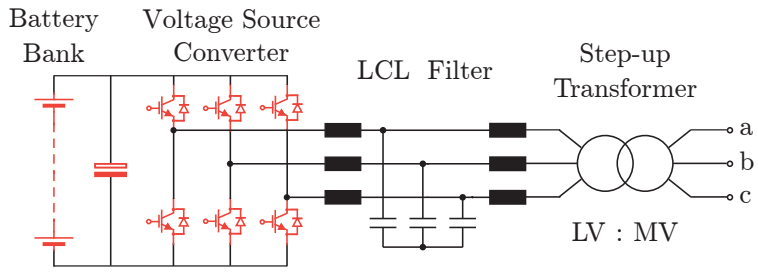

Figure 3.4: Circuit schematic of a grid-connected BESS with the critical components in terms of lifetime highlighted in red.

power will be considered. Therefore, the sum of the maximum power for SoC management $P_{SoC,max}$ and for the frequency regulation $P_{pfr,max}$ is always equal to the maximum system power, P_{tot}:

$$P_{tot} = P_{SoC,max} + P_{pfr,max}. \tag{3.1}$$

As previously mentioned, the payment for PFR is proportional to the power tendered. Then, withholding a fraction of the total power for managing the SoC would inherently reduce the frequency regulation market revenues. However, the system's power utilisation would reduce, and so it would advantageously extend the lifetime of the BESS. The algorithm for the provision of PFR is illustrated in Figure 3.3. The SoC regulation occurs in parallel to the PFR provision, targeting the re-establishing of the SoC at 50%, so that the BESS is able to deliver symmetrically for long time both up and down regulation, with the maximum energy available, in case of a strong frequency perturbation [224, 227]. Other parallel SoC re-establishing strategies could be implemented, for example containing the SoC into a range of values, however, these are not considered in this study.

3.3. BATTERY ENERGY STORAGE SYSTEM DESIGN

In this study, a BESS rated 150kW/150kWh has been considered, assuming that the BESS is aggregated with other BSPs to reach the minimum required power for PFR, i.e., clustering together up to 1 MW for PFR.

The VSC circuit topology consists of three half-bridge IGBT-Diode modules. A Low Voltage (LV) DC-link is taken into account, V_{dc} =750-1000V, coherently with the specifications of commercial battery racks [200, 125], and so for the connection at the Medium Voltage (MV) network, a LV/MV transformer is necessary to step up the voltage from the 400V line-to-line output of the VSC. The BESS' circuit schematic is shown in Figure 3.4 and the three components of which the lifetime is investigated, the electrochemical storage, the IGBT

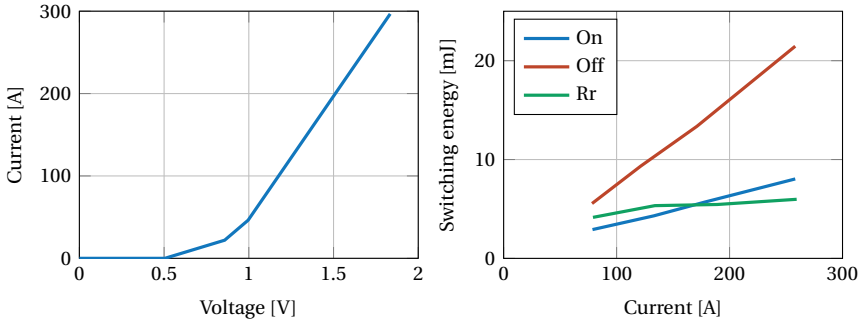

Figure 3.5: Conduction (a) and switching at $V_{dc} = 600V$ (b) characteristic of the IGBT-Diode modules FF300R12KE4 measured through the test board of FigureB.1 with junction temperature of 25°C and external gate resistance of 2Ω.

modules, and the electrolytic capacitors installed in the DC-link, are highlighted in red. The design specifications and the components selected, according to the procedure described in the following, are summarized in Table 3.1, where S_n stands for the rated VSC power, V_{dc} and $V_{ac,ll}$ for DC link and AC line-to-line voltages and f_s for the VSC's operating switching frequency.

The commercially available Trench/Fieldstop IGBT4-Diode modules FF300R12KE4, capable of withstanding up to 300A at junction and case temperatures of respectively 175°C and 100°C and of the 1200V voltage class, are selected [104]. These IGBT modules are selected based on the DC voltage, the peak collector current they have to carry and to ensure that the three VSC's legs deliver an efficiency greater or equal to 97.5% at the rated power of 150 kVA. The IGBT modules of a VSC are subject to power losses due to the current conduction and hard switching. The semiconductors' losses cause thermal stress in its chips and module package constituents, which drives their degradation [260]. The conduction losses, P_c, and the switching losses, P_s, for a Sinusoidal Pulse Width Modulation (SPWM) controlled VSC can be analytically calculated following the derivations of Appendix A.1.

The on-state and switching characteristics of the selected semiconductor modules are experimentally characterized using the double pulse test set up described in Appendix A. These are shown in Figure 3.5 (a) and (b). Given the experimentally derived conduction and switching losses of the IGBT modules, two loss-maps are created, relating IGBT and diode losses, VSC output power, and IGBT and diode junction temperatures. These loss-maps are used for the junction temperature estimation for a given mission profile, so to speed up the computation. These relate the power losses in the IGBTs and Diode to the junction temperature and converter output power and are generated through the methodology explained in Appendix A.2. An example of the IGBT loss-map is shown in Figure 3.6, where the losses in an IGBT are shown as function of its junction temperature and of the VSC output power.

Another component of the VSC of interest from the lifetime point of view is the electrolytic capacitor bank placed between the electrochemical storage and the IGBT modules in the DC-link. The DC-link capacitors function both as an energy buffer and limit the DC voltage ripple. The procedure used in this thesis for the design of the DC-link capacitor

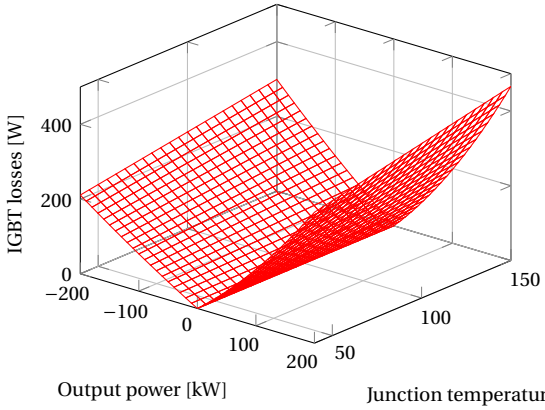

Figure 3.6: Loss-map of a single IGBT of the Trench/Fieldstop IGBT4-Diode modules FF300R12KE4 as function of its junction temperature and of the SPWM modulated at 12kHz VSC's output power, for a DC link voltage of 900V and an AC line-to-line voltage of 400V.

Table 3.2: Parameters for estimating power losses of the IGBT module FF300R12KE4 [260].

IGBT		**Diode**	
Parameter	Value	Parameter	Value
$v_{ce,25}$	0.9 V	$v_{f,25}$	1.05 V
$r_{ce,25}$	2.7 mΩ	$r_{f,25}$	1.9 mΩ
tc_{vt}	-0.0011	tc_{vd}	-0.0022
tc_{rt}	$1.28{\cdot}10^{-5}$	tc_{rd}	$7.2{\cdot}10^{-6}$
E_{on+off}	39 mJ	E_{rr}	6 mJ
a_t	0.003	a_d	0.006
k_{vt}	1.35	k_{vd}	0.6
		k_i	0.6

bank is detailed in Appendix A.2.

In this study, several commercially available capacitors of the $500V_{dc}$ class from [48] have been considered. Given the maximum value of I_{dcl} and the current capability of the single capacitors, the number of parallel capacitor strings, which consists of two series capacitors, are found. In this way, according to the components' characteristics, several DC-link designs are derived. The solutions that do not satisfy the minimum capacitance constraints derived in Subsection A.2.1 or that show a maximum hot-spot temperature higher than 95°C, the limit set in the data-sheet, are discarded. The volume, costs and base lifetime that stands for the number of guaranteed hours operating at 85°C, and maximum allowed ripple current of the remaining designs are plotted in Figure 3.7. These designs respect quality and performance constraints. For further analysis, the design that offers the least cost is selected, where the commercial cost figures are derived from [152]. This is done because market competitive industrial products are often designed, targeting the minimization of costs. Moreover, since grid-connected BESS are generally deployed in containers, volume minimization is not a driver as strong as cost minimization. Additionally, in terms of power losses, any substantial gain in efficiency by reducing capacitor losses would lead to prohibitive cost figures because the electrolytic capacitors' losses are relatively much smaller

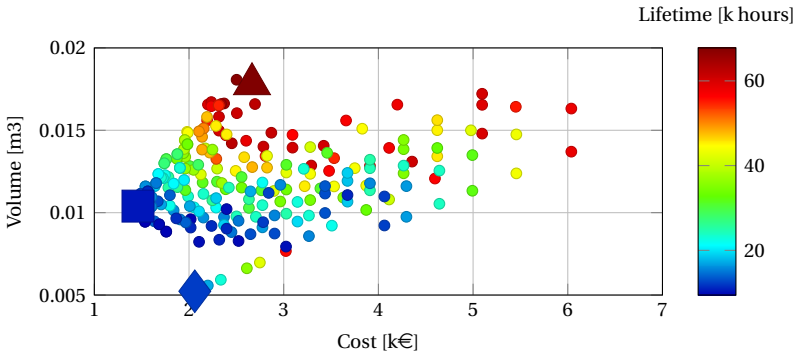

Figure 3.7: Volume, costs and lifetime of the DC-link capacitor designs that meet the design, thermal and base lifetime requirements. The star indicates the solution with the minimum cost, the diamond the one with minimum volume, and the triangle the one with maximum base lifetime.

than the ones seen in the semiconductors. Therefore, the design with the lowest cost that guarantees the quality and performance required, indicated with a star in Figure 3.7, is selected. This DC-link configuration consists of six parallel strings of two series connected capacitors of 3.9 mF.

3.4. BATTERY ENERGY STORAGE SYSTEM LIFETIME MODEL

In this Section, the lifetime models for the electrochemical storage, the IGBT modules and the electrolytic capacitors are discussed.

3.4.1. ELECTROCHEMICAL STORAGE LIFETIME

Lithium-ion batteries are subject to several ageing mechanisms. This causes an increase in the cell's impedance and the decrease of cyclable lithium [246, 35]. Such conditions lead to a lower battery's energy capacity, power capability, and round trip efficiency [151]. In this respect, it is common practice to consider a capacity fading of 20% as a reference value for the End of Life (EoL) of grid-connected BESS and EV battery packs.

Research has shown that both the power cycling and the idling condition contribute to the ageing of Li-ion based batteries. In this study, to evaluate the electrochemical cells lifetime, the empirical model for $LiFePO_4$ batteries developed through accelerated cycling of battery cells [222] and proposed in [220] is adopted. This model has been already adopted for the estimation of battery degradation in PFR [223, 224] and wind power applications [222, 220]. The capacity fading due to calendar ageing, C_{cal}, and cycling ageing, C_{cyc}, in percentage, are then evaluated according to (3.2) and (3.3) respectively [220].

$$C_{\text{cal}} = 0.1723 \cdot e^{0.007388 \cdot \text{SoC}_{\text{l}}} \cdot t^{0.8} \tag{3.2}$$

$$C_{\text{cyc}} = 0.021 \cdot e^{-0.01943 \cdot \text{SoC}_{\text{avg}}} \cdot cd^{0.7612} \cdot nc^{0.5}. \tag{3.3}$$

The capacity fading is then a function of the average SoC of a cycle SoC_{avg}, the number of cycles nc of a certain cycle depth cd, and the idling time t of the battery at a certain SoC level SoC_{l}. Equations (3.2) and (3.3), which describe the capacity fading, are derived for a Lithium-ion battery at a temperature of 25°C. However, temperature strongly influences

Table 3.3: Foster thermal model parameters of IGBTs, diodes and heatsink used for the study [104, 105].

	IGBT		Diode		Heatsink	
i	R [K/W]	τ [s]	R [K/W]	τ [s]	R [K/W]	τ [s]
1	0.00558	0.01	0.009	0.01	0.01374	2.23
2	0.03069	0.02	0.0495	0.02	0.04543	51.334
3	0.02976	0.05	0.048	0.05	0.0006	88.93
4	0.02697	0.1	0.0435	0.1	0.01573	88.93

Lithium-ion batteries' ageing [220], yet, grid-connected BESSs are generally deployed in containers equipped with air conditioning systems, used to control the temperature of the battery cells. Mostly, the temperature is kept stable at 25°C, to ensure optimal performances and extend its lifetime [223].

3.4.2. SEMICONDUCTOR LIFETIME

Power semiconductors and their packaging are subject to several failure mechanisms, such as bond wire lifting and breakage, and solder plate fatigue on the base plate and in the chip soldering [206]. Among these, bond wire related failures are the most prominent cause of power modules failures [241]. These are caused by the thermo-mechanical stress induced by the temperature gradients between the components due to the different materials and power losses [260]. In this context, research is focused on online junction temperature estimation methods, so to optimize the power module operation to enhance its reliability [266].

To evaluate the junction temperature of the semiconductors, the thermal behaviour of the semiconductor and the cooling aggregate is modelled through the Foster parameters as given by the manufacturer's datasheet [104, 105]. The forced air cooling aggregate implemented in the Infineon inverter stack 6PS0300R12KE3 has been taken as reference [105]. Its Foster parameters, R_i and τ_i, used to represent the thermal behaviour of the power modules, together with the one of IGBTs and diodes, are listed in Table 3.3. This heatsink has been chosen to guarantee that when the VSC operates at maximum power the steady-state junction temperature does not exceed 140 °C, leaving a safe margin from 150 °C, which is the maximum allowed temperature during switching conditions according to the IGBT modules' data-sheet [104].

The number of cycle to failure N_f of an IGBT module subject to a thermal cycle of amplitude ΔT_j, minimum junction temperature $T_\mathrm{j,min}$, and with heating time t_on are estimated through:

$$N_f = A \cdot \Delta T_\mathrm{j}^{\beta_1} \cdot e^{\frac{\beta_2}{T_\mathrm{j}+273}} \cdot t_\mathrm{on}^{\beta_3} \cdot I_\mathrm{B}^{\beta_4} \cdot V_\mathrm{C}^{\beta_5} \cdot D^{\beta_6}. \tag{3.4}$$

Equation (3.4) is resulting from several empirical studies, based on power cycling of multiple IGBT modules [15, 260]. The number of cycles to failure are determined also as function of the current per bond wire I_B, the module voltage class V_C, the bond wire diameter D. The coefficient A relates to the IGBT technology and it is equal to $9.34 \cdot 10^{-4}$ for Infineon IGBT4, while $\beta_1 ... \beta_7$ are selected according to [260]. Further experimental studies have updated (3.4), showing how semiconductor degradation saturates with thermal cycles with load periods (t_on) longer than 60s [102, 178]. Then, the influence of the loading time, when longer

than 60s, can be modelled in (3.4):

$$\frac{N_f(t_{\text{on}})}{N_f(1.5)} = 0.33, \quad t_{\text{on}} \geq 60\text{s}. \tag{3.5}$$

The IGBT module's consumed lifetime due to a specific cycle p is found as the reciprocal of $N_{f,p}(\Delta T_{\text{j},p}, T_{\text{j},p}, t_{\text{on},p})$. When the consumed lifetime reaches the unity the module is considered at the end of life. Hence, the semiconductor lifetime can be estimated as:

$$L_{\text{s}} = \frac{1}{\sum_{p=1}^{N} CL_{\text{s},p}} = \frac{1}{\sum_{p=1}^{N} \frac{n_p}{N_{f,p}}}, \tag{3.6}$$

where the index $p = 1...N$ represents the distinct thermal cycles and n_p the occurrences of the cycle p during a certain period of time.

3.4.3. ELECTROLYTIC CAPACITOR LIFETIME

The electrolytic capacitors' degradation mainly depends on two factors, operating voltage and the hot-spot temperature [252, 251]. Manufacturers often give lifetime models of aluminium electrolytic capacitors, and in this study, it is modelled as [49]:

$$L_{\text{c}} = L_{\text{b}} \cdot \left(4.3 - 3.3\frac{V_{\text{a}}}{V_{\text{r}}}\right) \cdot 2^{\frac{T_{\text{m}} - T_{\text{c}}}{10}} \tag{3.7}$$

where L_{b} is the rated capacitor lifetime, V_{a} is the applied voltage and V_{r} is rated voltage, T_{m} is the maximum rated core temperature, and T_{c} the operating core temperature [49]. T_{m} and L_{b} are related to the capacitor packaging and manufacturing, as specified by the manufacturer [49]. The operating hot-spot temperature, T_{c}, is estimated based on the capacitor Equivalent Series Resistance (ESR), the thermal resistance Z_{th}, both from data-sheet, and on the current flowing through the capacitor. In this regard, the full harmonic spectrum of the DC-link current, $I_{\text{cap,h}}$, and the ESR_h variation according to the current harmonic frequency h have to be considered [49]:

$$T_{\text{c}} = T_{\text{a}} + 1.5 \cdot Z_{\text{th}} \cdot \left(\sum_{h=1}^{\infty} I_{\text{cap},h}^2 \cdot \text{ESR}_h + I_{\text{leak}}(V_{\text{op}}) \cdot V_{\text{op}}\right), \tag{3.8}$$

where I_{leak} is the capacitor leakage current as function of V_{op}, given by the datasheet and V_{op} the operating voltage [48]. When (3.8) is adopted for lifetime estimation purposes, the capacitor manufacturer recommends the introduction of the coefficient 1.5, so that the heat rise due to current ripple weights more than the ambient temperature T_{a} effect [49].

Given the hot-spot temperature profile, the accumulated damage can be determined through Miner's rule [259]:

$$CL_{\text{c}} = \sum_{i=1}^{K} \frac{t_i}{L_{\text{c},i}}, \tag{3.9}$$

where t_i is the time during which the capacitor is operating in a specific condition i and $L_{\text{c},i}$ is the lifetime at this operating condition.

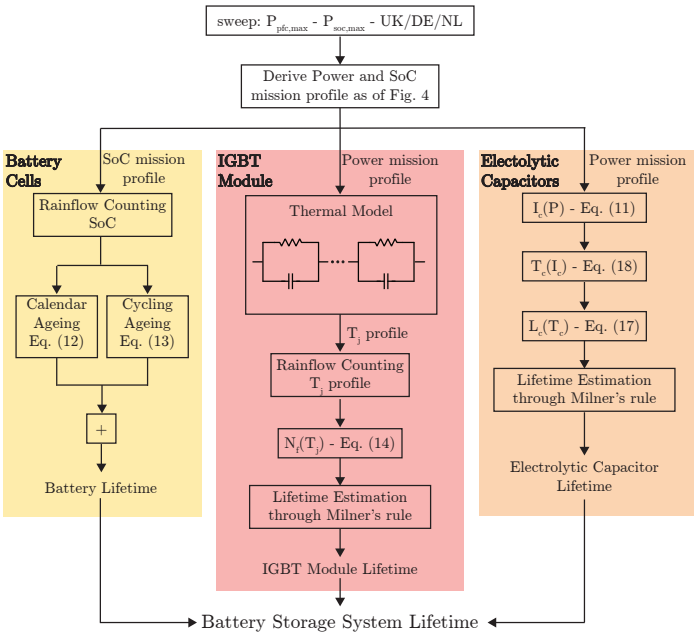

Figure 3.8: Methodology used for the lifetime estimation of electrochemical storage, semiconductor modules, and electrolytic capacitors.

3.5. LIFETIME EVALUATION METHODOLOGY

The procedure adopted for evaluating the BESS lifetime is illustrated in Figure 3.8. Such methodology has the peculiarity of considering not only the degradation of the electrochemical storage, left part of Figure 3.8, as proposed in literature [130, 224], but also the IGBT module and electrolytic capacitor one, centre and right parts of Figure 3.8.

Starting from the droop logic and the frequency trends, shown respectively in Figure 3.1 and Figure 3.2, the output power of the BESS is calculated. The algorithm for PFR provision is illustrated in Figure 3.3. As discusses in Section 3.2, this procedure is repeated varying the power sharing between PFR $P_{\text{pfr,max}}$ and SoC management $P_{\text{SoC,max}}$, respecting (3.1). Therefore, starting from the frequency trend, one year power and SoC mission profiles are defined, as detailed in Section 3.2. The SoC profiles are then decomposed between idling time when the battery system is not exchanging power with the grid and cycling time. The idling time and SoC levels are substituted in (3.2) to estimate the yearly calendar degradation. A rainflow counting algorithm is applied to the cycling profile, and so the equivalent cycles performed by the battery during the year are found [11]. These are substituted in (3.3) to determine the battery's capacity fading due to power cycling. The yearly capacity fading is derived by adding the contribution of calendar and cycling ageing. Finally, the storage lifetime is obtained by estimating when the capacity fading reaches 20% and thus, its EoL.

The output power found through the algorithm shown in Figure 3.3 is the main input for the lifetime estimation of the IGBT modules junction temperature and of the electrolytic capacitors. At the first iteration, the IGBT module junction temperature is considered 40 °C, the air cooling system's reference temperature. For each following iteration, given the semi-

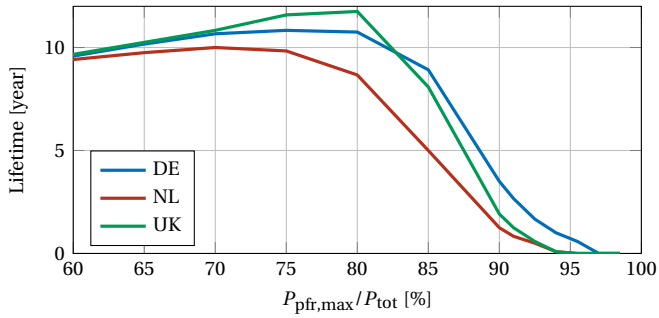

Figure 3.9: Battery cells' lifetime varying the percentage of the total power used for PFR provision, $P_{\text{pfr,max}}$ in the case scenarios of Germany, the Netherlands and the UK.

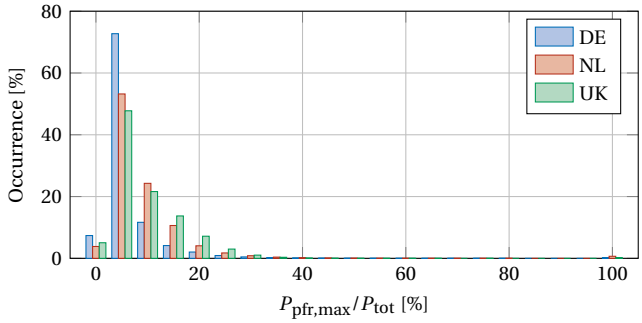

Figure 3.10: Time distribution of the BESS output power for PFR provision operating with $P_{\text{pfr,max}}$=150 kW in the case scenarios of Germany, the Netherlands and the UK.

conductors junction temperatures and the converter output power, the IGBT and diode losses can be estimated through the loss-maps generated with the methodology explained in Appendix A.2, of which an example is shown in Figure 3.6. Once derived the semiconductor power losses, the heatsink's temperature, power module case, and chip die junctions can be updated through the Foster thermal model.

Once the last iteration is reached and the thermal profile of the semiconductors junction is derived, this can be decomposed in equivalent thermal cycles through a rainflow counting algorithm [11]. Number of cycles to failure, $N_{f,p}$, for the specific cycles are calculated through (3.4). Then, the consumed lifetime of the power module $CL_{\text{s,year}}$ is estimated summing the contribution of each cycle p, $CL_{\text{s,year}} = \sum_{p=1}^{N} CL_{\text{s},p}$, and its lifetime through the reciprocal of the yearly consumed lifetime:

$$L_{\text{s}} = \frac{1}{\sum_{p=1}^{N} CL_{\text{s},p}}. \tag{3.10}$$

Regarding the electrolytic capacitor lifetime estimation, the capacitors current I_{dcl} can be estimated through (A.35) and starting from the output power and SoC mission profile. Then, the current flowing in each capacitor is found dividing I_{dcl} with the number of parallel capacitors strings. The current profile through the capacitors gives the hot-spot temperature profile that, implemented in (3.9), gives the capacitor wear due to the operation.

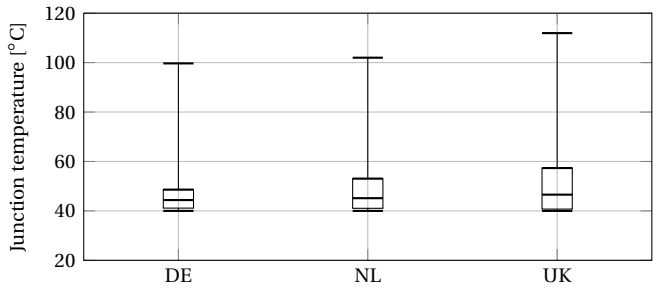

Figure 3.11: Estimated junction temperature analysis of the BESS's IGBTs providing PFR in the case scenarios of Germany, the Netherlands and the UK.

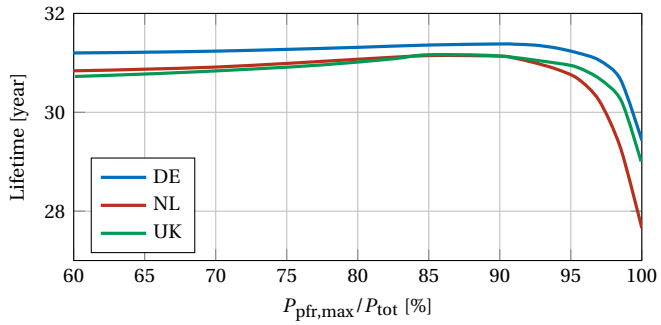

Figure 3.12: Electrolytic capacitor lifetime varying the percentage of the total power used for the provision of frequency regulation in the case scenarios of Germany, the Netherlands and the UK.

Following a similar procedure to the one of the IGBT modules, the capacitor lifetime is calculated as the reciprocal of its consumed lifetime CL_c, as described in Section 3.4.

3.5.1. RESULTS AND DISCUSSION

The BESS mission profile is generated varying fraction of power assigned to PFR $P_{pfr,max}$ and the one assigned to the SoC management $P_{SoC,max}$ following the algorithm described in Section 3.2.

Running the procedure detailed in Section 3.5 and Figure 3.8, the electrochemical storage lifetime is estimated, and shown in Figure 3.9. The results show that reducing the power reserved for PFR, $P_{pfr,max}$, the battery bank lifetime can be extended, reaching the peak at around $P_{pfr,max}$ equal to 70%-80% P_{tot}. However, by doing so, the revenues would decrease since the payment scheme depends on the power bid in the tenders, $P_{pfr,max}$, as the following section will discuss. The lifetime of the IGBT modules of the VSC is dependent on the junction temperature profile. These IGBT and Diode temperature profiles are estimated following the methodology detailed in Section 3.4.2 and in Figure 3.8.

As shown in Figure 3.10 analyzing the BESS power mission profile for $P_{pfr,max}$=150 kW, it can be seen that around 95% of the time during the year the system operates at a very low partial load, ≤20% of the total rated output power. This results from the nature of the P-f droop curves and the usually low frequency variations observed in the network. There-

Table 3.4: Parameters used for the NPV analysis.

Parameter	Value
Inflation rate	$r = 2.5\%$
Battery cost	330 €/kWh
PEC+BoP cost	150 €/kW
O&M costs	4.5 €/kWh/year
Average FCR price (NL)$^{+}$	19.08 €/h/MW
Average PCR price (DE)$^{+}$	12.77 €/h/MW
Average DLH price (UK)$^{++}$	7.22 £/h/MW

$^{+}$ data extracted from [231], $^{++}$ data extracted from [157]

fore, this functionality's very low power utilization inevitably leads the VSC to operate at low junction temperature and only seldom reach the thermal limits. Working at low temperature and seeing small power output variations, the IGBT and diode junction is subject to low thermal stress when applied for this specific application. In Figure 3.11, the estimated IGBT junction temperature average value and the 0.95 percentile over the yearly load profile are shown, and they can be seen to be very low. However, the derating of the cooling aggregate or of the semiconductor for reducing system costs is not a feasible option, since the BESS has to be capable to deliver the full power and as can be seen in Figure 3.11 the IGBTs' junction can reach high temperature values, although sporadically.

Such low thermal stress, as expressed in (3.4) and so by the manufacturer [15, 260], leads to low semiconductor degradation. Therefore, for BESS VSC performing PFR, the IGBT modules are not strongly subject to degradation due to the normal operation. Other causes of failure, related, for example, to the environmental conditions or grid transients, however, remain [265].

The electrolytic capacitors also encounter a similar lifetime trend to the one shown by the electrochemical storage and the IGBT modules. As it is possible to see in Figure 3.12, the reduction of $P_{\text{pfr,max}}$ leads to an increase of the lifetime. Nonetheless, the lifetime extension is less pronounced than the one seen by the electrochemical storage.

3.6. ECONOMIC ANALYSIS

The market for Lithium-ion batteries is rapidly growing due to increased demand for electric vehicles and stationary storage applications, reporting a 75% decrease in battery pack's price from 2013 to 2019 [214, 19, 20]. For this study, the capital cost of electrochemical storage has been considered 330 €/kWh, according to the latest published report by the US National Renewable Energy Laboratory [44]. The operation and maintenance (O&M) cost are set to 4.5€/kWh/year [130]. The cost for the Power Electronics Converter (PEC) and the Balance of the Plant (BoP) has been derived according to the solar utility market, since utility scale VSCs of photovoltaic generators are similar systems to the ones used in BESS, and fixed to 150€/kW [79, 74].

The remuneration scheme for the PFR provision in the selected countries foresees a payment to the service provider proportional to the regulating power and to the time of provision accepted in the tender, the price is then specified as €/MW/h. Germany fully contracts its regulating power through a joint auction between several central European countries. The Netherlands participates in the joint auction as well; however, it separately

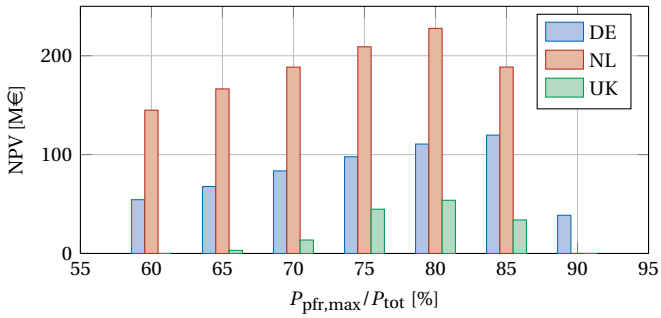

Figure 3.13: NPV over a 25 year project duration of a BESS systems rated 150kW / 150kWh varying the fraction of the maximum power allocated for PFR, $P_{pfr,max}$.

contracts a fraction of its total regulating power in a national auction. According to the documentation provided by the TSOs, the average contracted price for PFR in 2018 was 19.08 €/MW/h for the Netherlands and of 12.77 €/MW/h for the joint central European auction. In the UK, a similar remuneration scheme is provided in the Phase 2 auction trial, an innovation project that procures frequency regulation products through the EPEX SPOT Auction Platform [157]. The auctions for the procuring of Dynamic Low High (DLH) frequency products, technically similar to PFR, saw an average price of 7.22 £/MW/h, which is significantly lower than the prices seen in Germany and the Netherlands.

According to the investment cost and remuneration prices here discussed and summarized in Table 3.4, the Net Present Value (NPV) and break-even year of a BESS providing PFR in three case scenario have been evaluated. The NPV calculation was based on a time horizon of 25 years, compatible with the electrolytic capacitors and IGBT modules lifetime, as detailed in Section 3.4, and on a discount rate r of 2.5% [79]:

$$\text{NPV} = \sum_{t=1}^{25} \frac{R_t}{(1+r)^t} \tag{3.11}$$

The yearly revenue parameter, R_t, reflects the income due to PFR provision, proportional to $P_{pfr,max}$, the percentage of the total power allocated for PFR, the investment and O&M costs, as detailed in Table 3.4, and the costs associated to the components replacements, where the replacement times are derived according to Section 3.5.

The NPV is calculated for different $P_{pfr,max}$ percentages. As already mentioned, the revenues deriving from PFR provisions are proportional to $P_{pfr,max}$, thus higher $P_{pfr,max}$ gives higher revenues, however, components' wear increases as well, leading to earlier replacements of the BESS's components, as illustrated in Figure 3.9 and Sections 3.5. In Figure 3.13, the NPV presents an optimal value, so a point where the system shows the highest profitability. However, comparing these optimal points, with the results of Figure 3.9 and 3.12 it is possible to see that the $P_{pfr,max}$ value that leads to the highest NPV is not necessarily the one that leads to the lowest components degradation. It is also clear that such functionality is profitable in each country, since it is possible to find a positive NPV. Furthermore, the case of the Netherlands leads to considerably higher revenues, with a maximum NPV 47% and 76% higher than in Germany and the UK, due to the higher remuneration price [231].

3.7. CONCLUSION

This chapter has analyzed the provision of PFR through BESSs in three case scenarios reflecting the technical and economic regulation of Germany, the UK, and the Netherlands. The lifetime of the main BESS components subject to wear, the electrochemical storage, the IGBT modules, and the electrolytic capacitors have been investigated in different scenarios. As it has been illustrated in Section 3.5, the component that is subject to faster degradation is the electrochemical storage. Its lifetime peaks at 10-11 years, depending on the case scenario. The other two components whose lifetime has been investigated, electrolytic capacitors and IGBT modules, do not show significant wear due to the operation, when applied in BESS performing PFR, due to the very low power utilization of such functionality presented today. In the future, with the proliferation of distributed generation, a stronger effect of component aging may be found. Nonetheless, the BESS lifetime estimation methodology can be applied for studying BESS lifetime when performing other functionalities. Additionally, as detailed in this chapter, the power sharing between the SoC management and PFR provision is a key variable for evaluating the BESS lifetime and the revenues deriving from the PFR provision. In this respect, it has been shown that the value of $P_{\text{pfr,max}}$ that maximize the components lifetime does not necessarily coincide with the one that maximizes the BESS revenues.

Overall, the provision of PFR by means of BESS can be profitable in all the three countries analyzed, with the present remuneration tariffs and BESS capital costs. Furthermore, the higher remuneration tariffs seen in the Netherlands in recent years lead to the highest revenues between the analyzed countries. Future work should focus on BESSs lifetime estimation and economic benchmark when deployed for performing other grid-connected services, such as the participation of energy markets, peak shaving and load, and services for the DSOs.

4

HYBRID SI/SIC SWITCH FOR BATTERY ENERGY STORAGE CONVERTERS

This chapter investigates an hybrid Si/SiC switch (HyS) concept which can allow significant loss reduction for a limited cost increase. The mcHyS concept is analytically modelled, experimentally characterized, and a chip area model is used to benchmark the mcHyS modulation concepts against single technology switches and typical HyS modulation when implemented in a BESS' VSC when performing primary frequency regulation. Finally, a 10 kW two-level VSC assembled with mcHyS is tested so to compare its efficiency versus single technology switches, and the obtained results show that the HyS solutions are particularly competitive versus the full Si-based VSCs when the application at hand often operates at low partial loads.

This chapter is based on:

- M. Stecca, C. Tan, J. Xu, T.B. Soeiro, P. Bauer, P. Palensky, "Hybrid Si/SiC Switch Modulation with Minimum SiC MOSFET Conduction in Grid Connected Voltage Source Converters", IEEE Journal of Emerging and Selected Topics in Power Electronics, 2022, vol.10, pp. 4275-4289.

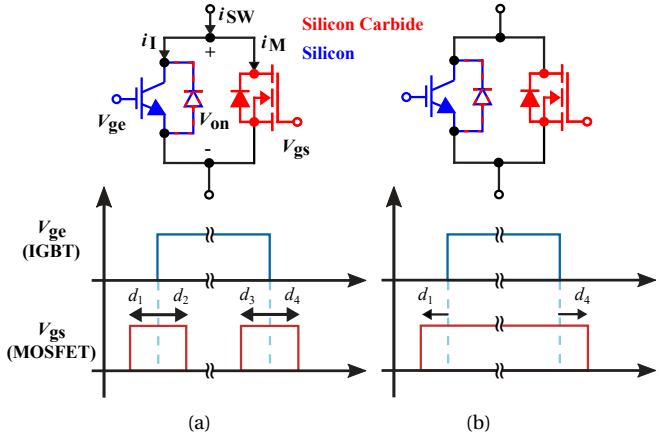

Figure 4.1: Si/SiC HyS arrangements and switching patterns: (a) mcHyS where the SiC MOSFET used for the switching transition only, and (b) tHyS where the SiC MOSFET used both for the switching transitions and for sharing the current conducted by the switch with the Si IGBT.

4.1. INTRODUCTION

Silicon (Si) IGBTs are currently the dominant power semiconductor technology for industrialized high power grid-connected Voltage Source Converters (VSCs), which are also used in battery systems. Nonetheless, Si IGBTs have unsatisfactory performance at low current conditions, e.g., partial load efficiency, and, especially high voltage class devices exhibit high switching losses [183]. In this context, silicon carbide (SiC) MOSFETs, which have superior performances, have gained popularity [264, 88, 277]. The major drawback of the SiC MOSFET is the higher manufacturing cost and unproven reliability when compared to the traditional Si IGBT [161]. The significantly higher cost of the SiC MOSFET calls for a compromised solution, e.g., a hybrid Si/SiC switch (HyS), which are obtained by paralleling Si IGBTs and SiC MOSFETs. Overall, HySs have demonstrated promising performances in several power electronics applications, including in grid connected inverters [258], while offering a compromised cost solution between full Si and SiC-based switches.

In this chapter an alternative HyS concept with minimum SiC MOSFET conduction (mcHyS) is investigated. The mcHyS concepts aims at further cost reduction with respect to SiC MOSFETs, since it allows the SiC device to have minimum conduction losses and therefore require a small chip area, but still offering improved performances respect to the traditional Si IGBT solution. In Section 4.2 the HyS arrangements and details the commutation process of the mcHyS is described. Section 4.3 provides the analytical models of 2L-VSCs based on the five switch configurations (mcHyS, tHyS, Si IGBT, and SiC MOSFET), and Section 4.4 details the HyS experimental characterization. The switch chip area and cost optimization procedure is described in Section 4.5, and based on this, in Section 4.6, the different switches are compared when adopted in grid-connected applications and the limitations of mcHyS are discusses. The concluding remarks are given in Section 4.7.

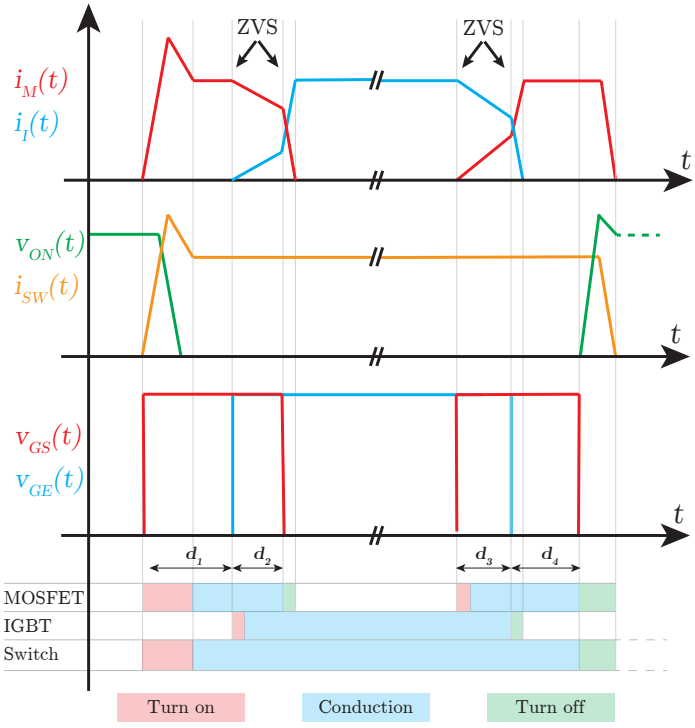

Figure 4.2: Commutation process of the mcHyS. The switching transitions and conduction periods are highlighted with different colors and the currents and voltages are referred to the schematic of Figure 4.1(a).

4.2. HYBRID SI/SIC SWITCHES

The assembly of Si/SiC HySs is realized paralleling a Silicon based device with a Silicon Carbide based one. The possible structures and modulation pattern are shown in Figure 4.1. The tHyS assembly and modulation is shown in Figure 4.1 (b). Here, a SiC MOSFET is paralleled to a Si IGBT, both to facilitate the switching transition and to share the conducting current. Such configuration, previously studied in literature [128, 129, 56], has shown to be well performing from both the conduction and switching losses point of view, placing itself in between the pure Si IGBT and SiC MOSFET in the cost efficiency matrix. In the tHyS the addition of a parallel diode is not strictly necessary. However, especially in grid connected application that require high reactive power operation and particularly during startup when all switches are kept off, it is useful to share the reverse conducting current with an anti-parallel diode, otherwise the SiC-MOSFET would have to be rated to withstand a high current, therefore losing its cost competitiveness.

The HyS with minimum SiC MOSFET conduction, mcHyS, shown in Figure 4.1 (a), is an alternative configuration for an HyS. The key difference from the tHyS consists in the switching pattern. The detailed commutation process of the mcHyS is shown in Figure 4.2, where it can be seen that switching losses occur only in the first and last MOSFET commutation, since the other switching events occur with the switch already on and so with ZVS soft switching because the parallel association is already conducting the impressed AC cur-

rent and the voltage across the switch is very small. The delays $d_1 ... d_4$ can be optimized so to enhance the switching and conduction performances of the mcHyS.

Furthermore, the additional diode for the mcHyS is a necessary component for the robust functioning of the switch, while in the tHyS of Figure 4.1(b) it is added for reducing the SiC MOSFET rating, and/or to de-risk body-diode degradation during startup [210]. This diode is required to conduct the reverse current, since the SiC MOSFET is used only for the switching transitions, as possible to see from the switching pattern of Figure 4.2. It has to be noted that this extra diode must be added, otherwise the current would forcefully flow through the SiC MOSFET body diode and/or the MOSFET channel which are not sized to withstand the high current. Additionally, enlarging the MOSFET channel for using it for the reverse conduction would not be economical, since the MOSFET area would considerably increase. Both a Si or a SiC diode are suitable for this purpose, in this study the mcHyS is assembled with Si diode, since there are commercially available devices already packaged together Si IGBT / Si diode. TO247 devices are used in the experimental characterization. In this way the commutation inductance loop are minimized and the two devices are properly designed and selected to be complementary. As just mentioned, the advantage of such configuration is that the SiC MOSFET can have a low current rating and so low cost, while the switching losses of the switch are greatly reduced with respect to a pure Si IGBT. Such cost-performance analysis for this mcHyS is missing from the literature, therefore the potential advantages and disadvantages and practical implementation issues of such HyS are not yet clear. These are discussed in the following sections.

4.3. HYBRID SWITCH ANALYTICAL MODELLING

The losses in an HyS-based 2L-VSC are modelled as detailed in Appendix A. The switching losses, which follow the derivations valid for pure Si-IGBT and SiC-MOSFET based 2L-VSC, are also influenced by the switching delays $d_1 ... d_4$. This point is extensively addressed in Section 4.4.

The accuracy of the proposed equations is verified with the circuit simulation software PLECS. A simulation model of a 2L-VSC assembled with different switch technologies has been built so to calculate the average and RMS current flowing through the different components of the HySs at different operating points. The simulation parameters considered are f_s=10 kHz, V_{dc}=900 V, $V_{ac,ll}$=400 V, P_n=100 kW, and φ=0. The 2L-VSC is interfaced with the grid through a filter inductance with a value of 1 mH, thus resulting in a low current ripple, below 1% the peak AC current. For the verification of the HySs arrangements, $v_{ce,0}$ and $v_{f,0}$ are set to 0.9V and 1V respectively. The on-state resistances considered are r_{ce}= 20 mΩ, $r_{ds,on}$= 40 mΩ, and r_f= 15 mΩ. These values are compatible with the I-V characteristics of the devices considered in the next section's experimental testing. The simulations are run with a variable step solver, DOPRI (non-stiff), with maximum step size and relative tolerance of 1μs.

Table 4.1 displays the average and RMS current values flowing through a single switch of a 2L-VSC operated as a full-power factor inverter calculated through the analytical method presented in this Section and the PLECS model. It can be noted that the analytical expressions provide excellent accuracy with respect to the circuit simulations.

Table 4.1: Validation of the equations proposed in Section 4.3-A through the circuit simulator PLECS.

		Analytical calculation	Simulation	Error %
mcHyS	$I_{avg,T}$	51.01	49.78	+2.41
	$I_{avg,D}$	13.97	14.09	-0.85
	$I_{rms,T}$	90.87	89.14	+1.90
	$I_{rms,D}$	46.48	46.08	+0.86
tHyS	$I_{rms,M}$	42.94	42.50	+1.02
	$I_{avg,T}$	28.51	28.23	+0.98
	$I_{rms,T}$	52.27	51.40	+1.66
	$I_{avg,D}$	8.06	8.11	-0.62
	$I_{rms,D}$	28.50	28.27	+0.81

4.4. EXPERIMENTAL CHARACTERIZATION

The conduction and switching performances are characterized through single and double pulse tests (SPT and DPT) whose circuit schematics and working principle are explained in Appendix A. The tests have been carried out with four devices in parallel with a common external gate resistor, R_g of 4 Ω and gate driver voltages, V_{gs}, V_{ge} for MOSFET and IGBT respectively, of +17/-4 V. The semiconductors under tests are the 1200 V class SCT3040KL SiC MOSFET manufactured by Rohm Semiconductor [196], and the IKQ40N120CT2 Si IGBT/diode manufactured by Infineon [103], both rated for 40 A. The choice of discrete TO-247 semiconductors for the HyS testing is driven by the necessity of minimizing the commutation loops between the switches which are detrimental for the switching performances. In this context, the paralleling of modules would require significantly larger connections between the individual components, due to their larger size compared to discrete TO-247 devices. Ideally, commercial HyS could be assembled with both Si and SiC devices inside the same power module, to further reduce stray inductances and ensure optimal performances.

The tests are carried with four devices in parallel to constitute a single switch, resulting in a 160 A switch, therefore the HySs are assembled with the hard-paralleling of two SiC MOSFETs and two Si IGBTs. The PCB layout aims at minimizing the parasitic inductances between the switches, placing them close to each other, so that they would properly share the dynamic current. A perfect current sharing during the switching transitions between the parallel devices can be ensured only by employing properly tuned separate gate driver for each device. This solution increases the complexity and cost of the system. Alternatively, one gate driver for each switch technology can be used, resulting in a good trade-off between optimal current sharing and system complexity. In this way the switching transitions are properly coordinated between the SiC-MOSFETs and the Si-IGBTs. Nonetheless, it is not guaranteed that the two SiC-MOSFETs exactly share the current during the switching transitions. In this context the PCB layout and minimization of parasitic inductances is crucial to ensure the best performances.

CONDUCTION LOSSES

The forward and reverse on-state characteristics of the single technology switches are shown in Figure 4.3 (a)-(b) together with the one of the HySs. Comparing the tHyS's conduction I-V curves with the IGBT and MOSFET ones [Figure 4.3 (a)-(b)] it can be seen that for low current level, such as below 50 A, the tHyS would perform significantly better than the IGBT

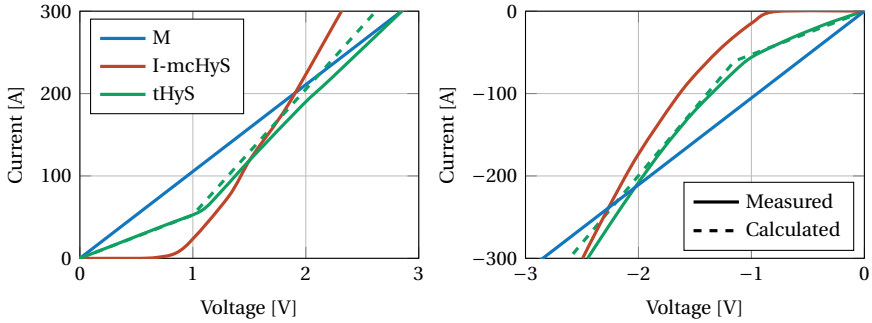

Figure 4.3: Forward (a) and reverse (b) on-state characteristics of four parallel SiC MOSFET, four parallel Si IGBT, and two Si IGBT plus two SiC MOSFET in parallel, derived for T_j=25° C, V_{gs} and V_{ge}=+17/-4 V, and R_g=4Ω, and analytically calculated according to (A.21).

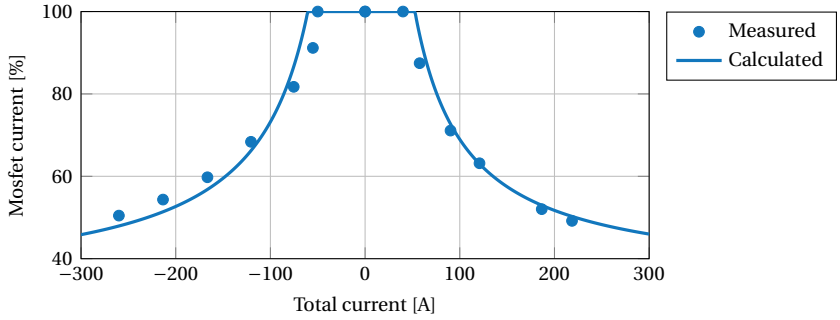

Figure 4.4: Percentage of the total conducted current by the tHyS flowing through the MOSFET channel; derived for T_j=25° C, V_{gs} and V_{ge}=+17/-4 V, and R_g=4Ω, and analytically calculated according to (A.17) and (A.19).

and mcHyS solution, very close to the MOSFET curve. In this context, the tHyS becomes attractive for applications that require frequent operation at low partial loads. Furthermore, at a high current level (>250 A) this hybrid solution starts having better conduction performances than the MOSFETs, but worse than the IGBT and mcHyS. It has to be noted that the mcHyS follows the Si IGBT-diode I-V curve, since the SiC MOSFET is activated only during the switching transitions. Therefore, only the tHyS shows an improved conduction characteristic with respect to the IGBT solution.

Together with the HyS I-V curve, the current sharing between IGBT/diode and MOSFET is a crucial information for the design and optimization of the HyS and its components. The current sharing at different total switch current with T_j=25° C, V_{gs}=17/-4 V and V_{ge}=17/-4 V is shown in Figure 4.4. As described in Section 4.3, the junction temperature influence the on-state parameters of the switches, and therefore the current sharing in the hybrid switch [228]. The resistance of the MOSFET channel increases with the rise in temperature, on the other hand, the pn junction barrier voltage of the IGBT decreases. In consequence, the starting value for the conduction of the IGBT is lower at higher temperature and overall the MOSFET will conduct a lower percentage of the total current, due to the higher on-state re-

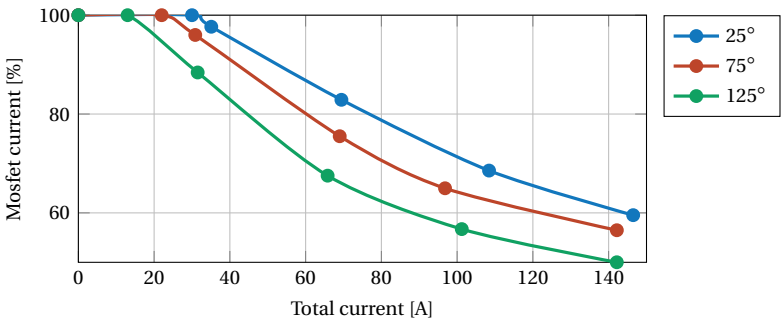

Figure 4.5: Measured current flowing through the MOSFET in a HyS at different junction temperatures; derived for V_{gs} and V_{ge}=+17/-4 V, and R_g=4Ω

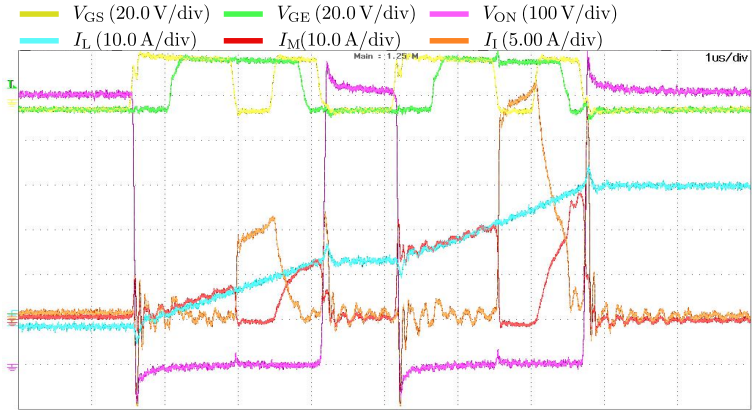

Figure 4.6: Double Pulse Test waveforms of mcHyS obtained through the test setup of Figure B.1 and referred to the circuit schematic of Figure B.2 (a).

sistance. This trend is shown in Figure 4.5 where the percentage of current flowing through the MOSFETs of the tHyS are measured at various junction temperatures, between 25°C and 125°C, which is the temperature range in which power semiconductor typically operate. The difference in current sharing is significant for a high temperature swing, as shown in Figure 4.5. During the switching transition and the 50Hz cycles, instead, the temperature rise is smaller, due to the lower time constants, and so the current sharing is not significantly influenced by such fast temperature swings [133, 218].

The HyS I-V curves and the IGBT/MOSFET current sharing can be analytically derived as presented in Section 4.3 from the single component's on-state characteristic and (A.17)-(A.20). The analytically calculated and the experimentally measured I-V curves and current sharing are compared in Figure 4.3 and Figure 4.4, where it can be seen that the analytical equations provide a fair accuracy.

SWITCHING LOSSES

Various tests have been performed, investigating the effect of temperature, turn on and off delays, and the losses sharing between IGBTs and MOSFETs in the HySs. The DC voltage

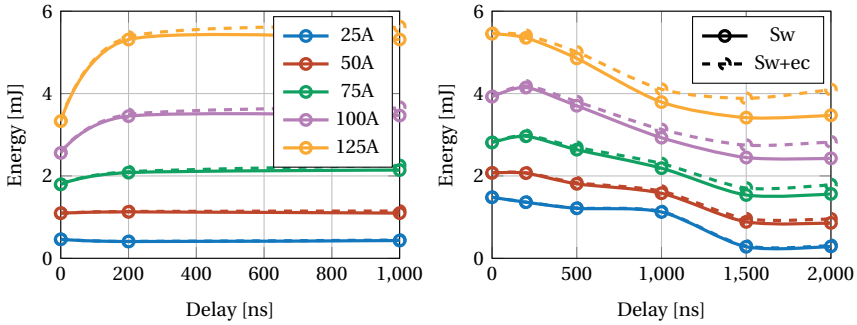

Figure 4.7: HySs turn on (a) and off (b) switching energies (sw) and extra conduction (ec) losses varying the switched current and the MOSFET-IGBT delays d_1 and d_4.

V_{dc} is kept to 600 V, while different current points are achieved varying the inductance value and the pulse width. An example of the DPT waveform for the alternative HyS is shown in Figure 4.6. After the deskew of the measurement probes the switching losses can then be calculated by multiplying the voltage and current waveforms during the switching event, as detailed in the datasheets of the components [196, 103].

The turn on and off delays, d_1 and d_4, have been proved in previous literature to strongly influence the switching performances of HySs. At the turn on, a small or even null delay between MOSFET and IGBT leads to minimized overall turn-on losses since both devices offer a path for the reverse recovery current and therefore shortens the turn-on time and reduces losses. This trend is also confirmed in the performed experiments, as possible to see in Figure4.7(a). Regarding the turn-off, instead, a longer delay, in the range of 1-2 μs, is found to be the most suitable to reduce the turn off losses, as shown in Figure4.7(b). This comes from the fact that a long delay allows the IGBT to be switched off with ZVS. However, after switching off the IGBT, the MOSFET conducts the full current, creating additional conduction losses. Therefore, long turn-off delays are penalized from these additional conduction losses, and so the optimal turn-off delay, for the considered components, has been found to be equal to 1.5 μs, a value compatible with the one reported in other studies [253]. In these conditions, simultaneous turn-on and 1.5 μs delay for turn-off, the switching losses are concentrated in the MOSFETs, with the IGBT operated in soft-switching. After all, HySs position themselves very well when compared with single technology Si and SiC switches, as indicated in Figure 4.8. Both HySs can significantly reduce switching losses with respect to Si IGBTs; however, full SiC MOSFETs still exhibits the best switching performances.

PARASITIC INDUCTANCE EFFECT IN THE MCHYS

The mcHyS concept, presented in Figure 4.1 (a), requires two additional switching events, defined by d_2 and d_3. These have been tested to be lossless since they happen when the switch is already conducting, and therefore, the voltage across the switch is in the order of few Volts, as it can be seen in Figure4.6.

This soft-switching condition is maintained when the parasitic inductance between MOSFET and IGBT is very low so that the current commutation between the two switches occurs

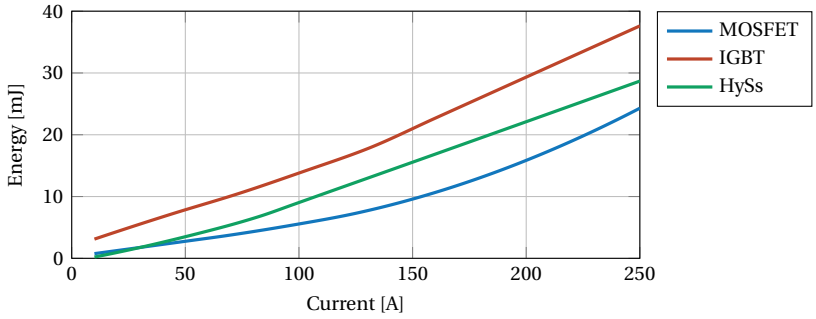

Figure 4.8: Switching characteristics of HySs, Si IGBTs and SiC MOSFETs derived through DPT at T_j=25° C, V_{dc}=600 V, R_g=4Ω.

smoothly. The two switch arrangements detailed in Appendix B are used to evaluate the impact of the parasitic inductances. When the low inductance arrangement is used the soft-switching condition is maintained and the current commutation between the two switches occurs smoothly as can be seen in Figure 4.9 (a). On the other hand, if the commutation inductance is increased, the voltage across this can force the conduction of the upper diode and the rise of the voltage across the switch, as possible to see in Figure 4.9 (b). This voltage spike introduces additional switching losses. Therefore a low inductive commutation path between the SiC MOSFET and Si IGBT is fundamental in HySs. Furthermore, no influence of d_2 on the switch turn on losses, dependant instead on d_1, has been found. Hence d_2 and d_3 can be set very small so to avoid extra conduction losses in the MOSFETs.

COMMON-MODE EMI

The conductive EMI of a grid connected converter is related to the switched terminal voltages amplitude and to switching transitions where the $^{dv}/_{dt}$ is particularly relevant for common-mode EMI. The switch terminal voltage amplitude is defined by V_{dc} and the selected circuit topology. Therefore, the main switching transitions and the amplitude of the terminal voltages will be defined by the circuit topology. Regarding the $^{dv}/_{dt}$ of the terminal voltages, as shown in Figure 4.6 and 4.9, only the first and last switching events of the SiC MOSFET in a mcHyS have influence in the voltage across the switch and the equivalent terminal voltage, since the other switching transitions within the pulse period are functional switching events so to shift the current conduction from the SiC MOSFET to the Si IGBT and vice-versa. Therefore, the voltage across the switch is driven by the first turn on and the last turn off of the SiC MOSFET, and so the $^{dv}/_{dt}$ at the mcHyS output terminals is driven by the switching speed of its SiC MOSFET. Hence, the mcHyS shows similar performances of the pure SiC MOSFET solution. Overall, the pure Si IGBT solution is the one with lower high frequency common mode noise, due to the slower switching transitions [18].

EFFICIENCY TESTING OF A 10KW 2L-VSC

After the experimental characterization of the mcHyS, its efficiency has been benchmarked versus pure technology switches using the test bench described in Appendix A. This 10 kW VSC could be used as a Power Electronic Building Block (PEBB) for a 100kW unit, however here the VSC is optimized only for verifying the advantage of the system in the 2L-VSC inverter application. Nonetheless, the performances should be similar in terms of efficiency.

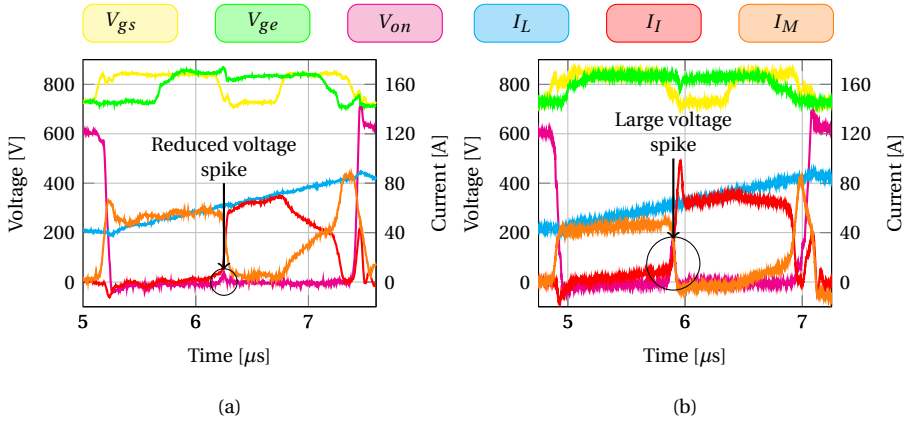

Figure 4.9: Experimental verification of the influence of parasitic inductance on switching behavior of hybrid switches: (a) low inductive commutation path, estimated to 50 nH, and (b) high inductive commutation path, estimated to 140 nH.

The mcHyS switching waveform during the inverter operation at 10kW is shown in Figure 4.10, where the VSC three phases converter side output currents are indicated with the green, orange and red waveforms, and the gate signals of the mcHyS MOSFET and IGBT with the blue and pink signals. The modulation pattern of Figure 4.1 (a) can be recognized in the zoomed lower part of Figure 4.10. Furthermore, the DC voltage waveform is displayed with purple color.

Three different switch configurations have been benchmarked: two pure switch technologies, the Si-IGBT and SiC-MOSFET; and the mcHyS. The switches are selected to have comparable rated continuous collector/drain current at 100 °C. The IKQ40N120CH3 Si-IGBT, rated for 40 A, from Infineon has been selected. Two SCT3105KL SiC MOSFETs, rated 17 A, from Rohm Semiconductors have been paralleled to assemble the SiC-based switch. Finally, the mcHyS, has been set up paralleling a IKQ40N120CH3 Si-IGBT, rated for 40 A, and one SCT3105KL SiC MOSFETs, rated for 17 A. Considering the cost figures from components distributors, the costs of a single switch are compared in Table 4.2 [59]. It can be seen that the pure SiC-MOSFET solution is nearly four times more expensive than the pure Si-IGBT, while, the mcHyS provides a trade-off solution, with triple the IGBT price.

The efficiency tests have been performed with an input DC voltage of 685 V, an output AC rms voltage of 230 V, modulation index of 0.95, and 10 kHz switching frequency. An LCL filter is placed between the VSC and the load resistors, to filter the current harmonics, as required by the grid connection standards. The LCL filter is assembled with the commercially available 750343810 inductors from Wurth Electronics rated 340mH both in the converter and in the grid side, L_c and L_g, and 9.9 uF capacitance, C. The efficiency, evaluated through the Yokogawa WT500 Power Analyzer, has been measured between the DC side of the VSC and the converter side inductance of the LCL filter, L_c. In this way, both the losses of the 2L-VSC and of L_c are measured. The power analyzer connection after L_c has been selected to ensure that the efficiency measurement has high accuracy, since the switched voltage at the output of the VSC has very high $^{dv}/_{dt}$ and cannot be properly measured by the power analyzer, while after L_c the voltage has a more sinusoidal shape with much lower $^{dv}/_{dt}$ than

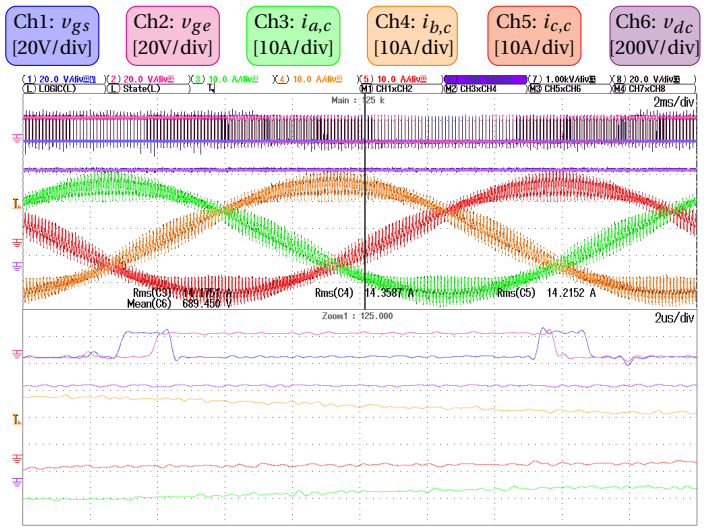

Figure 4.10: Waveforms of a mcHyS-based 2L-VSC supplying a resistive load. The switching pattern of the mcHyS can be distinguished in the zoomed bottom area of the figure, the gate signals of the SiC-MOSFET and of the Si-IGBT are shown with the blue and pink waveforms respectively.

Table 4.2: Switch cost and measured efficiency of a 10kW 2L-VSC assembled with various switch technologies [59].

Parameter	Si-IGBT	mcHyS	SiC-MOSFET
Single switch cost [€]	5.53	16.48	21.90
Cost ratio to Si-IGBT [p.u.]	1	2.98	3.96
2L-VSC efficiency at 10kW [%]	98.19	98.56	99.00
Loss reduction to Si-IGBT [%]	-	-37.45	-83.23

the WT500 power analyzer can accurately measure. In Figure 4.11(a) the measured efficiency of the three switch configuration in five operating points are shown. Additionally, the losses in the converter side inductors are calculated evaluating the AC winding losses, proximity effect losses and core losses through the methods described in [217]. The AC and DC resistance has been measured through the Agilent 4294a Impedance Analyzer, while the Steinmetz parameters are derived from the datasheet of the inductor's core material. The calculated inductor efficiency for different power flowing through it is also shown in Figure 4.11(a).

Finally, given the measured efficiency of the set up of Figure B.5, VSC+L_c, and the calculated losses of L_c, it is possible to provide a close estimate of the semiconductors efficiency, plotted in Figure 4.11. The pure SiC MOSFET switch, as expected, provides the most efficient solution. Furthermore, the efficiency gain of mcHyS with respect to the pure Si-IGBT is remarkable, positioning itself as good trade-off between Si-IGBT and SiC-MOSFET. As summarized in Table 4.2, the mcHyS allows a 37.45% reduction of power losses respect to the IGBT at 10kW.

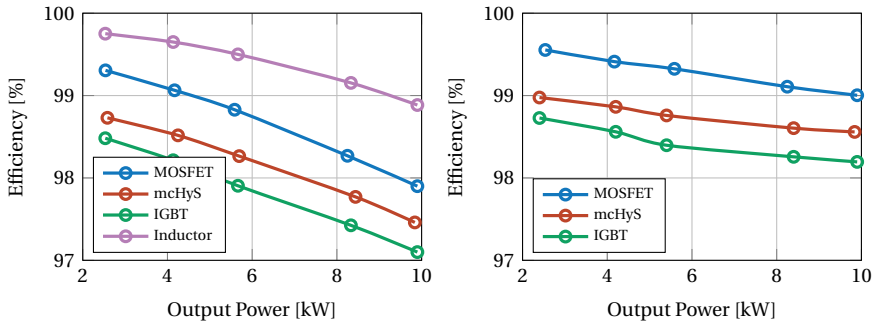

Figure 4.11: (a) Measured efficiency of a 10kW 2L-VSC and of the converter side inductor, assembled with different switch technologies, and calculated efficiency of the inductor at various power, and (b) derived VSC efficiency.

4.5. CHIP AREA AND COST OPTIMIZATION

In HySs the current ratio between the SiC MOSFET and Si IGBT defines not only the current sharing behavior, and thus the performance of the switch, but also its cost. A low current ratio, in fact, would result in a small SiC chip area and, therefore, lower switch costs since the silicon carbide devices are by far more expensive than their silicon based equivalents. However, a small chip area leads to worse conduction and thermal performances. On the other hand, a too high current ratio could result in over dimensioning the SiC area and thus loses cost-competitiveness versus the full Si IGBT based switches. In this context, optimizing the Si and SiC chip area ensures that both technologies are properly utilized and that the switch cost is optimized [56]. The chip area optimization consists of finding the minimum necessary Si and SiC chip area of each switch so that the semiconductors' thermal limitations are not exceeded, which means a maximum junction temperature of 150°C.

Therefore, in this section, the semiconductor chip area optimization of a grid-connected 100 kW 2L-VSC is presented. A low line-to-line AC voltage, $V_{\mathrm{ac,ll}}$, of 400 V, a DC-link voltage, V_{dc}, of 900 V, and a switching frequency, f_{s}, of 10 kHz are considered. The analysis here presented is based on the analytical equations provided in Section 4.3, on the experimentally derived switching energies, as illustrated in Section 4.4, on datasheet values from semiconductor manufacturers [103, 196, 50], and on the cost figures from components distributors [59].

Power semiconductors on-state resistance r_{on} and junction to case thermal resistance $R_{\mathrm{th,jc}}$ are generally modelled following an inverse correlation with the chip area A_{c}, as [78, 201]:

$$r_{\mathrm{on}} = \frac{x}{A_{\mathrm{c}}} \tag{4.1}$$

$$R_{\mathrm{th,jc}} = M \cdot A_{\mathrm{c}}^{-l}. \tag{4.2}$$

The pn junction barrier voltage of IGBTs and diodes instead depends on its manufacturing technology, not on the device chip area.

The switching losses and chip area can be correlated with piecewise linear functions as a function of the switched current. However, to provide a fair chip area analysis, it has to be considered that generally larger chips are switched faster through smaller gate resistances

Table 4.3: Parameters for the chip area analysis - from datasheets [103, 196, 50] and experimental measurement.

	Parameter		Si IGBT	Si diode	SiC MOSFET
Chip area	A_i	mm^2	20-70	10-60	2-20
Conduction	x_i	$m\Omega/mm^2$	723	233	357.3
	V_{ce}	V	0.9	1.05	-
Turn on/[1]	$m_{s,i}$	mJ/mm^2	-0.134	0.0814	-0.058
Reverse Rec	$q_{s,i}$	mJ	11.29	1.7456	1.945
Turn off [1]	$m_{s,i}$	mJ/mm^2	0.018	-	-0.033
	$q_{s,i}$	mJ	2.977	-	0.882
Thermal	M_i	-	6.558	3.022	1.585
	l_i	-	0.826	0.491	0.705
Cost [2]	$m_{c,i}$	€/mm^2	0.2	0.15	4.256
	$q_{c,i}$	€	2.846	0.827	-5.264

[1] at 50A/600V.
[2] for Si IGBT and Si diode referred to bare dies, while for SiC MOSFET to TO-247 packaged, subtracting the packaging cost (cf. [23]), due to the unavailability of bare die cost information.

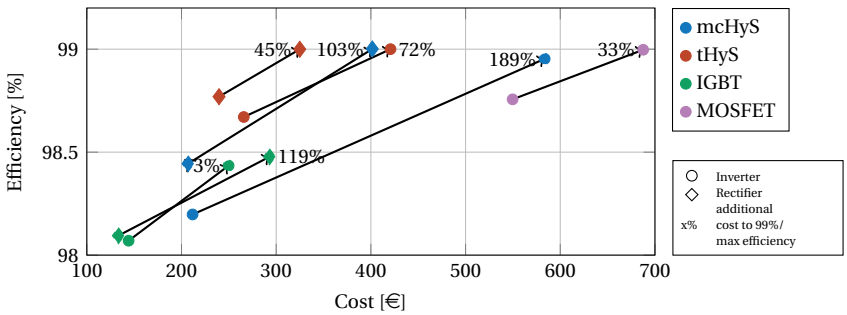

Figure 4.12: Semiconductor chip costs and efficiency design space for different switch configuration that satisfy the thermal limits during operation at full power in an 2L-VSC working as inverter and rectifier. The percentage shown is related to the incremental cost needed to bring the minimum cost designs to an efficiency of 99% or to the maximum efficiency.

[202, 201, 208, 103]. Therefore the switching losses are first to be scaled to have a fixed value of gate resistance per mm^2 of semiconductor area, according to the suggested values from the manufacturers, and then interpolated. The switching losses relation with chip area can then be modelled as:

$$E_{sw}(A_c, I, V) = m_s(I, V) \cdot A_c + q_s(I, V). \tag{4.3}$$

In addition to the performance indicators, the semiconductor cost can be expressed proportionally to its chip area and linearized in the form of:

$$C = m_c \cdot A_c + q_c. \tag{4.4}$$

The fitting coefficients of (4.1)-(4.4), listed in Table 4.3, have been derived consulting the manufacturer's datasheet, the components distributors prices, and the experimentally derived results presented in Section 4.4.

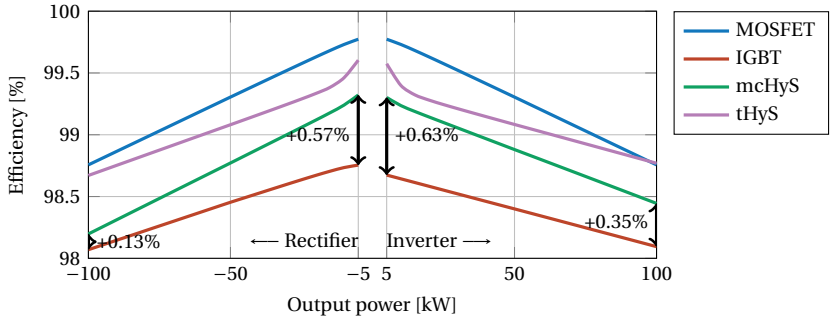

Figure 4.13: Semiconductor efficiency of the switch configurations of Figure 4.13 varying the output power operating as inverter and rectifier 2L-VSCs. The selected designs are shown in Figure 4.12 and represent the chip area optimized for minimal cost.

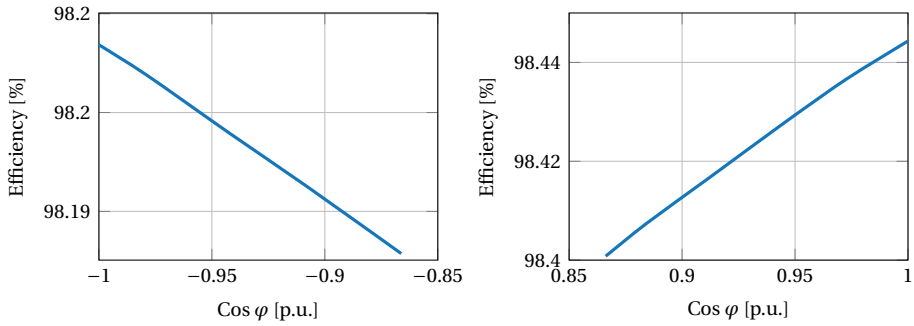

Figure 4.14: Semiconductor efficiency of a mcHyS-based 2L-VSC designed as (a) inverter and (b) rectifier operating at rated apparent power and varying the power factor.

The minimum cost chip area configurations are then calculated for a 2L-VSC, IGBT-based, MOSFET-based, and HyS-based, designed to operate as an inverter, or rectifier. The operation mode influences the conduction losses, e.g. the rectifier mode leads to a higher reverse conduction current in the switches. These are plotted versus their efficiency in Figure 4.12, where it can be noted that the IGBT based switch, as expected, provides the cheapest solution in both operating modes. In the same figure the designs that reach 99% semiconductor efficiency or, in the case of the IGBT, the maximum efficiency designs, are also plotted, so to show the required cost increase to reach such efficiency value. The mcHyS minimum cost solution shows relatively low costs compared to its full SiC MOSFETs equivalent. The tHyS still provides a cheaper solution than the pure SiC MOSFET one, however, since the SiC MOSFET is also used for conduction it requires a larger area than in the mcHyS and thus becomes more expensive. For high efficiency designs, $\eta \geq 99$ %, the tHyS shows low costs, lower than mcHyS and full SiC MOSFETs. Furthermore, in Figure 4.13, the minimum cost configurations' efficiency is plotted for various power outputs. Overall, at low power the efficiency gain of HySs and MOSFETs versus the IGBT-based solution is remarkable, with an efficiency gain of the mcHyS of up to 0.6% with respect to the IGBT. Grid connec-

tion standards typically require VSC to support the grid voltage with reactive power, therefore it is important to consider the standard required power factor, typically 0.9, in the VSC design [33, 32, 46]. In Figure 4.14, the efficiencies of mcHyS-based 2L-VSCs designed as inverter and rectifier are shown varying the power factor when operating at rated apparent power. It can be seen that the efficiency drops slightly when more reactive power is generated, nonetheless it remains satisfactory.

In this Section the semiconductor costs of various switch technologies have been considered. Nevertheless, the semiconductor die are not the only cost factor. Other elements are, for example, the packaging, gate driving and protection circuit, and digital controller cost.

A fixed cost disadvantage of HySs versus the pure technologies is found on the gate driving circuits. Such switch assembly, in fact, requires two separate gate driving circuit per single switch, since the Si-IGBT and SiC-MOSFET are controlled separately, as Figure 4.1 (a) details. Nonetheless, commercial dual channel digital isolators can be purchase with similar costs than their single channel counterparts, i.e. the ADUM1100 and ADUM1200 serie. Therefore the extra costs in the dual channel gate driver of the mcHyS consists on the two buffers required instead of one, which are a relatively cheap component, i.e. the ZXMC4559DN8. Regarding all the remaining previously mentioned elements, the HySs do not require higher fixed costs or significantly higher complexity. Packaging costs can be assumed to be constant between the switch technologies. Current implementation of HySs are based on paralleling separate discrete Si and SiC based devices [57, 258], therefore there is not an added packaging costs for HySs with respect to single technology switches. Furthermore, also if packaged in a power module there would not be significantly different packaging costs, since multi device packaging technology is already mature, as most high power semiconductors module are assembled with multiple dies in parallel [260]. This is particularly true in case where the die attachment and bond-wiring technologies can be the same for both Si and SiC, e. g., similar die sizes.

The protection of the switch can be ensured through several ways, depending on the switch short circuit withstanding time. Si-IGBT generally can withstand short circuits for longer time, up to 8-10 μs, therefore, the desaturation method, implemented in the gate driver, is the most commonly used protection systems [149]. SiC-MOSFETs, instead, require a faster clearing time, in the order of 1-2 μs, which is quite challenging to achieve through the desaturation method. Therefore, other protection system have been studied, such as di/dt measurement through Rogowski coils or direct switch current measurement [149, 216]. In this context, HyS have similar requirements of the pure SiC counterparts, however as the parallel IGBT is place into conduction within 1μs, the short-circuit current would be shared leading to lower thermal stress in the SiC Mosfet. Therefore, the hybrid switch could be more robust than the full SiC solution, but more studies need to be performed to verify this assumption.

The digital controller which is typically used for generating the PWM signals of the converter with single switch can be used also for the control of HySs-based converters. The gate signals, in fact, are typically generated through a counter compare technique, i.e., by comparing a value, which defines the switch duty cycle and varies each switching period, with a triangular carrier. In the same way, the gate signals strategies of a HyS can be generated, using an additional counter compare, shifted from the first counter compare accordingly to the delays between the IGBT and MOSFETs switching transitions.

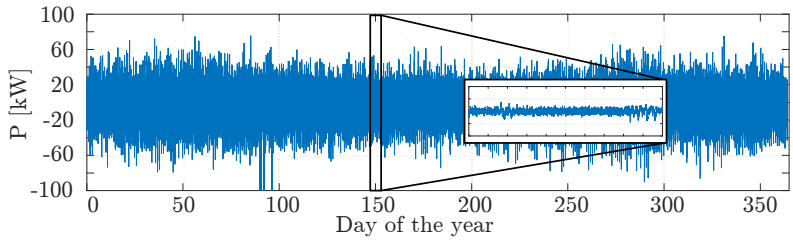

Figure 4.15: Yearly mission profiles of a 100 kW 2L-VSC used as grid interface for a BESS providing frequency regulation, with zoom in one day.

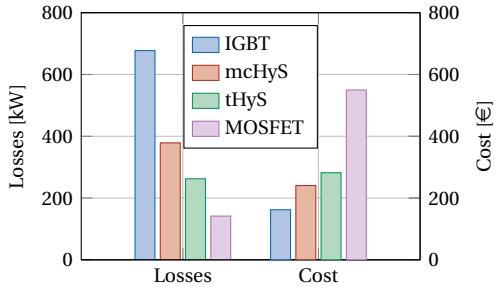

Figure 4.16: Semiconductor cost and losses of 2L-VSCs assembled with various switch technologies performing the mission profiles shown in Figure 4.15.

4.6. APPLICATIONS IN BESS PROVIDING PRIMARY FREQUENCY REGULATION

The particular characteristics of HySs make them valuable candidates for the utilization in power electronics converters for multiple applications. As shown in the previous sections, both HySs concepts exhibits excellent switching performances and lower cost than pure SiC MOSFETs, furthermore, tHySs have also low conduction losses at low partial load, both in forward and reverse conduction, since only the SiC MOSFET will be conducting, since to the junction barrier voltage of the Si IGBT, during forward conduction, and of the Si diode, during reverse conduction, will force the current to flow only through the MOSFET channel, as detailed in Section 4.3. Nonetheless, the SiC MOSFET exhibits the lowest conduction losses at low partial load. In this section, the performances of HySs are compared with the pure Si and SiC switches when implemented in 2L-VSC performing a specific load profile that reflects different applications of the converter. The minimum cost designs illustrated in Figure 4.12 are considered for the following study, as reflect the goal of competitive business. The selected applications consist of a BESS converter with the specifications previously used for the chip area analysis. More in detail, it is considered the application of HyS in a VSC of a BESS performing Primary frequency regulation. As detailed in Chapter 3, this application is of particular interests for BESS. A typical load profile of a BESS providing PFR would mostly consist of operation at very low partial loads, where HySs perform very well, due to the high inertia and regulating power of the central European transmission grid that effectively limit the frequency variations [159].

SWITCH COMPARISON

The yearly mission profiles described are shown in Figure 4.15. As it is possible to see the EV charging station has the profile that leads to the highest power utilization, followed by the PV, and the PFR application. On the other hand, the latter has a very high utilization rate, having the BESS working 98% of the considered time. The comparison of the switches for various applications is presented in Figure 4.16, where cost and losses of an mcHyS-based 2L-VSC performing different mission profiles compared with an tHyS-based 2L-VSC. From the figure it can be noticed that the mcHyS provides a cheaper solution than the typical HyS, however it also shows slightly worse performances. Overall HyS provides a substantial cost saving with respect to SiC MOSFETs. On the performance side, the smaller SiC MOSFET of the mcHyS leads to slightly higher losses than the tHyS. Nonetheless, the improvement with respect to the IGBT solution is substantial, almost halving the losses over the yearly profile.

LIMITATION OF THE MCHYS

To summarize, the analysis presented in this section suggests that HySs are a valid cost-performance trade-off alternative to the common Si IGBT and SiC MOSFETs when applied in industrial power electronics applications. HySs can offer various degrees of loss saving and power density increase versus single technology IGBT-based 2L-VSC. However, HySs, due to the fact that they are assembled through the paralleling of two active devices, presents also some drawbacks with respect to single technology switches. The main drawback consists in the fact that HyS requires two independent gate driving circuit per single switch, adding an extra cost versus single technology switches. However, in high power application, the costs of the extra gate driver is generally much lower than the power modules. An additional factor to consider for the mcHyS implementation is the commutation inductance between its elements. As shown in Section 4.4, a large inductance between the HyS components can be detrimental to its performances. In this context, it is of fundamental importance to consider a minimum distance between IGBTs and MOSFETs in PCB layout when discrete devices are used for the mcHyS realization. This issue could be solved packaging the Si-IGBT and SiC-MOSFET together in a custom power module, however, to the knowledge of the authors, such module is not a commercial product yet.

4.7. CONCLUSION

In this chapter, the conduction and switching performances of the mcHyS are experimentally characterized and compared with the one of SiC MOSFETs, Si IGBTs, and the tHyS concept. The experimental results proved that the analytical equations given for modeling HySs provided excellent accuracy and showed how HySs position themselves between the pure Si IGBTs and SiC MOSFETs in terms of performances and costs. Additionally, a 10kW 2L-VSC prototype has been assembled to test and benchmarked the efficiency of a mcHyS-based VSC versus single technology VSC. Furthermore, it was shown that the two additional switching events of the mcHyS happen in soft switching as long as the commutation inductance is minimized. Afterward, the switches have been compared in terms of chip area and thus in costs, upholding that the mcHyS provides a cheaper alternative to SiC MOSFETs and the commonly studied in literature tHyS. HySs have also been shown to be valuable candidates for 2L-VSC switches applied in battery energy storage systems deployed for grid ancillary service.

To conclude, in this chapter the mcHyS concept has been modelled and demonstrated.

Furthermore, it has been shown that such HyS concept can provide a valuable cost-efficiency trade off with respect to traditional Si IGBTs and SiC MOSFETs.

5

BATTERY ENERGY STORAGE SYSTEM AS POWER REDISTRIBUTOR

This chapter discusses the application of Battery Energy Storage Systems (BESSs) as power redistributors in three-phase distribution grids as an add-on functionality to the typical BESS applications, such as congestion management and energy arbitrage. Enabling the provision of these ancillary services in a single hardware device is not yet performed in practice but may constitute an emerging business opportunity to increase the BESS revenues. The unbalanced operation of the BESS voltage source converter (VSC) leads to the circulation of low-frequency current harmonics in the DC-link through the capacitors and battery cells. Therefore, it is particularly interesting whether relatively large 50Hz and 100Hz currents can safely circulate within these components. Analytical modeling and design guidelines for the DC-link of a three-leg four-wire two-level VSC operating under unbalanced loads are detailed. Furthermore, a low power VSC prototype is used to demonstrate the working principle of the BESS, providing power unbalance redistribution and the symmetric power exchange. Additionally, the ICR18650-26F Lithium-ion cells are cycled to reach end-of-life with different current profiles and C-ratings. The analysis shows that charging with a 100Hz ripple superimposed to the DC current leads to a 10% increment in degradation.

This chapter is based on:

- M. Stecca, T.B. Soeiro, A.K. Iyer P. Bauer, P. Palensky, "Battery Storage System as Power Unbalance Redistributor in Distribution Grids Based on Three Legs Four Wire Voltage Source Converter", IEEE Journal of Emerging and Selected Topics in Power Electronics, 2022, vol. 10, 7601-7614.

5.1. INTRODUCTION

Low Voltage (LV) distribution grids are characterized by the connection of single-phase loads, which can lead to unbalanced power consumption between the three phases during the real-time operation [138, 195], and this phenomenon can negatively affect the distribution grid. A power redistributor can be used to balance the phase powers and ensure an efficient and reliable grid operation [54]. Possible technical solutions to mitigate this problem are the implementation of shunt active power filters and STATCOM, which typically employ a grid-connected Voltage Source Converter (VSC) that can reroute the unbalanced active power from one phase to another[71, 126]. Grid connected VSCs of similar topologies to active filters and STATCOMs are also present in high power, e.g., >100kW, grid-connected Battery Energy Storage Systems (BESSs) [209, 215]. Typical BESS applications, such as voltage and frequency control, and congestion managements, require the exchange of symmetric three phase active or reactive power [148, 184], the power redistributor functionality, instead, targets the voltage and current waveforms symmetry between the three phases, by providing asymmetric power exchange. The power redistribution service, which does not strictly require large energy storage capabilities to function [54], and the various ancillary services which BESS can provide, are typically performed separately by different power units. Therefore, enabling the incorporation of adds-on ancillary services can maximize the utilization of the power unit. In such an interesting application, particular attention may need to be paid to the effects of the add-on functionality on the power unit's components. Such service cannot be achieved by the typical BESS circuitry which was optimized to the exchange of symmetric power, but it requires some adjustments. The DC-Link of VSC deployed as power redistributors requires particular design attention [54], since the unbalanced three-phase power operation of the VSC leads to low-frequency current harmonics in the DC-link, namely the 50Hz and 100Hz components, for a grid with frequency of 50Hz, which do not appear under balanced conditions.

This chapter thoroughly investigates the design and application of a BESS' 3L-4W VSC for power unbalance redistribution in distribution grids, when this functionality is provided as an add-on service to grid-connected BESS already deployed in the grid. The remainder of the chapter is organized as follows. Section II describes the application of a BESS as grid power redistributor and its control strategy. Section III derives the mathematical models for the DC-link current and voltage under different unbalance conditions, furthermore it provides an example on how to design the DC-link for a 100 kW BESS providing power redistribution. Section IV investigates the 100Hz AC ripple impacts on the degradation of Lithium-Ion battery cells. Section V provides the experimental results validating the DC-link mathematical models and showing the working principle of the unbalance compensation. Finally, Section VI concludes the work.

5.2. BATTERY STORAGE SYSTEM AS GRID POWER BALANCER

Power unbalance operation occurs when the phases currents of a three-phase AC network differ in terms of amplitude or they are not in perfect 120 degrees phase-shift between them. To better analyze the current unbalanced behavior of three-phase systems, the phase quantities can be transformed into their symmetrical components utilizing the Fortescue transformation [67]. In this way, a given three-phase network, whose phase's currents are expressed as I_a, I_b, and I_c, can be transformed into symmetrical components, I_+, I_- and I_0,

being, respectively, the positive, negative and zero-sequence components, as[77]:

$$\begin{bmatrix} I_0 \\ I_+ \\ I_- \end{bmatrix} = \frac{1}{3} \begin{bmatrix} 1 & 1 & 1 \\ 1 & a & a^2 \\ 1 & a^2 & a \end{bmatrix} \begin{bmatrix} I_a \\ I_b \\ I_c \end{bmatrix} \tag{5.1}$$

where $a = e^{j\frac{2\pi}{3}}$.

These symmetrical components are three sets of balanced phasors, the positive, negative, and zero sequence systems. The positive sequence has its phasors with same amplitude and shifted by 120 degrees rotating at the same frequency of the original system and in the same direction; the negative sequence phasors also have same amplitude and are shifted by 120 degrees rotating at the same frequency of the original system, but in the opposite direction. Finally, the zero sequence system is composed of three phasors of same amplitude and of same phase rotating at the same frequency of the original system and in the same direction. More details regarding the symmetrical components analysis of polyphase power systems can be found in [77]. The positive-sequence current represents the power flow from the source to load, responsible for the active and reactive power transfer. The negative-sequence current is caused by the ripple power, which oscillates at the double the grid frequency. The zero-sequence current is the summation of the individual line currents. Thus the unbalance factor of a three-phase network, as specified by the IEC[97], can be defined as the ratio between the negative and zero sequence currents and positive sequence currents:

$$\mathrm{Un}_- = \frac{I_-}{I_+} \cdot 100[\%] \tag{5.2}$$

$$\mathrm{Un}_0 = \frac{I_0}{I_+} \cdot 100[\%] \tag{5.3}$$

Following (5.1)-(5.3), the unbalance factors are found to reach considerably high values, up to 90%, when the phase currents strongly differ between them in terms of amplitude or power factors.

In this context, a BESS can act as a power redistributor by helping to balance the three-phase currents seen by the upstream grid or local distribution transformer. A typical layout of a distribution grid is shown in Figure 5.1, where it can be seen that in the low voltage (LV) feeders, households loads are connected between a single-phase terminal and the neutral. Additionally, one has seen the proliferation of residential and industrial PV generation and EV chargers in recent years. Furthermore, a BESS can be connected at the MV/LV substation to utilize the locally produced renewable energy better, boosting its self-consumption and deferring network investments. A BESS connected as shown in Figure 5.1 can also be used as a power redistributor. In fact, in this arrangement, the BESS can monitor the currents through the transformer, and if an unbalance is detected, the BESS could compensate it through its intrinsic three-phase VSC.

5.2.1. THREE-PHASE VSC FOR BESS BASED POWER REDISTRIBUTOR

As previously mentioned, the BESS uses a VSC to interface the battery with the AC grid, and this allows, among other functionalities, the possibility for the BESS to act as a power redistributor. The VSC can be realized using various topologies, each with advantages and limitations. Typical high power BESSs rely on three-phase two- or three-level VSC topologies. A three-phase two-level converter is assembled with three half-bridge legs, i.e., one

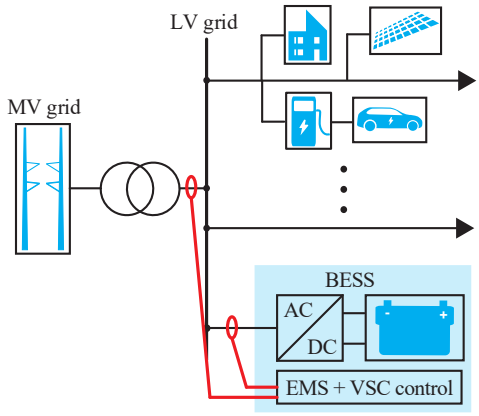

Figure 5.1: Example of a LV distribution grid where unbalanced loads are connected in the LV side and a BESS acts as power redistributor balancing the MV currents.

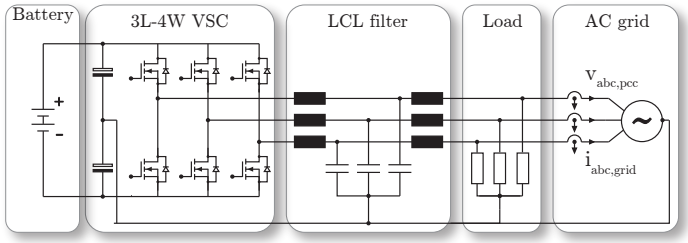

Figure 5.2: Circuit schematic of a BESS based on a 3L-4W VSC while supplying three phase loads and interfacing with the distribution AC grid and.

per AC phase. Instead, three-level topologies use more complex bridge leg configurations, such as the neutral-point-clamped and T-type converters [215]. This chapter focuses on the two-level topology due to its robustness and widespread usage in commercial high-power BESS.

Unbalance grid currents lead to negative and zero sequence currents. Negative sequence currents flow uniquely in between the three-phase terminals, as the positive sequence does; however, zero sequence currents have a return path through the neutral conductor. Therefore, the application of BESS as power redistribution requires a VSC topology that can control zero sequence currents. So the VSC must have access to the neutral conductor of the distribution grid. The three half-bridge legs of the VSC are connected one per phase; therefore, the neutral conductor can be connected to the mid-point of the DC-link capacitors, as shown in Figure 5.2. The capacitor mid-point voltage indirectly controls the neutral current in the system since the zero-sequence current flows through the two split capacitors. The circuit schematic of this three-phase legs four-wires (3L-4W) VSC is depicted in Figure 5.2.

5.2.2. BESS 3L-4W VSC CONTROL FOR POWER REDISTRIBUTOR

To achieve the power redistribution functionality, the VSC needs to control independently the active, reactive and zero sequence power. The control scheme of a BESS's VSC operating

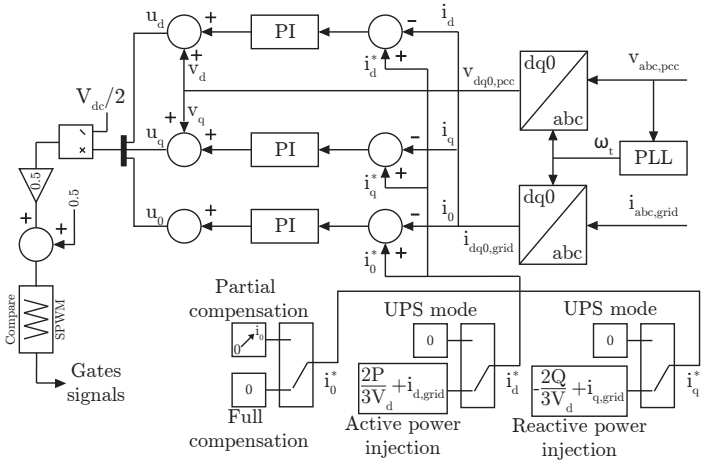

Figure 5.3: Current control and grid synchronization loop of a BESS's VSC operating as power redistributor.

as power redistributor is conceptually similar to standard grid connected VSC control, and it is shown in Figure 5.3. A phase-locked-loop circuit is used to synchronize the VSC with the grid, then the converter is controlled in the $dq0$ frame, allowing the independent control of active, reactive and zero sequence power. In fact, the current references, i_d^*, i_q^*, and i_0^*, can be set to match the unbalance calculated from the measured grid currents, following (5.1). Additionally, the current references i_d^* and i_q^* can be increased or decreased so to inject or absorb active and reactive power from the grid. In this way, the converter currents can be efficiently controlled to supply unbalanced loads and therefore balance the grid currents.

5.3. DC-LINK DESIGN FOR POWER UNBALANCE COMPENSATION

The DC-link is the critical part of a VSC for enabling the power redistribution capability in a BESS. In this context, it is fundamental to analyze how the provision of this functionality impacts its design. The general methodology used to design the DC-link is described in Appendix A.

5.3.1. DC-LINK CAPACITANCE SIZING

The high frequency harmonics and the energy storage requirements, described in Appendix A respectively with (A.30) and (A.29), which are typical to the symmetric operation are still applicable during unbalance compensation. However, when a VSC supplies an unbalance load, additional components, as the negative and zero sequence currents, flow through the DC-link as well.

The negative sequence unbalance generates a second harmonic component in the DC-link, of with a frequency double the one of the grid, i.e. 100Hz for a grid frequency of 50Hz. This creates a low-frequency ripple in the voltage [174] which dominates the high-frequency one, and so the DC voltage ripple takes the following expression [174]:

$$\Delta V_{\mathrm{dc,r}} = \frac{3m\hat{I}_{-}}{8\pi f_{\mathrm{g}} C_{\mathrm{dc}}}, \tag{5.4}$$

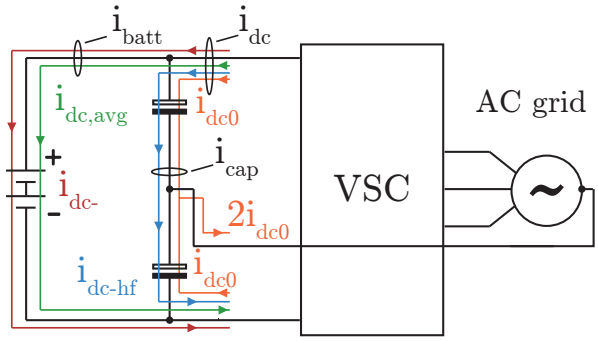

Figure 5.4: Current paths of the various DC-link current harmonic components in a BESS' VSC operating as power redistributor.

where $\hat{I}_-$ is the peak value of the negative sequence current and ω_g is the grid nominal frequency of 50Hz.

The neutral current I_n, instead, does not create a voltage ripple in the full DC-link, but it causes the split capacitors mid point to oscillates. I_n is three times the zero-sequence current, since each phase zero sequence currents gets summed in the neutral conductor. Therefore, given the neutral current flowing through the capacitors, the mid point voltage ripple, $\Delta V_{dc,0}$ can be calculated solving the capacitor differential equation and expressed as:

$$\Delta V_{dc,0} = \frac{3I_0}{4\pi f_g C_{dc}} \tag{5.5}$$

The oscillation of the mid point has to be limited to ensure that the capacitors do not see negative voltage, otherwise they get reverse polarized which causes the failure of electrolytic capacitors.

All in all, the DC-link capacitors have to be sized to fulfill several requirements, namely, the energy buffer, (A.29), limiting the DC-link voltage ripple to ensure a safe DC-AC energy conversion, (A.30)-(5.4), and limiting the mid point oscillation to avoid the reverse polarization of the capacitors, (5.5). Each of these equations defines a minimum capacitance which satisfy the requirement, and therefore, the DC-link capacitance must be chosen as the largest between them.

5.3.2. DC-LINK CURRENT CALCULATION

The DC-link current of a VSC is inevitably related to the nature of its AC currents. In Appendix A the methodology for deriving the DC-link current is explained. When a VSC processes unbalanced power, the negative and zero sequence terms of (A.32) are non zero and need to included in the expression of the sector currents, described in (A.33). Therefore, the total DC-link rms current can be found as:

$$I_{dc}^2 = \frac{\sqrt{3}}{4\pi} \cdot \left[\left(1 + 4\cos^2\phi_1\right)\hat{I}_+^2 m + 3m\hat{I}_-^2 + \left(\sqrt{3}\pi - 2m\right)3\hat{I}_0^2 - 2m\hat{I}_-\hat{I}_0\cos\left(\phi_- + \phi_0\right) \right] \tag{5.6}$$

where m stands for the modulation index, which is function of the peak single-phase AC voltage, $\hat{V}_{ac}$, and the total DC-link voltage, V_{dc}, and it is defined as $m = 2 \cdot \hat{V}_{ac}/V_{dc}$.

Table 5.1: Parameters implemented in the circuit simulator software PLECS used for the verification of the derived analytical equations (5.6)-(5.14) derived in Appendix A.1.

Parameter	V_{dc} [V]	$V_{ac,ph}$ [V]	f_{sw} [kHz]	L_f [mH]	C_{dc} [μF]
Value	400	110	36	1.45	492

Equation (5.6) predicts the full DC-link *rms* current, considering all its harmonic components: the high-frequency, the DC, the 50Hz, and the 100Hz sequence components. This equation is therefore the starting point for the estimation of the current flowing through the capacitors and the battery. Figure 5.4 shows the current paths of the various DC-link current harmonic components in a BESS' VSC operating as power redistributor. As possible to see, the DC and the 100Hz component flow through the battery cells, while the zero sequence and the 50Hz component through the capacitors. also, it is important to note that the zero sequence component, I_{dc0}, flows in equal value from the positive and the negative DC-link rail, and then goes back to the grid neutral conductor through the capacitors' mid point.

The average value of the DC-link current defines the active power flowing through the converter, and therefore it is not influenced by the unbalanced operation. Therefore, the average DC-link current for one fundamental period is given as:

$$I_{dc,avg} = \frac{3m\hat{I}_+}{4}\cos\phi_+. \tag{5.7}$$

The 100Hz component, in a 3L-4W VSC, is shared between the DC-link capacitors and the battery cells. However, in contrast with the battery cells, the capacitor bank has a significantly higher impedance at low frequency. Therefore, it can be assumed that the low-frequency components flow entirely through the battery cells and not through the capacitors unless a bulky DC LC filter filters these out. Due to the necessary low cut-off frequency, it would require very large component values and, therefore, it is impractical. As presented in [174], the *rms* value of the negative sequence current in the DC-link can be determined:

$$I_{dc-} = \frac{3m}{4\sqrt{2}}\hat{I}_-. \tag{5.8}$$

The zero-sequence currents of the three AC phases are summed up in the DC-link. In the symmetric and conventional SPWM, this flows evenly in the positive and negative rail of the DC-link; therefore, the *rms* value of the zero sequence component in the positive rail of the DC-link is half the three times the phase zero sequence current, since it is equally split between the positive and negative DC-link rails, and can be expressed as:

$$I_{dc0} = \frac{3I_0}{2} = \frac{3\hat{I}_0}{2\sqrt{2}}. \tag{5.9}$$

Having quantified the various components of the DC-link *rms* current, it is possible to evaluate the current flowing through the capacitors, I_{cap}, which is composed by the 50Hz and the high-frequency component. I_{cap} can be derived subtracting (5.7) and (5.8) from (5.6).

$$I_{cap} = \sqrt{I_{dc}^2 - I_{dc,avg}^2 - I_{dc-}^2}, \tag{5.10}$$

$$I_{\text{cap}} = \sqrt{\frac{\sqrt{3}}{4\pi} \cdot \left[\left(1 + \left(4 - \frac{9\pi}{4\sqrt{3}} m\right) \cos^2 \phi_1\right) \hat{I}_+^2 m + 3m\hat{I}_-^2 \left(1 - \frac{\sqrt{3}\pi m}{8}\right) + \right.} \\ \overline{\left. \left(\sqrt{3}\pi - 2m\right) 3\hat{I}_0^2 - 2m\hat{I}_- \hat{I}_0 \cos\left(\phi_- + \phi_0\right) \right]}. \tag{5.11}$$

The 50Hz component flows through the capacitors because their mid point provides the connection to the neutral conductor. The high frequency component, instead, flows through them because the electrolytic capacitors offer a lower impedance path for the high-frequency currents than the battery. From (5.11), the *rms* value of high frequency DC-link current can be calculated by nullifying the negative and zero sequence component as:

$$I_{\text{cap,hf}} = \sqrt{\frac{\sqrt{3}}{4\pi} \cdot \left[\left(1 + \left(4 - \frac{9\pi}{4\sqrt{3}} m\right) \cos^2 \phi_1\right) \hat{I}_+^2 m \right.} \tag{5.12}$$

The DC and 100Hz components flow through the battery cells, therefore the *rms* current flowing through the battery, I_{batt}, can be calculated as:

$$I_{\text{batt}} = \sqrt{I_{\text{dc,avg}}^2 + I_{\text{dc-}}^2}, \tag{5.13}$$

$$I_{\text{batt}} = \frac{3m}{2\sqrt{2}} \sqrt{\hat{I}_+^2 \cdot \cos^2 \phi_+ + \frac{\hat{I}_-^2}{4}}. \tag{5.14}$$

To verify the accuracy of the derived equations, the circuit simulation software PLECS is used. A simulation model of a 3L-4W VSC has been built so to calculate the *rms* current flowing through the DC-link and its components. The parameters implemented in the circuit simulation software PLECS are listed in Table 5.1. The simulations are run with a variable step solver, DOPRI (non-stiff), with a maximum step size and relative tolerance of 1μs. Several values of unbalance are analysed. In fact, the loading of one phase is varied from 0 to 100% of the loading of the other two phases, which are kept constant at rated power. Figure 5.5 displays the total *rms* current in the DC-link and its various components, following the conditions of Table 5.1. Figure 5.6, instead, plots the *rms* currents flowing through the DC-link split capacitors and the battery cells. In the two figures, both the analytically calculated values through (5.11) and (5.14) and the ones derived from the circuit simulator PLECS are reported. The analytical equations slightly underestimate the current values, and this is because the AC current is not perfectly sinusoidal, as assumed in the derivation of the equations. In fact, in PLECS, the high-frequency ripple has a peak value of 20% of the low-frequency 50Hz component. This ripple level of 20% is compatible with the typical design criteria of L and LCL filter for the grid connection of VSC [110, 217]. All in all, it can be noted that the analytical expressions provide excellent accuracy to the circuit simulator; hence such equations can be used to design the DC-link components of a 3L-4W VSC.

5.3.3. EXAMPLE DESIGN OF AN 100 KW 3L-4W VSC

The conventional approach for achieving the power redistribution functionality consists on using a separate compensator for processing the unbalanced power. This solution requires an additional converter which is inevitably more expensive than the integrated solution proposed in this chapter. Figure 5.7 shows that integrating the power redistributor functionality in a single BESS unit is advantageous in terms of DC-link overall ratings, such

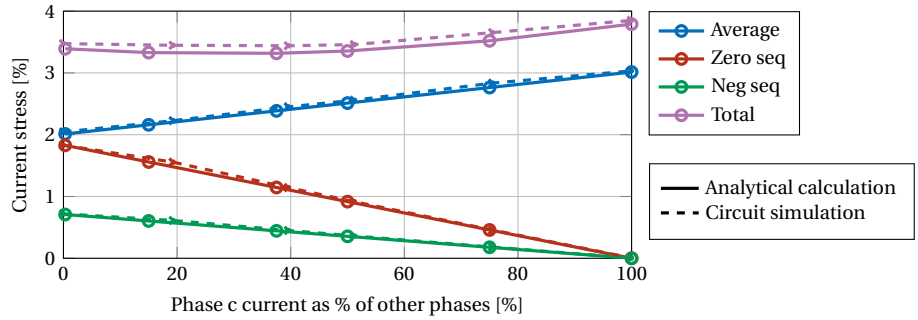

Figure 5.5: Total *rms* current in the DC-link and its various components, when I_a and I_b are equal to 3.7A and I_c is varied from 0 to 3.7A. Both the analytically calculated values through (5.6)-(5.9), and the ones derived from the circuit simulator PLECS are reported.

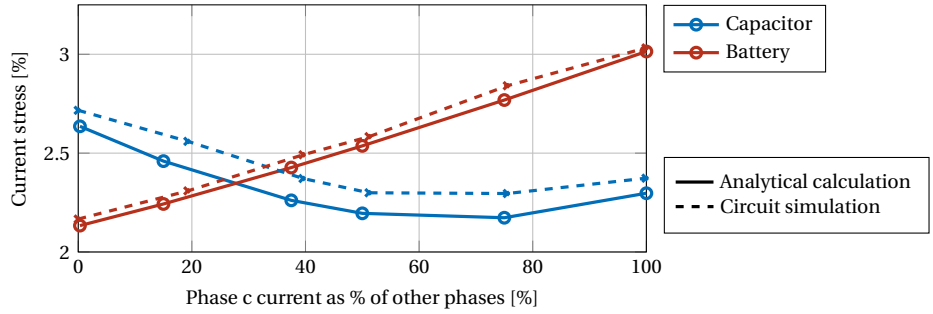

Figure 5.6: *Rms* currents flowing through the DC-link split capacitors and the battery cells, when I_a and I_b are equal to 3.7A and I_c is varied from 0 to 3.7A. Both the analytically calculated values through (5.11) and (5.14), and the ones derived from the circuit simulator PLECS are reported.

as current stress and capacitance requirement, when compared to two separate devices, a BESS operating symmetric active power and an external compensator to manage the unbalance. Figure 5.7 plots the DC-link current stress and required capacitance on the external compensators and on the BESS providing symmetric power as percentage of the values of the integrated solution. In terms of current stress, it is seen in Figure 5.7(a) that splitting the unbalance management and symmetric power exchange between two units leads to lower current stress in the individual units, but when aggregated it is always higher than the integrated solution. Additionally, Figure 5.7(b) shows that an external compensator would require the same capacitance of the integrated solution nullifying the advantage of splitting the functionalities between two units. Moreover, an external compensator would require additional, power semiconductor half-bridge modules, LCL filters for the interconnection to the grid, control systems, measurements sensors, protection systems, and finally the mechanical switches and structure. However, in an integrated solution such as the one proposed here, all these components are already present since they are necessary for interfacing the battery storage system to the AC grid. Therefore these can be leveraged as power redistributor, resulting in a much lower overall component count and costs.

The design process of a two-level 3L-4W VSC consists of several steps. At first, the power

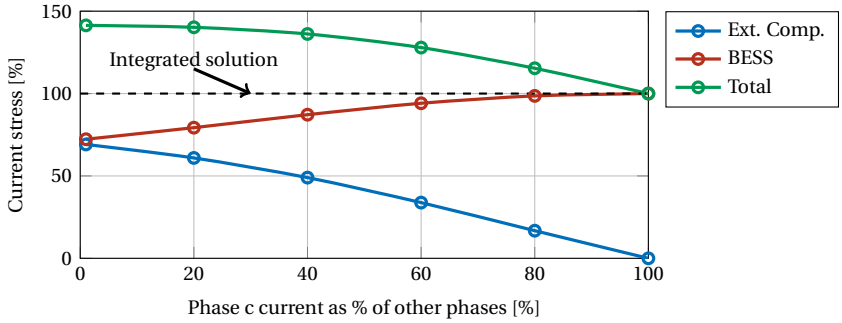

(a)

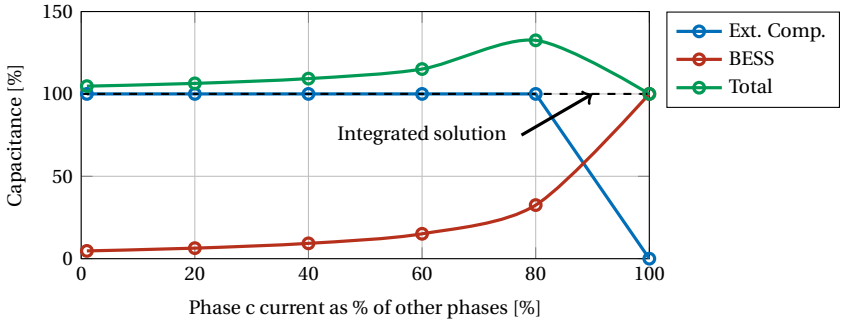

(b)

Figure 5.7: DC-link current stress (a) and required capacitance (b) on the external compensators and on the BESS providing symmetric power as percentage of the values of the integrated solution while varying the unbalance processed by the system. The BESS' values are calculated for the active power processed by an integrated solution at that unbalance point.

and voltage levels of the converter have to be set. A Low Voltage (LV) DC-link is taken into account, V_{dc} =750-950V, coherently with the specifications of commercial battery racks [200, 125]. The AC voltage is set to 400V line-to-line, a standard rating found in the European's low voltage distribution grids. Given these specifications, it is possible to select the semiconductors and design the output LCL filter properly [110, 217, 215]. Therefore, the design of the DC-link capacitor bank is of particular interest to this chapter. In fact, The DC-link capacitor bank is also the main component whose size is affected by the unbalance redistribution. Therefore, the system size increment is related to the increase of the required capacitance. The other components, e.g., the semiconductor modules, the cooling systems, and the LCL output filters, do not see size increase when enabling the power redistributor functionality in a 3L-4W VSC.

As already mentioned in this Section, the capacitors have to be rated for a certain capacitance and current to respect the component's thermal limits. Such design requirements are listed in Table 5.2, for certain operating conditions. Table 5.2, reports the DC-link currents and capacitance values required in a 100 kW VSC, operating under balanced power conditions, Case A, and for different power unbalanced conditions, Cases B to E. In these case studies, I_a is fixed to the nominal value and I_b and I_c are intentionally varied. Cases B and

Table 5.2: DC-link capacitors currents and capacitance requirements for a 100kW VSC, under balanced and unbalanced conditions, derived through the method described in Section IV, where I_a is fixed to the nominal value and I_b and I_c varied.

		Operating condition				
Parameter and relevant equation		Case A I_b=I_a I_c=I_a	Case B I_b=$I_s/2$ I_c=$I_s/2$	Case C I_b=0 I_c=0	Case D I_b=I_a I_c=0	Case E I_b=I_a I_c=$I_s/2$
I_+ [A]	(5.1)	144.34	96.23	48.11	120.28	96.23
I_{cap} [A]	(5.11)	83.70	68.93	85.62	80.64	98.31
I_{dc0} [A]	(5.9)	0	36.08	72.17	36.08	72.17
$I_{cap,hf}$ [A]	(5.12)	83.70	58.73	46.06	72.12	66.76
$C_{dc,e}$ [mF]	(A.29)	0.794	0.794	0.794	0.794	0.794
C_{dchf} [mF]	(A.31)	0.306	0.204	0.102	0.255	0.204
C_{dc-} [mF]	(5.4)	0	2.063	4.125	2.063	4.125
C_{dc0} [mF]	(5.5)	0	1.911	3.822	1.911	3.882

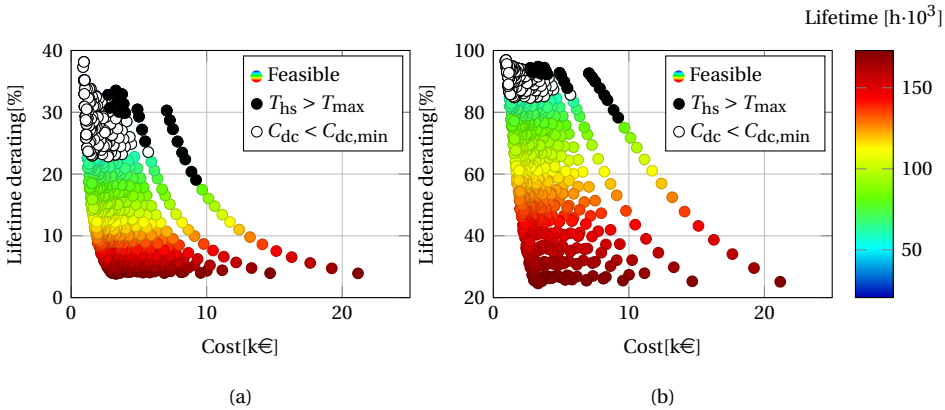

Figure 5.8: Costs and expected operating hours of the DC-link capacitors designs for a 100kW VSC operating under balanced conditions. The y-axis shows the lifetime derating of such designs when operating in unbalanced condition: (a) Case C, and (b) Case E of Table 5.2.

C see phase *b* and *c* operating at equal value at 50% I_n and 0% I_n respectively. Case D and E consider two phases at nominal current and one phase at 50%I_n and 0% I_n respectively. The highest capacitance requirement is found in Case C and E, together with the highest 50Hz current harmonics in the capacitor. In comparison, the highest total rms current in the capacitors is found in Case E, which is, therefore, the most demanding case for the design of the DC-link capacitors.

For this study, the commercially available capacitors of the 500V_{dc} class from Cornell Dubilier [48] have been considered. Given the maximum value of I_{cap} and the current capability of the single capacitors, the number of parallel capacitor strings, which consists of two series capacitors, are found. In this way, several DC-link designs are derived according to the components' characteristics. The solutions that do not satisfy the minimum capacitance constraints or that show a maximum hot-spot temperature, T_{hs}, higher than 95°C, the limit set in the data-sheet, T_{max}, are discarded. Following this procedure, in Figure 5.8, the

cost of several DC-link capacitors designs which meet the requirements for a 100kW VSC operating under balanced load is plotted versus their expected lifetime. The commercial cost figures are derived from a component distributor [152], while the capacitor lifetime is derived according to the methodology suggested by the manufacturer [49]. The capacitors' operating voltage and the hot-spot temperature are the main degradation drivers. [252, 251]. The manufacturers of the considered capacitors gives the capacitor lifetime model as [49]:

$$L_c = L_b \cdot \left(4.3 - 3.3\frac{V_{dc}}{V_r}\right) \cdot 2^{\frac{T_m - T_c}{10}} \tag{5.15}$$

where L_b is the rated lifetime, V_r is rated voltage, T_m is the maximum rated core temperature, and T_c the operating core temperature [49]. T_m and L_b are related to the capacitor packaging and manufacturing, as specified by the manufacturer [49]. The operating hot-spot temperature, T_c, is estimated based on the capacitor equivalent series resistance, ESR, the thermal resistance Z_{th}, both from data-sheet, and on the current flowing through the capacitor [49]:

$$T_c = T_a + 1.5 \cdot Z_{th} \cdot (I_{cap}^2 \cdot \mathrm{ESR} + I_{leak}(V_{op}) \cdot V_{op}), \tag{5.16}$$

where I_{leak} is the capacitor leakage current as function of V_{dc}, given by the datasheet and V_{dc} the operating voltage [48]. The manufacturer recommends the addition of the coefficient 1.5, so that the heat rise due to current ripple weights more than the ambient temperature T_a effect [49].

Furthermore, in Figure 5.8 (a) and (b), the y-axis shows the lifetime derating of such designs when operating in two unbalanced conditions, which are Case C and E of Table 5.2, respectively. The lifetime derating indicates the capacitor lifetime if operating in unbalanced conditions, $L_{c,ub}$, as percentage of their lifetime if operating under balanced conditions, $L_{c,b}$, and it is calculated as:

$$\mathrm{Derating} = \frac{L_{c,ub}}{L_{c,b}} \cdot 100[\%] \tag{5.17}$$

In Figure 5.8, the designs in black and white are the ones that are feasible for the operation under balanced load, but not for unbalanced loads, due to a too low capacitance value or a thermal reason, respectively. Nonetheless, the designs in the top left of the figures are the ones that typically offer low safety margins, especially in terms of thermal performances. Therefore, for a marginal cost increase, the designs at the bottom left of the graphs significantly improve operating hours during both balanced and unbalanced operations. Hence these designs should be prioritized for the DC-link of the grid-connected VSC.

5.4. 100HZ RIPPLE BATTERY TESTING

As discussed in Section IV, due to the high impedance, the DC-link capacitors cannot filter the 100Hz component of the DC-link current, which then flows through the battery. In this regard, it is important to investigate whether the 100Hz component impacts the battery degradation. Researches available in the literature [37, 6, 39, 16, 245, 22] have investigated the electrochemical phenomena that drive the cells' impedance variation with frequency, and the effect of AC current ripple on Lithium-ion batteries charging. However, the focus on these studies is typically found on AC frequencies at which the battery shows the minimum impedance to optimize the charging time and power efficiency. Several waveform

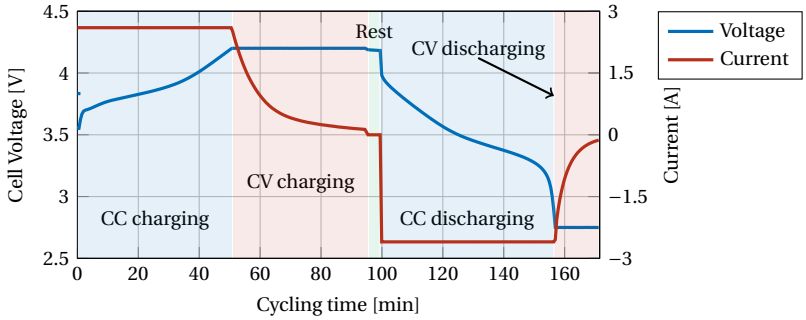

Figure 5.9: Measured cycling parameters of the ICR18650-26F battery cell when cycled with the CC-CV method at 1-C. The cell is cycled with the Arbin Laboratory Battery Testing LBT22043 of Figure B.6 and the cell voltage and current are measured with a 30-second sampling time.

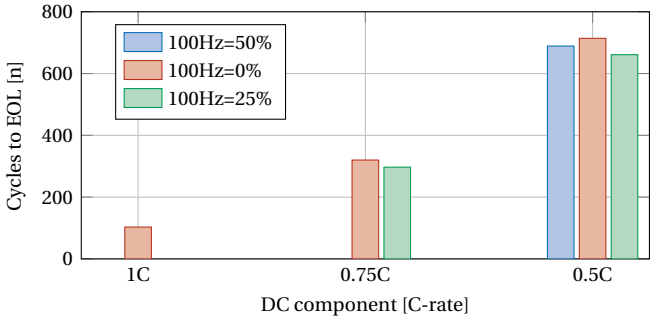

Figure 5.10: Charge-discharge cycles performed by the ICR18650-26F Lithium-ion cell to reach EoL under different charging and discharging conditions. Note that for all cases the superimposed instant peak current, i.e. DC + AC components, circulating through the battery cells is limited to 1 C-rating.

shapes have been investigated, such as sinusoidal, triangular, and square, and some of the reviewed literature claim positive results when superimposing an AC ripple at the minimum impedance frequency [245]. However, other studies challenge these results, showing contrasting facts [16].

In this context, the effect of the AC current ripple in Lithium-ion cells is investigated. The test setup used for the cycling of battery cells is described in Appendix B.3. The tested cells are the ICR18650-26F from Samsung SDI, based on the NMC cathode technology, which is well suitable for stationary application [214]. Their nominal voltage is 3.7V, and they have a rated capacity of 2600 mAh. These low-voltage cells are the building blocks for high-capacity battery packs. Several lithium-ion cells of this kind can be stacked up together in series and parallel strings to assemble battery packs with higher voltage and capacity ratings.

Various ICR18650-26F cells have been cycled to evaluate the impact of the 100Hz ripple. The manufacturer recommended method for charging and discharging such cells consists of the constant current and constant voltage (CC-CV) method [203]. The CC-CV method is the industry standard for the charging of electrochemical batteries [137, 136]. This method consists in two parts. The first part, constant current, foresees the charging of the battery

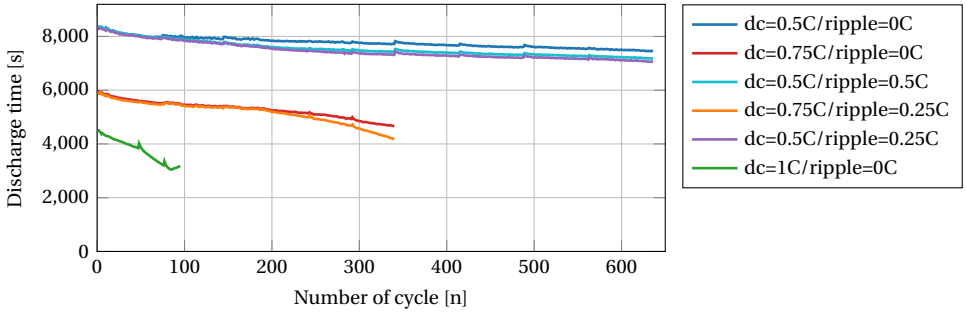

Figure 5.11: Discharge time during the cycling life of the ICR18650-26F battery cell when cycled in different conditions. It can bee seen that higher dc C-rate leads to faster discharging time, as well as the superimposition of the 100Hz AC ripple.

with constant current, I_{cc} until the cell voltage reaches a threshold, which is the maximum allowed cell voltage, V_{max}. Once this voltage is reached, the current is gradually reduced until it reaches a cut-off threshold. The measured current and voltage waveform of the CC-CV method of a charge and discharge cycle at 1-C of a ICR18650-26F cell is shown in Figure 5.9. The cell is cycled with the Arbin Laboratory Battery Testing LBT22043 of Figure B.6 and the cell voltage and current are measured with a 30-second sampling time. Note that the plotted CC-CV profile of Figure 5.9 is obtained from a new cell which has not been cycled before. As possible to see in Figure 5.9, the manufacturer recommends a cell charging voltage of 4.2V and a discharge cut-off voltage of 2.75V; the maximum charging current allowed (1-C) is 2.6 A [203]. The cells under test are cycled with 100% depth of discharge (DoD), following the manufacturer's recommended maximum and cut-off voltages to reach 20% capacity fading, the threshold for the battery End-of-Life (EoL).

Three battery cells are cycled with CC-CV method, with different C-rates of 0.5, 0.75, and 1. The cycling method of the other cells, instead, differs during the CC region. Two cells, in fact, are charged and discharged with a DC C-rate of 0.5 with a superimposed AC sinusoidal current ripple of 100Hz with a peak amplitude of 25% and 50% the rated charging current. Lastly, one battery cell is cycled with a DC C-rate of 0.75 with a superimposed 100Hz ripple with a peak amplitude of 25% the rated charging current of 1C. The combination between DC current and AC ripple is set not to exceed the maximum allowed charging and discharging current, which is 1C. Note that during the tests of the cells which are cycled with superimposed AC ripple, when the cell reaches the maximum voltage allowed by the manufacturer during charging, the current is gradually reduced so to keep the cell voltage constant at the maximum value, as shown in Figure 5.9. For the discharging of the cell, when the cut-off voltage is reached, the discharging current is reduced so to keep the cell voltage from not dropping below the minimum allowed value.

The batteries are tested with the Arbin Laboratory Battery Testing LBT22043 [9] which allows precision measurements for simultaneous testing and characterization of up to 16 battery cells. The battery tester can be seen in Figure B.6. The cells are kept at a temperature of 20 °C, which is compatible with the operating temperature of large scale BESS, where the cells are stored in containers equipped with air conditioning which keep the cells at a constant temperature in the range of 20-25 °C [223].

The number of cycles performed to reach EoL of the ICR18650-26F Lithium-ion cell un-

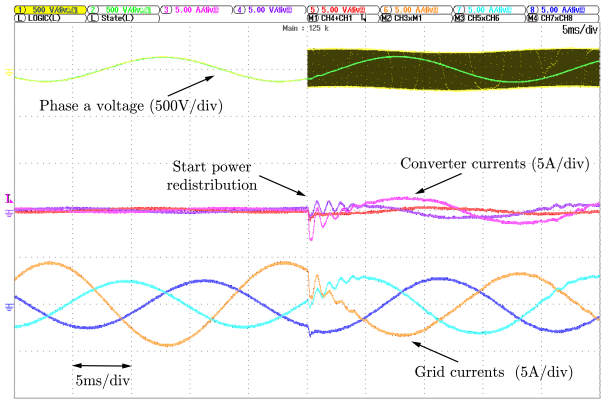

Figure 5.12: Grid and VSC currents when supplying an unbalanced load; when it is turned on, the VSC redistributes the power among the phases, compensating the unbalance in the grid currents. The yellow and green waveforms represent the phase *a* voltage before and after the LCL filter. The other channels represent the grid and converter phase currents, as indicated in this figure.

der different charging conditions is shown in Figure 5.10. The lifetime of the ICR18650-26F cells cycled with the CC-CV method is used as a benchmark versus the charging with the superimposed ripple. It can be noted that there is a strong correlation between the cell's degradation and the DC C-rate; with a high C-rate the cells degrade more and reach EoL sooner, which is compatible with previous literature finds [245]. Furthermore, regarding the influence of the 100Hz ripple, Figure 5.10 shows that the cells which have been cycled with the superimposed ripple shows higher degradation than the ones cycled with pure DC current, with approximately 10% fewer cycles to reach EoL. This phenomenon can be traced back to the additional losses due to the ripple component. The 100Hz ripple, in fact, does not match the minimum impedance frequency of the battery, which is generally found at higher frequencies than 100Hz, e.g. ≥400Hz [245], and therefore leads to additional losses. Additionally, in Figure 5.11 the discharge time of the ICR18650-26F battery cells when cycled in different conditions are shown. These are displayed under the different cycling conditions previously mentioned, where the DC C-rate and the amplitude of the superimposed 100Hz AC ripple are varied. It can bee seen that higher DC C-rate leads to faster discharging time, as well as the superimposition of the 100Hz AC ripple. The discharge times of Figure 5.11 are in agreement with the number of cycle displayed in Figure 5.10, where the cycling pattern that leads to faster degradation also leads to faster discharge time.

The application of BESS as power redistributors, when interfaced to the grid with a 3L-4W VSC, has the drawback of the higher cells degradation during unbalance compensation when a negative sequence arises. To contrast this, an additional half-bridge leg can be added to prevent the 100Hz ripple from flowing to the battery. All in all, from the cycling tests performed, it is clear that keeping the other cycling parameters fixed, the DC C-rate is the dominant factor for cells degradation, and that superimposing the 100 Hz ripple leads to additional cell degradation.

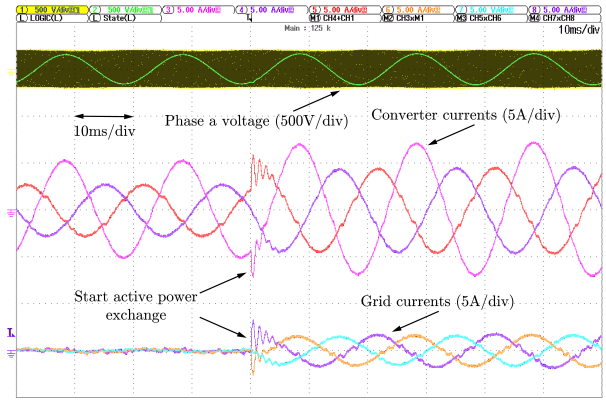

Figure 5.13: VSC supplying an unbalanced loads and injecting active power to the AC source. The yellow and green waveforms represent the phase *a* voltage before and after the LCL filter. The other channels represent the grid and converter phase currents, as indicated in the figure.

5

5.5. EXPERIMENTAL VERIFICATION OF THE POWER REDISTRIBUTOR FUNCTIONALITY

This section shows experimentally the working principle of a BESS acting as a power redistributor. The setup used for the verification is described in Appendix B.4. The setup consists of a 2 kW 3L-4W VSC which interfaces a SM500-CP-90 DC voltage source from Delta Elektronika, representing a battery storage, with the GE15 AC source from Cinergia, which emulates the AC distribution grid. A LCL filter between the VSC and the AC grid is used to attenuate the current harmonics according to the IEEE-519/2014 [101]. The VSC is digitally controlled, with Sinusoidal PWM, through an OP5700 real-time simulator from OPAL-RT Technologies. The experimental testing fixed the DC-link voltage to 400V and the AC phase rms voltage to 110V. Furthermore, unbalanced loads, consisting of two resistors of 60Ω and one resistor of 30Ω and whose unbalance the BESS is tasked to compensate, are connected in parallel with the AC source. The experimental setup, based on the 3L-4W VSC is used to demonstrate the capability of such VSC to operate as power redistributor, Uninterruptible Power Supply (UPS), and exchanging power with the grid.

Figure 5.12 shows the BESS working as a power redistributor, therefore supplying only the unbalance power. When the converter turns on, the grid currents get balanced by the converter operation. The VSC provides the negative and zero sequence powers, leaving the AC grid balanced and supplying only the load active power. On top of the power redistribution functionality, the 3L-4W BESS can also operate as a UPS and exchange active and reactive power with the grid. These functionalities are demonstrated in Figure 5.13. In the left part, the BESS is acting as UPS, fully supplying the load, while in the right side of the figure, together with the UPS operation, the BESS can superimpose the exchange of active power to the AC grid. Hence, it is shown the technical compatibility of the power redistribution functionality with the core grid-connected BESS applications, which require symmetric active and reactive power exchange with the grid.

Figure 5.14 displays the neutral currents of the AC grid and of the VSC, together with the voltages across the two split DC-link capacitors, the green, and orange waveforms. When

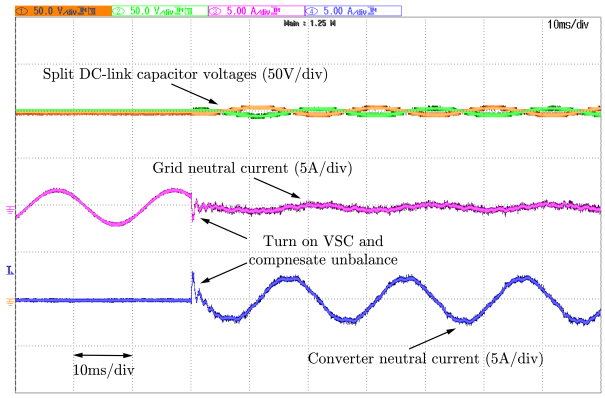

Figure 5.14: VSC and grid neutral current when supplying power unbalanced loads. The green and orange waveforms show the voltage across the two split DC-link capacitors.

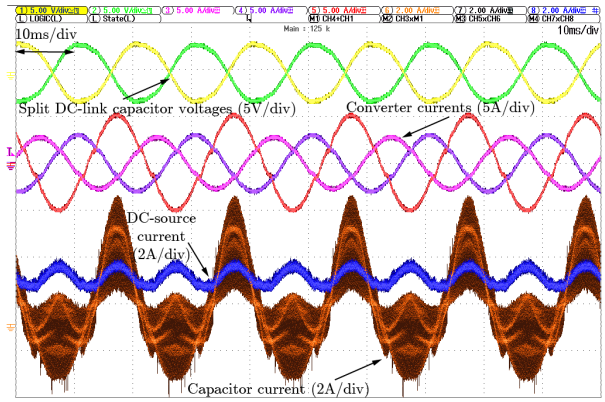

Figure 5.15: AC currents, DC-link split capacitor voltages, and current flowing through the capacitor and the DC-source of a 3L-4W VSC when supplying an unbalanced load.

the VSC starts compensating the power unbalance, it provides the neutral current to the load or the whole zero-sequence current component; therefore, the current in the neutral conductor of the AC grid will be considerably reduced. It can be seen that the split DC-link capacitors are subject to a 50Hz ripple, deriving by the flow of the neutral current. This fact can be seen better in Figure 5.15, where the DC-link split capacitors voltages are displayed with the oscilloscope in AC coupling in so to better show the 50 Hz AC ripple. Furthermore, Figure 5.15 shows the current flowing through the DC-link capacitors, in orange, and the DC-source, in blue, which represents the electrochemical battery storage. Note that, since the 3L-4W VSC of Figure B.8 (a) is assembled with two parallel boards, the current flowing through the DC-link capacitors shown in Figure 5.15 is measured in only one of the two boards capacitors. Therefore, the DC-link capacitors current shown in Figure 5.15 represents half of the total DC-link capacitors current. The experimental verification confirms the theoretical analysis of Section III-B, which predicted that the DC source would absorb the 100 Hz current ripple, while the DC-link capacitor takes the high frequency ripple and

the 50 Hz current which then flows to the neutral conductor.

5.6. CONCLUSIONS

This chapter investigated the application of BESSs as power redistributors in unbalanced distribution grids. The modeling and design guidelines for the DC-link of a two-level 3L-4W VSC operating under unbalanced loads have been detailed. Closed-form expression for the rms currents in the DC-link capacitors and the voltage ripple across them, which can be used for their design, have been derived. The analysis shows that the DC-link capacitors can satisfy the thermal and capacitance requirements under unbalanced power loads if designed adequately for the balanced power operation. Furthermore, a down-scaled VSC prototype is used to demonstrate the working principle of the BESS providing unbalance redistribution. The VSC was able to verify the study, demonstrating that the power redistributor functionality can be added as an optional grid ancillary service to the classic BESS applications. Additionally, several ICR18650-26F Lithium-ion cells have been cycled with an Arbin LBT22043 to reach end-of-life. A 100Hz AC current sinusoidal ripple has been superimposed, and its effect on the cells' lifetime has been compared to the standard CC-CV charging method. The cycling tests show that the AC ripple's superimposition leads to an increase in degradation of 10% with respect to the standard CC-CV method; nonetheless, the main driving for degradation remains the charging and discharging C-rate.

All in all, in this chapter, it was shown that the power redistribution functionality could be successfully implemented in commercially available BESSs as an add-on functionality without significant hardware upgrades and performance deterioration.

6

DISPATCH OF BATTERY ENERGY STORAGE SYSTEMS IN DISTRIBUTION GRIDS

This chapter evaluates how a Battery Energy Storage System (BESS) can participate in energy and ancillary services markets while providing services to a third party, in this case a photovoltaic (PV) assisted electric vehicle fast-charging station (FCS). A mathematical deterministic optimization problem is formulated using mixed-integer linear programming to combine battery storage system operation in the day-ahead and frequency regulation market and the remunerated services offered to the FCS. The technical and economic feasibility of the solution and the applicability of the proposed framework is verified through a case study reflecting an existing PV assisted FCS in the Netherlands and considering the Dutch energy market framework and prices. The study shows that such battery storage system implementation is economically and technically advantageous for the players involved. The battery storage system can stack additional revenues on top of the market revenues. The FCS benefits from a reduced peak power and a 30% tariff reduction, and the system operator would indirectly benefit from the shaved FCS profile. Furthermore, the analysis shows that providing services to the FCS from the battery storage system does not significantly impact its market-related revenues.

This chapter is based on:

- L.Argiolas, M. Stecca, L.M. Ramirez Elizondo, T.B. Soeiro, P. Bauer, "Optimal Battery Energy Storage Dispatch in Energy and Frequency Regulation Markets while Peak Shaving an EV Fast Charging Station", IEEE Open Access Journal of Power and Energy, 2022, vol. 9, pp. 374-385.

6.1. INTRODUCTION

Battery Energy Storage Systems (BESSs) can relieve the distribution networks of peak demand, line congestion, and power quality issues, which are caused by RES generator and electric vehicles (EVs) Fast Charging Stations (FCS) [255]. Furthermore, BESSs can buy and sell energy for profits, leveraging on the intraday price spread or during a week of operation. However, the sole participation in energy products underestimates revenues and the batteries' capabilities. The combination with TSO's ancillary services makes BESS capitalize on higher revenues, e.g., providing primary frequency control to the grid [38, 275, 160]. In this context, the dual participation of BESS in remunerated energy and ancillary services markets has been proven to be profitable in several European countries [117]. Previous literature has investigated the application of BESS in energy and ancillary services markets, both in terms of its technical performance and schedule definition [170, 38, 275, 160, 218]. Additionally, several studies have presented the benefits of deploying BESS in the premises of a FCS, or a RES plant [106, 86, 127]. Nonetheless, the stacking of these two service categories has not been widely investigated due to technical and regulatory issues. Moreover, the lack of an explicit remuneration scheme makes the usage of BESS for supporting the distribution grids do not hold a clear business case. In this regard, it is crucial to assess the feasibility of providing support to a third-party network user, such as a FCS. Stacking such functionality on top of the market-related activities can lead to a reduced BESS availability for market activities, decreasing the revenues from the energy markets.

This chapter evaluates the potential of stacking energy and ancillary services market activities and the provision of services to a third party, such as a FCS owner. In this way, the BESS can simultaneously operate in profitable and regulated markets, and provide technical aid to a PV-FCS, reducing its grid exchange and demand for power and the impact of the FCS on the distribution grid. While the participation of BESSs in the energy and ancillary services market has already been explored in literature and industrial applications, the coordination of these market activities with the provision of remunerated services to a third party is more innovative and worth exploring. Therefore, this study aims to provide a case study for grid-connected BESS, which generate its revenues from regulated market activities and has the possibility of supporting other network users connected nearby. The chapter is structured as follows. Section 6.2 illustrates the optimization model's objective functions, design constraints, and working principle. In Section 6.3 the case study of a BESS integrated with a PV-FCS and the input data related to the Dutch energy markets are presented. In Section 6.4 the outcome of the case studies is illustrated in terms of financial and technical benefits for the involved stakeholders. Section 6.5 provides the concluding remarks.

6.2. BESS OPTIMAL DISPATCHING MODEL

This section illustrates the model of a profit-maximizing BESS operating in different markets. The proposed model considers that the BESS can perform energy arbitrage in the DAM, provide FCR, and offer recompensed services to an FCS or a RES owner with grid power injection and absorption.

The model developed is provided with perfect foresight; therefore, actual market prices are assumed to be known upfront, leading to an estimation of the maximum reachable revenues. This approach was chosen to show the maximum revenue potential, and not to eval-

uate the impact of using non-perfect forecasting methods, as there are many deviations between existing state-of-the-art and commercial forecasting methods. A forecasting method could be implemented for real-time application to provide the input to the model [47], however leading to a higher computation burden. When the market is cleared, a bid may be accepted or rejected, including forecasting of price and quantity bids into the problem, makes the model a stochastic programming problem. Studies have proved that stochastic price-quantity MILP formulation provides a higher cumulative profit under different forecasting techniques than a deterministic one. However, it correspondingly generates a higher risk exposure and higher BESS cycles. Since adjustments are made, the battery tends to place more bids in the DAM. In this context, increased revenue from the energy market must be weighed against the cycling costs and risk exposure for the specific battery [118]. In this work, the considered asset acts as a price-taker. Hence, it does not report effective changes in the market, and the bids in the spot market and the FCR market are both assumed to be entirely accepted.

6.2.1. THE OPTIMIZATION PROBLEM

OBJECTIVE FUNCTION

The objective function, which aims at maximizing the BESS revenues from the DAM and FCR market, is defined as:

$$\underset{P_{\mathrm{d}},P_{\mathrm{c}},P_{\mathrm{fcr}}}{\mathbf{max}_{(\mathbf{t},\mathbf{z})}} DAM[t] + FCR[z] \tag{6.1}$$

$$\begin{aligned} DAM[t] = &\sum_{t}^{t_n} (\lambda - C_{\mathrm{r}}) \cdot P_{\mathrm{d}}[t] \cdot t \\ &- \sum_{t}^{t_n} (\lambda + C_{\mathrm{r}}) \cdot P_{\mathrm{c}}[t] \cdot t \end{aligned} \tag{6.2}$$

$$FCR[z] = \sum_{z}^{z_m} P_{\mathrm{fcr}}[z] \cdot (\lambda_{\mathrm{fcr}} - C_{\mathrm{fcr-r}}) \cdot z. \tag{6.3}$$

where t and z are the time step of the DAM and FCR market respectively, P_{d} and P_{c} are respectively the discharging and charging power bidden in the DAM, and P_{fcr} the power offered for FCR. Equations (6.2) and (6.3) represent the revenues from the volumes of electricity sold on the DAM and the FCR markets multiplied by the respective market price (λ and λ_{fcr}) of that time slot. A ramp cost C_{r} is instituted to guide the decision-making process and reduce the battery cycles. The value of this parameter represents the marginal cost of the system, considered as the O&M cost, which is based on the average of one cycle per day considered as full energy throughput [120]. Such opportunity cost means that at least an 8 €/MWh price spread is needed in the DAM for the BESS to be profitable. The same strategy has been adopted for the maximization of FCR market participation. In here, $C_{\mathrm{fcr-r}}$ represents the ratio of the sum of the cost of the battery system and the Balance of Plants on the max operative hours in a year [120]. The value oscillates around 13-14 €/MW. Utilizing those two ramp costs, the battery number of cycles is constrained and lower than 400 per year to avoid excessive cycling and, therefore, fast degradation, which leads to lower performance over the years [221].

CONSTRAINTS

The system's constraints are divided into battery operative boundaries, market requirements, and external third-party operations.

The first set of constraints, (6.5)-(6.8), includes the modelling of the battery functioning. The power battery boundaries are shown in (6.5) and (6.6), where P_c^* and P_d^* are respectively the battery power charging and discharging limits.

For physical limits, the BESS cannot be charged and discharged simultaneously:

$$P_c[t] \cdot P_d[t] = 0 \tag{6.4}$$

To linearize (6.4), the binary variable δ is introduced. The energy limits expressing the maximum charging and discharging capacity for each time step are so defined in (6.7) and (6.8):

$$0 \leq P_d[t] \leq P_d^* \; \forall t \tag{6.5}$$
$$0 \leq P_c[t] \leq P_c^* \; \forall t \tag{6.6}$$
$$P_d[t] \leq \delta[t] \cdot P_d^* \tag{6.7}$$
$$P_c[t] \leq (1 - \delta[t]) \cdot P_c^* \tag{6.8}$$

The updated State of Charge (SoC) of the battery in each time interval is calculated in (6.9). It ensures the proper battery operation, charging or discharging, according to the limits on the SoC and to the charging and discharging efficiency, η_c and η_d. In (6.9), the State of Charge is indicated with the variable SoC and expressed as percentage of the the total battery energy E^*. The limits for battery SoC are defined in (6.10). Since the model is not linked with specific battery size and technology, the SoC is expressed in per unit and can span between 0 and 1. Nonetheless, these values can be adapted to reflect the physical limitations of specific technology. Equation (6.11) assumes that the battery has an initialized state of charge and ensures that the battery has 50% of capacity at the beginning and at the end of the optimization period. This constraint is not enforced in the daily operation but in the full yearly optimization period.

$$\text{SoC}[t+1] = \text{SoC}[t] + \left(P_c[t] \cdot \eta_c - \frac{P_d[t]}{\eta_d} \right) \cdot \frac{t}{E^*} \tag{6.9}$$
$$0 \leq \text{SoC}[t] \leq 1 \; \forall t \tag{6.10}$$
$$\text{SoC}[t_0] = \text{SoC}[t_n] = 0.5 \tag{6.11}$$

The DAM and FCR markets have different block duration. The DAM operates on an hourly basis, while the FCR on four-hour blocks. Therefore time discretization is based on two levels. Level 1 comprises one-hour time intervals in the day-ahead market $t \in [t_0 ... t_n]$. While level 2 corresponds to the four-hours frequency market $z \in [z_0 ... z_m]$, four hours time interval. The market with the lowest resolution (DAM) is used as the default time step for that purpose. Hence with t_0, we indicate the first hour of operation, and t_n denotes the last hour of the year. An indexed mapping is derived to couple the time step of the model. According to the time increment employed by the market, the device will charge or discharge at the commanded power level over the market time increment. Hence, the BESS would maintain a constant charge or discharge level for the 1-hour time step.

The constraints defining FCR operations are gathered in (6.12)-(6.16).

$$\beta \cdot \gamma_{\text{fcr}}[z] \cdot \leq P_{\text{fcr-u}}[z] \leq \boldsymbol{\gamma}_{\text{fcr}}[z] \cdot P_{\text{d}}^{*} \tag{6.12}$$

$$\beta \cdot \gamma_{\text{fcr}}[z] \cdot \leq P_{\text{fcr-d}}[z] \leq \gamma[z] \cdot P_{\text{c}}^{*} \tag{6.13}$$

$$-\text{SoC}[z] \cdot E^{*} \leq -P_{\text{fcr-u}}[z] \cdot \Gamma \tag{6.14}$$

$$(\text{SoC}[z] - 1) \cdot E^{*} \leq -P_{\text{fcr-d}}[z] \cdot \Gamma \tag{6.15}$$

$$P_{\text{fcr-u}}[z] = P_{\text{fcr-d}}[z] \tag{6.16}$$

According to the European Transmission System Operators (TSOs) associations, the minimum bid of FCR capacity is 1 MW, which is constrained as (6.12) and (6.13) [233, 70]. The binary variable, γ_{fcr}, is introduced to indicate whether the TSO requires FCR regulation. It is assumed that the electricity flowing into the battery does not influence the SoC during the service and once completed, since an internal SoC management algorithm, which focuses on maintaining the SoC to a specified level, is necessary to operate in the FCR market [155, 218, 225]. An 80% factor is used to limit the P_{fcr} and take into account the SoC management power that should be reserved for FCR. This choice is driven by the necessity of withholding a percentage of the BESS power for SoC management to ensure the continuous FCR delivery [155, 218].

For limited energy sources, the TSO requires that the FCR supply must occur as soon as the deviation happens and for at least 15 minutes [233]. Since the frequency perturbations are not predictable, the only way to ensure the respect of this constraint is to operate the BESS with a SoC between 25% or above 75%, to always have energy available for full power delivery for 15 minutes. The equation's reference SoC value is indicated as Γ. This constraint is expressed via (6.14) and (6.15). Furthermore, in many European countries the FCR bid is symmetric. The symmetrical bidding for upward $P_{\text{fcr-u}}$ and downward $P_{\text{fcr-d}}$ regulation capacities are constrained as (6.16).

The possibility to split the power and bid simultaneously in both markets is shown in equations (6.17) and (6.18). Additionally, these equations determine that buying and selling within one time step is allowed in the model. For example, electricity purchased on the DAM can be directly committed to the FCR market, yet it cannot be sold to DAM again. Nevertheless, if it is established to commit only frequency regulation, (6.19) and (6.20) are enforced, and bidding in both markets is avoided.

$$P_{\text{d}}[t] + P_{\text{fcr-d}}[z] \leq P_{\text{d}}^{*} \tag{6.17}$$

$$P_{\text{c}}[t] + P_{\text{fcr-u}}[z] \leq \cdot P_{\text{c}}^{*} \tag{6.18}$$

$$P_{\text{d}}[t] \leq \left(1 - \boldsymbol{\gamma}_{\text{fcr}}[z]\right) \cdot P_{\text{d}}^{*} \tag{6.19}$$

$$P_{\text{c}}[t] \leq \left(1 - \boldsymbol{\gamma}_{\text{fcr}}[z]\right) \cdot P_{\text{c}}^{*} \tag{6.20}$$

In order to integrate the provision of services by the BESS to other grid users in the optimization problem, the following constraints are introduced:

$$P_{\text{out}}[t] + P_{\text{fcr}}[z] + P_{\text{bk}}[t] = P_{\text{r}}^{*} \tag{6.21}$$

$$P_{\text{out}}[t] \cdot \eta_{\text{d}} = P_{\text{d}}[t] + P_{\text{fcr}}[z] \tag{6.22}$$

$$P_{\text{in}}[t] = (P_{\text{c}}[t] + P_{\text{fcr}}[z]) \cdot \eta_{\text{c}} \tag{6.23}$$

Starting from (6.21), where P_{r}^{*} is the rated power of the battery, expresses the power balance of the system for every time step. The power flowing in and out of the battery system, P_{in}

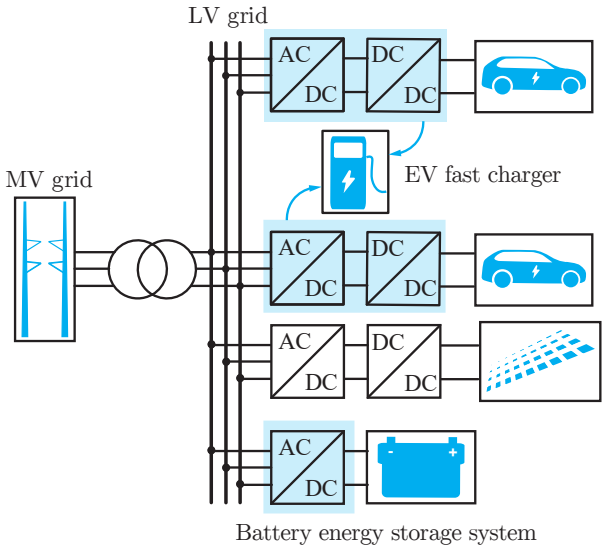

Figure 6.1: Schematic of a BESS assisted PV-FCS.

and P_{out} respectively, needs to be equal to the energy sold or bought on the DAM and the power used to procure FCR. Furthermore, some of the available power, P_{bk}, and the SoC, SoC_{bk}, has been reserved for auxiliary operations. Therefore blocks parameters are introduced to simulate the activities related to the FCS. In particular, (6.9) is updated as follows:

$$\text{SoC}[t+1] = \text{SoC}[t] + \left(P_{\text{c}}[t] \cdot \eta_{\text{c}} - \frac{P_{\text{d}}[t]}{\eta_{\text{d}}}\right) \cdot \frac{t}{E^*} + \text{SoC}_{\text{bk}} \tag{6.24}$$

in which the block values are negative if the battery has to provide energy and positive when energy is stored into the system. Moreover, the outflow and inflow of electricity to the BESS is subject to efficiency loss. These statements lead to the constraints (6.22) and (6.23).

6.3. CASE STUDY: PV-FCS LAYOUT AND INPUT ANALYSIS

A scenario composed of a PV-FCS equipped with a BESS owned by a third-party owner that can provide services to the charging station is considered. This scenario is used to validate the proposed model and case study. The system layout for the FCS consists of four DC fast charging stalls of 50kW for a total power of 200kW, a 500 kW solar system, a 500kW/500kWh BESS, and an LV/MV transformer that couples the station to the MV grid. The schematic of a PV-FCS is shown in Figure 6.1. The BESS used as a reference in the case study is rated 500kW/500kWh, which can be fully charged in one hour or one time step, and the round trip energy efficiency is assumed to be equal to 90% [279]. In this study, a fixed round trip efficiency value is used. Despite that this choice brings a simplification of the actual BESS behavior since it does not capture the variations of efficiency according to the output power, this approach has been widely used in literature and is adequate for planning and investigating potential evaluation studies [26], [170]. A higher level of detail is necessary mainly

for real-time or near real-time operation scheduling of the battery [214, 41, 123]. The selection of the appropriate battery model is discussed in [214]. Nevertheless, since the scope of the study is to understand and evaluate the BESS potential in the proposed framework, using a simplified and conservative approach strongly reduces computational time and formulation problems. Furthermore, the implemented MILP can be easily adapted to more complex linearized efficiency curves by introducing additional constraints.

6.3.1. PV AND FC POWER PROFILES ANALYSIS

An existing reference environment of a PV-FCS in the Netherlands has been selected. The demand profiles extracted from energy measurements performed for the 2020 year roll-out at a sampling frequency of one minute are used as input data. Stedin, a dutch DSO, has provided these. The task intended for the BESS is to perform load-shaving on the EV demand, renewable firming, and boost the self-consumption of solar energy to restrict the grid power exchange. Furthermore, the BESS will operate in the energy and ancillary services markets. The tasks are related to the grid stability; therefore, load and peak shaving of the PV-FCS are prioritized concerning the market activities. Hence, the first step is to evaluate the FCS requirements regarding power and energy from the BESS to be reserved to accomplish such operations.

Figure 6.2 shows the power flowing through the grid of the considered PV-FCS when no BESS is included. It can be seen that the EV load is relatively high throughout the year, with the values evenly distributed around the mean of 40 kW, with a peak load of 200kW. It can be concluded that there is no perfect timing between the necessity of charging the EV and the power produced by the PV plant, with excess in both directions, which fosters a battery system integration. Furthermore, it is relevant to mention that the power shaving will be performed both on the power injected into the grid due to PV overproduction and on the power absorbed from the grid due to EV charging.

As a direct consequence of the curtailment, the FCS would benefit from lower contracted grid power and so lower connection fees. Additionally, the DSO would indirectly benefit by relieving the grid from high peak demand and line congestion. The BESS owner would ask the FCS to remunerate for this service.

As mentioned in Section 6.2 the parameters P_{bk} and SoC_{bk} have to be extracted to be implemented in the optimization algorithm. Hence, after investigating the excess of power, the respective energy needed is examined. Such values are rationalized with the battery nameplate capacity, which is 500kWh in this case study, and the SoC_{bk} is defined. The P_{bk}, instead, is a direct result of the shaving. Several values of the BESS power, which will shave the FCS power profiles, have been investigated to achieve the optimal compromise between revenues and technical aid to the PV-FCS owner. In Figure 6.3 the drop of market related revenues depending on the power shaved of the PV, $P_{PV,curt}$, and of the FCS, $P_{FCS,curt}$, is drawn. This reduction is the outcome of the amount of time step blocked by the P_{bk} and SoC_{bk} parameters. Figure 6.3 displays that an outcome with less than 5% of market revenues losses would mean shaving 20% of the PV power and up to 40% of the FCS intake.

The output mentioned above has been used as a reference example in Figure 6.4 to show which volume and how often the storage system will be called upon. It is worth highlighting how the solar intake is null during winter, while the FCS requests a more periodic, although lower in power, demand.

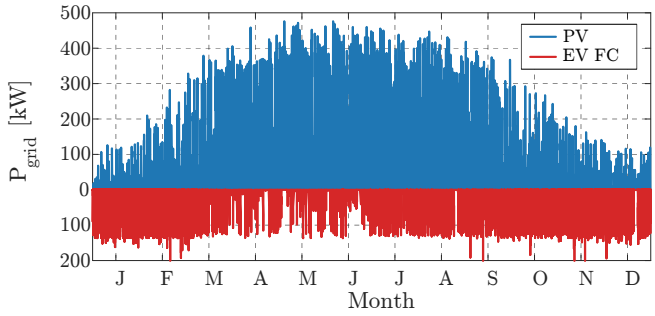

Figure 6.2: PV-FCS power exchange with the distribution grid. The power flow above zero represents the power produced by the solar plant, while the one below zero the power demand due to EV charging.

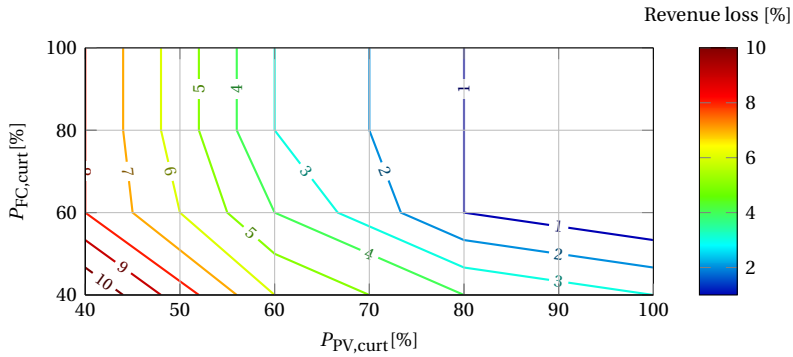

Figure 6.3: Revenues decrease depending on the power shaved from the PV-EV charging station

6.3.2. DAM AND FCR PRICE ANALYSIS

The DAM price λ and the FCR prices λ_{fcr} are essential inputs to the optimization model. The Netherlands is used as the reference country. The dutch DAM market prices between 2017 and 2020 are shown in Figure 6.5 [164]. Observing the normal distribution of the values in Figure 6.6, several observations can be made. Firstly, there seem to denote long and thick tails and significant outliers. Secondly, although not a strict condition for a linear model, the distribution seems slightly negatively skewed. Median and mean values result to be 39.5 €/MWh and 38 €/MWh, respectively.

In the grid of continental Europe, a market has been set to secure sufficient FCR volumes. Due to the technical requirements, the potential providers are usually power generators with fast ramping rates, i.e., fire gas power plants or hydro generators [112]. Consequently, in some countries like the Netherlands, the FCR price has increased. This price increment encourages evaluating other solutions for providing these reserves, such as BESSs. The dutch FCR prices from mid 2019 to end 2020 are shown in the heat-map of Figure 6.7 [164, 190].

From the heat-map of Figure 6.7 it is hard to visualize a recurrent pattern. Nevertheless, it is noticeable how the prices increase after July 2020. Such an event could be a direct consequence of the fact that until July 2020, the FCR market was split into daily delivery periods. The price data are given only from July 2020 onward as four-hour blocks. From

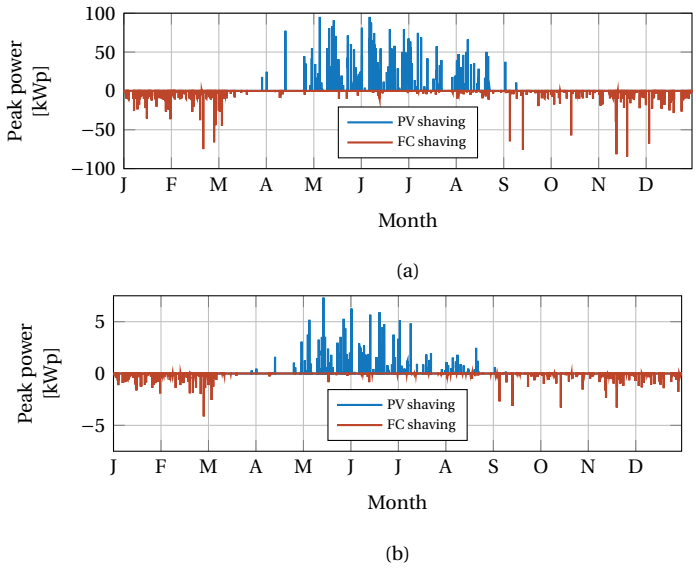

Figure 6.4: Example of (a) Power block and (b) SoC block profile obtained after have shaved 20% of the PV power and 40% of the FCS.

Figure 6.7 it is also visible that intraday price spike does not occur often. However, the Dutch market usually has the highest prices for the 08-11 and 16-19 hour blocks. Unlike energy arbitrage in this market, the revenues will be more driven by the high average price than its volatility. Therefore, prices for FCR behave very differently than DAM prices, which are usually higher when consumption is high. Among the factors influencing the price, since natural gas generators account for most FCR provisions, aspects affecting the commodities prices are likely to influence the FCR price. Moreover, DAM price is also correlated with FCR prices related to the opportunity cost for a producer to deviate from its optimal output level to provide FCR [112].

6.4. MODEL OPERATION AND RESULTS

In this section the operation and results of the performed simulation are displayed and discussed.

6.4.1. MODEL OPERATION

The linear problem has been modeled into a Python-based simulation environment using the Pyomo optimization library. Any MILP solver compatible with Pyomo is applicable for executing the optimization model. Figure 6.8 depicts the algorithm's block structure, with their corresponding interconnection data exchange. The Python-based framework offers state-of-the-art single objective optimization algorithms and is designed to be extendable and applicable to various battery technology and national electricity markets due to its modularity in code development. An example of the linear optimization applied to the BESS operation is shown in Figure 6.9 and 6.10, where the BESS operation is evaluated in

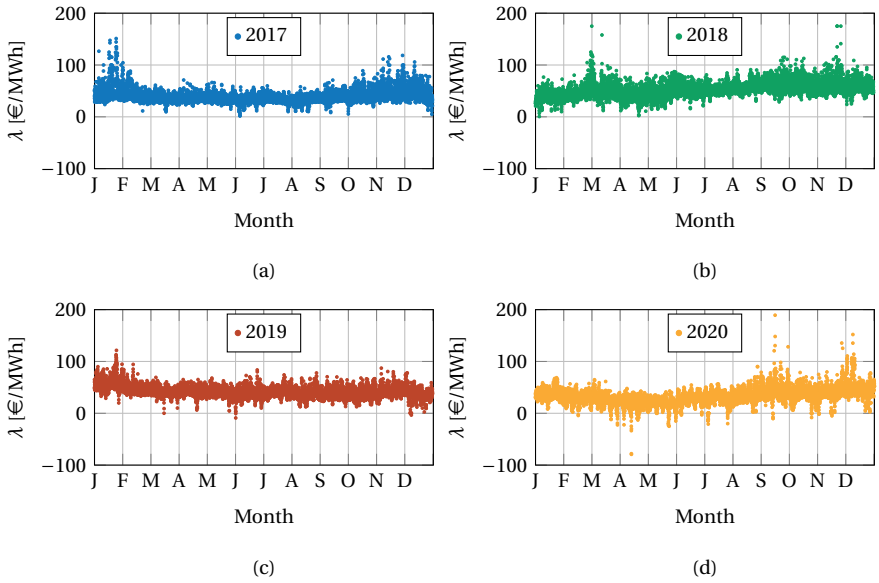

Figure 6.5: Scattered plot of the dutch DAM market prices from 2018 to 2020 plotted in a single year roll-out.

the studied PV-FCS environment considering 24 hours astride of the 5th of November.

Figure 6.9 illustrates how the system dispatches the power and how the price-driven optimization performs in the DAM and FCR markets, showing bid amount and price. The battery is commissioned to perform FCR for 8 hours during the highest price blocks. Additionally, it performs energy arbitrage during the most favorable price slots of the day, i.e., discharging at the highest price and charging at the lowest. However, due to FCR and FCS-operation model constraints, this double market bidding schedule is not always possible. This can be noted in Figure 6.9 when right before midnight, although the price was not optimal, i.e., it is higher than a couple of hours later, the BESS buys energy from the market. In this way, the BESS is recharging to properly participate in the FCR market in the next period since its SoC was nearly zero, and it would have excluded the possibility of performing FCR for the following settlement period. Thus, the BESS charges enough to satisfy the constraints (6.14) and (6.15) by leveling the SoC at 25%.

Additionally, in Figure 6.9, from the time slot, 3 am to 6 am, the double bidding function is shown, which means that no constraint limiting the participation in both markets is active. As noted, in the same slots, the optimization algorithm controls the discharge by placing consecutive bids to increase the battery's level of charge gradually. Due to the perfect foresight strategy, the algorithm is aware that the price would maintain low for some time step. Hence, the optimization prefers to fill the battery cells progressively. Consequently, reducing the effect of cycling degradation on the battery cells thanks to a low C-rate charge, rather than using a total cycle bid.

Figure 6.10 shows the SoC of the battery. Comparing the SoC trend with the overall power output of the system, it may be noted how only the DAM bid and SoC_{bk} influence the SoC variation. As a direct consequence of being an energy market, the volume traded in the DAM drives the charging level of the battery. On the other hand, the charging station

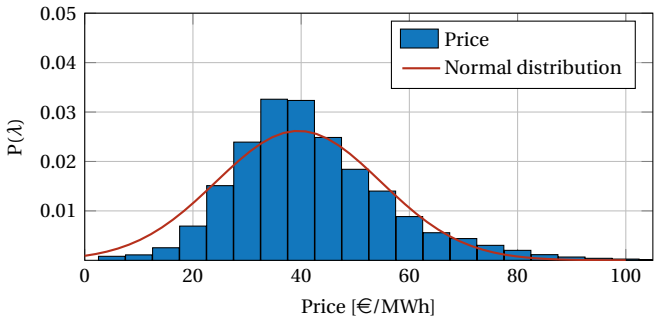

Figure 6.6: Histogram of normalized historic dutch day-ahead market data (2017-2020).

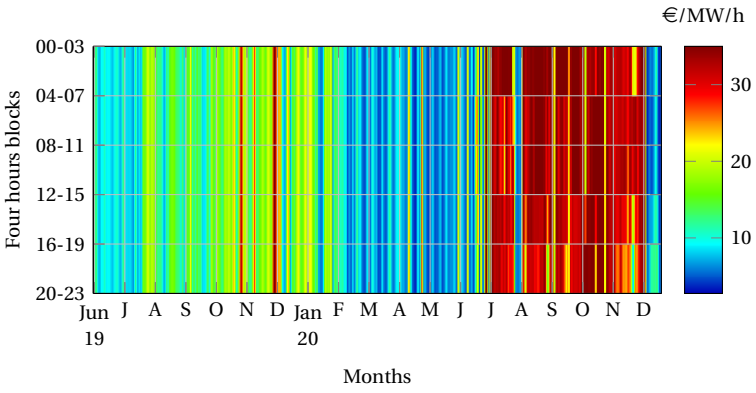

Figure 6.7: Heat-map of hourly FCR prices of the Netherlands from June 2019 to December 2020. Warmer colors indicate higher prices.

demanding extra battery capacity, i.e., negative SoC_{bk} values, leads the SoC to drop accordingly. The primary frequency regulation also affects the SoC by generating a continuous oscillation. Nevertheless, such behavior has not been modeled. It is assumed that the SoC at the beginning and end of the service does not change, thanks to the SoC management algorithm that BESSs providing FCR typically implement [154, 225, 218]. At 18.00h in Figure 6.10, the plot displays why the battery did not dispatch the total capacity in DAM, answering why the SoC was nearly zero before performing FCR. This limitation is forced by the BESS allocation of a fraction of power for the FCS, P_{bk}.

6.4.2. FINANCIAL ANALYSIS

The different revenue streams for the BESS considered in this chapter are the profits from the energy and ancillary services market and the avoided grid connection costs of the PV-FCS. In Subsection 6.3.1 it has been highlighted how possible shaves of power could be performed on the PV-FCS case study considered. In particular, it has been assessed that shaving 20% of the PV power and 40% of the FCS intake would lead to less than 5% of market revenue loss. This revenue loss is because the BESS cannot participate in market operations when load-peak shaving the PV-FCS, and this could happen during the profitable hours of

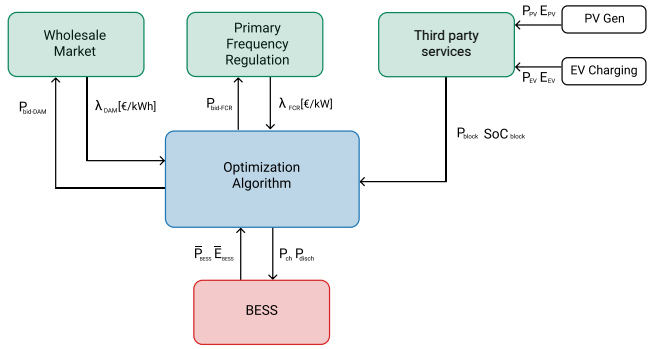

Figure 6.8: The algorithm's block structure shows the exchange of information among the different modules: wholesale market, primary frequency regulation, third party operations and the BESS.

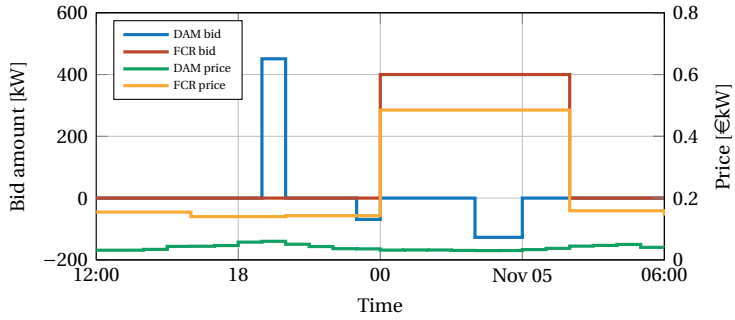

Figure 6.9: Profit maximizing BESS' participation in Day-ahead market and Primary frequency regulation market for a sample 24h time-shift.

the day. Such peak shaving level, 20% of the PV power and 40% of the FCS, is then a valid trade-off and will be considered in the remainder of the study.

Table 6.1 displays the revenues and activation hours of a BESS deployed for market participation and load-peak shaving the PV-FCS considered. These have been calculated by the model presented in Section 6.2 running the input data and case study of Section 6.3. FCR leads to a considerably higher amount of revenue than DAM. Thus, it confirms that European wholesale market prices, at the present day, might not be high enough to deem energy arbitrage as the only revenue stream for a grid-connected BESS, as also reported in other studies [270]. Despite the high revenues, the number of activations is also noteworthy. Simultaneous participation in DAM and FCR markets occurs 320 times a year. Overall, when the constraints (6.19) and (6.20) are not enforced, and a double bid is allowed, the BESS is online for about 1950 h/year, combining DAM and FCR activation, which corresponds to slightly more than 20% of the year. Furthermore, as stated earlier, the decrease in revenues due to the FCS operation is minimal; however, the number of operations increased. Therefore, online and idling time is price-driven and determined by additional input constraints. The additional service offered to the FCS increased the BESS's online time by almost 500 hours in a year, reducing the overall idling time by 23%. Such a high number of activations and cycles may be addressed to the unexpected block provided by the FCS, limiting the

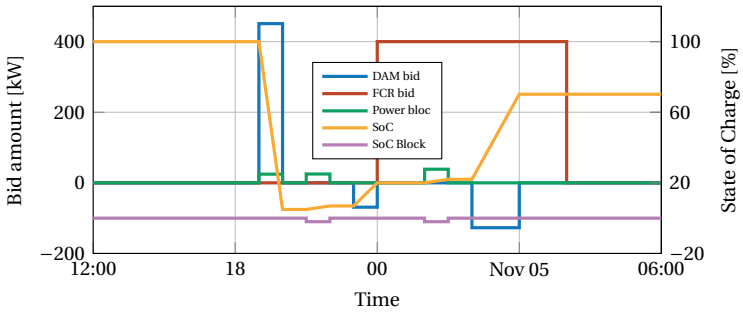

Figure 6.10: Comparison between BESS operations and its state of charge for a sample 24h time-shift

Table 6.1: Revenues from different markets and avoided connection costs of a BESS coupled with a PV-FCS considering prices and tariffs of the Dutch electricity market 2020.

	DAM	FCR	PV-FCS
Revenues [k€]	3.1	76	3.5
Activations [h]	450	1850	495
Cycles	240	-	105

power output and changing the BESS SoC.

Regarding the connection costs, the BESS is used for peak shaving and load shifting. As previously detailed, a power shaving of 20% of the PV power and 40% on the FCS demand results in a limited decrease of market-related revenues, and therefore this condition is considered. In Figure 6.11 the monthly maximum grid exchange power, which is used to calculate the connection fees, and the relative connection fees of a PV-FCS are displayed with and without the BESS aid on peak and load shaving. Thanks to the BESS operation, the overall grid peak connection has been reduced by around 100kW. In particular, a notable reduction is registered during the central months of the year due to high PV power production during the summer season. It also results in a relatively higher shaving in other periods of the year, where the grid congestion is mainly dominated by the EV charging demand. Given the maximum power, it is possible to derive the connection fees to be paid to the DSOs. These are based on the publicly available tariffs from Stedin [219], a dutch DSO operating in the region of Rotterdam, whose tariffs are a representation of the DSOs tariffs in the Netherlands. The connection charges are split in two, a one-off fee at the time of the new connection, related to the type of connection and proportional to the rated requested power, and a monthly periodic tariff, which is composed of several factors, such as contracted power, maximum measured power, and transported energy [219].

The BESS operation leads to an overall 30% of connection cost savings. In particular, the PV-FCS owner could save more than 3500 euros a year on the variable transport tariff fees related to the peak power of the connection to the DSO. This economic benefit is transferred to the BESS owner for the service offered. This could be accomplished via bilateral contracts between the two parties. Additionally, such avoided cost is achieved with a very low time utilization of the BESS since this will provide services to the PV-FCS for 495 hours in the analyzed year, which corresponds to about 6 % of the year's total hours, as listed in Table 6.1. Moreover, it is essential to mention that the benefits of a possible feed-in tariff

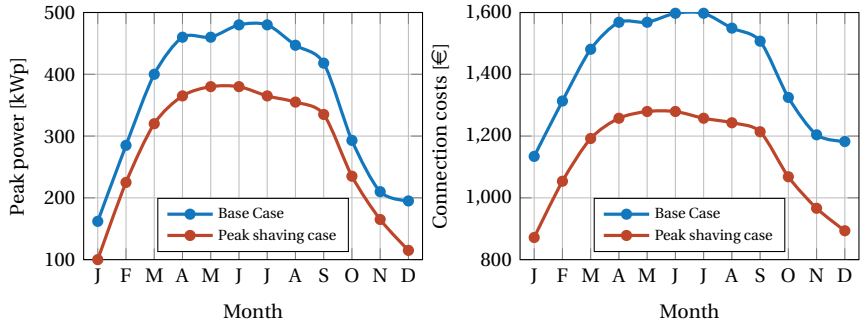

Figure 6.11: Monthly PV-FCS maximum grid exchange power (a), and relative connection charge (b), with and without a BESS deployed to shave 20% of the PV rated power and 40% of the FCS rated power.

of selling green power to the grid and other bilateral agreements on the increased PV self-consumption in the act with the DSO are not considered. As mentioned, DSO and BESSs owners would stipulate a direct contract for the service. Therefore, the revenues from the BESS installation are underestimated. All in all, it is shown that an FCS or RES plant owner can benefit from the operation of BESS installed on its premises.

The German DAM and FCR prices have been used to estimate the near future revenues of a BESS placed in the Netherlands. The main reasons behind this choice are that the German energy map is intensively determined by RES production, whose unpredictability strongly influences the spot market prices. Furthermore, higher uncertainty is driven by factors that influence such prices, i.e., gas price, grid expansion, integration of new European platforms, and European tendency of FCR prices to decrease due to new green assets participating in the market. Additionally, as studied in [117], Germany has been highlighted as a country where BESSs are a mature technology exploited in procuring ancillary services. Therefore, it has been assumed that Dutch DAM and FCR prices will follow that direction, and German data are a suitable reference for the near future price trends. Instead, the grid connection savings are assumed constant in the following years.ons

Given the revenue streams, it is possible to estimate the financial performance of the BESS in the PV-FCS environment. In this context, CAPEX, OPEX, and the discount rate (r) of the BESS are fixed to 330 €/kWh, 150 €/kW, and 3.5%, respectively [218]. In Figure 6.12 the projected cash flow of Case A and Case B, which refer respectively to when only remuneration coming from electricity market application and when the FCS shaving revenues are also taken into account, are compared. In green, it is highlighted the potential proposed extra income based on FCS service speculation. Interestingly, the projected annual profit increases compared to the base case only thanks to the additional revenues stream due to the FCS operation. In a future scenario characterized by a saturation of the FCR market and consequent price decrease, such service will become almost a quarter of the total forecasted profit. Given the estimated cashflow due to market revenues and services to the FCS, and the investment costs, the Net Present Value (NPV), of the BESS project can be calculated as:

$$\text{NPV} = \sum_{t=1}^{n} \frac{R_t}{(1+r)^t}, \tag{6.25}$$

Table 6.2: Financial analysis of a BESS participating to only energy and FCR market, Case A, and of a BESS participating to markets activities and also providing services to the FCS, Case B.

Parameter	**Case A Only market**	**Case B PV-FCS addition**
Cycles [n]	233	243
NPV [k€]	95	108
IRR [%]	11	12
Payback time [years]	4	3.9

where R_t is the net cash flow during a time period t, which can be seen in Figure 6.12, r is the discount rate, and n the number of the considered time periods. Additionally, the Internal Rate of Return (IRR) can be found setting the project NPV to zero and finding the IRR coefficients that respects the equation:

$$0 = \text{NPV} = \sum_{t=1}^{n} \frac{R_t}{(1+\text{IRR})^t} - R_0, \tag{6.26}$$

where R_0 corresponds to the total investment costs.

These two indicators, NPV and IRR, are financial parameters that help evaluate the economic feasibility of a project. In Table 6.2 these are summarized. The table shows that by adding the revenue stream from the PV-FCS, the monetary return has improved from 11% to 12% and that the payback time, which is the time when the cumulative project cash flow reaches zero, can be slightly reduced below four years. Furthermore, the NPV increases from 95 k€ to 108 k€, with an increase of 14%. Then, additional remunerated services are beneficial from an investor's point of view. Although deviations from the optimal market revenues occur, the financial indicators display positive results.

Additionally, if the DAM and FCR market are less profitable in the future, the BESS will presumably cycle less along the years since its activation will be primarily linked to local grid services. It will be even more beneficial if the DSO will pay for availability rather than actual activation time. Due to this conceivable scenario, degradation factors to estimate future revenues are not assessed. However, a detailed analysis of battery capacity fading is left to future research in this domain. All in all, it can be concluded that installing a BESS in the considered case study is a technical and economically beneficial investment for the players involved in the distribution grids.

6.5. CONCLUSION

The chapter presented a mixed-integer linear model which can be used as a flexible tool to evaluate the economic feasibility of a BESS operating in distribution networks. In the analyzed case study, which reflects the Dutch energy market from 2017 to 2020, a BESS of 500 kW / 500 kWh coupled with a PV-FCS is shown to be economically profitable. The system NPV, in fact, is calculated to be 95k€. Furthermore, by adding the service to the third party, the FCS, the system NPV can be increased, and it is calculated to be 108 k€. As discussed, BESSs can be coupled with PV-FCSs to flatten their generation and load profiles, decreasing the maximum power exchange at the connection point with the grid. By reducing the power exchanged to the grid, the owner of the PV-FCS would benefit from the lower grid connection costs. Additionally, BESSs can participate in energy and ancillary services mar-

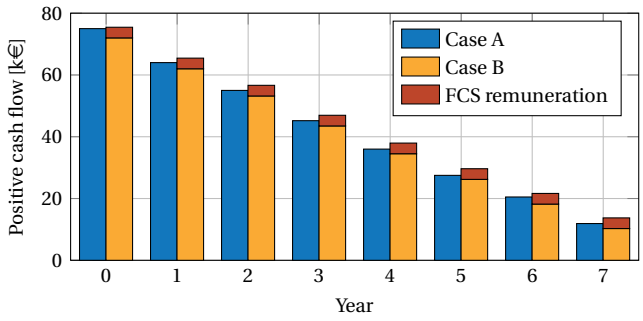

Figure 6.12: Projected cash flow of a 500kW/500kWh BESS operating in electricity markets and with FCS operation included. Case A indicates the cash flow coming only from market applications and Case B the cash flows with the FCS extra remuneration

kets, such as FCR and DAM. Nowadays, BESSs are still an expensive technology; therefore, combining ancillary services and other grid services will drive to capitalize higher revenues. The analysis has shown that such configuration allows economic and technical benefits for the players involved in the case study, namely the BESS owner, the FCS owner, and the local DSO indirectly. The BESS owner would profit from a positive NPV and a low payback time which could be reduced in under four years whether higher speculation is executed on the FCS remuneration agreement described. Economically speaking, no assessment is outlined for the DSO. Its benefit relies on the technical aid that the BESS could provide by waiving the grid from power peaks, which are detrimental to the distribution network operation. Finally, the PV-FCS owner would benefit from an overall 30% of grid connection tariff reduction, and such a solution can boost the self-consumption of locally produced solar energy.

Future work could be oriented on including a sensitivity analysis on the model inputs, especially in light of the drastically changed economical and geopolitical scenario respect to when this study was performed. Energy prices in 2022 are very different to the ones shown in Fig. 6.5, and the significantly higher price volatility seen in recent months could potentially boost revenues from DAM. It would be then interesting to evaluate the BESS profitability with the current scenario and updated forecasts.

All in all, it can be concluded that such BESS implementation is economically and technically advantageous for the involved parties in the distribution grids. The BESS can stack additional revenues on top of the market revenues, the FCS benefits from a reduced peak power and consequently tariff reduction, and the system operator would indirectly benefit from the shaved FCS profile.

7

CONCLUSION AND FUTURE WORK

The objective of this thesis was to research methods and components to improve the design of the power electronics interface of grid-connected battery storage systems and to make the integration of batteries in distribution grids more profitable. The research objective has been partitioned into four research questions and in this chapter, the main conclusions of each research question and recommendations for future research are given.

Q1 *To what extent can the lifetime of a BESS providing primary frequency regulation be optimized to yield the maximum economic profits?*

The main BESS components subject to wear are the electrochemical storage, the IGBT modules, and the electrolytic capacitors. However, for a BESS providing primary frequency regulation, the component that is subject to faster degradation is the electrochemical storage. The IGBT modules and the electrolytic capacitors do not see high degradation due to the very low power utilization which is typical of this BESS functionality. In the analysis presented, the electrochemical storage lifetime peaks at 10-11 years, and varies according to the PFR implementation parameters, which are country dependent. Additionally, as detailed in Chapter 3, the power-sharing between the SoC management and PFR provision is a key variable for evaluating the BESS lifetime and the revenues deriving from the PFR provision. In this respect, it has been shown that the value of $P_{\text{pfr,max}}$ that maximizes the components' lifetime does not necessarily coincide with the one that maximizes the BESS revenues.

Overall, the provision of PFR through BESSs can be profitable in all three countries analyzed, with the present remuneration tariffs and BESS capital costs. Furthermore, the higher remuneration tariffs seen in the Netherlands in recent years lead to the highest revenues among the analyzed countries. Additionally, the BESS lifetime estimation methodology provided in Chapter 3 can be applied for studying BESS lifetime when performing other functionalities.

Q2 *How much can efficiency and costs of a BESS converter be improved by hybrid switches?*

Hybrid switches can be used in VSCs as a more performing alternative to Si IGBTs and a cheaper solution than SiC MOSFETs. In Chapter 4, the conduction and switching performances of HySs are experimentally characterized and compared with the one of SiC MOSFETs, Si IGBTs. Chapter 4 also provided the analytical methods for the component selections and the chip area optimization of such HySs. The experimental results showed how HySs position themselves between the pure Si IGBTs and SiC MOSFETs in terms of performance and costs. Afterward, the switches have been compared in terms of chip area and thus in costs, upholding that the mcHyS provides a cheaper alternative to SiC MOSFETs and the commonly studied in literature tHyS. HySs have also been shown to be valuable candidates for 2L-VSC of BESSs deployed for grid ancillary service, providing significant loss reduction over the mission profile, while having lower costs than SiC MOSFETs. To conclude, it has been shown that such HyS concept can provide a valuable cost-efficiency trade-off with respect to traditional Si IGBTs and SiC MOSFETs, which can be particularly interesting in BESS, where the high initial investment costs and poor efficiency are often a barrier for BESS deployment.

Q3 *How can unbalanced compensation be enabled in a BESS without significant hardware expansion?*

In Chapter 5 the modeling and design guidelines for the DC-link of a two-level three-legs four-wires VSC operating under unbalanced loads have been detailed. The analysis shows that the DC-link capacitors can satisfy the thermal and capacitance requirements under unbalanced power loads if designed adequately for balanced power operation. The tests operated on a down-scaled VSC prototype demonstrate the working principle of the BESS providing unbalance redistribution, showing that the power redistributor functionality can be added as an optional grid ancillary service to the classic BESS applications. Additionally, several ICR18650-26F Lithium-ion cells have been cycled to investigate the effect of the 100Hz AC current sinusoidal ripple, which derives from the unbalanced operation. The cycling tests show that the AC ripple's superimposition leads to an increase in degradation of 10% with respect to the standard CC-CV method; nonetheless, the main driving for degradation remains the charging and discharging C-rate.

All in all, in Chapter 5, it was shown that the power redistribution functionality could be successfully implemented in commercially available BESSs as an add-on functionality without significant hardware upgrades and performance deterioration.

Q4 *How can a BESS participate in energy and ancillary services markets and provide services to a third party in a profitable way?*

Chapter 6 presented a case study, which reflects the Dutch energy market, where a BESS of 500 kW / 500 kWh is coupled with a PV-FCS, and such an arrangement is shown to be economically profitable. The system NPV is calculated to be 95k€. Furthermore, by adding the service to the third party, the FCS, the system NPV can be increased, and it is calculated to be 108 k€. As discussed, BESSs can be coupled with PV-FCSs to flatten their generation and load profiles, decreasing the maximum power exchange at the connection point with the grid. By reducing the power exchanged to the grid, the owner of the PV-FCS would benefit from the lower grid connection costs. Additionally, BESSs can participate in energy

and ancillary services markets, such as FCR and DAM. Nowadays, BESSs are still an expensive technology; therefore, combining ancillary services and other grid services will drive to capitalize higher revenues. In the future, with less attractive electricity markets, it will turn out to be the main source of income. The analysis has shown that such configuration allows economic and technical benefits for the players involved in the case study, namely the BESS owner, the FCS owner, and the local DSO indirectly. The BESS owner would profit from a positive NPV and a low payback time which could be reduced in under four years if higher speculation is executed on the FCS remuneration agreement described. Economically speaking, no assessment is outlined for the DSO. Its benefit relies on the technical aid that the BESS could provide by waiving the grid from power peaks, which are detrimental to the distribution network operation. Finally, the PV-FCS owner would benefit from an overall 30% of grid connection tariff reduction, and such a solution can boost the self-consumption of locally produced solar energy.

On the whole, it can be concluded that such BESS implementation is economically and technically advantageous for the involved parties in the distribution grids. The BESS can stack additional revenues on top of the market revenues, the FCS benefits from a reduced peak power and consequently tariff reduction, and the system operator would indirectly benefit from the shaved FCS profile.

7.1. FUTURE WORK

This thesis treated various topics related to BESS integration in distribution grids, from the power electronics part to the dispatch algorithm. There are research gaps in the area of grid-connected BESS which due to the scope of this thesis or time constraints have not been investigated.

In multiple parts of this thesis, various models of electrochemical cells have been used, which differ in terms of accuracy and computational time. However, in the literature, it was not possible to find a scalable, flexible and integrated model of Lithium-ion batteries that could be used both at the design and at the real-time dispatch scale. Studies have proved that a too simplified battery model can lead to excessive capacity fading due to non-optimal scheduling. The usage of detailed models comes at the price of computational performance. Therefore, developing accurate and computationally performing battery models is needed to fully unlock the BESS potential. Further research should then be focused on developing models that precisely describe the battery performance and lifetime, but at the same time do not overly rise the computational time. In this way, these may be applied not only for short-term scheduling but also for network planning.

In terms of the power electronics interface of BESS, in this thesis multilevel topologies have been briefly mentioned. However due to the scope of the thesis and the time constraints they have not been properly investigated. Future work should address the application of three-level and multi-level topologies in BESS and how to optimize their design, to achieve higher performances. Furthermore, the hybrid switch concept has been discussed in Chapter 4. The proposed mcHyS could be further optimized by exploiting the internal delays, further boosting the partial load efficiency, which is fundamental in BESS applications, as it has been extensively repeated in the thesis.

Further investigations are also required on the aggregation of multiple BESSs. In future grids, there will be multiple storage elements connected, especially at the Low Voltage level. Therefore, it is important to implement a coordination layer between them, not only to

optimize the grid performance, but also to avoid conflicting actions. Future research could also look at this aspect of BESSs.

Lastly, the regulatory framework is still one of the main challenges for BESSs' deployment. A clear remuneration scheme for many of the possible grid services is still not implemented in national regulations outside pilot projects. For example, a key challenge would be defining a remuneration scheme of the power redistribution functionality described in Chapter 5. Future work should address how to allow a BESS owner to provide services to the various grid players, such as generators, loads, and operators.

A

VOLTAGE SOURCE CONVERTER MODELLING AND DESIGN

A

In this Appendix, the approach used to model the main components of VSC, which are semiconductors, DC-link capacitors, and the LCL filter is discussed.

A.1. SEMICONDUCTOR LOSSES

The losses in power semiconductors of VSCs are mainly caused by the conduction of current by the device, and by its switching on and off. The estimation of the two is discussed in this Section.

A.1.1. CONDUCTION LOSSES

Conduction losses in power semiconductors can be modeled as:

$$P_c = v \cdot I_{avg} + r \cdot I_{rms}^2, \tag{A.1}$$

where v stands for the pn junction barrier voltage, present in IGBTs and diodes, r for the on-state resistance of the device, and I_{avg} and I_{rms} are the average and RMS value of the current flowing through the device, respectively. The on-state parameters, v and r, of semiconductors can be extracted by the I-V curves presented in datasheets or experimentally derived. Furthermore, they are influenced by the junction temperature, T_j, following [260]:

$$r(T_j) = r_{25°C} + tc_r\left(T_j - 25\right), \tag{A.2}$$

$$v(T_j) = v_{25°C} + tc_v\left(T_j - 25\right). \tag{A.3}$$

where v and r are the semiconductor pn junction barrier voltage and the on-state resistance, and tc_v and tc_r their respective thermal coefficients. These can be derived from the datasheet of the semiconductor, for example, the thermal coefficient of the on-state resistance:

$$tc_r = \frac{r_{Tj,max} - r_{Tj,min}}{T_{j,max} - T_{j,min}}. \tag{A.4}$$

where $T_{j,max}$ and $T_{j,min}$ indicate the maximum and minimum junction temperature. The on-state resistance of a device increases with the temperature, and so tc_r is positive, while v decreases with temperature, therefore tc_v takes negative values.

Typically, for the estimation of the conduction losses through (A.1), the on-state characteristics are taken at the maximum allowed operating temperature, in the range of 125-150 °C, depending on the semiconductor and packaging technologies [50, 103, 196, 260]. Following this approach, the losses can be accurately estimated at full power, when, with a properly designed cooling system, it is expected that the junction temperature reaches its maximum level. At lower power, however, the power losses will be slightly overestimated.

A.1.2. CURRENT STRESS DERIVATION

In a grid-connected VSC, the analytical expression of I_{avg} and I_{rms} can be found averaging the line current during a switching period according to the switch duty cycle.

$$I_{avg} = \frac{1}{2\pi}\int_a^b I_c(\omega)D(\omega)\mathrm{d}\omega, \tag{A.5}$$

$$I_{rms} = \sqrt{\frac{1}{2\pi}\int_a^b I_c^2(\omega)D(\omega)\mathrm{d}\omega}, \tag{A.6}$$

where I_c is the expression of the conducted current of the switch, a and b are the angular positions of the beginning and end of the conduction period, and $D(\omega)$ is the switch duty cycle expression. This approach provides accurate results if the converter switching frequency f_s is much greater than the grid frequency f_g, the bridge-leg dead time is negligible with respect to the switching period, and the maximum current ripple within a switching period is much smaller than $\hat{I}$. Therefore, in all the following derivations a pure sinusoidal phase current is considered, assuming that the output filter can damp the AC ripple current [217]:

$$I(\omega) = \hat{I}\sin(\omega + \varphi), \tag{A.7}$$

where φ is the phase shift between the fundamental line voltage and current, and $\hat{I}$ is the peak AC line current.

Such assumptions typically hold in grid-connected VSCs, since f_s is in the order of kHz and an L or LCL filter, which are typically designed to strongly limit the current ripple flowing in the converter, has to be placed between the VSC and the grid, so to respect the grid connection standards.

TWO-LEVEL CONVERTER

In case of PWM modulated VSC [94], the duty cycle of the upper ($D_u(\omega)$) and bottom ($D_b(\omega)$) switch can be expressed respectively as:

$$\begin{aligned} D_u(\omega) &= \frac{1}{2} + \frac{m}{2}\sin(\omega) + v_z; \\ D_b(\omega) &= 1 - D_u(\omega); \end{aligned} \tag{A.8}$$

where m is the modulation index, ω is the phase angle, and v_z is the zero sequence vector which can be added to obtain space vector modulation or discontinuous modulation methods. In the following derivations, sinusoidal PWM is considered.

Then, depending on the switch technology on which the VSC is assembled, the current stress in a 2L-VSC can be found. For instance, if Si-IGBTs are used, the current conduction is shared between the IGBT and its anti-parallel diode. In a MOSFET-based VSC, the full current is conducted by the MOSFET. In hybrid switches, since two devices are conducting at the same time, the current sharing is more complex and depends on the on-state parameters and the temperature of the switches. The different switch configurations are shown in Fig. A.1.

MOSFET-based In a MOSFET-based 2L-VSC, shown in Fig. A.1 (a), the current stress in a half-bridge leg can be modeled as:

$$I_{\mathrm{rms,M_{1,2}}} = \frac{\hat{I}}{2} \tag{A.9}$$

IGBT-based In an IGBT-based 2L-VSC, shown in Fig. A.1 (b), the current stress in a half-bridge leg can be modeled as:

$$I_{\mathrm{avg,T_{1,2}}} = \frac{\hat{I}}{8\pi}\left(m\pi\cos\varphi + 4\right) \tag{A.10}$$

$$I_{\mathrm{avg,D_{1,2}}} = \frac{\hat{I}}{8\pi}\left(4 - m\pi\cos\varphi\right) \tag{A.11}$$

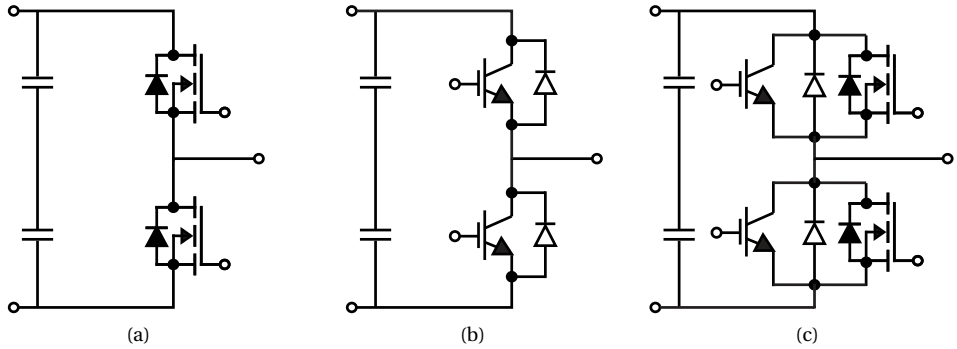

Figure A.1: Half-bridge legs for two-level VSC converters with different switch configurations; (a) MOSFET-based, (b) IGBT-based, and (c) Hybrid switch based.

$$I_{\mathrm{rms,T_{1,2}}} = \frac{\hat{I}}{2}\sqrt{\frac{8m\cos\varphi + 3\pi}{6\pi}} \tag{A.12}$$

$$I_{\mathrm{rms,D_{1,2}}} = \frac{\hat{I}}{2}\sqrt{\frac{3\pi - 8m\cos\varphi}{6\pi}} \tag{A.13}$$

mcHyS-based 2L-VSC In a mcHyS-based 2L-VSC, shown in Fig. A.1 (c), the MOSFET is used only for switching and the full current conduction happens through the Si-based devices. Therefore, the conduction losses in this HyS arrangement can be calculated as the ones of a Si IGBT-based 2L-VSC.

Nonetheless, as shown Fig. 4.1, the switching strategy can be optimized by the proper selection of the switching delays $d_1 ... d_4$. Therefore, if the MOSFET is turned on before the IGBT and turned off after the IGBT, in this time period, it will conduct the full current. These extra conduction losses depend on the total time in which the SiC MOSFETs conduct the full current, d_{tot}, and they can be evaluated as:

$$P_{\mathrm{exC-M,mcHyS}} = d_{\mathrm{tot}} f_{\mathrm{s}} r_{\mathrm{ds,on}} \hat{I}^2 \frac{8m\cos\varphi + 3\pi}{24\pi}, \tag{A.14}$$

where $r_{\mathrm{ds,on}}$ is the MOSFET on-state resistance.

tHyS-based 2L-VSC In a tHyS-based 2L-VSC both the IGBT and MOSFET conduct current. This hybrid switch is typically implemented paralleling Si IGBTs and its anti-parallel Si Diode and SiC MOSFETs. Furthermore, it is considered that the SiC MOSFET body diode does not conduct, due to its high forward voltage drop. Such an assumption is confirmed by the third quadrant operation I-V curves provided by the device manufacturer [196, 50]. The Si devices will not conduct until the voltage across the switch, V_{on}, overcomes its pn junction barrier potential v_{pn}, that is $v_{\mathrm{ce,0}}$ in the case of the IGBT and $v_{\mathrm{f,0}}$ in the case of the diode. Therefore, the current values over which the bipolar devices start conducting and their angular position are defined as:

$$I^* = \frac{v_{\mathrm{pn}}}{r_{\mathrm{ds,on}}}, \tag{A.15}$$

$$\delta^* = \arcsin\left(\frac{v_{\text{pn}}}{r_{\text{ds,on}} \cdot \hat{I}}\right). \tag{A.16}$$

The Si IGBT conducts in the angular interval $\omega \in [\delta - \varphi\ ;\ \pi - \delta - \varphi]$ and the diode during the interval $\omega \in [\pi + \delta_{\text{r}} - \varphi\ ;\ 2\pi - \delta_{\text{r}} - \varphi]$, where δ and δ_{r} are found substituting respectively the IGBT and diode on-state parameters in (A.16).

For line current values, $I(\omega)$, larger than I_{f}^* and lower than I_{r}^* the current sharing between Si devices and MOSFET can be derived according to the devices on-state characteristics, as:

$$I_{\text{M,f}}(\omega) = \frac{I(\omega) r_{\text{ce}} + v_{\text{ce,0}}}{r_{\text{ds,on}} + r_{\text{ce}}}, \tag{A.17}$$

$$I_{\text{I}}(\omega) = \frac{I(\omega) r_{\text{ds,on}} - v_{\text{ce,0}}}{r_{\text{ds,on}} + r_{\text{ce}}}, \tag{A.18}$$

$$I_{\text{M,r}}(\omega) = \frac{I(\omega) r_{\text{f}} + v_{\text{f}}}{r_{\text{ds,on}} + r_{\text{f}}}, \tag{A.19}$$

$$I_{\text{d}}(\omega) = \frac{I(\omega) r_{\text{ds,on}} - v_{\text{f}}}{r_{\text{ds,on}} + r_{\text{f}}}, \tag{A.20}$$

where r_{ce} and r_{f} are the on-state resistance of the Si IGBT and Si diode respectively. Equations (A.17) and (A.18) are referred to the forward conduction stage of the switch, while (A.19) and (A.20) to the reverse conduction stage. Overall, the tHyS on-state characteristics can be expressed as:

$$V_{\text{on,tHyS}}(I) = \begin{cases} r_{\text{ds,on}} \cdot I_{\text{M,r}} & \text{if } I <= I_{\text{r}}^* \\ r_{\text{ds,on}} \cdot I & \text{if } I_{\text{r}}^* < I < I_{\text{f}}^* \\ r_{\text{ds,on}} \cdot I_{\text{M}} & \text{if } I >= I_{\text{f}}^*. \end{cases} \tag{A.21}$$

The average and RMS current flowing through the IGBT can then be calculated substituting $I_{\text{I}}(\omega)$ in (A.5)-(A.6) and integrating during its conduction interval:

$$I_{\text{avg,I}} = \frac{1}{2\pi} \int_{\delta-\varphi}^{\pi-\delta-\varphi} I_{\text{I}}(\omega) D_{\text{u}}(\omega) \text{d}\omega, \tag{A.22}$$

$$I_{\text{rms,I}} = \sqrt{\frac{1}{2\pi} \int_{\delta-\varphi}^{\pi-\delta-\varphi} I_{\text{I}}^2(\omega) D_{\text{u}}(\omega) \text{d}\omega}. \tag{A.23}$$

Similarly, the diode current stress can be found as:

$$I_{\text{avg,d}} = \frac{1}{2\pi} \int_{\pi+\delta_{\text{r}}-\varphi}^{2\pi-\delta_{\text{r}}-\varphi} I_{\text{d}}(\omega) D_{\text{u}}(\omega) \text{d}\omega, \tag{A.24}$$

$$I_{\text{rms,d}} = \sqrt{\frac{1}{2\pi} \int_{\pi+\delta_{\text{r}}-\varphi}^{2\pi-\delta_{\text{r}}-\varphi} I_{\text{d}}^2(\omega) D_{\text{u}}(\omega) \text{d}\omega}. \tag{A.25}$$

It has to be noted that for peak AC current lower than the minimum current necessary for the IGBT to conduct, the value of δ becomes equal to $\pi/2$, and therefore the integration interval in (A.22)-(A.25) becomes null. The conduction losses are then fully flowing across the SiC MOSFET.

As previously mentioned, the MOSFET conducts during the full period, however, when the bipolar devices are conducting the MOSFET sees only a fraction of the total current. The rms current flowing through it is then found according to:

$$I_{\mathrm{ms,M}} = \sqrt{\frac{1}{2\pi}\left(\int_{\delta-\varphi}^{\pi-\delta-\varphi} I_{\mathrm{M}}^2(\omega) D_{\mathrm{u}}(\omega)\mathrm{d}\omega + \int_{\pi-\delta-\varphi}^{\pi+\delta_{\mathrm{r}}-\varphi} I^2(\omega) D_{\mathrm{u}}(\omega)\mathrm{d}\omega + \int_{\pi+\delta_{\mathrm{r}}-\varphi}^{2\pi-\delta_{\mathrm{r}}-\varphi} I_{\mathrm{M,r}}^2(\omega) D_{\mathrm{u}}(\omega)\mathrm{d}\omega + \int_{2\pi-\delta_{\mathrm{r}}-\varphi}^{2\pi+\delta-\varphi} I^2(\omega) D_{\mathrm{u}}(\omega)\mathrm{d}\omega\right)}. \quad \text{(A.26)}$$

Additionally, the extra conduction losses in the MOSFET due to the turn-on and off delay would then only happen for current levels higher than I^*, since for lower current the MOSFET would conduct the full current anyway. These can then be estimated by:

$$P_{\mathrm{exC-M,tHyS}} = \frac{r_{\mathrm{ds,on}} d_{\mathrm{tot}} f_{\mathrm{s}} \hat{I}^2}{24\pi}\Big[6(2m + \sin\delta)\cos\delta - 4m\cos^3\delta + 3(\pi - 2\delta)\Big]. \quad \text{(A.27)}$$

A.1.3. SWITCHING LOSSES

The switching losses of a 2L-VSC can be analytically calculated through the following general equation:

$$P_{\mathrm{s}} = \frac{f_{\mathrm{s}}}{2\pi}\int_0^{2\pi} E_{\mathrm{sw}}(V_{\mathrm{dc,sw}}, I(\omega))\mathrm{d}\omega. \quad \text{(A.28)}$$

where E_{sw} represents the device switching energy as function of the switched voltage $V_{\mathrm{dc,sw}}$ and current I. The voltage dependence can be considered linear, while the current dependence can be approximated by quadratic functions. This approach is valid for 2L-VSCs, regardless of the switch configuration. E_{sw}, instead, is characteristic of each device.

A.2. DC-LINK CAPACITORS

DC link capacitors in VSC must be sized following two main parameters:

- Capacitance, which is necessary to deliver their functionality;
- Current rating, which they need to withstand during the operation.

In this section, the modeling of these two aspects is presented.

A.2.1. CAPACITANCE REQUIREMENT

DC-link capacitors are used to limit the DC voltage ripple as an energy buffer. The capacitance required for such functionality can be derived according to [143]:

$$C_{\mathrm{dc}} \geq \frac{T_{\mathrm{r}} \cdot \Delta P}{(2 \cdot V_{\mathrm{dc}} \cdot \Delta V_{\mathrm{dc}})}, \quad \text{(A.29)}$$

where the load step is indicated with ΔP, T_{r} is the period during which the capacitors have to provide the load step power, which depends on the VSC control delay and it is usually selected as 5 to 10 modulation periods, and ΔV_{dc} is the allowed voltage deviation. This design consideration is important for the BESS' VSC since grid-connected BESS are required

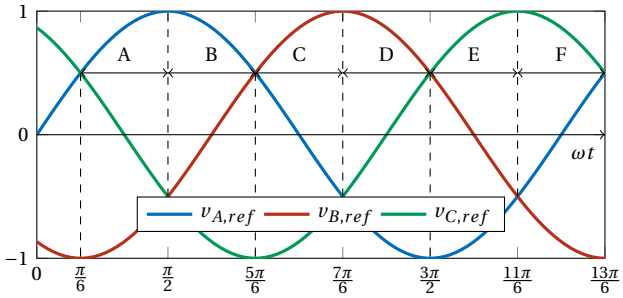

Figure A.2: Modulation waveforms, $v_{A,ref}$, $v_{B,ref}$, and $v_{C,ref}$, of a three-phase VSC with the highlighted sector division, A-F according to the relative position of the modulation waveforms.

to provide fast load steps, but also because of the grid connection standards which require fault tolerance and low voltage ride through [212, 239].

Regarding the voltage ripple limitation, DC-link capacitors ensure that the absolute partial DC-link voltage (the voltage across the upper and bottom capacitors) is higher than the maximum absolute AC phase-to-neutral voltage $\hat{V}_{\text{ac,max}}$, to allow a safe DC-AC power conversion, [215]:

$$\frac{V_{\text{dc,min}}}{2} - \frac{\Delta V_{\text{dc,r}}}{2} \geq \hat{V}_{\text{ac,max}}, \tag{A.30}$$

where $V_{\text{dc,min}}$ is the minimum battery DC voltage and $\Delta V_{\text{dc,r}}$ is the DC voltage ripple. Hence, the battery's open-circuit voltage variations due to the SoC, and the international grid codes, that require the normal operation for ±10% AC grid voltage deviation from the nominal value play a crucial role.

$V_{\text{dc,min}}$ and $\hat{V}_{\text{ac,max}}$ are dependent on the battery and grid conditions and cannot be controlled by the VSC. On the other hand, $\Delta V_{\text{dc,r}}$ depends on the loading conditions and the DC-link capacitance, and therefore it must be addressed in the VSC design stage.

As discussed in [174], the DC-link voltage ripple $\Delta V_{\text{dc,r}}$, for sinusoidal PWM (SPWM) modulation strategy, symmetrical grid, and balanced load, is composed of only the high-frequency components, and it can be expressed as:

$$\Delta V_{\text{dc,r}} = \frac{3m\hat{I}_{+}\cos\varphi}{8f_{\text{sw}}C_{\text{dc}}}(1+m), \tag{A.31}$$

where m is the modulation index, $\hat{I}_{+}$ is the peak value of the positive sequence current, $\cos\varphi$ is the power factor, and f_{sw} is the converter switching frequency. However, in the case of unbalanced fundamental frequency loading, other current components, namely the negative and zero sequences, can cause a ripple in the DC-link voltage, and therefore need to be carefully evaluated.

All in all, the DC-link capacitors have to be sized to fulfill several requirements, namely, the energy buffer, (A.29), limiting the DC-link voltage ripple to ensure a safe DC-AC energy conversion, (A.30), which in turn depends on the DC-link current harmonics. Each of these equations defines a minimum capacitance that satisfies the requirement, and therefore, the DC-link capacitance must be chosen as the largest between them, so that all the constraints are met.

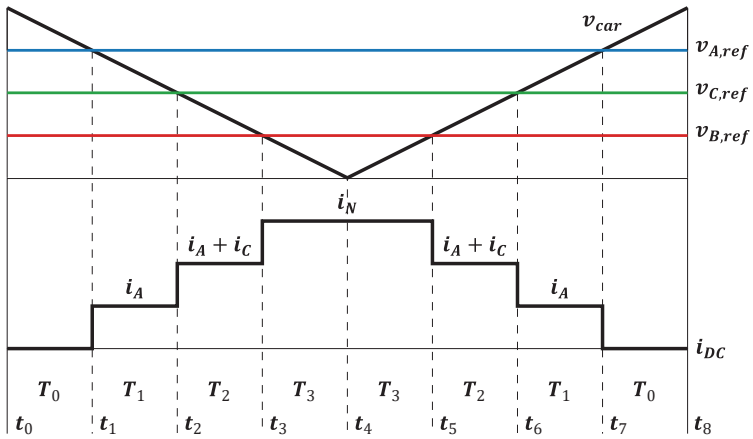

Figure A.3: Modulation, $v_{A,ref}$, $v_{B,ref}$, and $v_{C,ref}$, and carrier, v_{car}, waveforms over one carrier period for interval A of Fig. A.2 and current profile in the positive rail of the DC-link.

A.2.2. CURRENT CAPABILITIES

The DC-link current of a VSC is inevitably related to the nature of its AC currents. If these are unbalanced, the negative and zero sequence components, arise in the DC-link current. The approach used in [174] is extended here to consider all the sequence components. The three-phase currents can be decomposed into their respective symmetrical components and expressed as:

$$\begin{cases} i_{\mathrm{a}}(t) = \hat{I}_+ \sin(\omega \mathrm{t} - \phi_+) + \\ \qquad \hat{I}_- \sin(\omega_- \mathrm{t} - \phi_-) + \hat{I}_0 \sin(\omega_0 \mathrm{t} - \phi_0) \\ i_{\mathrm{b}}(t) = \hat{I}_+ \sin(\omega \mathrm{t} - \phi_+ - \dfrac{2\pi}{3}) + \\ \qquad \hat{I}_- \sin(\omega_- \mathrm{t} - \phi_- + \dfrac{2\pi}{3}) + \hat{I}_0 \sin(\omega_0 \mathrm{t} - \phi_0) \\ i_{\mathrm{c}}(t) = \hat{I}_+ \sin(\omega \mathrm{t} - \phi_+ + \dfrac{2\pi}{3}) \\ \qquad + \hat{I}_- \sin(\omega_- \mathrm{t} - \phi_- - \dfrac{2\pi}{3}) + \hat{I}_0 \sin(\omega_0 \mathrm{t} - \phi_0) \end{cases} \tag{A.32}$$

where $\hat{I}_+$, $\hat{I}_-$, $\hat{I}_0$ are the positive, negative and zero-sequence currents peak values, ω, ω_-, and, ω_0 the angular frequencies, and ϕ_+, ϕ_-, ϕ_0 are the phase-angle differences of the positive, negative and zero-sequence currents with their respective voltage reference vector. In the following derivation, $\hat{I}$ denotes the peak current value and I the rms value. The phase output currents are assumed to be perfect sinusoidal currents, neglecting the high-frequency ripple. The converter side AC current ripple can be limited with an LCL filter designed to have a large converter side inductance [217]. Furthermore, the DC-link current derivation is based on the fact that the switching frequency, f_{sw} is much larger than the grid frequency, f_{g}, so that in a switching period the quantities at grid frequency can be approximated as a constant.

In this context, one grid frequency period can be divided into six sub-periods, depending on the relative position between the three-phase reference voltages, and therefore on

the switching sequence of the upper switches during a switching period, T_{sw}, as shown in Fig. A.2. In one interval, the DC-link current in the positive rail can be derived according to the switching sequence of the upper switches, which is given by the position between the voltage reference signals and the carrier waveform. Fig. A.3 shows the DC-link current profile during a switching period in the interval *A*. When the modulating waveform, $v_{\text{A,ref}}$, $v_{\text{B,ref}}$, or $v_{\text{C,ref}}$, is above than the carrier signal, v_{car}, the upper switch of that half-bridge leg will turn on and therefore the current of that phase will flow through the positive rail of the DC-link. When all the three upper switches are turned on, the three AC phase currents are summed in the positive rail of the DC-link, and the resulting current will be equal to three times the zero-sequence current $i_{\text{n}} = 3 \cdot i_0$.

Then, starting from the interval T_0, one can see that the carrier waveform v_{car} is above all the modulation waveforms, therefore the upper switches of the three half-bridge legs are turned off. Consequently i_{dc}=0. During T_1 only $v_{A,ref}$ is above v_{car} and so $i_{dc} = i_a$, during T_2 instead $v_{A,ref}$ and $v_{C,ref}$ are above v_{car} and so $i_{dc} = i_a + i_c$. In T_3 sees all modulation waveforms above the carrier and so $i_{dc} = i_n$ in all intervals. Following this method, it is possible to derive the waveform of i_{dc} during interval A. Accordingly, the mean square value of i_{dc} during interval A can be found as:

$$\begin{aligned} I_{\text{dc},A}^2 &= \frac{1}{T_{\text{sw}}} \int_{t_0}^{t_8} i_{\text{dc}}^2 \text{dt} \\ &= \frac{2T_1}{T_s} i_a^2 + \frac{2T_2}{T_s} (i_a + i_c)^2 + \frac{2T_3}{T_{\text{sw}}} i_n^2 \end{aligned} \tag{A.33}$$

The same approach can be extended to intervals B-F. These intervals only differ from each other by the relative position of the modulation waveforms, therefore, the methodology applied in one interval can be directly applied in the other ones, with only difference in the i_{dc} values in T_1 and T_2 of Fig. A.3.

Finally, the total DC-link *rms* current can be found summing the mean square components of each interval, and substituting the expression of (A.32) to i_a, i_b, and i_c, resulting in:

$$\begin{aligned} I_{\text{dc}}^2 = \frac{\sqrt{3}}{4\pi} \cdot \Big[&\left(1 + 4\cos^2\phi_1\right) \hat{I}_+^2 m + 3m\hat{I}_-^2 + \\ &\left(\sqrt{3}\pi - 2m\right) 3\hat{I}_0^2 - 2m\hat{I}_- \hat{I}_0 \cos\left(\phi_- + \phi_0\right) \Big] \end{aligned} \tag{A.34}$$

where m stands for the modulation index, which is function of the peak single-phase AC voltage, $\hat{V}_{\text{ac}}$, and the total DC-link voltage, V_{dc}, and it is defined as $m = {}^{2 \cdot \hat{V}_{\text{ac}}}/_{V_{\text{dc}}}$.

Equation (A.34) predicts the full DC-link *rms* current, considering all its harmonic components: the high-frequency, the DC, the 50Hz, and the 100Hz sequence components. This equation is therefore the starting point for the estimation of the current flowing through the capacitors and the battery.

In case of balanced VSC operation, the negative and zero sequence components in (A.32) are equal to zero, and therefore, (A.34) becomes:

$$I_{\text{dcl}} = \hat{I} \sqrt{M \left[\frac{\sqrt{3}}{4\pi} + \left(\frac{\sqrt{3}}{\pi} - \frac{9}{16} M \right) \cos^2 \varphi \right]}. \tag{A.35}$$

which only comprises the high-frequency harmonics consequence of the symmetric power conversion.

The average value of the DC-link current defines the active power flowing through the converter. It can flow only from and to the battery since the other elements cannot deliver continuous active power. Therefore, the average DC-link current for one fundamental period of the converter is given by only the positive sequence component, and it can be derived equalling the converter's active DC and AC powers:

$$I_{\mathrm{dc,avg}} \cdot V_{\mathrm{dc}} = 3 V_{ac} I_{+} \cos\phi_{+}. \tag{A.36}$$

$$I_{\mathrm{dc,avg}} = \frac{3 m \hat{I}_{+}}{4} \cos\phi_{+}. \tag{A.37}$$

A.3. LCL FILTER

VSCs are typically controlled by PWM methods, which intrinsically generate harmonics in the AC output terminal. However, the connection to the main network requires compliance with several standards that regulate, i.e., the current harmonic limits [101]. In this context, LCL filters are widely adopted for the reduction of high-order harmonics. In this Section, the LCL filter design procedure which has been used in the thesis is explained.

A.3.1. FILTER PARAMETER SELECTION

According to the IEEE 519-2014 standard, high frequency odd current harmonics (h >35) need to be contained to less than 0.3% of the nominal line frequency current, I_{n}, and even harmonics to 0.075% of it [101]. The amplitude of the h^{th} current harmonic produced by the converters can be calculated as the ratio between the peak harmonic voltage and the filter impedance at that specific frequency. The voltage harmonic spectrum for the three-wire two-level VSC operated with PWM modulation can be analytically calculated through double Fourier integration [93]. The first relevant harmonic is the side-band $f_{\mathrm{s}} - 2f_{\mathrm{g}}$, thus, starting from this harmonic, the filter needs to be able to provide the minimum required attenuation that guarantees the compliance to the standards. The -60 dB slope of the filter transfer function will effectively further attenuate the higher-order harmonics. Once obtained the harmonic voltage amplitude, if $f_{\mathrm{s}} - 2f_{\mathrm{g}} > 35 f_{\mathrm{g}}$, the required attenuation, according to the IEEE 519 standard, can be found through equation (A.38):

$$Att_{\mathrm{IEEE-519}} = 0.003 \frac{P_{\mathrm{nom}}}{\sqrt{3} V_{\mathrm{ll}} V_{1,-2}}. \tag{A.38}$$

where P_{nom} is the nominal power of the converter, V_{ll} is the line-to-line AC voltage, and $V_{1,-2}$ is the $f_{\mathrm{s}} - 2f_{\mathrm{g}}$ side-band harmonic voltage. The transfer function of a LCL filter is given by equation (A.39):

$$H(s) = \frac{\omega_{\mathrm{res}}^2}{s\left(L_{\mathrm{g}} + L_{\mathrm{c}}\right)\left(s^2 + \omega_{\mathrm{res}}^2\right)}, \tag{A.39}$$

where:

$$\omega_{\mathrm{res}} = k_{\mathrm{res}} \omega_{\mathrm{s}} = \sqrt{\frac{L_{\mathrm{c}} + L_{\mathrm{g}}}{L_{\mathrm{c}} L_{\mathrm{g}} C}} \tag{A.40}$$

and L_c and L_g are respectively the converter side and grid side inductances and C the capacitance of the filter. The resonance frequency of the filter needs to be carefully evaluated to avoid the amplification of the side-band harmonics and to guarantee control stability [263]. Knowing the attenuation required, as defined in Equation (A.38), and given the LCL filter transfer function, Equation (A.39), the minimum total inductance that guarantees standards' compliance can be found as:

$$L_{\text{tot,min}} = \frac{k_{\text{res}}^2 \omega_s^2}{\omega_h \left(\omega_h^2 - k_{\text{res}}^2 \omega_s^2\right) A t t_{\text{IEEE}-519}}. \tag{A.41}$$

The maximum value of L_{tot}, instead, is limited by the voltage drop across the filter. For S-PWM, Equation (A.42) gives the upper boundary [110]:

$$L_{\text{tot,max}} = \frac{\sqrt{\frac{V_{\text{dc}}^2}{8} - \frac{V_{\text{ll}}^2}{3}}}{2\pi f_c I_n} \tag{A.42}$$

As shown in Equation (A.39), the harmonic attenuation in the grid side current for a fixed filter resonance frequency is given by the sum of the converter side L_c and grid side L_g inductances. Additionally, the converter side inductance, for a fixed filter resonance frequency, defines the amplitude of the AC current ripple flowing through the semiconductors, since the transconductance $Y_{1,1} = i_1 / v_1$ that defines the convert side current harmonics is expressed as:

$$Y_{11}(s) = \frac{s^2 + \omega_{\text{lc}}^2}{sL_c(s^2 + \omega_{\text{res}}^2)}, \tag{A.43}$$

where:

$$\omega_{\text{lc}} = \frac{1}{CL_c}. \tag{A.44}$$

The grid side inductance, L_g, can be found subtracting L_c from L_{tot}. Having the values of the inductances L_c and L_g and fixing the resonance frequency, the capacitance value is derived rearranging Equation (A.39). The maximum reactive power absorption at grid frequency gives the upper boundary for the capacitance value, usually limited to 5% of the nominal power. The reactive power injected by the capacitor needs to be compensated by the converter, lowering its efficiency, especially at low partial loads. Once defined the parameter boundaries, several possible designs for the LCL filter can be found by varying L_c, and the optimal one is chosen depending on the VSC application.

A.3.2. INDUCTORS DESIGN

The bulk of the losses in the LCL filter is usually found in the converter side inductor since the high-frequency ripple will flow through it, affecting both high-frequency winding losses and core losses. Starting from the core material permeability μ, the mean magnetic path length $l[m]$ and the effective cross area section $A[m^2]$, the number of turns that give the required inductance $L[H]$ can be found as:

$$N = \sqrt{\frac{Ll}{0.4\mu\pi A 10^{-2}}}. \tag{A.45}$$

Then, the total winding length l_w can be found according to the number of turns N and the core material dimensions. The power losses in the inductors can be separated into winding losses, due to the skin and proximity effect, and core losses:

$$P_{ind} = P_{skin} + P_{prox} + P_{core}. \tag{A.46}$$

The skin effect losses are evaluated through:

$$P_{skin} = l_w R_{ac} \hat{I}_{hf}^2 + \frac{1}{2} l_w R_{dc} \hat{I}^2, \tag{A.47}$$

where $\hat{I}_{hf}$ is the high-frequency peak current, $\hat{I}$ the peak sinusoidal AC current, R_{ac} and R_{dc} are the AC and DC resistance of the windings, and δ the skin depth which are found according to the wire diameter d and its conductance σ:

$$R_{dc} = \frac{4}{\sigma d^2 \pi}, \tag{A.48}$$

$$\delta = \frac{1}{\sqrt{\pi \mu_0 \sigma f}}. \tag{A.49}$$

The AC resistance of the inductor winding, instead, is calculated through the analytical approximation given by [280]:

$$R_{ac} = R_{dc} \frac{\gamma}{4\sqrt{2}} \left(\frac{\mathrm{ber}_0\gamma \mathrm{bei}_1\gamma - \mathrm{bei}_0\gamma \mathrm{ber}_1\gamma}{\mathrm{ber}_1^2\gamma + \mathrm{bei}_1^2\gamma} - \frac{\mathrm{bei}_0\gamma \mathrm{ber}_1\gamma - \mathrm{bei}_0\gamma \mathrm{bei}_1\gamma}{\mathrm{ber}_1^2\gamma + \mathrm{bei}_1^2\gamma} \right) \tag{A.50}$$

with ber_r and bei_i the real and imaginary parts of the Kelvin function of the i^{th} order, and γ defined as:

$$\gamma = \frac{d}{\sqrt{2}\delta}. \tag{A.51}$$

The proximity effect losses depend on the external magnetic field $\hat{H}_e$, derived following the approach of [62], and can be calculated as [280, 153]:

$$P_{prox} = R_{dc} G_R \hat{H}_e^2 \tag{A.52}$$

$$G_R = \frac{\gamma \pi^2 d^2}{2\sqrt{2}} \left(\frac{\mathrm{ber}_2\gamma \mathrm{ber}_1\gamma - \mathrm{ber}_2\gamma \mathrm{bei}_1\gamma}{\mathrm{ber}_0^2\gamma + \mathrm{bei}_0^2\gamma} + \frac{\mathrm{bei}_2\gamma \mathrm{bei}_1\gamma - \mathrm{bei}_2\gamma \mathrm{ber}_1\gamma}{\mathrm{ber}_0^2\gamma + \mathrm{bei}_0^2\gamma} \right) \tag{A.53}$$

Equations (A.47)-(A.53) are then applied for evaluating the winding losses caused by each current harmonic in which the current flowing through the inductor can be decomposed. Finally, the total winding losses are found by summing the contribution of each harmonic.

The core losses are calculated through the *improved Generalized Steinmetz Equation* (iGSE). For a triangular waveform the iGSE takes the following formulation [192]:

$$P_{core} = k f_s \left(\frac{2}{\pi^2} 4 f_s \right)^{\alpha - 1} \hat{B}^\beta V_{core} \tag{A.54}$$

$$k = \frac{k}{(2\pi)^{\alpha-1} \int_0^{2\pi} |\cos\theta|^\alpha 2^{\beta-\alpha} \mathrm{d}\theta} \tag{A.55}$$

where V_{core} is the core volume, k, α and β are the Steinmetz parameters derived from the core material, and $\hat{B}$ is the peak to peak flux density given in Equation (A.56) as a function of the peak to peak current ripple $I_{\text{r,pp}}$ and the inductor geometry:

$$\hat{B} = \frac{LI_{\text{r,pp}}}{2NA} \tag{A.56}$$

As previously mentioned, the *iGSE* estimates the core losses derived by a triangular-shaped current. The total inductor core losses are then calculated by summing the contribution of each triangular minor loop in which the switched current can be divided and averaging the total in the 50 Hz period.

B

EXPERIMENTAL SETUPS

In the development of this thesis, several hardware platforms have been used. This Chapter describes their components and functionalities.

B.1. DOUBLE PULSE TESTER

A double pulse testing platform has been used for the characterization of conduction and switching performances of power semiconductors. The experimental implementation of the double pulse tester is shown in Figure B.1(a), together with the semiconductor board and its gate driver in Figure B.1(b), and the thermal management devices and their arrangement together with the semiconductors in Figure B.1(c). This platform can be used to characterize single or multiple discrete TO-247 devices, and standard 62mm^2 modules.

The circuit schematic of the single and double pulse tests (SPT and DPT) are illustrated in Figure B.2(a)-(b). To control the temperature of the device under test, a heating resistor MP9100-100 and an NTC thermistor TO-103J2F are attached to the semiconductors' heatsink. The thermal circuit for the control and monitoring of the semiconductor case temperature is shown in Figure B.2(c). Additionally, during the tests, a FLIR thermal camera is used to ensure that the temperature is within the test range.

SINGLE PULSE TEST

The forward conduction losses are evaluated through a resistive SPT where a resistive load is connected in parallel to a diode and a short pulse is sent to the bottom switch [Fig B.2(b)]. The pulse width is selected to be 15 μs, to limit self-heating, but long enough to compensate for the parasitic circuit voltage drops. For the reverse conduction characteristics, the circuit is slightly modified and the device under test is connected between a switch and the DC capacitors with the emitter/source connected with the emitter of the switch [Fig B.2(a)]. A low DC voltage, in the range of 5-20 V, is impressed across the half-bridge so that low voltage probes can be used for measuring the voltage drop over the switch, guaranteeing higher accuracy since the voltage across the switch under test is in the order of few volts.

DOUBLE PULSE TEST

The switching performances are characterized by inductive DPT, as illustrated in Figure B.2(a). After the deskew of the measurement probes the switching losses can then be cal-

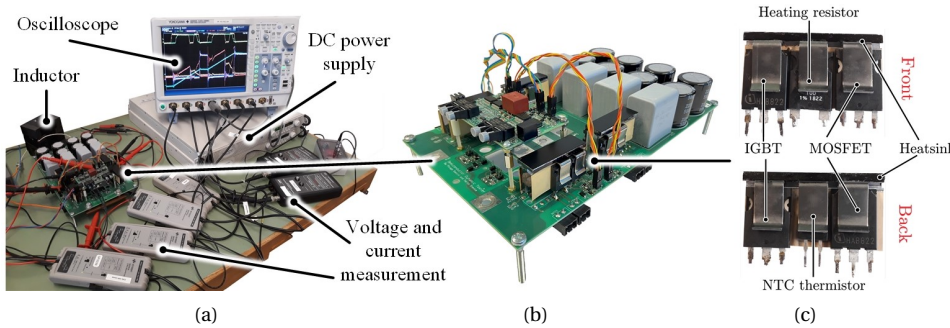

Figure B.1: (a) Test set up, (b) DPT board with gate driver on top, and (c) semiconductors and thermal management devices for the characterization of the semiconductors devices.

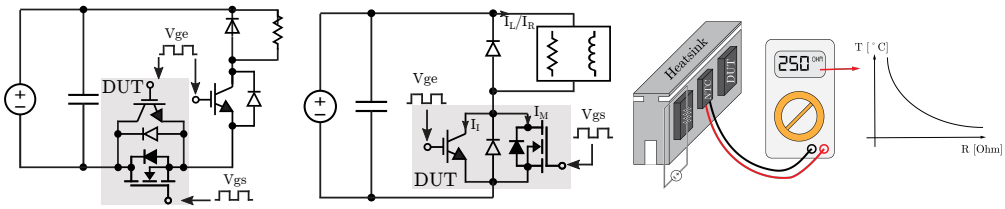

Figure B.2: Electrical circuit schematics for the experimental derivation of (a) the reverse conduction characteristics of various switches, (b) the forward conduction and switching characteristics, and (c) the thermal circuit for the control and monitoring of the semiconductor case temperature.

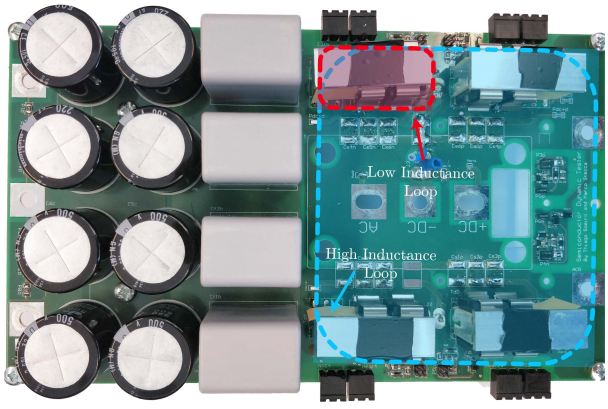

Figure B.3: Large (blue) and low (red) inductance commutation loops between parallel switches in the experimental prototype.

culated by multiplying the voltage and current waveforms during the switching event, as detailed in the datasheets of the components [103, 196].

PARALLELING MULTIPLE SWITCHES

In the case of hybrid switches, which are assembled through paralleling multiple switches, there are additional commutation events, as explained in Section 4.2. In this context, the parasitic inductance between the switches plays an important role. The DPT board can be used to investigate the effect of the stray inductances. As shown in B.3, two arrangements for the semiconductors can be used, leading to different parasitic inductances, estimated to be 50nH and 140nH.

B.2. 10KW TWO LEVEL VOLTAGE SOURCE CONVERTER

The 10kW 2L-VSC laboratory prototype is shown in Figure B.4, with at the bottom the output LCL filter. This 10kW prototype has been used for the efficiency benchmark of various switch technology when operating as an inverter supplying a resistive load. The input DC voltage can be set as high as 800 V, the switching frequency, instead, is limited by the semiconductor used. This prototype can be configured to operate with discrete TO-247 packaged Si-IGBT, SiC-MOSFET, and hybrid switches as well. The LCL filter at the bottom

Figure B.4: Prototype of the 10kW 2L-VSC used for the efficiency testing of the mcHyS with LCL filter in the bottom.

is assembled with the commercially available 750343810 inductors from Wurth Electronics rated 340mH both in the converter and in the grid side, L_c and L_g, and 9.9 uF capacitance, C.

This prototype has been used to benchmark the efficiency of different switch technologies. The efficiency, evaluated through the Yokogawa WT500 Power Analyzer, has been measured between the DC side of the VSC and the converter side inductance of the LCL filter, L_c. In this way, both the losses of the 2L-VSC and L_c are measured. The circuit schematic of the efficiency measurement is illustrated in Figure B.5. The power analyzer connection after L_c has been selected to ensure that the efficiency measurement has high accuracy, since the switched voltage at the output of the VSC has very high $^{dv}/_{dt}$ and cannot be properly measured by the power analyzer, while after L_c the voltage has a more sinusoidal shape with much lower $^{dv}/_{dt}$ than the WT500 power analyzer can accurately measure.

B.3. BATTERY CELL TESTER

The application of BESS as a power redistributor leads to additional current harmonic components flowing through the VSC DC-link and ultimately through the battery cells. To evaluate the impact of these additional current harmonics on battery performance and degradation, battery cells need to be tested.

The battery test setup consists of the Arbin Laboratory Battery Testing LBT22043 [9] which allows precision measurements for simultaneous testing and characterization of up to 16 battery cells. The battery tester can be seen in Figure B.6. the battery tester allows the simultaneous testing of 16 cells, with a maximum current of +/- 10A and a cell voltage of up to 25V. The tested cells are the ICR18650-26F from Samsung SDI, based on the NMC cathode technology, which is well suitable for stationary application [214]. Their nominal voltage is 3.7V, and they have a rated capacity of 2600 mAh. These low-voltage cells are the building blocks for high-capacity battery packs. Several lithium-ion cells of this kind can be stacked together in series and parallel strings to assemble battery packs with higher volt-

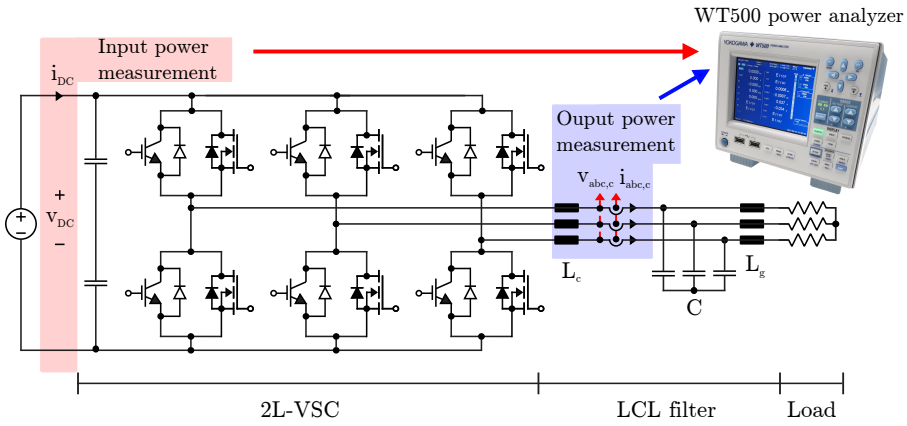

Figure B.5: Circuit schematic of a 2L-VSC operating as inverter supplying a resistive load. The connection points for the efficiency measurements through the WT500 power analyzer are highlighted.

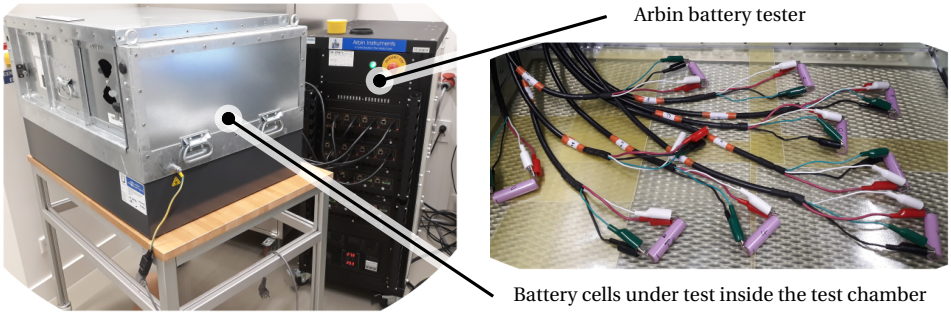

Figure B.6: Battery cells test set up consisting of test chamber and the Arbin Laboratory Battery Testing LBT22043 used to perform the power cycling tests.

age and capacity ratings. The battery tester provides built-in testing functions of standard modes, such as Constant Current (CC), Constant Voltage (CV), and Constant Power (CP). Furthermore, it is fully programmable, so that custom current, voltage, or power profiles can be uploaded and used to test the cells, with a minimum time step of 1ms.

B.4. HARDWARE IN THE LOOP

An Hardware in the Loop setup has been built to evaluate the behavior of a BESS when integrated into a distribution grid. The setup consists of a VSC, shown in Figure B.8 (a), which interfaces an SM500-CP-90 DC voltage source from Delta Elektronika, representing a battery storage, with the GE15 AC source from Cinergia, which emulates the AC distribution grid. An LCL filter, shown in Figure B.8 (b), between the VSC and the AC grid is used to attenuate the current harmonics according to the IEEE-519/2014 [101]. The VSC is digitally controlled, with Sinusoidal PWM, through an OP5700 real-time simulator from OPAL-RT Technologies. Additionally, the OP5700 can be used to emulate in real-time a distribution grid, such as the one of Figure 2.12, so to evaluate the grid impact of the BESS.

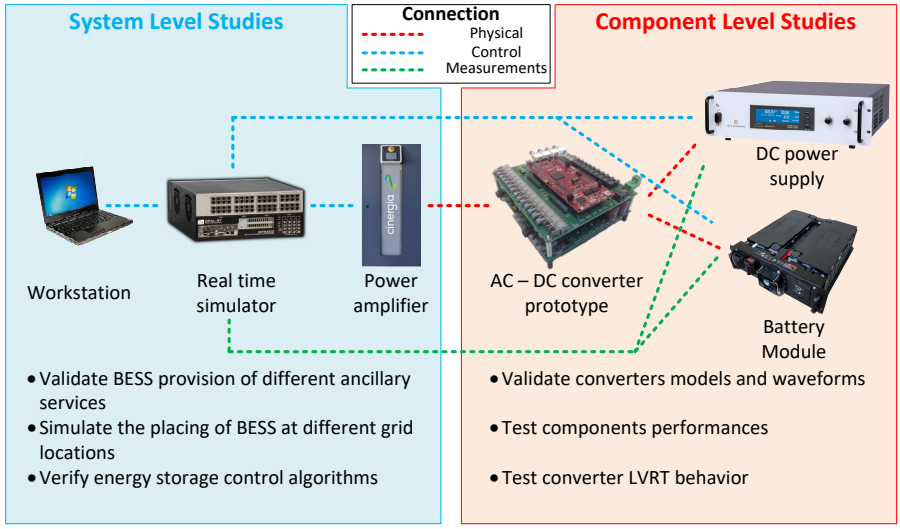

Figure B.7: Hardware in the loop set-up and its functionalities.

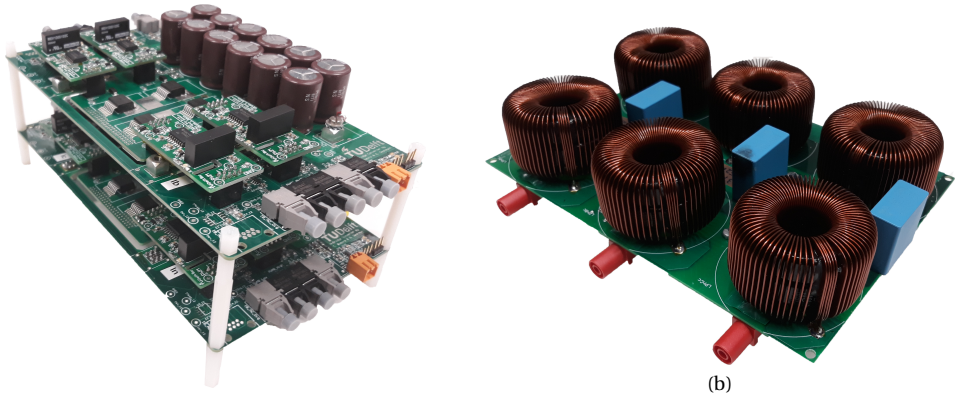

(a) (b)

Figure B.8: (a) Three-phase legs two-level VSC prototype used for the experimental verification of the BESS functionality as power redistributor, and (b) LCL filter used to interface the VSC to the AC grid.

BIBLIOGRAPHY

[1] Mohammad A. Abusara, Josep M. Guerrero, and Suleiman M. Sharkh. "Line-interactive UPS for microgrids". In: *IEEE Trans. Ind. Electron.* 61.3 (2014), pp. 1292–1300. ISSN: 02780046. DOI: 10.1109/TIE.2013.2262763.

[2] R S C Advances et al. "Progress in redox flow batteries, remaining challenges and their applications in energy storage". In: *RSC Adv.* 2.27 (2012), pp. 10125–10156. ISSN: 20462069. DOI: 10.1039/c2ra21342g.

[3] Hossein Akhavan-Hejazi and Hamed Mohsenian-Rad. "Energy Storage Planning in Active Distribution Grids: A Chance-Constrained Optimization With Non-Parametric Probability Functions". In: *IEEE Trans. Smart Grid* 9.3 (2018), pp. 1972–1985. ISSN: 19493053. DOI: 10.1109/TSG.2016.2604286.

[4] *Alfen B.V.* URL: https://alfen.com/nl/nieuws/solar-global-kiest-voor-mega-energieopslagsysteem-van-alfen.

[5] Sahban W. Alnaser and Luis F. Ochoa. "Optimal Sizing and Control of Energy Storage in Wind Power-Rich Distribution Networks". In: *IEEE Trans. Power Syst.* 31.3 (2016), pp. 2004–2013. ISSN: 08858950. DOI: 10.1109/TPWRS.2015.2465181.

[6] Judy M. Amanor-Boadu et al. "Search for optimal pulse charging parameters for li-ion polymer batteries using taguchi orthogonal arrays". In: *IEEE Trans. Ind. Electron.* 65.11 (2018), pp. 8982–8992. ISSN: 02780046. DOI: 10.1109/TIE.2018.2807419.

[7] Mathew Aneke and Meihong Wang. "Energy storage technologies and real life applications – A state of the art review". In: *Appl. Energy* 179 (2016), pp. 350–377. ISSN: 03062619. DOI: 10.1016/j.apenergy.2016.06.097. URL: http://dx.doi.org/10.1016/j.apenergy.2016.06.097.

[8] Kyriaki E Antoniadou-Plytaria et al. "Distributed and Decentralized Voltage Control of Smart Distribution Networks". In: *IEEE Trans. Smart Grid* 8.6 (2017), pp. 2999–3008. ISSN: 1949-3053. DOI: 10.1109/TSG.2017.2679238T4-Models,Methods,andFutureResearchM4-Citavi. URL: https://doi.org/10.1109/TSG.2017.2679238.

[9] *Arbin Instruments.* URL: https://www.arbin.com/products/battery-test-equipment/.

[10] Prabha Ariyaratna, Kashem M. Muttaqi, and Danny Sutanto. "A novel control strategy to mitigate slow and fast fluctuations of the voltage profile at common coupling Point of rooftop solar PV unit with an integrated hybrid energy storage system". In: *J. Energy Storage* 20.July (2018), pp. 409–417. ISSN: 2352152X. DOI: 10.1016/j.est.2018.10.016. URL: https://doi.org/10.1016/j.est.2018.10.016.

[11] ASTM International. *ASTM E1049-85(2017) - Standard Practices for Cycle Counting in Fatigue Analysis.* 2011. URL: https://www.astm.org/cgi-bin/resolver.cgi?E1049.

[12] Autoriteit Consument & Market (ACM). *Netcode elektriciteit*. 2016. URL: https://wetten.overheid.nl/BWBR0037940/2019-10-22.

[13] Ahmed S.A. Awad, Tarek H.M. EL-Fouly, and Magdy M.A. Salama. "Optimal ESS Allocation for Benefit Maximization in Distribution Networks". In: *IEEE Trans. Smart Grid* 8.4 (2017), pp. 1668–1678. ISSN: 19493053. DOI: 10.1109/TSG.2015.2499264.

[14] Lennart Baruschka and Axel Mertens. "Comparison of cascaded H-bridge and modular multilevel converters for BESS application". In: *IEEE Energy Convers. Congr. Expo. Energy Convers. Innov. a Clean Energy Futur. ECCE 2011, Proc.* (2011), pp. 909–916. DOI: 10.1109/ECCE.2011.6063868.

[15] Reinhold Bayerer et al. "Model for Power Cycling lifetime of IGBT Modules". In: *Integr. Power Syst. (CIPS), 2008 5th Int. Conf.* (2008), pp. 1–6.

[16] Alexander Bessman et al. "Challenging Sinusoidal Ripple-Current Charging of Lithium-Ion Batteries". In: *IEEE Trans. Ind. Electron.* 65.6 (2018), pp. 4750–4757. ISSN: 02780046. DOI: 10.1109/TIE.2017.2772160.

[17] Sing Bhim, Kamal Al-Haddad, and Ambrish Chandra. "Harmonic elimination, reactive power compensation an load balancing in three-phase, four-wire electric distribution systems supplying non-linear loads". In: *Electr. Power Syst. Res.* 44 (1998), pp. 93–100.

[18] Hemant Bishnoi et al. "Analysis of EMI terminal modeling of switched power converters". In: *IEEE Trans. Power Electron.* 27.9 (2012), pp. 3924–3933. ISSN: 08858993. DOI: 10.1109/TPEL.2012.2190100.

[19] BloombergNEF. 2019. URL: https://about.bnef.com/blog/behind-scenes-take-lithium-ion-battery-prices/.

[20] BloombergNEF. 2022. URL: https://about.bnef.com/blog/lithium-ion-battery-pack-prices-rise-for-first-time-to-an-average-of-151-kwh/.

[21] Michael Bragard et al. "The Balance of Renewable Sources and User Demands in Grids : Power Electronics for Modular Battery Energy Storage Systems". In: *IEEE Trans. Power Electron.* 25.12 (2010), pp. 3049–3056.

[22] Claudio Brivio et al. "A Physically-Based Electrical Model for Lithium-Ion Cells". In: *IEEE Trans. Energy Convers.* 34.2 (2019), pp. 594–603. ISSN: 08858969. DOI: 10.1109/TEC.2018.2869272.

[23] Ralph Burkart and Johann W. Kolar. "Component cost models for multi-objective optimizations of switched-mode power converters". In: *2013 IEEE Energy Convers. Congr. Expo. ECCE 2013* (2013), pp. 2139–2146. DOI: 10.1109/ECCE.2013.6646971.

[24] BYD. *B-Box BYD*. URL: https://en.byd.com/energy/b-box-ess/.

[25] Raymond H. Byrne et al. "Energy Management and Optimization Methods for Grid Energy Storage Systems". In: *IEEE Access* 6 (2017), pp. 13231–13260. ISSN: 21693536. DOI: 10.1109/ACCESS.2017.2741578.

[26] Raymond H. Byrne et al. "Energy Management and Optimization Methods for Grid Energy Storage Systems". In: *IEEE Access* 6 (2017), pp. 13231–13260. ISSN: 21693536. DOI: 10.1109/ACCESS.2017.2741578.

[27] C. Brivio. “Battery energy storage systems: Modelling, applications and design criteria”. PhD thesis. 2012, pp. 1–223. URL: http://hdl.handle.net/10589/136844.

[28] Alison R. Camargo, Carlos A. Castro, and Marina Lavorato. “Optimal allocation of energy storage devices in distribution systems considering lifetime characteristics of batteries”. In: *2016 IEEE Int. Conf. Power Syst. Technol. POWERCON 2016* (2016), pp. 1–6. DOI: 10.1109/POWERCON.2016.7753965.

[29] Aldo Canova et al. “Electrical impact of photovoltaic plant in distributed network”. In: *IEEE Trans. Ind. Appl.* 45.1 (2009), pp. 341–347. ISSN: 00939994. DOI: 10.1109/TIA.2009.2009726.

[30] Guido Carpinelli et al. “Optimal integration of distributed energy storage devices in smart grids”. In: *IEEE Trans. Smart Grid* 4.2 (2013), pp. 985–995. ISSN: 19493053. DOI: 10.1109/TSG.2012.2231100. arXiv: 10 [1540-7977].

[31] Giorgio Castagneto Gissey, Paul E. Dodds, and Jonathan Radcliffe. “Market and regulatory barriers to electrical energy storage innovation”. In: *Renew. Sustain. Energy Rev.* 82.July 2017 (2018), pp. 781–790. ISSN: 18790690. DOI: 10.1016/j.rser.2017.09.079.

[32] CEI - Comitato Elettrotecnico Italiano. *CEI 0-16*. 2019. URL: https://www.ceinorme.it/it/norme-cei-0-16-e-0-21.html.

[33] CENELEC. “EN 50160 - Voltage characteristics of electricity supplied by public distribution systems”. In: *Eur. Stand.* (2010).

[34] Efstratios Chatzinikolaou et al. “A Comparison of Grid-Connected Battery Energy Storage System Designs”. In: *IEEE Trans. Power Electron.* 32.9 (2017), pp. 6913–6923. ISSN: 08858993. DOI: 10.1109/TPEL.2016.2629020.

[35] Ephrem Chemali et al. “Electrochemical and Electrostatic Energy Storage and Management Systems for Electric Drive Vehicles: State-of-the-Art Review and Future Trends”. In: *IEEE J. Emerg. Sel. Top. Power Electron.* 4.3 (2016), pp. 1117–1134. ISSN: 21686785. DOI: 10.1109/JESTPE.2016.2566583.

[36] Haisheng Chen et al. “Progress in electrical energy storage system: A critical review”. In: *Prog. Nat. Sci.* 19.3 (2009), pp. 291–312. ISSN: 10020071. DOI: 10.1016/j.pnsc.2008.07.014. URL: http://dx.doi.org/10.1016/j.pnsc.2008.07.014.

[37] Liang Rui Chen et al. “Sinusoidal-ripple-current charging strategy and optimal charging frequency study for Li-ion batteries”. In: *IEEE Trans. Ind. Electron.* 60.1 (2013), pp. 88–97. ISSN: 02780046. DOI: 10.1109/TIE.2012.2186106.

[38] Bolong Cheng and Warren B. Powell. “Co-Optimizing Battery Storage for the Frequency Regulation and Energy Arbitrage Using Multi-Scale Dynamic Programming”. In: *IEEE Trans. Smart Grid* 9.3 (2018), pp. 1997–2005. ISSN: 19493053. DOI: 10.1109/TSG.2016.2605141.

[39] Shin-young Young Cho et al. “Battery Impedance Analysis Considering DC Component in Sinusoidal Ripple-Current Charging”. In: *IEEE Trans. Ind. Electron.* 63.3 (2016), pp. 1561–1573. ISSN: 02780046. DOI: 10.1109/TIE.2015.2497661.

[40] Bastien Chopard et al. “Particle swarm optimization”. In: *Nat. Comput. Ser.* 4 (2018), pp. 1942–1948. ISSN: 16197127. DOI: 10.1007/978-3-319-93073-2_6. arXiv: 9780201398298.

[41] Konstantina Christakou, Mario Paolone, and Ali Abur. “Voltage control in active distribution networks under uncertainty in the system model: A robust optimization approach”. In: *IEEE Trans. Smart Grid* 9.6 (2018), pp. 5631–5642. ISSN: 19493053. DOI: 10.1109/TSG.2017.2693212.

[42] Konstantina Christakou et al. “Primary voltage control in active distribution networks via broadcast signals: The case of distributed storage”. In: *IEEE Trans. Smart Grid* 5.5 (2014), pp. 2314–2325. ISSN: 19493053. DOI: 10.1109/TSG.2014.2319303.

[43] Kristien Clement, Edwin Haesen, and Johan Driesen. “Stochastic analysis of the impact of plug-in hybrid electric vehicles on the distribution grid”. In: *IET Conf. Publ.* 550 CP (2009), pp. 8–11. DOI: 10.1049/cp.2009.0590.

[44] Wesley Cole and A Will Frazier. *Cost Projections for Utility- Scale Battery Storage*. Tech. rep. Golded, CO: National Renewable Energy Laboratory, 2019. URL: https://www.nrel.gov/docs/fy19osti/73222.pdf.

[45] European Commission. 2022. URL: https://ec.europa.eu/commission/presscorner/detail/en/IP_22_7588.

[46] *Connection and Operation to Medium-Voltage Grid*. 2018. URL: VDE-AR-N4110.

[47] Javier Contreras et al. “ARIMA models to predict next-day electricity prices”. In: *IEEE Transactions on Power Systems* 18.3 (Aug. 2003), pp. 1014–1020. ISSN: 08858950. DOI: 10.1109/TPWRS.2002.804943.

[48] Cornell Dubilier. *500C Capacitors*. URL: https://www.cde.com/capacitors/aluminum-electrolytic/screw-terminal.

[49] Cornell Dublier. *Aluminum Electrolytic Capacitor Application Guide*. Tech. rep. URL: http://www.cde.com/resources/catalogs/AEappGUIDE.pdf.

[50] Cree Wolfspeed. *Cree Wolfspeed SiC Power Products*. URL: https://www.wolfspeed.com/power/products.

[51] A. F. Crossland, D. Jones, and N. S. Wade. “Planning the location and rating of distributed energy storage in LV networks using a genetic algorithm with simulated annealing”. In: *Int. J. Electr. Power Energy Syst.* 59 (2014), pp. 103–110. ISSN: 01420615. DOI: 10.1016/j.ijepes.2014.02.001. URL: http://dx.doi.org/10.1016/j.ijepes.2014.02.001.

[52] Adam Daggett, Meysam Qadrdan, and Nick Jenkins. “Feasibility of a battery storage system for a renewable energy park operating with price arbitrage”. In: *2017 IEEE PES Innov. Smart Grid Technol. Conf. Eur. ISGT-Europe 2017 - Proc.* 2018-Janua (2018), pp. 1–6. DOI: 10.1109/ISGTEurope.2017.8260249.

[53] Choton K. Das et al. “Overview of energy storage systems in distribution networks: Placement, sizing, operation, and power quality”. In: *Renew. Sustain. Energy Rev.* 91.November 2016 (2018), pp. 1205–1230. ISSN: 18790690. DOI: 10.1016/j.rser.2018.03.068. URL: https://doi.org/10.1016/j.rser.2018.03.068.

[54] Aniel Silva De Morais, Fernando Lessa Tofoli, and Ivo Barbi. “Modeling, digital control, and implementation of a three-phase four-wire power converter used as a power redistribution device”. In: *IEEE Trans. Ind. Informatics* 12.3 (2016), pp. 1035–1042. ISSN: 15513203. DOI: 10.1109/TII.2016.2544248.

[55] Joaquim Delgado et al. “Impacts of plug-in electric vehicles in the portuguese electrical grid”. In: *Transp. Res. Part D Transp. Environ.* 62.March (2018), pp. 372–385. ISSN: 13619209. DOI: 10.1016/j.trd.2018.03.005. URL: https://doi.org/10.1016/j.trd.2018.03.005.

[56] Amol Deshpande and Fang Luo. “Practical Design Considerations for a Si IGBT + SiC MOSFET Hybrid Switch: Parasitic Interconnect Influences, Cost, and Current Ratio Optimization”. In: *IEEE Trans. Power Electron.* 34.1 (2018), pp. 724–737. ISSN: 08858993. DOI: 10.1109/TPEL.2018.2827989.

[57] Amol Deshpande et al. “A Three-Level, T-Type, Power Electronics Building Block Using Si-SiC Hybrid Switch for High-Speed Drives”. In: *Conf. Proc. - IEEE Appl. Power Electron. Conf. Expo. - APEC* 2018-March (2018), pp. 2609–2616. DOI: 10.1109/APEC.2018.8341385.

[58] Alessandro Di Giorgio et al. “Model Predictive Control of Energy Storage Systems for Power Tracking and Shaving in Distribution Grids”. In: *IEEE Trans. Sustain. Energy* 8.2 (2017), pp. 496–504. ISSN: 19493029. DOI: 10.1109/TSTE.2016.2608279.

[59] Digi-Key. *Digi-Key Electronics*. URL: https://www.digikey.nl/.

[60] Boucar Diouf and Ramchandra Pode. “Potential of lithium-ion batteries in renewable energy”. In: *Renew. Energy* 76 (2015), pp. 375–380. ISSN: 18790682. DOI: 10.1016/j.renene.2014.11.058. URL: http://dx.doi.org/10.1016/j.renene.2014.11.058.

[61] Pablo Donolo, Guillermo Bossio, and Cristian De Angelo. “Analysis of voltage unbalance effects on induction motors with open and closed slots”. In: *Energy Convers. Manag.* 52.5 (2011), pp. 2024–2030. ISSN: 01968904. DOI: 10.1016/j.enconman.2010.10.045. URL: http://dx.doi.org/10.1016/j.enconman.2010.10.045.

[62] P.L. Dowell. “Effects of eddy currents in transformer windings”. In: *Proc. Inst. Electr. Eng.* 113.8 (1966), p. 1387. ISSN: 00203270. DOI: 10.1049/piee.1966.0236.

[63] Silvanus D’silva et al. “Towards Grid of Microgrids: Seamless Transition between Grid-Connected and Islanded Modes of Operation”. In: *IEEE Open J. Ind. Electron. Soc.* 1.June (2020), pp. 66–81. DOI: 10.1109/ojies.2020.2988618.

[64] Matthieu Dubarry and Arnaud Devie. “Battery durability and reliability under electric utility grid operations: Representative usage aging and calendar aging”. In: *J. Energy Storage* 18.May (2018), pp. 185–195. ISSN: 2352152X. DOI: 10.1016/j.est.2018.04.004. URL: https://doi.org/10.1016/j.est.2018.04.004.

[65] Roger C. Dugan, Jason A. Taylor, and Davis Montenegro. “Energy storage modeling for distribution planning”. In: *IEEE Trans. Ind. Appl.* 53.2 (2017), pp. 954–962. ISSN: 00939994. DOI: 10.1109/TIA.2016.2639455.

[66] Bruce Dunn, Haresh Kamath, and Jean-Marie Tarascon. “Electrical Energy Storage for the Grid : A Battery of Choices”. In: *Science (80-.).* 334.6058 (2011), p. 928. DOI: 10.1126/science.1212741.

[67] I. Dzafic, T. Donlagic, and S. Henselmeyer. “Fortescue transformations for three-phase power flow analysis in distribution networks”. In: *IEEE Power Energy Soc. Gen. Meet.* (2012), pp. 1–7. ISSN: 19449925. DOI: 10.1109/PESGM.2012.6345581.

[68] Hassan H. Eldeeb, Samy Faddel, and Osama A. Mohammed. "Multi-Objective Optimization Technique for the Operation of Grid tied PV Powered EV Charging Station". In: *Electr. Power Syst. Res.* 164.July (2018), pp. 201–211. ISSN: 03787796. DOI: 10.1016/j.epsr.2018.08.004. URL: https://doi.org/10.1016/j.epsr.2018.08.004.

[69] *Elia Group*. URL: https://www.elia.be/en/grid-data/balancing.

[70] ENTSO-E. *Transparency Platform*. 2021. URL: https://transparency.entsoe.eu/dashboard/show.

[71] Edgard Luiz Lopes Fabricio et al. "Analysis of Main Topologies of Shunt Active Power Filters Applied to Four-Wire Systems". In: *IEEE Trans. Power Electron.* 33.3 (2018), pp. 2100–2112. ISSN: 08858993. DOI: 10.1109/TPEL.2017.2698439.

[72] Jingyang Fang et al. "On the Inertia of Future More-Electronics Power Systems". In: *IEEE J. Emerg. Sel. Top. Power Electron.* 7.4 (2019), pp. 2130–2146. ISSN: 21686785. DOI: 10.1109/JESTPE.2018.2877766.

[73] M Farrokhifar, S Grillo, and E Tironi. "Loss Minimization in Medium Voltage Distribution Grids by Optimal Management of Energy Storage Devices". In: *2013 IEEE PowerTech Grenoble Conf.* (), pp. 1–5. DOI: 10.1109/PTC.2013.6652316.

[74] David Feldman, Eric O'Shaughnessy, and Robert Margolis. *Solar Industry Update*. Tech. rep. February. National Renewable Energy Laboratory, 2020, pp. 1–83. DOI: NREL/PR-6A20-68425.

[75] V. Fernão Pires et al. "Power converter interfaces for electrochemical energy storage systems - A review". In: *Energy Convers. Manag.* 86 (2014), pp. 453–475. ISSN: 01968904. DOI: 10.1016/j.enconman.2014.05.003.

[76] *Fluence*. URL: https://fluenceenergy.com/wp-content/uploads/2019/02/lb-essi-18-executive-summary.pdf.

[77] C. L. FORTESCUE. "Method of symmetrical co-ordinates applied to the solution of polyphase networks". In: *Trans. Am. Inst. Electr. Eng.* 37 (1918), pp. 1027–1140. ISSN: 00963860. DOI: 10.1109/T-AIEE.1918.4765570.

[78] T. Friedli and J. W. Kolar. "A semiconductor area based assessment of AC motor drive converter topologies". In: *Conf. Proc. - IEEE Appl. Power Electron. Conf. Expo. - APEC* 3.c (2009), pp. 336–342. DOI: 10.1109/APEC.2009.4802678.

[79] Ran Fu, David Feldman, and Robert Margolis. *U.S. Solar Photovoltaic System Cost Benchmark: Q1 2018*. Tech. rep. October. National Renewable Energy Laboratory, 2018, pp. 1–47. DOI: 10.7799/1325002. URL: https://www.nrel.gov/docs/fy16osti/66532.pdf.

[80] Jesse M. Gantz, S. Massoud Amin, and Anthony M. Giacomoni. "Optimal capacity partitioning of multi-use customer-premise energy storage systems". In: *IEEE Trans. Smart Grid* 5.3 (2014), pp. 1292–1299. ISSN: 19493053. DOI: 10.1109/TSG.2014.2312182.

[81] Xiang Gao et al. "Concurrent Voltage Control and Dispatch of Active Distribution Networks by Means of Smart Transformer and Storage". In: *IEEE Trans. Ind. Electron.* 65.8 (2018), pp. 6657–6666. ISSN: 02780046. DOI: 10.1109/TIE.2017.2772181.

[82] *Gestore dei Mercati Energetici S.p.A.* URL: https://www.mercatoelettrico.org/It/Statistiche/ME/DatiSintesi.aspx.

[83] Antonio Giannitrapani et al. "Optimal Allocation of Energy Storage Systems for Voltage Control in LV Distribution Networks". In: *IEEE Trans. Smart Grid* 8.6 (2017), pp. 2859–2870. ISSN: 19493053. DOI: 10.1109/TSG.2016.2602480.

[84] Etta Grover-Silva, Robin Girard, and George Kariniotakis. "Optimal sizing and placement of distribution grid connected battery systems through an SOCP optimal power flow algorithm". In: *Appl. Energy* 219.October 2017 (2018), pp. 385–393. ISSN: 03062619. DOI: 10.1016/j.apenergy.2017.09.008. URL: https://doi.org/10.1016/j.apenergy.2017.09.008.

[85] Ioannis Hadjipaschalis, Andreas Poullikkas, and Venizelos Efthimiou. "Overview of current and future energy storage technologies for electric power applications". In: *Renew. Sustain. Energy Rev.* 13.6-7 (2009), pp. 1513–1522. ISSN: 13640321. DOI: 10.1016/j.rser.2008.09.028.

[86] Seyedmostafa Hashemi and Jacob Østergaard. "Efficient Control of Energy Storage for Increasing the PV Hosting Capacity of LV Grids". In: *IEEE Trans. Smart Grid* 9.3 (2018), pp. 2295–2303. DOI: 10.1109/TSG.2016.2609892.

[87] Nikos D. Hatziargyriou et al. "Review of energy storage allocation in power distribution networks: applications, methods and future research". In: *IET Gener. Transm. Distrib.* 10.3 (2016), pp. 645–652. ISSN: 1751-8687. DOI: 10.1049/iet-gtd.2015.0447. URL: http://digital-library.theiet.org/content/journals/10.1049/iet-gtd.2015.0447.

[88] Samir Hazra et al. "Design Considerations and Performance Evaluation of 1200-V 100-A SiC MOSFET-Based Two-Level Voltage Source Converter". In: *IEEE Trans. Ind. Appl.* 52.5 (2016), pp. 4257–4268.

[89] Reza Hemmati, Hedayat Saboori, and Mehdi Ahmadi Jirdehi. "Stochastic planning and scheduling of energy storage systems for congestion management in electric power systems including renewable energy resources". In: *Energy* 133 (2017), pp. 380–387. ISSN: 03605442. DOI: 10.1016/j.energy.2017.05.167. URL: http://dx.doi.org/10.1016/j.energy.2017.05.167https://linkinghub.elsevier.com/retrieve/pii/S036054421730957X.

[90] Holger C. Hesse et al. "Lithium-ion battery storage for the grid - A review of stationary battery storage system design tailored for applications in modern power grids". In: *Energies* 10.12 (2017), pp. 1–42. ISSN: 19961073. DOI: 10.3390/en10122107.

[91] A. Hillers and J. Biela. "Optimal design of the modular multilevel converter for an energy storage system based on split batteries". In: *2013 15th Eur. Conf. Power Electron. Appl. EPE 2013* (2013), pp. 1–11. DOI: 10.1109/EPE.2013.6634660.

[92] John H. Holland. *Adaptation in Natural and Artificial Systems*. Cambridge, MA, USA: MIT Press, 1992. ISBN: 0-262-58111-6.

[93] D Grahame Holmes and Thomas A Lipo. "Pulse Width Modulation for Power Converters: Principles and Practice". In: *Pulse Width Modul. Power Convert.* (), pp. 531–554.

[94] D. Grahame Holmes and Thomas A. Lipo. *Pulse Width Modulation for Power Converters: Principles and Practice*. 2003. ISBN: 0471234397. DOI: 10.1109/9780470546284.

[95] Hui Huang and P A Mawby. "A Lifetime Estimation Technique for Voltage Source Inverters". In: *IEEE Trans. Power Electron.* 28.8 (2013), pp. 4113–4119.

[96] H Ibrahim, A Ilinca, and J Perron. "Energy storage systems — Characteristics and comparisons". In: 12 (2008), pp. 1221–1250. DOI: 10.1016/j.rser.2007.01.023.

[97] IEC. *International Electrotechnical Commission 61000-2: Compatibility Levels for Low Frequency Conducted Disturbances and Signaling in Public Medium Voltage Power Supply Systems*. IEC 61000-2, 2018.

[98] *IEC 60038:2009: IEC Standard Voltages*. IEC Standard. June 2009.

[99] IEEE PES Distribution Systems Analysis Subcommittee Radial Test Feeders. *IEEE European LV Test Feeder*. 2015. URL: https://site.ieee.org/pes-testfeeders/resources/.

[100] IEEE Standards Association. *IEEE Std. 1547-2018. IEEE Standard for Interconnection and Interoperability of Distributed Energy Resources with Associated Electric Power Systems Interfaces*. 2018. DOI: 10.1109/IEEESTD.2018.8332112.

[101] IEEE Standards Association. "IEEE Std. 519-2014. IEEE Recommended Practice and Requirements for Harmonic Control in Electric Power Systems". In: (2014), pp. 1–29.

[102] Infineon. *AN2019-05 - PC and TC Diagrams*. Tech. rep.

[103] Infineon. *Infineon IGBT discrete*. URL: https://www.infineon.com/cms/en/product/power/igbt/igbt-discretes/.

[104] Infineon. *Infineon IGBT Modules*. URL: https://www.infineon.com/cms/en/product/power/igbt/igbt-modules/.

[105] Infineon. *Infineon IGBT Stack*. URL: https://www.infineon.com/cms/en/product/power/igbt/igbt-stacks-igbt-assemblies/.

[106] Md Shariful Islam, Nadarajah Mithulananthan, and Kwang Y. Lee. "Suitability of PV and Battery Storage in EV Charging at Business Premises". In: *IEEE Trans. Power Syst.* 33.4 (2018), pp. 4382–4396. ISSN: 08858950. DOI: 10.1109/TPWRS.2017.2774361.

[107] Walid R. Issa, Mohammad A. Abusara, and Suleiman M. Sharkh. "Control of Transient Power during Unintentional Islanding of Microgrids". In: *IEEE Trans. Power Electron.* 30.8 (2015), pp. 4573–4584. ISSN: 08858993. DOI: 10.1109/TPEL.2014.2359792.

[108] CEI Comitato Elettrotecnico Italiano. *CEI 0-21*. 2019. URL: https://www.ceinorme.it/it/norme-cei-0-16-e-0-21.html.

[109] Seyedmahdi DOI Izadkhast. "Aggregation of Plug-in Electric Vehicles in Power Systems for Primary Frequency Control". PhD thesis. 2017, p. 240. ISBN: 9788461799466. DOI: 10.4233/uuid:8217e2d7-6e04-496b-bcda-7c7367d8e2bc.

[110] Kamram Jalili and Steffen Bernet. "Design of LCL filters of active-front-end two-level voltage-source converters". In: *IEEE Trans. Ind. Electron.* 56.5 (2009), pp. 1674–1689. ISSN: 02780046. DOI: 10.1109/TIE.2008.2011251.

[111] Mohammad Rasol Jannesar et al. “Optimal placement, sizing, and daily charge/discharge of battery energy storage in low voltage distribution network with high photovoltaic penetration”. In: *Appl. Energy* 226.March (2018), pp. 957–966. ISSN: 03062619. DOI: 10.1016/j.apenergy.2018.06.036. URL: https://doi.org/10.1016/j.apenergy.2018.06.036.

[112] Julien Jomaux, Arnaud Latiers, and Emmanuel De Jaeger. “Cost-based dimensioning of Battery Energy Storage and energy management system for Frequency Containment Reserves provision”. In: *IEEE Power and Energy Society General Meeting*. Vol. 2015-September. IEEE Computer Society, Sept. 2015. ISBN: 9781467380409. DOI: 10.1109/PESGM.2015.7285849.

[113] Paul D. Judge and Tim C. Green. “Modular Multilevel Converter with Partially Rated Integrated Energy Storage Suitable for Frequency Support and Ancillary Service Provision”. In: *IEEE Trans. Power Deliv.* 34.1 (2019), pp. 208–219. ISSN: 08858977. DOI: 10.1109/TPWRD.2018.2874209.

[114] Srinivas Bhaskar Karanki et al. “Optimal location of battery energy storage systems in power distribution network for integrating renewable energy sources”. In: *2013 IEEE Energy Convers. Congr. Expo. ECCE 2013* (2013), pp. 4553–4558. DOI: 10.1109/ECCE.2013.6647310.

[115] Noriko Kawakami et al. “Development and field experiences of stabilization system using 34MW NAS batteries for a 51MW Wind farm”. In: *IEEE Int. Symp. Ind. Electron.* (2010), pp. 2371–2376. DOI: 10.1109/ISIE.2010.5637487.

[116] Khawaja Khalid Mehmood et al. “Optimal sizing and allocation of battery energy storage systems with wind and solar power DGs in a distribution network for voltage regulation considering the lifespan of batteries”. In: *IET Renew. Power Gener.* 11.10 (2017), pp. 1305–1315. ISSN: 1752-1416. DOI: 10.1049/iet-rpg.2016.0938. URL: http://digital-library.theiet.org/content/journals/10.1049/iet-rpg.2016.0938.

[117] Marvin Killer, Mana Farrokhseresht, and Nikolaos G Paterakis. “Implementation of large-scale Li-ion battery energy storage systems within the EMEA region”. In: *Applied Energy* 260.June 2019 (2020), p. 114166. ISSN: 0306-2619. DOI: 10.1016/j.apenergy.2019.114166. URL: https://doi.org/10.1016/j.apenergy.2019.114166.

[118] Dheepak Krishnamurthy et al. “Energy Storage Arbitrage Under Day-Ahead and Real-Time Price Uncertainty”. In: *IEEE Transactions on Power Systems* 33.1 (2017), pp. 84–93. ISSN: 0885-8950. DOI: 10.1109/tpwrs.2017.2685347.

[119] Matthew T Lawder et al. “Battery Energy Storage System (BESS) and Battery Management System (BMS) for Grid-Scale Applications This paper provides a comprehensive review of battery management systems for grid-scale energy storage applications”. In: *Proc. IEEE* 102.6 (2014), pp. 1014–1030. URL: https://pdfs.semanticscholar.org/4c38/39b9145a8b528497faaebfabb81bbd042c72.pdf.

[120] Lazard. “Lazard’s levelized cost of storage analysis-v5”. In: *Nihon Naika Gakkai Zasshi* 108.1 (2019), Contents1–Contents1. ISSN: 0021-5384. DOI: 10.2169/naika.108.contents1.

[121] P. Lazzeroni and M. Repetto. “Optimal planning of battery systems for power losses reduction in distribution grids”. In: *Electr. Power Syst. Res.* 167.March 2018 (2018), pp. 94–112. ISSN: 03787796. DOI: 10.1016/j.epsr.2018.10.027. URL: https://linkinghub.elsevier.com/retrieve/pii/S0378779618303432.

[122] Hansang Lee et al. “Compensation for the power fluctuation of the large scale wind farm using hybrid energy storage applications”. In: *IEEE Trans. Appl. Supercond.* 22.3 (2012), p. 5701904. ISSN: 10518223. DOI: 10.1109/TASC.2011.2180881.

[123] Soon Jeong Lee et al. “Coordinated Control Algorithm for Distributed Battery Energy Storage Systems for Mitigating Voltage and Frequency Deviations”. In: *IEEE Trans. Smart Grid* 7.3 (2016), pp. 1713–1722. ISSN: 19493053. DOI: 10.1109/TSG.2015.2429919.

[124] P. Leung et al. “Recent developments in organic redox flow batteries: A critical review”. In: *J. Power Sources* 360 (2017), pp. 243–283. ISSN: 03787753. DOI: 10.1016/j.jpowsour.2017.05.057.

[125] LG Chem ESS. “LG-Chem Energy Storage Li-ion NMC Battery Data Sheet”. In: (2018).

[126] Gaoxiang Li et al. “Design and Operation Analysis of Virtual Synchronous Compensator”. In: *IEEE J. Emerg. Sel. Top. Power Electron.* 8.4 (2020), pp. 3835–3845. ISSN: 21686785. DOI: 10.1109/JESTPE.2019.2943723.

[127] Xiangjun Li, Dong Hui, and Xiaokang Lai. “Battery energy storage station (BESS)-based smoothing control of photovoltaic (PV) and wind power generation fluctuations”. In: *IEEE Trans. Sustain. Energy* 4.2 (2013), pp. 464–473. ISSN: 19493029. DOI: 10.1109/TSTE.2013.2247428.

[128] Zongjian Li et al. “Performance Comparison of Two Hybrid Si/SiC Device Concepts”. In: *IEEE J. Emerg. Sel. Top. Power Electron.* 8.1 (2020), pp. 42–53. ISSN: 21686785. DOI: 10.1109/JESTPE.2019.2947252.

[129] Zongjian Li et al. “Power Loss Model and Device Sizing Optimization of Si/SiC Hybrid Switches”. In: *IEEE Trans. Power Electron.* 35.8 (2020), pp. 8512–8523. ISSN: 19410107. DOI: 10.1109/TPEL.2019.2954288.

[130] Bo Lian et al. “Optimizing LiFePO4 Battery Energy Storage Systems for Frequency Response in the UK System”. In: *IEEE Trans. Sustain. Energy* 8.1 (2017), pp. 385–394. ISSN: 19493029. DOI: 10.1109/TSTE.2016.2600274.

[131] Xiaodong Liang and Senior Member. “Emerging Power Quality Challenges Due to Integration of Renewable Energy Sources”. In: *IEEE Trans. Ind. Appl.* 53.2 (2017), pp. 855–866. ISSN: 00939994. DOI: 10.1109/TIA.2016.2626253.

[132] Qiangqiang Liao et al. “A techno-economic analysis on NaS battery energy storage system supporting peak shaving”. In: *Int. J. Energy Res.* 33.4 (2016), pp. 23–40. ISSN: 12310956. DOI: 10.1002/er. arXiv: arXiv:1011.1669v3.

[133] Marco Liserre et al. “Thermal loading and lifetime estimation for power device considering mission profiles in wind power converter”. In: *IEEE Trans. Power Electron.* 30.2 (2015), pp. 590–602. ISSN: 08858993. DOI: 10.1109/TPEL.2014.2312335.

[134] Mingjun Liu et al. “Reliability Evaluation of Large Scale Battery Energy Storage Systems”. In: *IEEE Trans. Smart Grid* 8.6 (2017), pp. 2733–2743. URL: http://repository.lib.polyu.edu.hk/jspui/handle/10397/1682.

[135] Xing Luo et al. “Overview of current development in electrical energy storage technologies and the application potential in power system operation”. In: *Appl. Energy* 137 (2015), pp. 511–536. ISSN: 03062619. DOI: 10.1016/j.apenergy.2014.09.081. URL: http://dx.doi.org/10.1016/j.apenergy.2014.09.081https://linkinghub.elsevier.com/retrieve/pii/S0306261914010290.

[136] Dingsihao Lyu, Thiago Batista Soeiro, and Pavol Bauer. “Design and Implementation of a Re-configurable Phase-Shift Full-Bridge Converter for Wide Voltage Range EV Charging Application”. In: *IEEE Trans. Transp. Electrif.* PP.c (2022), pp. 1–1. ISSN: 23327782. DOI: 10.1109/tte.2022.3176826.

[137] Dingsihao Lyu, Thiago Batista Soeiro, and Pavol Bauer. “Impacts of Different Charging Strategies on the Electric Vehicle Battery Charger Circuit Using Phase-Shift Full-Bridge Converter”. In: *Proc. - 2021 IEEE 19th Int. Power Electron. Motion Control Conf. PEMC 2021* (2021), pp. 256–263. DOI: 10.1109/PEMC48073.2021.9432497.

[138] Kang Ma, Lurui Fang, and Wangwei Kong. “Review of distribution network phase unbalance: Scale, causes, consequences, solutions, and future research directions”. In: *CSEE J. Power Energy Syst.* 6.3 (2020), pp. 479–488. ISSN: 20960042. DOI: 10.17775/CSEEJPES.2019.03280.

[139] Kang Ma et al. “Quantification of Additional Reinforcement Cost from Severe Three-Phase Imbalance”. In: *IEEE Trans. Power Syst.* 32.5 (2017), pp. 4143–4144. ISSN: 08858950. DOI: 10.1109/TPWRS.2016.2635383.

[140] Leonardo H Macedo, John F Franco, and Marcos J Rider. “Optimal Operation of Distribution Networks Considering Energy Storage Devices”. In: *IEEE Trans. Smart Grid* 6.6 (2015), pp. 2825–2836. DOI: 10.1109/TSG.2015.2419134.

[141] Khashayar Mahani, Farbod Farzan, and Mohsen A. Jafari. “Network-aware approach for energy storage planning and control in the network with high penetration of renewables”. In: *Appl. Energy* 195 (2017), pp. 974–990. ISSN: 03062619. DOI: 10.1016/j.apenergy.2017.03.118. URL: http://dx.doi.org/10.1016/j.apenergy.2017.03.118.

[142] Nasif Mahmud and A. Zahedi. “Review of control strategies for voltage regulation of the smart distribution network with high penetration of renewable distributed generation”. In: *Renew. Sustain. Energy Rev.* 64 (2016), pp. 582–595. ISSN: 18790690. DOI: 10.1016/j.rser.2016.06.030. arXiv: ISBN:978-958-8363-06-6. URL: http://dx.doi.org/10.1016/j.rser.2016.06.030.

[143] Luigi Malesani et al. “AC/DC/AC PWM Cnverter with Minimum Energy Storage in the DC Link”. In: *IEEE Appl. Power Electron. Conf. Expo. - APEC*. 1993, pp. 306–311. ISBN: 0780309820.

[144] Burcu Mantar Gundogdu et al. “A battery energy management strategy for U.K. enhanced frequency response and triad avoidance”. In: *IEEE Trans. Ind. Electron.* 65.12 (2018), pp. 9509–9517. ISSN: 02780046. DOI: 10.1109/TIE.2018.2818642.

[145] Lexuan Meng et al. “Fast Frequency Response from Energy Storage Systems - A Review of Grid Standards, Projects and Technical Issues”. In: *IEEE Trans. Smart Grid* 11.2 (2020), pp. 1566–1581. ISSN: 19493061. DOI: 10.1109/TSG.2019.2940173.

[146] Pascal Mercier, Rachid Cherkaoui, and Alexandre Oudalov. “Optimizing a Battery Energy Storage System for Frequency Control Application in an Isolated Power System”. In: *IEEE Trans. Power Syst.* 24.3 (2009), pp. 1469–1477. DOI: 10.1109/TPWRS.2009.2022997.

[147] S.A.R. Mir Mohammadi Kooshknow and C.B. Davis. “Business models design space for electricity storage systems: Case study of the Netherlands”. In: *J. Energy Storage* 20.August (2018), pp. 590–604. ISSN: 2352152X. DOI: 10.1016/j.est.2018.10.001. URL: https://linkinghub.elsevier.com/retrieve/pii/S2352152X18301609.

[148] Yasuaki Mitsugi et al. “Control Hardware-in-the-Loop Simulation on Fast Frequency Response of Battery Energy Storage System Equipped with Advanced Frequency Detection Algorithm”. In: *IEEE Trans. Ind. Appl.* 57.6 (2021), pp. 5541–5551. ISSN: 19399367. DOI: 10.1109/TIA.2021.3107223.

[149] Slavko Mocevic et al. “Comparison and Discussion on Shortcircuit Protections for Silicon-Carbide MOSFET Modules: Desaturation Versus Rogowski Switch-Current Sensor”. In: *IEEE Trans. Ind. Appl.* 56.3 (2020), pp. 2880–2893. ISSN: 19399367. DOI: 10.1109/TIA.2020.2972816.

[150] Rodrigo Moreno, Roberto Moreira, and Goran Strbac. “A MILP model for optimising multi-service portfolios of distributed energy storage”. In: *Appl. Energy* 137 (2015), pp. 554–566. ISSN: 03062619. DOI: 10.1016/j.apenergy.2014.08.080. URL: http://dx.doi.org/10.1016/j.apenergy.2014.08.080.

[151] Souleman N. Motapon et al. “A Generic Cycle Life Model for Lithium-Ion Batteries Based on Fatigue Theory and Equivalent Cycle Counting”. In: *IEEE Open J. Ind. Electron. Soc.* 1.August (2020), pp. 207–217. DOI: 10.1109/ojies.2020.3015396.

[152] *Mouser Electronics*. URL: https://eu.mouser.com/.

[153] Jonas Mühlethaler et al. “Optimal design of lcl harmonic filters for three-phase pfc rectifiers”. In: *IEEE Trans. Power Electron.* 28.7 (2013), pp. 3114–3125. ISSN: 08858993. DOI: 10.1109/TPEL.2012.2225641.

[154] National Grid. *State of Charge Management Guidance for FFR Providers*. Tech. rep. 2018. URL: https://www.nationalgrideso.com/balancing-services/frequency-response-services/firm-frequency-response-ffr.

[155] National Grid. *State of Charge Management Guidance for FRR Providers*. Tech. rep. 2018. URL: https://www.nationalgrid.com/uk/electricity/balancing-services/future-balancing-.

[156] National Grid ESO. “Demand Side Flexibility Annual Report 2018”. In: (2019). URL: www.powerresponsive.com..

[157] NationalGridESO. Access on: Feb. 25 2020. URL: https://www.nationalgrideso.com/balancing-services/frequency-response-services/historic-frequency-data.

[158] *Navigant Research Leaderboard: Utility-Scale Energy Storage Systems Integrators*. URL: https://www.navigantresearch.com/reports/.

[159] Netzfrequenzmessung. Access on: Feb. 25 2020. URL: https://www.netzfrequenzmessung.de.

[160] Tu A. Nguyen et al. “Maximizing revenue from electrical energy storage in MISO energy & frequency regulation markets”. In: *IEEE Power Energy Soc. Gen. Meet.* 2018-Janua (2018), pp. 1–5. ISSN: 19449933. DOI: 10.1109/PESGM.2017.8274348.

[161] Ze Ni et al. “Overview of Real-Time Lifetime Prediction and Extension for SiC Power Converters”. In: *IEEE Trans. Power Electron.* 35.8 (2019), pp. 7765–7794. ISSN: 0885-8993. DOI: 10.1109/tpel.2019.2962503.

[162] Mostafa Nick, Rachid Cherkaoui, and Mario Paolone. “Optimal Planning of Distributed Energy Storage Systems in Active Distribution Networks Embedding Grid Reconfiguration”. In: *IEEE Trans. Power Syst.* 33.2 (2018), pp. 1577–1590. ISSN: 08858950. DOI: 10.1109/TPWRS.2017.2734942.

[163] Mostafa Nick, Rachid Cherkaoui, and Mario Paolone. “Optimal siting and sizing of distributed energy storage systems via alternating direction method of multipliers”. In: *Int. J. Electr. Power Energy Syst.* 72 (2015), pp. 33–39. ISSN: 01420615. DOI: 10.1016/j.ijepes.2015.02.008. URL: http://dx.doi.org/10.1016/j.ijepes.2015.02.008.

[164] Noord Pool. *Market Data*. 2021. URL: https://www.nordpoolgroup.com/Market-data1/Dayahead/.

[165] *Nord Pool AS*. URL: https://www.nordpoolgroup.com/historical-market-data/.

[166] Ali Nourai, V .I. Kogan, and Chris M. Schafer. “Load Leveling Reduces T&D Line Losses”. In: *IEEE Trans. Power Deliv.* 23.4 (2008), pp. 2168–2173. ISSN: 0885-8977 VO - 23. DOI: 10.1109/TPWRD.2008.921128.

[167] Luis F. Ochoa, Antonio Padilha-Feltrin, and Gareth P. Harrison. “Evaluating distributed generation impacts with a multiobjective index”. In: *IEEE Trans. Power Deliv.* 21.3 (2006), pp. 1452–1458. ISSN: 08858977. DOI: 10.1109/TPWRD.2005.860262.

[168] Blazej Olek and Michal Wierzbowski. “Local Energy Balancing and Ancillary Services in Low-Voltage Networks with Distributed Generation, Energy Storage, and Active Loads”. In: *IEEE Trans. Ind. Electron.* 62.4 (2015), pp. 2499–2508. ISSN: 02780046. DOI: 10.1109/TIE.2014.2377134.

[169] Walid A. Omran et al. “Investigation of methods for reduction of power fluctuations generated from large grid-connected photovoltaic systems”. In: *IEEE Trans. Energy Convers.* 26.1 (2011), pp. 318–327. ISSN: 08858969. DOI: 10.1109/TEC.2010.2062515.

[170] C. Opathella et al. “Optimal Scheduling of Merchant-Owned Energy Storage Systems With Multiple Ancillary Services”. In: *IEEE Open Access Journal of Power and Energy* 7.November 2019 (2020), pp. 31–40. DOI: 10.1109/oajpe.2019.2952811.

[171] Niall Oswald et al. “An Experimental Investigation of the Tradeoff between Switching Losses and EMI Generation With Hard-Switched All-Si, Si-SiC, and All-SiC Device Combinations”. In: *IEEE Trans. Power Electron.* 29.5 (2014), pp. 2393–2407. ISSN: 08858993. DOI: 10.1109/TPEL.2013.2278919.

[172] João Inácio Yutaka Ota, Takuya Sato, and Hirofumi Akagi. "Enhancement of performance, availability, and flexibility of a battery energy storage system based on a modular multilevel cascaded converter (MMCC-SSBC)". In: *IEEE Trans. Power Electron.* 31.4 (2016), pp. 2791–2799. ISSN: 08858993. DOI: 10.1109/TPEL.2015.2450757.

[173] Alexandre Oudalov, Daniel Chartouni, and Christian Ohler. "Optimizing a battery energy storage system for primary frequency control". In: *IEEE Trans. Power Syst.* 22.3 (2007), pp. 1259–1266. ISSN: 08858950. DOI: 10.1109/TPWRS.2007.901459.

[174] Xuejun Pei, Wu Zhou, and Yong Kang. "Analysis and Calculation of DC-Link Current and Voltage Ripples for Three-Phase Inverter With Unbalanced Load". In: *IEEE Trans. Power Electron.* 30.10 (2015), pp. 5401–5412. ISSN: 08858993. DOI: 10.1109/TPEL.2014.2375353.

[175] Aramis Perez et al. "Effect of Battery Degradation on Multi-Service Portfolios of Energy Storage". In: *IEEE Trans. Sustain. Energy* 7.4 (2016), pp. 1718–1729. ISSN: 19493029. DOI: 10.1109/TSTE.2016.2589943.

[176] Saeed Peyghami, Frede Blaabjerg, and Peter Palensky. "Incorporating Power Electronic Converters Reliability into Modern Power System Reliability Analysis". In: *IEEE J. Emerg. Sel. Top. Power Electron.* (2020). DOI: 10.1109/JESTPE.2020.2967216.

[177] Saeed Peyghami, Peter Palensky, and Frede Blaabjerg. "An Overview on the Reliability of Modern Power Electronic Based Power Systems". In: *IEEE Open J. Power Electron.* 1.December 2019 (2020), pp. 34–50. DOI: 10.1109/ojpel.2020.2973926.

[178] Saeed Peyghami et al. "Mission-Profile-Based System-Level Reliability Analysis in DC Microgrids". In: *IEEE Trans. Ind. Appl.* 55.5 (2019), pp. 5055–5067. ISSN: 19399367. DOI: 10.1109/TIA.2019.2920470.

[179] Andrew J. Pimm, Tim T. Cockerill, and Peter G. Taylor. "The potential for peak shaving on low voltage distribution networks using electricity storage". In: *J. Energy Storage* 16 (2018), pp. 231–242. ISSN: 2352152X. DOI: 10.1016/j.est.2018.02.002. URL: https://doi.org/10.1016/j.est.2018.02.002.

[180] C. Ponce de León et al. "Redox flow cells for energy conversion". In: *J. Power Sources* 160.1 (2006), pp. 716–732. ISSN: 03787753. DOI: 10.1016/j.jpowsour.2006.02.095.

[181] Danny Pudjianto et al. "Whole-systems assessment of the value of energy storage in low-carbon electricity systems". In: *IEEE Trans. Smart Grid* 5.2 (2014), pp. 1098–1109. ISSN: 19493053. DOI: 10.1109/TSG.2013.2282039.

[182] A. Rahimi et al. "A simple and effective approach for peak load shaving using Battery Storage Systems". In: *45th North Am. Power Symp. NAPS 2013* (2013), pp. 1–5. DOI: 10.1109/NAPS.2013.6666824.

[183] Munaf Rahimo et al. "Characterization of a Silicon IGBT and Silicon Carbide MOSFET Cross-switch hybrid". In: *IEEE Trans. Power Electron.* 30.9 (2015), pp. 4638–4642. ISSN: 08858993. DOI: 10.1109/TPEL.2015.2402595.

[184] Jorge A. Ramos-Ruiz et al. "Power electronics intelligence at the network edge (PINE) - An approach to interface PV and battery energy storage systems at the grid edge". In: *IEEE J. Emerg. Sel. Top. Power Electron.* 9.5 (2021), pp. 5219–5227. ISSN: 21686785. DOI: 10.1109/JESTPE.2020.2991019.

[185] Yann G Rebours et al. “A Survey of Frequency and Voltage Control Ancillary Services - Part I: Technical Features”. In: *IEEE Trans. Power Syst.* 22.1 (2007), pp. 350–357. ISSN: 0885-8950. DOI: 10.1109/TPWRS.2006.888963.

[186] Yann G. Rebours et al. “A survey of frequency and voltage control ancillary services - Part I: Technical features”. In: *IEEE Trans. Power Syst.* 22.1 (2007), pp. 350–357. ISSN: 08858950. DOI: 10.1109/TPWRS.2006.888963.

[187] T. Narsa Reddy et al. “Grid interactive combined supercapacitor/battery energy storage system with power quality features”. In: *Proc. IEEE Int. Conf. Ind. Technol.* 2015-June.June (2015), pp. 2600–2605. DOI: 10.1109/ICIT.2015.7125481.

[188] *Rede Eléctrica de España*. URL: https://www.ree.es/es/actividades/operacion-del-sistema-electrico/procedimientos-de-operaciong.

[189] Regelleistung. Access on: Feb. 25 2020. URL: https://www.regelleistung.net/.

[190] Regelleistung. *Regelleistung Data Center*. URL: https://www.regelleistung.net/.

[191] Paula Diaz Reigosa et al. “Prediction of Bond Wire Fatigue of IGBTs in a PV Inverter under a Long-Term Operation”. In: *IEEE Trans. Power Electron.* 31.10 (2016), pp. 7171–7182. ISSN: 08858993. DOI: 10.1109/TPEL.2015.2509643.

[192] Jürgen Reinert, Ansgar Brockmeyer, and Rik W.A.A. De Doncker. “Calculation of losses in ferro- and ferrimagnetic materials based on the modified Steinmetz equation”. In: *IEEE Trans. Ind. Appl.* 37.4 (2001), pp. 1055–1061. ISSN: 00939994. DOI: 10.1109/28.936396.

[193] International Renewable, Energy Agency, and IRENA. *Electricity storage and renewables: Costs and markets to 2030*. October. 2017, p. 132. ISBN: 9789292600389. DOI: ISBN978-92-9260-038-9(PDF). URL: http://irena.org/publications/2017/Oct/Electricity-storage-and-renewables-costs-and-markets.

[194] Réseau de Transport d’Électricité. “Frequency Ancillary Services Terms and Conditions”. In: October (2018).

[195] Valentin Rigoni et al. “Representative residential LV feeders: A case study for the North West of England”. In: *IEEE Trans. Power Syst.* 31.1 (2016), pp. 348–360. ISSN: 08858950. DOI: 10.1109/TPWRS.2015.2403252.

[196] Rohm Semiconductor. *Rohm Semiconductor SiC Power Devices*. URL: https://www.rohm.com/products/sic-power-devices.

[197] Carlos Sabillon-Antunez et al. “Volt-VAr Control and Energy Storage Device Operation to Improve the Electric Vehicle Charging Coordination in Unbalanced Distribution Networks”. In: *IEEE Trans. Sustain. Energy* 8.4 (2017), pp. 1560–1570. ISSN: 19493029. DOI: 10.1109/TSTE.2017.2695195.

[198] Hedayat Saboori et al. “Energy storage planning in electric power distribution networks – A state-of-the-art review”. In: *Renew. Sustain. Energy Rev.* 79.May (2017), pp. 1108–1121. ISSN: 18790690. DOI: 10.1016/j.rser.2017.05.171. URL: http://dx.doi.org/10.1016/j.rser.2017.05.171.

[199] Andoni Saez-De-Ibarra et al. “Co-Optimization of Storage System Sizing and Control Strategy for Intelligent Photovoltaic Power Plants Market Integration”. In: *IEEE Trans. Sustain. Energy* 7.4 (2016), pp. 1749–1761. ISSN: 19493029. DOI: 10.1109/TSTE.2016.2555704.

[200] Samsung SDI. *ESS Batteries by Samsung SDI*. 2019. URL: https://www.samsungsdi.com/ess/index.html.

[201] Mario Schweizer, Thomas Friedli, and Johann W. Kolar. “Comparative evaluation of advanced three-phase three-level inverter/converter topologies against two-level systems”. In: *IEEE Trans. Ind. Electron.* 60.12 (2013), pp. 5515–5527. ISSN: 02780046. DOI: 10.1109/TIE.2012.2233698.

[202] Mario Schweizer et al. “Comparison of the Chip Area Usage of 2-level and 3-level Voltage Source Converter Topologies”. In: *IECON 2010 - 36th Annu. Conf. IEEE Ind. Electron. Soc.* (2010), pp. 391–396. DOI: 10.1109/IECON.2010.5674994.

[203] Samsung SDI. *Specification of product INR18650-25R*. 2014. URL: http://www.datasheet-pdf.com/datasheet/Samsung/799163/INR18650-20R.pdf.html.

[204] M. Sedghi, M. Aliakbar-Golkar, and M. R. Haghifam. “Distribution network expansion considering distributed generation and storage units using modified PSO algorithm”. In: *Int. J. Electr. Power Energy Syst.* 52.1 (2013), pp. 221–230. ISSN: 01420615. DOI: 10.1016/j.ijepes.2013.03.041. URL: http://dx.doi.org/10.1016/j.ijepes.2013.03.041.

[205] Semikron. *Semikron IGBT Modules*. URL: https://www.semikron.com/products/product-classes/igbt-modules.html.

[206] Udai Shipurkar et al. “A review of failure mechanisms in wind turbine generator systems”. In: *2015 17th Eur. Conf. Power Electron. Appl. EPE-ECCE Eur. 2015* (2015). DOI: 10.1109/EPE.2015.7311669.

[207] Udai Shipurkar et al. “Lifetime Comparison of Power Semiconductors in Three-Level Converters for 10-MW Wind Turbine Systems”. In: *IEEE J. Emerg. Sel. Top. Power Electron.* 6.3 (2018), pp. 1366–1377. ISSN: 21686785. DOI: 10.1109/JESTPE.2018.2833631.

[208] Thiago B Soeiro and Johann W Kolar. “The New High-Efficiency Hybrid Neutral-Point-Clamped Converter”. In: *IEEE Trans. Ind. Electron.* 60.5 (2013), pp. 1919–1935. DOI: 10.1109/TIE.2012.2209611.

[209] Thiago B. Soeiro et al. “Comparison of 2- and 3-level active filters with enhanced bridge-leg loss distribution”. In: *8th Int. Conf. Power Electron. - ECCE Asia "Green World with Power Electron. ICPE 2011-ECCE Asia* c (2011), pp. 1835–1842. DOI: 10.1109/ICPE.2011.5944519.

[210] Thiago Batista Soeiro et al. “Performance Evaluation of the Body-Diode of SiC Mosfets under Repetitive Surge Current Operation”. In: *IECON Proc. (Industrial Electron. Conf.* 2019-Octob (2019), pp. 5154–5159. DOI: 10.1109/IECON.2019.8927774.

[211] Yue Song et al. “Optimal Operation of Battery Energy Storage System Considering Distribution System Uncertainty”. In: *IEEE Trans. Sustain. Energy* 9.3 (2017), pp. 1051–1060. ISSN: 1949-3029. DOI: 10.1109/tste.2017.2762364.

[212] Constantinos Sourkounis and Pavlos Tourou. “Grid Code Requirements for Wind Power Integration in Europe”. In: *Conf. Pap. Energy* 2013 (2013), pp. 1–9. DOI: 10.1155/2013/437674.

[213] Ana Irina Stan et al. “Lithium ion battery chemistries from renewable energy storage to automotive and back-up power applications - An overview”. In: *2014 Int. Conf. Optim. Electr. Electron. Equipment, OPTIM 2014* (2014), pp. 713–720. DOI: 10.1109/OPTIM.2014.6850936.

[214] Marco Stecca et al. “A Comprehensive Review of the Integration of Battery Energy Storage Systems into Distribution Networks”. In: *IEEE Open J. Ind. Electron. Soc.* 1 (2020), pp. 46–65. DOI: 10.1109/ojies.2020.2981832.

[215] Marco Stecca et al. “Comparison of Two and Three-Level DC-AC Converters for a 100 kW Battery Energy Storage System”. In: *IEEE Int. Symp. Ind. Electron.* 2020-June (2020), pp. 677–682. DOI: 10.1109/ISIE45063.2020.9152545.

[216] Marco Stecca et al. “Gate Driver Design for 1 . 2 kV SiC Module with PCB Integrated Rogowski Coil Protection Circuit”. In: *2021 IEEE Energy Convers. Congr. Expo.* 2021.

[217] Marco Stecca et al. “LCL Filter Design for Three Phase AC-DC Converters Considering Semiconductor Modules and Magnetics Components Performance”. In: *2020 22nd Eur. Conf. Power Electron. Appl. (EPE’20 ECCE Eur.* 2020, P.1–P.8. ISBN: 9789075815368. DOI: 10.23919/epe20ecceeurope43536.2020.9215864.

[218] Marco Stecca et al. “Lifetime Estimation of Grid-Connected Battery Storage and Power Electronics Inverter Providing Primary Frequency”. In: *IEEE Open J. Ind. Electron. Soc.* (2021), pp. 1–12. DOI: 10.1109/OJIES.2021.3064635.

[219] Stedin. *Elektriciteit Tarieven 2020*. Tech. rep. URL: https://www.stedin.net/zakelijk/betalingen-en-facturen/tarieven.

[220] Daniel Ioan Stroe. “Lifetime Models for Lithium-ion Batteries used in Virtual Power Plant Applications”. PhD thesis. Aalborg University, 2014, p. 274.

[221] Daniel-Ioan Stroe. *Lifetime Models for Lithium Ion Batteries used in Virtual Power Plants*. Tech. rep. 2014. URL: http://www.et.aau.dk.

[222] Daniel Ioan Stroe et al. “Accelerated lifetime testing methodology for lifetime estimation of lithium-ion batteries used in augmented wind power plants”. In: *IEEE Trans. Ind. Appl.* 50.6 (2014), pp. 4006–4017. ISSN: 00939994. DOI: 10.1109/TIA.2014.2321028.

[223] Daniel Ioan Stroe et al. “Degradation behaviour of Lithium-ion batteries based on field measured frequency regulation mission profile”. In: *2015 IEEE Energy Convers. Congr. Expo. ECCE 2015* (2015), pp. 14–21. DOI: 10.1109/ECCE.2015.7309663.

[224] Daniel-Ioan Stroe et al. “Operation of a Grid-Connected Lithium-Ion Battery Energy Storage System for Primary Frequency Regulation: A Battery Lifetime Perspective”. In: *IEEE Trans. Ind. Appl.* 53.1 (2017), pp. 430–438. ISSN: 0093-9994. DOI: 10.1109/TIA.2016.2616319. URL: http://ieeexplore.ieee.org/document/7588052/.

[225] Daniel Ioan Stroe et al. “Operation of a grid-connected lithium-ion battery energy storage system for primary frequency regulation: A battery lifetime perspective”. In: *IEEE Transactions on Industry Applications* 53.1 (2017), pp. 430–438. ISSN: 00939994. DOI: 10.1109/TIA.2016.2616319.

[226] Sebastian Stynski et al. “Utility-Scale Energy Storage Systems”. In: *IEEE Ind. Electron. Mag.* 14.4 (2020), pp. 32–52.

[227] Maciej Swierczynski et al. “Primary frequency regulation with Li-ion battery energy storage system: A case study for Denmark”. In: *2013 IEEE ECCE Asia Downunder - 5th IEEE Annu. Int. Energy Convers. Congr. Exhib. IEEE ECCE Asia 2013* (2013), pp. 487–492. DOI: 10.1109/ECCE-Asia.2013.6579141.

[228] Changyu Tan et al. “Performance Evaluation of an Electric Vehicle Traction Drive using Si/SiC Hybrid Switches”. In: *Proc. - 2021 IEEE 19th Int. Power Electron. Motion Control Conf. PEMC 2021* (2021), pp. 278–283. DOI: 10.1109/PEMC48073.2021.9432574.

[229] *Technical Requirements for the Connection to and Parallel Operation With Low-Voltage Distribution Networks*. 2018. URL: VDE-AR-N4105.

[230] E. Telaretti and L. Dusonchet. “Stationary battery technologies in the U.S.: Development Trends and prospects”. In: *Renew. Sustain. Energy Rev.* 75.November 2016 (2017), pp. 380–392. ISSN: 18790690. DOI: 10.1016/j.rser.2016.11.003. URL: http://dx.doi.org/10.1016/j.rser.2016.11.003.

[231] Tennet. “Annual Market Update 2018”. In: *Electr. Mark. insights* (2013).

[232] TenneT. “FCR Manual for BSPs - Requirements and procedures for supply of FCR”. In: (2019).

[233] Tennet. *FCR Manual for BSPs Requirements and procedures for supply of FCR*. Tech. rep. 2019.

[234] *TenneT B.V.* URL: https://www.tennet.eu/electricity-market/ancillary-services/fcr-documents/.

[235] TenneT TSO BV. *End report FCR pilot*. 2018. URL: https://www.tennet.eu/electricity-market/ancillary-services/fcr-documents/.

[236] Saurabh Tewari and Ned Mohan. “Value of NAS energy storage toward integrating wind: Results from the wind to battery project”. In: *IEEE Trans. Power Syst.* 28.1 (2013), pp. 532–541. ISSN: 08858950. DOI: 10.1109/TPWRS.2012.2205278.

[237] Lawrence (NASA) Thaller. “Electrically Rechargeable Redox Flow Cells”. In: *9th Intersoc. Energy Convers. Eng. Conf.* (1974).

[238] Ionut Trintis, Stig Munk-Nielsen, and Remus Teodorescu. “Cascaded H-bridge with bidirectional boost converters for energy storage”. In: *Proc. 2011 14th Eur. Conf. Power Electron. Appl.* (2011), pp. 1–9.

[239] Terng Wei Tsai et al. “Per-Phase Active Power Distribution Strategy for Three-Phase Grid-Tied Inverters Under Unbalanced Conditions Without DC Sources”. In: *IEEE J. Emerg. Sel. Top. Power Electron.* 9.6 (2021), pp. 6624–6636. ISSN: 21686785. DOI: 10.1109/JESTPE.2021.3064331.

[240] I Tsiropoulos and N Lebedeva. *Li-ion batteries for mobility and stationary storage applications*. 2018. ISBN: 9789279972546. DOI: 10.2760/87175.

[241] Chunming Tu et al. “Study on the failure of IGBT bonding wire based on temperature gradient”. In: *IECON Proc. (Industrial Electron. Conf.* 2020-Octob (2020), pp. 3011–3016. DOI: 10.1109/IECON43393.2020.9255166.

[242] *US Department of Energy, Global energy storage database.* URL: http://www.energystorageexchange
org/.

[243] Yamille del Valle et al. "Particle swarm optimization: Basic concepts, variants and applications in power systems". In: *IEEE Trans. Evol. Comput.* 12.2 (2008), pp. 171–195. ISSN: 1089778X. DOI: 10.1109/TEVC.2007.896686.

[244] Sergio Vazquez et al. "Energy storage systems for transport and grid applications". In: *IEEE Trans. Ind. Electron.* 57.12 (2010), pp. 3881–3895. ISSN: 02780046. DOI: 10.1109/TIE.2010.2076414.

[245] Wiljan Vermeer et al. "A Critical Review on the Effects of Pulse Charging of Li-ion Batteries". In: *Proc. - 2021 IEEE 19th Int. Power Electron. Motion Control Conf. PEMC 2021* (2021), pp. 217–224. DOI: 10.1109/PEMC48073.2021.9432555.

[246] J. Vetter et al. "Ageing mechanisms in lithium-ion batteries". In: *J. Power Sources* 147.1-2 (2005), pp. 269–281. ISSN: 03787753. DOI: 10.1016/j.jpowsour.2005.01.006.

[247] A. Vieira Pombo, J. Murta-Pina, and V. Fernão Pires. "Multiobjective formulation of the integration of storage systems within distribution networks for improving reliability". In: *Electr. Power Syst. Res.* 148 (2017), pp. 87–96. ISSN: 03787796. DOI: 10.1016/j.epsr.2017.03.012. URL: http://dx.doi.org/10.1016/j.epsr.2017.03.012.

[248] Jan Von Appen et al. "Local voltage control strategies for PV storage systems in distribution grids". In: *IEEE Trans. Smart Grid* 5.2 (2014), pp. 1002–1009. ISSN: 19493053. DOI: 10.1109/TSG.2013.2291116.

[249] Reigh A. Walling et al. "Summary of distributed resources impact on power delivery systems". In: *IEEE Trans. Power Deliv.* 23.3 (2008), pp. 1636–1644. ISSN: 08858977. DOI: 10.1109/TPWRD.2007.909115.

[250] Guishi Wang et al. "A review of power electronics for grid connection of utility-scale battery energy storage systems". In: *IEEE Trans. Sustain. Energy* 7.4 (2016), pp. 1778–1790. ISSN: 19493029. DOI: 10.1109/TSTE.2016.2586941.

[251] Huai Wang and Frede Blaabjerg. "Reliability of capacitors for DC-link applications in power electronic converters - An overview". In: *IEEE Trans. Ind. Appl.* 50.5 (2014), pp. 3569–3578. ISSN: 00939994. DOI: 10.1109/TIA.2014.2308357.

[252] Huai Haoran Wang et al. "Lifetime Estimation of DC-Link Capacitors in Adjustable Speed Drives under Grid Voltage Unbalances". In: *IEEE Trans. Power Electron.* 34.5 (2019), pp. 4064–4078. ISSN: 08858993. DOI: 10.1109/TPEL.2018.2863701.

[253] Jun Wang et al. "Gate Control Optimization of Si/SiC Hybrid Switch for Junction Temperature Balance and Power Loss Reduction". In: *IEEE Trans. Power Electron.* 34.2 (2019), pp. 1744–1754. ISSN: 08858993. DOI: 10.1109/TPEL.2018.2829624.

[254] Lei Wang et al. "Coordination of Multiple Energy Storage Units in a Low-Voltage Distribution Network". In: *IEEE Trans. Smart Grid* 6.6 (2015), pp. 2906–2918. ISSN: 19493053. DOI: 10.1109/TSG.2015.2452579.

[255] Lu Wang et al. "Grid Impact of Electric Vehicle Fast Charging Stations: Trends, Standards, Issues and Mitigation Measures - An Overview". In: *IEEE Open J. Power Electron.* 2.February (2021), pp. 56–74. DOI: 10.1109/ojpel.2021.3054601.

[256] Pengfei Wang et al. “Integrating Electrical Energy Storage Into Coordinated Voltage Control Schemes for Distribution Networks”. In: *IEEE Trans. Smart Grid* 5.2 (2014), pp. 1018–1030.

[257] Y. Wang et al. “Coordinated Control of Distributed Energy-Storage Systems for Voltage Regulation in Distribution Networks”. In: *IEEE Trans. Power Deliv.* 31.3 (2016), pp. 1132–1141. ISSN: 08858977. DOI: 10.1109/TPWRD.2015.2462723.

[258] Ye Wang et al. “Efficiency Improvement of Grid Inverters with Hybrid Devices”. In: *IEEE Trans. Power Electron.* 34.8 (2019), pp. 7558–7572. ISSN: 08858993. DOI: 10.1109/TPEL.2018.2881115.

[259] E W C Wilkins. “Cumulative damage in fatigue”. In: *Colloq. Fatigue / Colloq. Fatigue / Kolloquium über Ermüdungsfestigkeit*. Ed. by Waloddi Weibull and Folke K G Odqvist. Berlin, Heidelberg: Springer Berlin Heidelberg, 1956, pp. 321–332. ISBN: 978-3-642-99854-6.

[260] Arendt Wintrich et al. *Application Manual Power Semiconductors - SEMIKRON*. 2015, p. 466. ISBN: 9783938843666. DOI: 10.1109/50.762905.

[261] World Energy Council. *World Energy Resources 2016*. Tech. rep. 2016, pp. 1–1028. DOI: http://www.worldenergy.org/wp-content/uploads/2013/09/Complete_WER_2013_Survey.pdf.

[262] Karl Worthmann et al. “Distributed and Decentralized Control of Residential Energy Systems Incorporating Battery Storage”. In: *IEEE Trans. Smart Grid* 6.4 (2015), pp. 1914–1923. ISSN: 19493053. DOI: 10.1109/TSG.2015.2392081.

[263] Yang Wu et al. “Voltage Source Converter Control under Distorted Grid Voltage for Hybrid AC-DC Distribution Links”. In: *IECON 2019 - 45th Annu. Conf. IEEE Ind. Electron. Soc.* 1 (2019), pp. 5694–5699.

[264] Junzhong Xu et al. “High-Frequency SiC Three-Phase VSIs with Common-Mode Voltage Reduction and Improved Performance Using Novel Tri-State PWM Method”. In: *IEEE Trans. Power Electron.* 34.2 (2019), pp. 1809–1822. ISSN: 08858993. DOI: 10.1109/TPEL.2018.2829530.

[265] Shaoyong Yang et al. “An industry-based survey of reliability in power electronic converters”. In: *IEEE Trans. Ind. Appl.* 47.3 (2011), pp. 1441–1451. ISSN: 00939994. DOI: 10.1109/TIA.2011.2124436.

[266] Yanyong Yang and Pinjia Zhang. “In situ IGBT Junction Temperature Estimation Method via a Bond Wire Degradation Independent Parameter Turn-off Vce Overshoot”. In: *IEEE Trans. Ind. Electron.* 0046.c (2020), pp. 1–1. ISSN: 0278-0046. DOI: 10.1109/tie.2020.3022526.

[267] Yuqing Yang et al. “Battery energy storage system size determination in renewable energy systems : A review”. In: *Renew. Sustain. Energy Rev.* 91.January (2018), pp. 109–125. ISSN: 1364-0321. DOI: 10.1016/j.rser.2018.03.047. URL: https://doi.org/10.1016/j.rser.2018.03.047.

[268] Amirnaser Yazdani and Reza Iravani. *Voltage-Sourced Converters in Power Systems*. 2010. Wiley-IEEE Press, 2010, pp. 1–473. ISBN: 9780470521564.

[269] Behnam Zakeri and Sanna Syri. “Electrical energy storage systems: A comparative life cycle cost analysis”. In: *Renew. Sustain. Energy Rev.* 42 (2015), pp. 569–596.

[270] Behnam Zakeri, Sanna Syri, and Friedrich Wagner. "Economics of energy storage in the German electricity and reserve markets". In: *Int. Conf. Eur. Energy Mark. EEM* (2017), pp. 1–6. ISSN: 21654093. DOI: 10.1109/EEM.2017.7981914.

[271] Kenneth K. Zame et al. "Smart grid and energy storage: Policy recommendations". In: *Renew. Sustain. Energy Rev.* 82.May 2017 (2018), pp. 1646–1654. ISSN: 18790690. DOI: 10.1016/j.rser.2017.07.011. URL: https://doi.org/10.1016/j.rser.2017.07.011.

[272] Donato Zarrilli et al. "Energy Storage Operation for Voltage Control in Distribution Networks: A Receding Horizon Approach". In: *IEEE Trans. Control Syst. Technol.* 26.2 (2018), pp. 599–609. ISSN: 10636536. DOI: 10.1109/TCST.2017.2692719.

[273] Mehdi Zeraati, Mohamad Esmail Hamedani Golshan, and Josep M. Guerrero. "Distributed Control of Battery Energy Storage Systems for Voltage Regulation in Distribution Networks with High PV Penetration". In: *IEEE Trans. Smart Grid* 9.4 (2018), pp. 3582–3593. ISSN: 19493053. DOI: 10.1109/TSG.2016.2636217.

[274] Bei Zhang, Payman Dehghanian, and Mladen Kezunovic. "Optimal Allocation of PV Generation and Battery Storage for Enhanced Resilience". In: *IEEE Trans. Smart Grid* 10.1 (2019), pp. 535–545. ISSN: 19493053. DOI: 10.1109/TSG.2017.2747136.

[275] Ying Jun Angela Zhang et al. "Profit-maximizing planning and control of battery energy storage systems for primary frequency control". In: *IEEE Trans. Smart Grid* 9.2 (2018), pp. 712–723. ISSN: 19493053. DOI: 10.1109/TSG.2016.2562672. arXiv: 1604.00952.

[276] Zhenyuan Zhang et al. "Market-oriented optimal dispatching strategy for a wind farm with a multiple stage hybrid energy storage system". In: *CSEE J. Power Energy Syst.* 4.4 (2018), pp. 417–424. ISSN: 20960042. DOI: 10.17775/cseejpes.2018.00130.

[277] Zheyu Zhang et al. "Evaluation of Switching Performance of SiC Devices in PWM Inverter-Fed Induction Motor Drives". In: *2014 IEEE Energy Convers. Congr. Expo. ECCE 2014* 30.10 (2014), pp. 1597–1604. DOI: 10.1109/ECCE.2014.6953609.

[278] Tom Zhao. *Sustainable Development Strategy for EV Battery*. 2018. URL: https://www.iea.org/media/Workshops/2018/Session2ZhaoTongBYD.pdf.

[279] Ghassan Zubi et al. "The lithium-ion battery: State of the art and future perspectives". In: *Renew. Sustain. Energy Rev.* 89.April 2017 (2018), pp. 292–308. ISSN: 18790690. DOI: 10.1016/j.rser.2018.03.002.

[280] E T H Zurich and Jonas Mühlethaler. "Modeling and multi-objective optimization of inductive power components". In: 20217 (2012). DOI: 10.3929/ethz-a-007328104. URL: http://e-collection.library.ethz.ch/view/eth:5781.

LIST OF PUBLICATIONS

PUBLICATION RELATED TO THE THESIS

Journal papers

1. **M. Stecca**, L.R. Elizondo, T.B. Soeiro, P. Bauer, P. Palensky, "A Comprehensive Review of the Integration of Battery Energy Storage Systems Into Distribution Networks", IEEE Open Journal of the Industrial Electronics Society, 2020, vol.1, pp. 46-65;

2. **M. Stecca**, T.B. Soeiro, L.R. Elizondo, P. Bauer, P. Palensky, "Lifetime Estimation of Grid-Connected Battery Storage and Power Electronics Providing Primary Frequency Regulation", IEEE Open Journal of the Industrial Electronics Society, 2021, vol.2, pp. 240-251;

3. **M. Stecca**, C. Tan, J. Xu, T.B. Soeiro, P. Bauer, P. Palensky, "Hybrid Si/SiC Switch Modulation with Minimum SiC MOSFET Conduction in Grid Connected Voltage Source Converters", IEEE Journal of Emerging and Selected Topics in Power Electronics, 2022, vol.10, pp. 4275-4289;

4. **M. Stecca**, T.B. Soeiro, A.K. Iyer P. Bauer, P. Palensky, "Battery Storage System as Power Unbalance Redistributor in Distribution Grids Based on Three Legs Four Wire Voltage Source Converter", IEEE Journal of Emerging and Selected Topics in Power Electronics, 2022, vol. 10, pp. 7601-7614;

5. L. Argiolas, **M. Stecca**, L.M. Ramirez Elizondo, T.B. Soeiro, P. Bauer, "Optimal Battery Energy Storage Dispatch in Energy and Frequency Regulation Markets while Peak Shaving an EV Fast Charging Station", IEEE Open Access Journal of Power and Energy, 2022, vol. 9, pp. 374-385.

Conference papers

1. **M. Stecca**, L.M. Ramirez Elizondo, T.B. Soeiro, P. Bauer, "Energy Storage Sizing and Location in Distribution Networks Considering Overall Grid Performance", 2020 IEEE Power & Energy Society General Meeting (PESGM), 1-5;

2. **M. Stecca**, T.B. Soeiro, L.M. Ramirez Elizondo, P. Bauer, P. Palensky, "Comparison of Two and Three-Level DC-AC Converters for a 100 kW Battery Energy Storage System", 2020 IEEE 29th International Symposium on Industrial Electronics (ISIE), 677-682;

3. **M. Stecca**, T.B. Soeiro, L.M. Ramirez Elizondo, P. Bauer, P. Palensky, "LCL Filter Design for Three Phase AC-DC Converters Considering Semiconductor Modules and Magnetics Components Performance", 2020 22nd European Conference on Power Electronics and Applications (EPE'20 ECCE Europe).

OTHER PUBLICATIONS

Journal papers

1. Y. Wu, J. Xu, T.B. Soeiro, **M. Stecca**, P Bauer, "Optimal Periodic Variable Switching PWM for Harmonic Performance Enhancement in Grid-Connected Voltage Source Converters", IEEE Transactions on Power Electronics, vol. 37, pp. 7247-7262, 2022;

2. A. Abdelhakim, T.B. Soeiro, **M. Stecca**, F Canales, “Multiport Hybrid Converter (MHC) for Electrified Transportation Systems”, IEEE Transaction on Industrial Electronics, 2022, early access;.

3. **M. Stecca**, A. Abdelhakim, T.B. Soeiro, F Canales, P. Bauer, P. Palensky, “Hybrid Space Vector Modulation Scheme for the Multiport Hybrid Converter”, IEEE Transaction on Power Electronics, 2023, vol. 1, pp. 60-65.

Conference papers

1. **M. Stecca**, P. Tiftikidis, T.B. Soeiro, P. Bauer, “Gate Driver Design for 1.2 kV SiC Module with PCB Integrated Rogowski Coil Protection Circuit”, 2021 IEEE Energy Conversion Congress and Exposition (ECCE), 5723-5728;

2. C. Tan, **M. Stecca**, T.B. Soeiro, J. Dong, P. Bauer, “Performance Evaluation of an Electric Vehicle Traction Drive using Si/SiC Hybrid Switches”, 2021 IEEE 19th International Power Electronics and Motion Control Conference (PEMC);

3. W. Vermeer, **M. Stecca** , G.R.C. Mouli, P. Bauer, “Critical Review on The Effects of Pulse Charging of Li-ion Batteries”, 2021 IEEE 19th International Power Electronics and Motion Control Conference (PEMC).

4. G. Koolman, **M. Stecca**, P. Bauer, “Optimal Battery Energy Storage System Sizing for Demand Charge Management in EV Fast Charging Stations”, 2021 IEEE Transportation Electrification Conference & Expo (ITEC), 588-594.

5. **M. Stecca**, W. Vermeer, T.B. Soeiro, L.R. Elizondo, P. Bauer, P. Palensky, “Battery Storage Integration in EV Fast Charging Station for Increasing its Revenues and Reducing the Grid Impact”, 2022 IEEE Transportation Electrification Conference & Expo (ITEC), 109-113.

ACKNOWLEDGEMENTS

This work is the result of the guidance, effort, and support of many. For this I wish to acknowledge them.

Firstly, I would like to thank prof. Bauer for giving me the opportunity to join TU Delft and his group, and the means and freedom for carrying out this research, and prof. Palensky for the supportive and enthusiastic conversations, and the spot-on feedback. I would also like to thank Laura, for guiding me throughout these four years and for helping me grow as a researcher.

I want to thank Thiago, without your help and support, much of what I presented in this thesis would not have been possible. Your passion for power electronics and research is truly inspiring, it has been really great working with you.

I also want to thank the staff of DCE&S group, Sharmila, Harrie, Bart, Mladen, Radek, and Joris, which helped me for all administrative and laboratory issues.

Throughout the PhD, I was lucky to collaborate with many researchers. You helped me not only in my work but also in growing as a person, thank you Micky, Jarek, George, Panagiotis, Luca, Anand, Rohan, and Margarita. I want to especially thank Junzhong, for helping me when I first started going to the lab, your knowledge and willingness to help really kick-started my laboratory work, you have been an example for me on how to support junior colleagues. I would also like to thank Ahmed for giving me the opportunity to work on a cool topic and the fruitful collaboration.

Four years of PhD means lots of time spent in the office and in the lab. Thankfully I had the pleasure of sharing this time with great friends. Wenli, you have always been there, from the first days, when we would wonder why we are doing literature review, to the struggles of getting the papers accepted. Thank you my fratello, and I wish you the best for your future with Meiling. Francesca, thank you for being always a good friend, and for sharing the Italianness in the office, it made home a bit closer, and I did not have to answer by myself all the questions on whether pineapple on pizza is legit or not. Wiljan, thank you for being a good travel companion in LA and at the summer schools, and for the many discussions on power electronics. Lyu, the bouldering king, our evenings at DB have been the highlight of the work week for a long time, thank you for that. I would also like to thank the rest of the bouldering team, Calvin, Christian, Djurre, and Luis. Sachin, I enjoyed our long and challenging discussions on life, power electronics, and, more often, on bullshit, thank you bro. Mladen, thank you for the alternative and let's say unusual knowledge that you brought into the conversation, and for always being open to brainstorming how to solve practical problems in the lab. Yang, from working on the prototypes to the conversations about the spa, you were always full of surprises, thank you for that. Thank you Ibra for the post-lunch heated discussions on politics, economics, and especially Shell, I enjoyed being the devil's advocate. Aditya, thank you for being always open and honest with me, and for our late afternoon talks and discussion on what is fair and what is not. I know that you are now trying to "re-brand" yourself, but in my opinion, it would be a pity for the group to lose the old-time Aditya, so maybe you should reconsider it. Farshid, thank you for always being

available for losing a football match, you constantly proved that no matter who is on your team, that team would always lose. Dhanashree, thank you for always being kind, I enjoyed our daily conversations.

I also would like to thank Nils, Pavel, Soumya, and Guillermo for welcoming me into the group in 2018, and for the peculiar discussions during lunch and coffee breaks, and Yunhe, Lucia, Faezeh, Guangyao, Lu, Sorabh, Gautam, Miad, Dario, Joel, Nikos, Alvaro, Siddesh, Reza, Junjie, David, Pierpaolo, Jianning, Zian, and Gautham for the nice time shared in and outside the department.

My time in Delft has been enjoyable especially thanks to the friends I made during these years. Thank you Cristian, Jhon, Ana, Jithin, Raquel, Fabio, Soroush, Eszter, Daniel, and Rosana for all the barbecues, parties, tobacco, and nice days we spent together, with the hope of many more to come.

Elisa and Kevin, thank you for our continued friendship in spite living in different countries, and for always finding ways to connected.

My friends from Manzoni also deserve a special mention, for almost 15 years we have our own haven, where our friendship became a second family, thank you Ale, Ceres, Figo, Nazzo, Pisto, Toni, Trizio, and Zeta.

All of this would not have been possible without the unconditional support of my family. Through the good and difficult moments I have always felt your support, grazie mamma, papà, ed Elena.

Lastly I would like to thank Vitoria. You have been by my side since day 1, witness to all the joys and frustrations. When I look back, I cannot imagine how I could have done this without you. Thank you for always encouraging me and for being the best partner I could have asked in this journey. I cannot wait to see what the future has in store for us.

Biography

Marco Stecca was born in Abano Terme, Italy in 1994. He received the Bachelor's degree in energy engineering from the University of Padova, Italy, in 2016, and the Master's degree in electrical engineering from Politecnico di Milano, Italy, in 2018. From 2018 to 2022 he has been working towards a Ph.D. in the field of grid-scale battery energy storage systems at the Delft University of Technology. In November 2022 he joined McKinsey & Company as sustainability consultant.